UNIVERSITY OF LONDON THESIS

Degree PhD Year 2007 Name of Author TRICKETT, Susannah Kay

Mapping lithofacies within the D/K1 Kimberlite Pipe at Letlhakane, Botswana: An assessment of petrographic, geochemical and mineralogical indicators

Susannah Kay Trickett
Department of Earth Sciences
University College London

A thesis submitted for the degree of
Doctor of Philosophy

November 2007

ProQuest LLC
789 East Eisenhower Parkway
P.O. Box 1346
Ann Arbor, MI 48106-1346

For Mum and Dad, who always encouraged me to ask why.

Abstract

Mapping and characterisation of the Letlhakane D/K1 kimberlite pipe has allowed a detailed reconstruction of rock forming events and petrogenetic processes during near-surface emplacement of this kimberlite. This study combines different disciplines within geology, petrography, mineral chemistry and bulk rock geochemistry to delineate separate mappable lithofacies, and uses these groupings to understand the petrological processes responsible for forming each deposit and how these relate to physical emplacement conditions, chemical compositions of the parental magmas and sub-volcanic intrusion and emplacement processes. The primary geological field data was acquired by extended mine visits to examine drill cores through detailed logging and quarry face mapping, and describing variations in petrographic textures between lithofacies. Groundmass spinel compositions were used to establish mineralogical variations within discrete lithofacies and show that some lithofacies were derived from separate batches of magma and that mixing had taken place between lithofacies. Analysis of perovskite, abundant at Letlhakane, was used with spinel compositions to estimate the crystallisation sequence of the kimberlite groundmass; inferred changes in oxygen fugacity in the magma may have been particularly important. Multivariate statistical analysis of the bulk rock geochemistry provided confirmation of the lithofacies groupings which appear to represent discrete units of kimberlite. This also demonstrated a grainsize relationship with the geochemistry.

The major conclusions from this thesis show that the D/K1 kimberlite pipe was produced by dynamic and energetic eruptive processes which took place over sufficient time to allow crystallisation of one phase of

deposits before the eruption of another. The final chapter combines all the field observations and analytical results into a hypothetical phase diagram for kimberlite magma, extrapolated from high to low pressures and temperatures, and a new emplacement model. This model is specific to the Letlhakane D/K1 pipe, but it may prove to be applicable to other kimberlite bodies.

Acknowledgements

This thesis has been an amazing journey, both academically and personally. I have been incredibly fortunate to have taken part in a project which has involved interacting with so many people and which has given me the chance to experience new places and ways of thinking.

First and foremost I would like to express my warm thanks to my two supervisors, Adrian Jones and Matthew Field. Adrian has continued to support my research from when I was an undergraduate. Many thanks to Adrian for all his support and encouragement, and for carefully reviewing my work. I would like to thank Matthew for his teaching and guidance, enthusiasm, patience and support throughout the past few years. Through Matthew, De Beers and Debswana have provided the resources to travel out to Botswana so many times and the analytical aspect of much of this research, for which I am very grateful. I am also very appreciative for the opportunitites Matthew has provided to me, including particpating in De Beers workshops, meetings and discussions with the research group at Bristol University, field trips and training. I am in no doubt that without Matthew's thorough revisions of my work I would not have reached the level of understanding and experience of kimberlites which I have attained. Debswana Mining Coorporation is thanked for allowing me access to their mines, to collect samples and for providing me with super accomodation. De Beers and the EPSRC are thanked for providing the sponsorship for this research.

The five visits to Botswana would not have been as easy and enjoyable without the efforts and kindness of many people. Many thanks to

Johann Stiefenhofer for greeting me in Johannesburg on my first visit to southern Africa, and for the support on-site at Letlhakane and remotely back in London throughout the past few years. I would like to especially express my sincere thanks to Ashok and Lezel Doorgapershad who made their home my own on so many occasions and included me in many nights out, game drives and the camping trip into the Makgadikgadi Pans; even if I did end up soaked to the bone! Thanks also to Ashok, Volker Gartz, Augustine Lebani, Polite Khutjwe, Peter Kesebonye, James Kirby, Thabare Kango, Thebe Tlhaodi, Sipho Tefu, Alistair Gilbert, Brazil and Palapye for all their assistance and friendship on site at Letlhakane. Many thanks to Claire and Jason Palmer for their kindness and hospitality when I have passed through Johannesburg. Thanks to Claire also for being a good friend when she visited Orapa. I am grateful to Craig Smith for allowing me into the De Beers Geoscience Centre for a few days to look through their thin section collections and internal reports. Many thanks also to Ingrid Chinn for introducing me to flea markets in Johannesburg.

At UCL I would like to thank John Guest for many interesting and informative discussions about volcanology. Warm thanks to Andy Beard for teaching me how to use the electron microprobe at Birkbeck College, and for many discussions about kimberlites. I am very grateful to Judith Milledge for her support and sharing her knowlegde, and loaning me many books from her collection. Warm thanks go to Richard Brooker for numerous kimberlite chats and updating me in his research. Also for good company during the Kimberlite Emplacement Workshop in Canada. Jim Davy is thanked for showing me how to use the scanning electron microscope. I am indebted to Terry Williams and John Spratt at the Natural History Museum for use and assistance of the CAMECA wavelength dispersive spectrometer. Thanks to Teresa Jeffries, also of the Natural History Museum, who assisted in dating perovskites using the LA-ICP-MS, which was conducted as a pilot study by Craig Storey. Many thanks to Craig for involving me in trying to date the perovskites which I collected

from Letlhakane, and taking the time to carefully explain the theory. I am very grateful to everyone who was involved in transporting and preparing my samples both for probe sections (Sean Hughes at UCL) and bulk rock analysis (Gavin Martin of SGS Lakefield and Vanessa Bocks of the Anglo American Research Laboratories).

I am very grateful to Steve Sparks and the research group at Bristol University for including me in their discussions and inviting me on field trips. Many thanks to Steve for his kind support after I presented at the Kimberlite Workshop, and for sharing his knowledge unpublished work. I am very grateful to Richy Brown for reviewing my work and for his good humour and friendship.

There are many friends and peers who have continually supported me throughout this research. At UCL I would like to express my thanks to Katie Joy for great friendship and tireless support; for picking me up on countless occasions with well needed tea and cake! Thanks to Dominic Fortes, Peter Grindrod and Emma Tomlinson for many discussions, continued encouragement and for reading my work. I would also like to thank Ed, Dan, Emily, Helen, Terry, Joyce, Mike, Olly and Claire for their continued friendship. At Bristol University my thanks go to Tom and Janine for their support and good company in Africa and Canada. Thanks to Clare, Charly, Emma and Becca for never getting bored of me talking about my thesis.

Finally, I must extend my warm appreciation to all of my family for their love and strong support. In particular, Neil for distracting me when needed. I am incredibly grateful to my Mum who has tirelessley listened, read, corrected and nudged me forwards when I was stuck in a rut. Thank you for picking me up at the point when I thought I couldn't continue, and for keeping my feet on the ground. Last, but by no means least (!) I would like to say thank you to Andrew for being an endless wall of support and love, and for persistently encouraging me to "get on with it"! Thanks to Andrew for never

complaining when I go away and letting me have my own space to think and write.

Contents

List of Figures

Chapter 1

Introduction

1.1 Objectives

The objective of this study was to assess the potential of geological, mineralogical, petrographic and geochemical indicators in characterising the kimberlite within the D/K1 pipe at the Letlhakane Mine in Botswana. This research demonstrated that many types of kimberlite occur within this one pipe which were characterised by different geology, mineralogy, petrography and geochemistry. This investigation has given much greater insight into the nature of diatreme facies volcaniclastic kimberlite deposits. Even though gross-scale differences exist, there are also considerable variations within lithofacies, in particular at the microscopic scale. Differences between kimberlite lithofacies and subtle differences within lithofacies are formed by a series of eruptive phases from pulses of magmatic activity in the conduit which produce many eruptions with periods of intermittent quiescence. Each major eruptive phase has a subtly different path of evolution, which may have been controlled by pressure, temperature, oxygen fugacity (fO_2), co-crystallising phases, entrainment of xenoliths and xenocrysts and the proportion of gas phase in the melt. This variation cannot easily be explained by a single process but suggests a complex, perhaps long-lasting formation of the diatreme facies kimberlite at Letlhakane.

The first step in characterising the kimberlite body was a study of the large field-scale features by drill core logging and face mapping in the mine during field trips in 2003, 2004 and 2005. These observations, together with the pet-

rography, were used to identify six texturally discernable types of kimberlite, or major lithofacies associations[1]. A detailed electron microprobe study was carried out on groundmass spinels which are effective petrogenetic and geochemical indicators (e.g. Irvine 1965, 1967). The spinel compositions were used to gain an understanding of how the kimberlite melt or melts evolved and showed how they can fingerprint the individual lithofacies. A similar study was conducted on groundmass perovskites due to their high abundance at Letlhakane. Groundmass spinel and perovskite compositions were used to propose a crystallisation sequence for the kimberlite melt. Bulk rock major and trace element geochemistry was analysed using XRF on an extenisve set of samples collected during field visits to Letlhakane. The results were processed using multivariate statistical analysis which permits the data to be divided into clusters that reinforced the kimberlite lithofacies. This method also illustrated which elements controlled the separation of the data into these clusters, which related to mantle, magma or the crust components. Multivariate statistics proved to be a powerful tool in delineating kimberlite lithofacies. Finally, an inexpensive technique of dating kimberlite emplacement was also investigated, however, this did not contribute significantly to characterising the D/K1 pipe, but it has promoted an independent further study of this kind (Appendix D). Chapter 7 draws together all geological and petrological observations, mineralogical and geochemical data into a final discussion to propose a model for the evolution of the D/K1 kimberlite pipe at Letlhakane.

1.2 Brief Outline of Chapters

Chapter 2 provides a constructive review of the kimberlite literature for the ensuing chapters and discussions. Particular attention was given to reviewing kimberlite emplacement and the formation of pipes and their deposits. This was done in conjunction with recent papers which contest some of the previous theories.

[1] "A mappable subdivision of a stratigraphic unit that can be distinguished by its facies or lithology; the texture, mineralogy, grain size and the depositional environment that produced it." (http://www.glossary.oilfield.slb.com).

Chapter 3 presents the geological and petrological variations of the kimberlite body and the criteria used to divide it into six texturally discernable major lithofacies associations. The chapter outlines the previous work carried out on the D/K1 kimberlite including the old geological model and why this needed updating. Drill core logs are presented in Appendix A. A synopsis of each lithofacies is presented along with petrographic descriptions illustrated by photomicrographs. An interpretation of each lithofacies is proposed and drawn together as an emplacement model for the D/K1 kimberlite pipe.

Chapter 4 investigates how variations in groundmass spinel compositions relate to petrogenetic and physiochemical processes. This includes understanding the relationships between spinel composition and co-crystallising phases, changes in pressure, temperature and oxygen fugacity (fO_2). D/K1 spinel compositions are enriched in TiO_2, which was considered inherent of the parent melt composition. The chapter also demonstrates how spinel compositions can be used to fingerprint kimberlite lithofacies and endorses the original statement that the kimberlite in the D/K1 pipe is made up of multiple eruptive phases.

Chapter 5 presents groundmass perovskite compositions, considered to be an important part of the study due to the minerals unusually high abundance at D/K1 compared with groundmass spinels. Groundmass perovskites are believed to have crystallised later than groundmass spinels (Mitchell, 1986b), and therefore their composition furthers the understanding of the groundmass crystallisation sequence at Letlhakane. Calculations of oxygen fugacity show that this may have been an important parameter during crystallisation.

Bulk rock geochemistry of heavily altered kimberlite deposits, such as those at Letlhakane, are not considered representative of the parent melt because:

> "...the hybrid nature of the rocks formed from magmas which carry a high proportion of crystalline phases at their time of emplacement: and by the high probability of contamination of some facies by crustal materials and/or groundwater." Mitchell (1986b)

However, a study by Nowicki (1993) demonstrated how bulk rock geochemistry could be used to distinguish between the main lithofacies in the D/K1 pipe. Chapter 6 expands this study by collecting an extenisve set of samples covering

the pipe laterally and vertically from which bulk rock geochemistry was analysed by XRF. Multivariate statistical analysis of the data provided confirmation of the lithofacies identified in Chapter 3 by forming geochemical groupings which appear to represent discrete units of kimberlite.

The final chapter combines all the field observations and analytical results into a hypothetical phase diagram for kimberlite magma, which was extrapolated from high to low pressures and temperatures, and a new emplacement model for the D/K1 pipe.

1.3 Geology of the Study Area

The Letlhakane kimberlite belongs to a cluster of approximately 85 kimberlite pipes (Field, *pers. comm.*) located ~200 km west of Francistown in the Boteti District of Central Botswana (Fig.1.1). It is one of four pipes (A/K1, B/K9, B/K12 and D/K1) currently mined in the area by the Debswana mining corporation. The largest mine locally is Orapa A/K1, 40 km to the north west of Letlhakane Mine, which is well known for its preserved crater deposits (Field et al., 1997; Shee & Gurney, 1979). The smallest is Damstshaa which consists of two mined pipes (B/K9 and B/K12) that were officially opened in October 2003. Letlhakane comprises of two pipes, D/K1 and D/K2, which intruded into the Achaean Zimbabwe Craton (2.5-3.0 Ga) (Deines & Harris, 2004; James et al., 2001). No definitive age data is available for the Letlhakane kimberlite, however Orapa was dated to 93 Ma, and Letlhakane is considered to have a roughly similar age by Stiefenhofer et al. (1997) and Deines & Harris (2004). The surface area of the D/K1 and D/K2 pipes at the current surface outcrop is 11.6 and 3.6 hectares respectively (Stiefenhofer et al., 1997). The D/K2 pipe consists of massive volcaniclastic kimberlite, a later-stage dark, coherent kimberlite and a zone of country rock breccia concentrically arranged around the edge of the kimberlite pipe (Field & Scott Smith, 1998). Only the larger D/K1 pipe is mined today, and is the one studied in this thesis.

The Letlhakane Kimberlite was emplaced through Archean basement of gneiss and granite and into the Karoo Supergroup. The basement belongs to the cratonic root of the Zimbabwe Craton, which is believed to reach depths of 300 km based

on seismic tomography surveys (e.g. James et al. (2001) and Shirey et al. (2004)). The Karoo is overlain by 4 to 10 m of Cretaceous to recent Kalahari sediments and calcrete (Smith, 1984; Stiefenhofer et al., 1997). The Karoo Supergroup consists of an upper basaltic flood deposit called the Stormberg Basalts. These are a series of lava flows, with individual flow units up to 30 m thick characterised by concentration of pipe vesicles (now infilled by calcite and zeolite) at the base and small vesicles towards the top of each flow. The basalt can be quite coarse grained in places, resembling a dolerite. These flows have been constrained to 180 $\pm$ 7 Ma, which corresponds with the ages of Karoo basalt in South Africa (Smith, 1984). At Letlhakane the Stormberg basalt has an average thickness of 130 m (SRK, 2001) and lies uncomformably over the Ntane Sandstone unit below. This sandstone has aeolian and fluviate facies. Again, this lies unconformably over laminated sandstones and mudstones of the Mosolotsane Formation. The contact between Ntane and Mosolotsane is taken where a red, coarser grained sandstone first occurs. The Mosolotsane grades into red and green silty mudstones and finally into a lighter grey, fine grained mudstone of the Tlhabala Formation, the lower part of which progresses into the Tlpana carbonaceous mudstones. The Tlpana Formation contains around 26 coal seams interbedded with brown-grey mudstones, of which 6 bands are $\geq$0.3 m thick (Smith, 1984). This sedimentary sequence is about 300 m thick beneath the basalt. The basement granite and gneiss is intersected at $\sim$500 m below surface level.

Today the mine excavation is 1050 m in diameter. The rim of the mine lies at an elevation of 1010 m above mean sea level and the mine excavation was at 275 m deep at the time of the last visit (2005). The mine is currently operated through open-cast mining (Fig. 1.2), however by 2012 production will have to change to underground mining if this is economically feasible (P. Kesebonye, *pers. comm.*). The research carried out for this thesis has provided supplementary information to aid this decision.

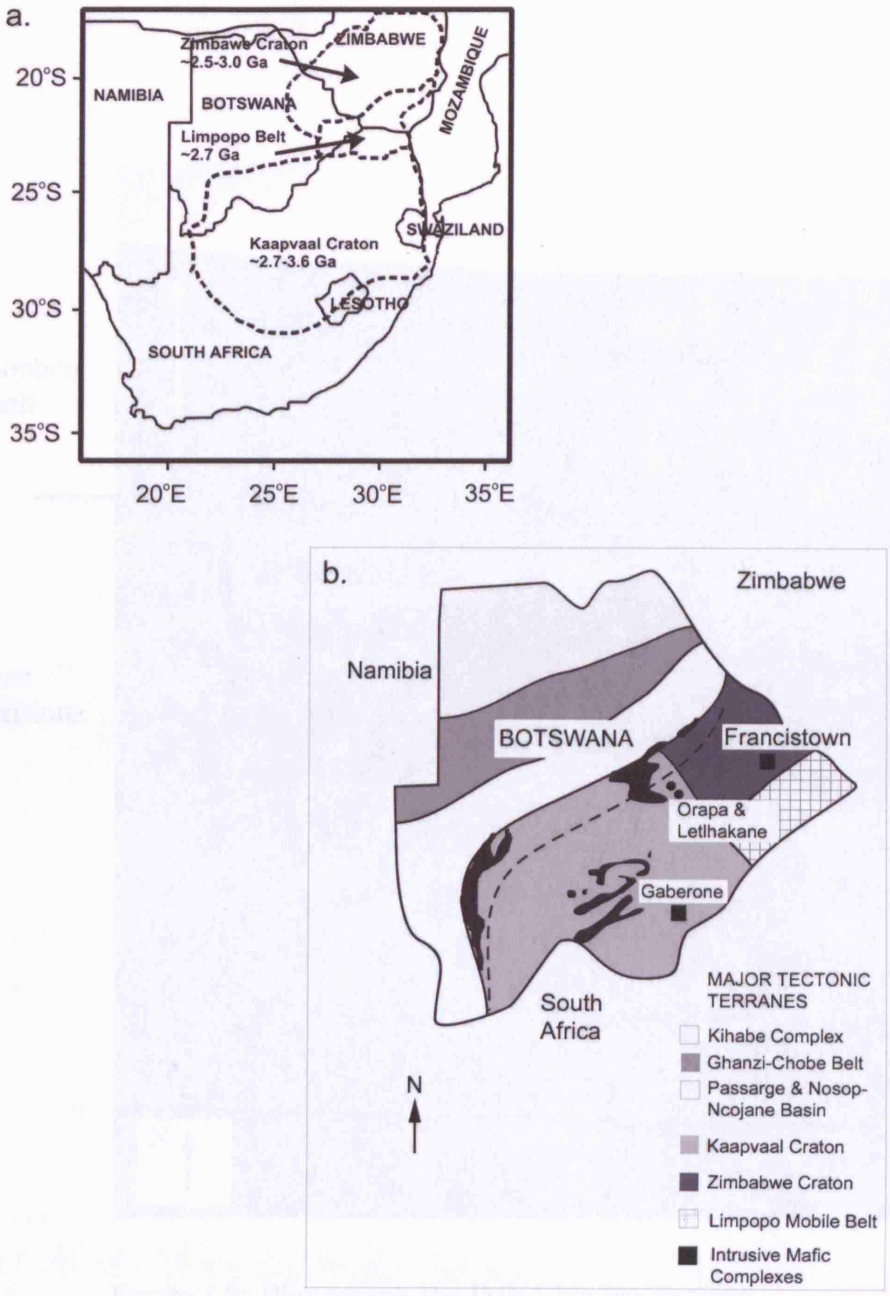

Figure 1.1: (a) Geological map of Southern Africa; solid lines are country borders, dashed lines are the boundaries of the Kaapvaal and Zimbabwe Cratons, and the Limpopo Mobile Belt (modified from James et al. (2001)). (b) Enlarged sketch-map of Botswana showing major tectonic and geological terranes, and the location of the Orapa and Letlhakane Mines (dashed line is the Kalahari Suture Zone). Adapted from Key & Ayres (2000).

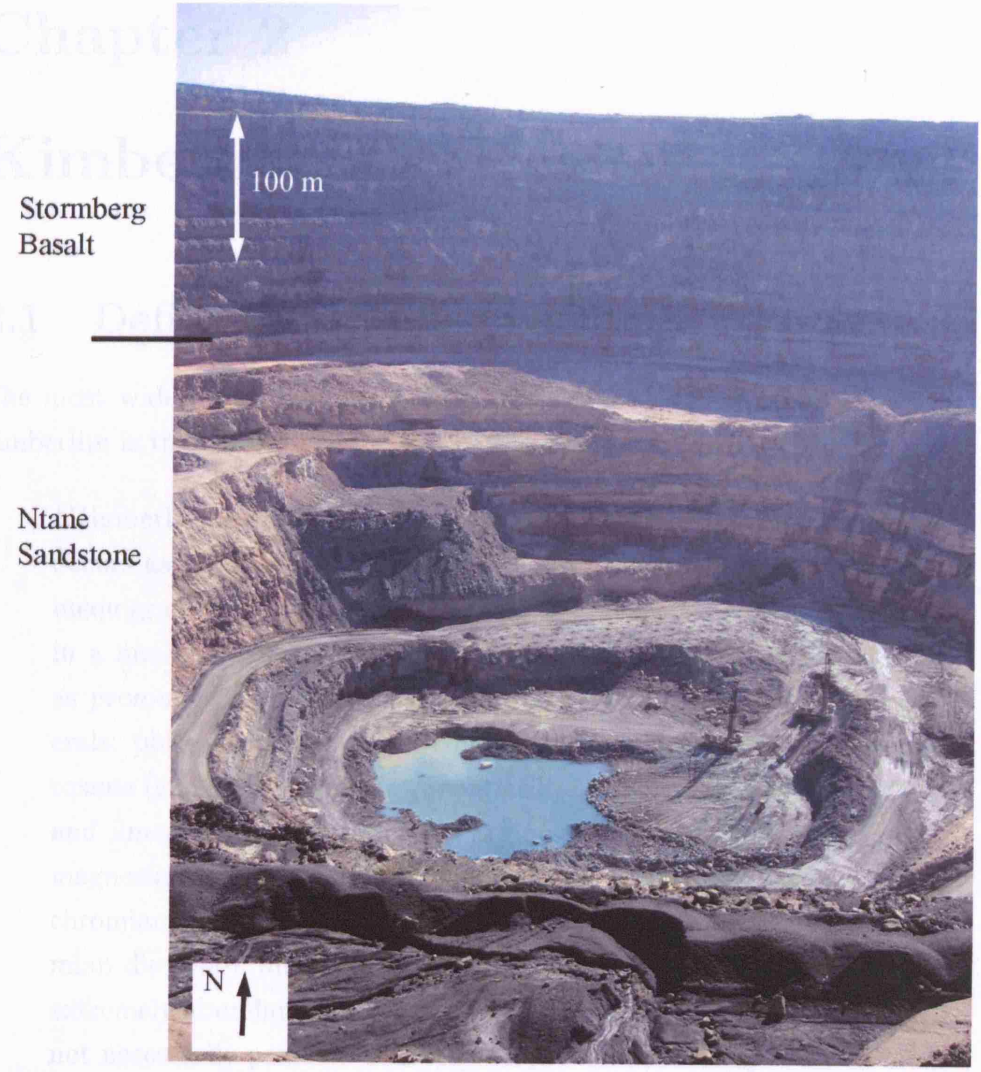

Figure 1.2: Photograph the D/K1 kimberlite pipe.

Chapter 2

Kimberlites: A Review

2.1 Definition of a Kimberlite

The most widely cited definition (e.g. Shee (1985) and Mitchell (1986a)) of a kimberlite is that of Clement et al. (1984):

> "Kimberlite is a volatile-rich, potassic, ultrabasic, igneous rock which occurs as small volcanic pipes, dykes, and sills. It has a distinctively inequigranular texture resulting from the presence of macrocrysts set in a fine-grained matrix. This matrix and/or groundmass contains, as prominent constituents, olivine and several of the following minerals: phlogopite, carbonate (commonly calcite), serpentine, clinopyroxene (commonly diopside), monticellite, apatite, spinels, perovskite and ilmenite. The macrocrysts are anhedral, mantle-derived, ferromagnesian minerals which include olivine, phlogopite, picroilmenite, chromian spinel, magnesian garnet, clinopyroxene (commonly chromian diopside), and orthopyroxene (commonly enstatite). Olivine is extremely abundant relative to the other macrocrysts, all of which are not necessarily present. The macrocrysts and relatively early-formed matrix minerals are commonly altered by *deuteric* processes, mainly serpentinisation and carbonitisation. Kimberlite commonly contains inclusions of upper mantle-derived ultramafic rocks. Variable quantities of crustal xenoliths and xenocrysts may also be present. Kimberlite may contain diamond but only as a very rare constituent."

This definition forms the basis for the following discussion, which develops the concepts further by considering kimberlite emplacement. The word deuteric is italicised above on account of a recent study by Stripp et al. (2006) who proposed that the interclast matrix is composed of alteration products produced by hydrothermal metamorphism, not the higher temperature residual kimberlite fluids as suggested by Trofimov (1970) and Clement et al. (1984). An additional key observation by Wagner (1914, 1971) was the identification of two texturally and mineralogically distinct types of kimberlite in southern Africa. Smith (1984) later reinforced this with an isotopic study and divided kimberlites into 'non-micaceous' Group I, and 'micaceous' Group II. Letlhakane is a Group I, non-micaceous kimberlite. For a more comprehensive review of kimberlites see Dawson (1980); Mitchell (1986b) and Mitchell (1995) and references therein.

2.1.1 Kimberlite Occurrence

Kimberlites are found within and at the edges of ancient continental cratons (Fig. 2.1). They are volumetrically insignificant (Dawson, 1972) and only 5000 kimberlite bodies are known worldwide, 500 of which are diamondifereous (Janse & Sheahan, 1995). Diamondiferous deposits are associated with kimberlite bodies located within Archean cratons (Boyd & Gurney, 1986) and kimberlite exploration in these terranes is relentless due to the economic value of diamonds. Kimberlites typically occur in clusters, fields, districts and provinces (Gregoire et al., 2006) (Fig. 2.1). A comprehensive review of global kimberlite distribution is given by Dawson (1986) and Janse & Sheahan (1995). Figure 2.2 show the distribution of kimberlites and related rocks across the southern African subcontinent.

Kimberlites also cluster into time periods. Kimberlite emplacement in southern Africa took place principally during six major time peaks:

1. **85-100 Ma** - including Orapa, Letlhakane (Stiefenhofer, 1993) and the Kimberley cluster (Le Roex et al., 2003)
2. **~120 Ma** - Barkley West (Phillips et al., 1998)
3. **~240 Ma** - Jwaneng (Richardson et al., 2004)

4. **519 Ma** - Venetia (Barnett, 2004)

5. **~1200 Ma** - Premier (Smith, 1983 *cited in* Gregoire et al. (2005))

6. **1600 Ma** - the Kuruman kimberlites (Dawson, 1986)

Canadian kimberlites predominantly date to the Cretaceous (Janse & Sheahan, 1995), with the exception of the Ekati kimberlites which have been dated between 45-61 Ma (Creaser et al., 2004). Kimberlites found within the Dhawar craton in India, Venezuala, West Greenland and Western Australia were generally emplaced during the Proterozoic (Chalapathi Rao et al., 2004).

Wagner (1914, 1971) noted how kimberlites in southern Africa are confined to old continental crust and suggested a connection with their deep origin. Although there has been considerable research into potential triggers of kimberlite events, a general concensus has not been reached (Helmstaedt & Gurney, 1995).

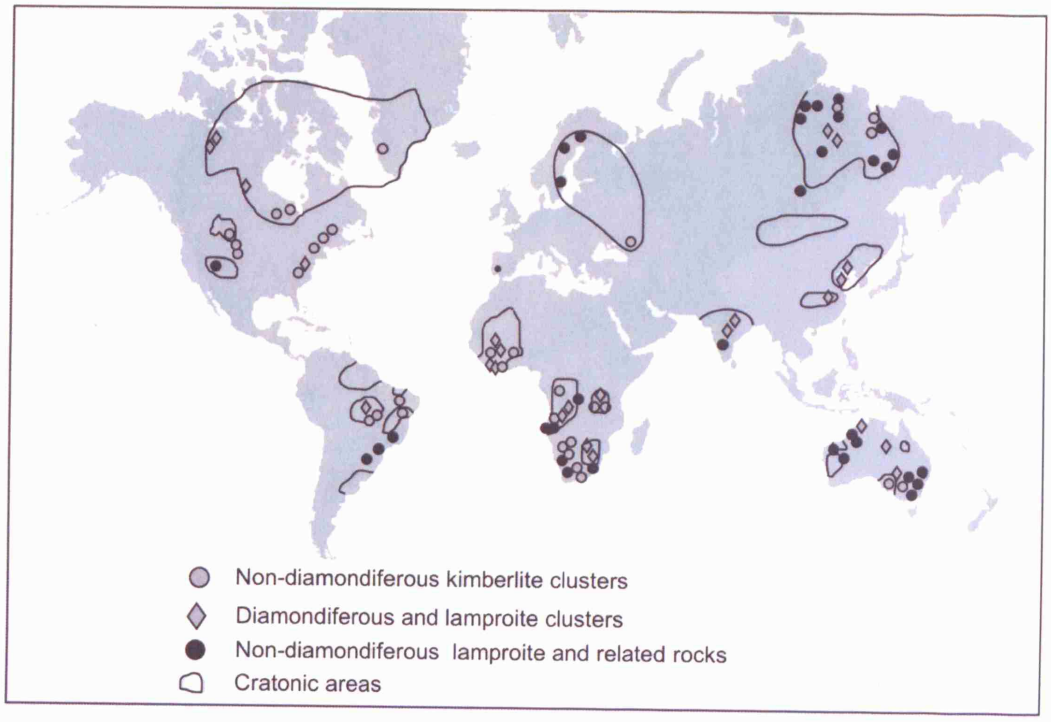

Figure 2.1: Global distribution of kimberlites and related rocks. Modified from Fipke et al. (1995) p16.

2.2 Model of a Kimberlite Pipe

Kimberlites are found as sills, dykes and pipes (Dawson, 1980; Mitchell, 1986b), although the research bias has focussed on the geology of pipes as many have been exposed through diamond mining. Hawthorne (1975) investigated many different kimberlite bodies in southern Africa and designed a model which is still widely accepted. Clement & Skinner (1985, 1979) developed this model further by dividing the pipe into three zones which are charactersied by texturally distinct kimberlite. A combination of these two studies is shown in Figure 2.3 and summarised as: (i) an irregular root zone at depths $\geq$600 m comprising of magmatic or hypabyssal kimberlite, (ii) a steep-sided diatreme with an average dip of 80^o, infilled with fragmental, massive volcaniclastic kimberlite, and (iii) a flared

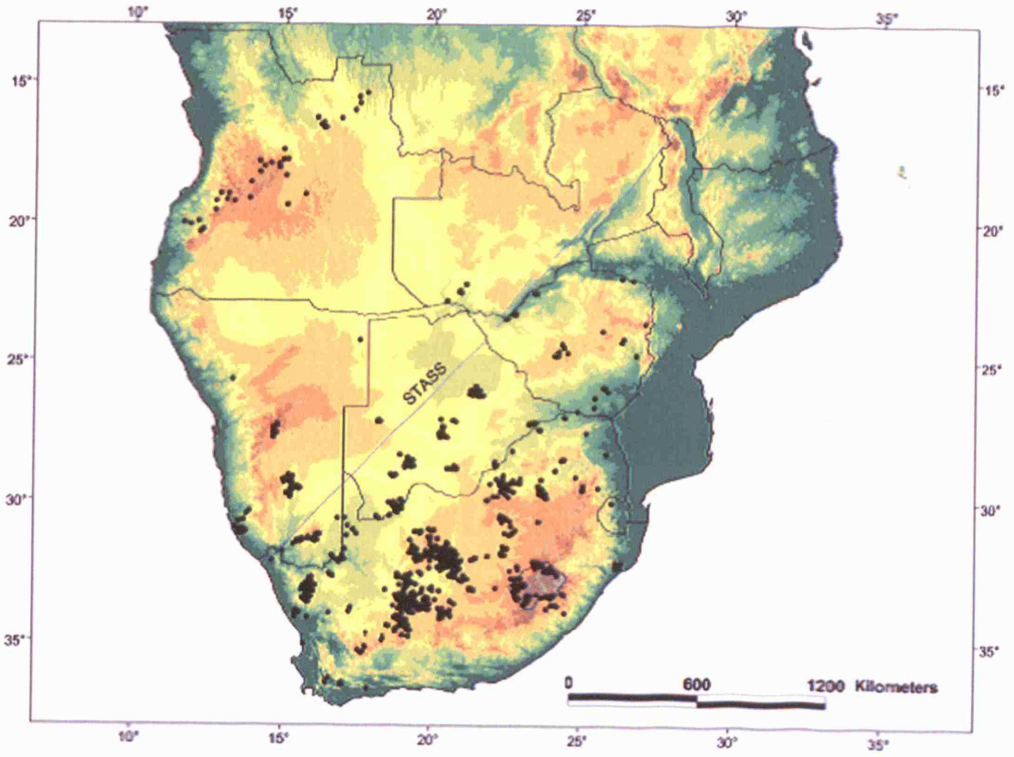

Figure 2.2: Distribution of kimberlites and related rocks across Southern Africa displayed on digital elevation model. Shows the Southern Trans-Africa Shear System (STASS). From Jelsma et al. (2004).

($\sim 50 - 70°$) crater basin and a possible tuff ring with a diameter of around 300 m, infilled with volcaniclastic, probably pyroclastic kimberlite (Clement & Skinner, 1985; Hawthorne, 1975). Simplified, the pipe has a 'carrot'-shaped geometry with a flared crater at the top. The root zone, however, is much more complex as highlighted by Clement & Reid (1989) at the Wesselton, De Beers and Dutoitspan pipes where there is evidence of multiple discrete intrusions, contact breccias and intrusions which did not breach the surface. The textural definitions of hypabyssal, diatreme and crater facies kimberlite are discussed below.

Hawthorne's model was created at a time when research focussed on southern African kimberlites. As exploration and the study of kimberlites grew at other locations, notably Canada and Russia, additional types of pipe were identified (e.g. Field & Scott Smith (1998)). Skinner & Marsh (2004) defined two new types of kimberlite pipe in Canada: Class 2 are shallow, wide pipes infilled with pyroclastic kimberlite and Class 3 are steep-sided pipes infilled with reworked deposits, including epiclastic kimberlite (Fig. 2.4). Such variations are intuitively attributed to emplacement mechanisms. Field & Scott Smith (1998) have further interpreted these different pipe structures by different host rock stratigraphies: Class 1 pipes were emplaced into competent country rocks, e.g. the Karoo at Letlhakane; Class 2 into poorly consolidated sediments, e.g. the shales and clay-rich silts at Fort a la Corne in Canada; Class 3 into soft sediments overlying competent basement (Field & Scott Smith, 1998). Skinner & Marsh (2004) showed that these three different types of pipe can be found within the same geological setting, e.g. north-east Angola, the Ekati cluster in Canada and in Siberia.

2.2.1 Erosion of Kimberlite Pipes

Hawthorne (1975) outlined the different levels of present day exposure between individual kimberlite bodies in southern Africa, which raised the question of how do we accurately know how much of a kimberlite body has been eroded? Gallagher & Brown (1999) determined denudation of $\sim$2 km from the Atlantic margin of southern Africa since the Jurassic, and Brown et al. (2002) determined 2.5-3.0 km from the Drakensburg Escarpment of southern Africa. Although these studies do not extend to the study region of Orapa and Letlhakane, they can be

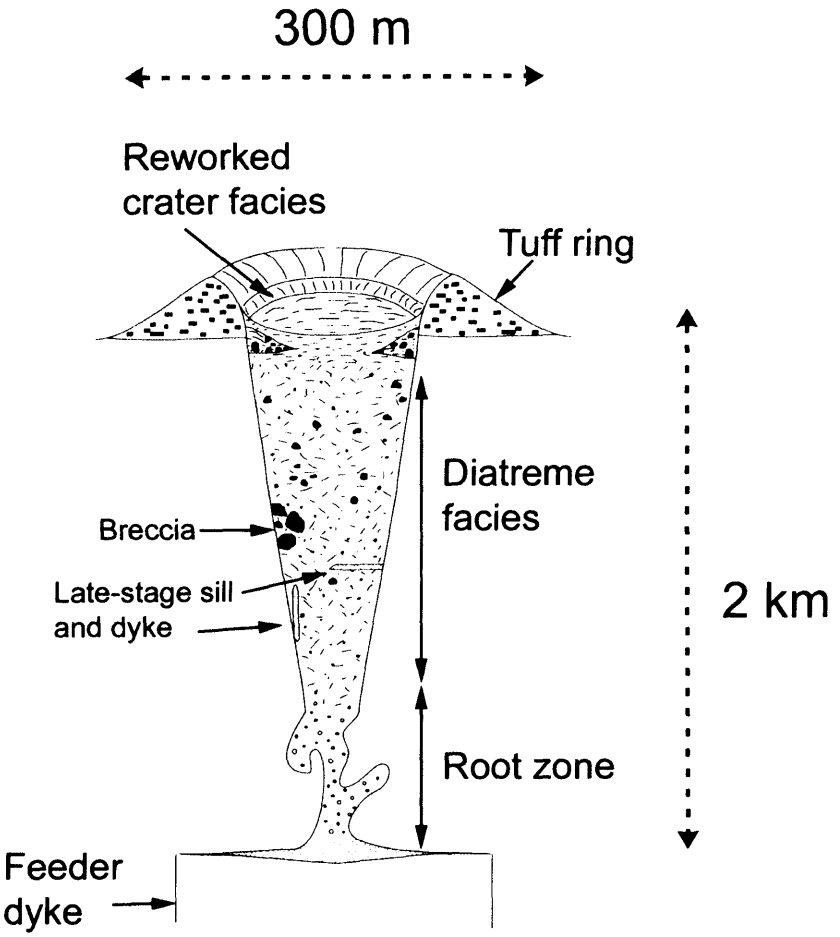

Figure 2.3: Model of a "classic" or Class 1 kimberlite pipe (modified from Mitchell (1986b) p30).

used to estimate that between 2-3 km has been eroded from the southern African sub-continent. Hawthorne (1975) divided kimberlite occurrences of the southern African sub-continent by provinces which had crater facies kimberlite and those that did not. There is a clear dichotomy as shown in Figure 1 from Hawthorne (1975). Preserved craters (defined by Hawthorne (1975) as basins filled with kimberlitic lacustrine deposits) are found in Tanzania, Zambia, Botswana, Zaire, Angola, Mali and South Africa. Included fragments of lithics from lithologies that are no longer present at a particular pipe are good indicators of erosion. Examples

of these bodies include the Venetia mine where the kimberlite contains fragments from the Soutspanberg which is found at elevations 800 m above the current surface; Premier Mine which contains fragments of the Waterberg formation which no longer form the wall rock; at Koffiefontein and Jagersfontein kimberlites which both contain basaltic lava fragments which detailed surveys of the local stratigraphy indicate could only have originated from the Stormberg flood deposits, again no longer present as wall rock at these two locations (Hawthorne, 1975). Exactly how much has been eroded however is difficult to determine and this restricts our understanding of kimberlite emplacement because the complete structure of a pipe is hardly ever preserved in the geological record. The Orapa and Letlhakane cluster is a good example of how complex this issue is. Orapa has a preserved crater (Field et al., 1997) whereas Letlhakane does not (although a block interpreted as crater facies was found by Field (1988b)). A second preserved structure is the Mwadui Pipe in Tanzania (Stiefenhofer & Farrow, 2004).

2.3 Kimberlite Petrography

Petrographically kimberlites are complicated rocks for the following reasons: (i) they contain a diverse range of *non-primary*/accidental components (Dawson,

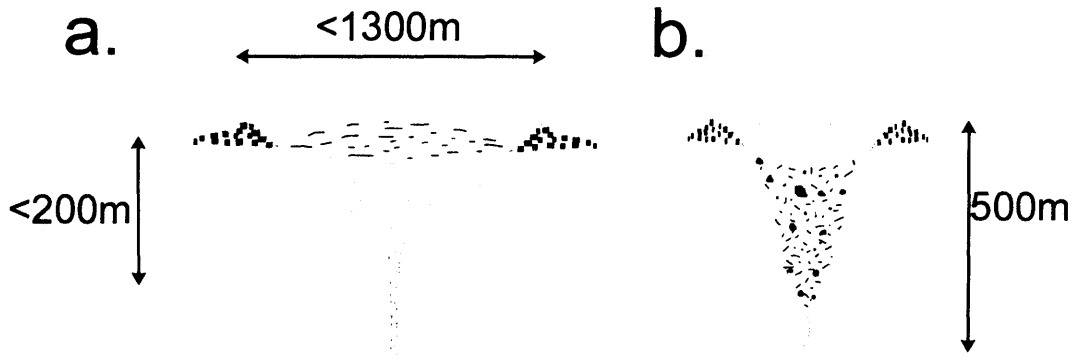

Figure 2.4: Model of (a) class 2 and (b) class 3 kimberlite pipes (modified from Field & Scott Smith (1999); Walters et al. (2006)).

1980; Mitchell, 1986b); (ii) they have undergone extensive alteration (Skinner & Clement, 1979; Stripp et al., 2006) and the deposits which are seen today have probably greatly changed from their original form; (iii) there are different petrographic varieties of kimberlite (Clement & Skinner, 1979). This section will summarise kimberlite petrography by first considering the included fragments followed by consideration of the different types of kimberlite deposits.

2.3.1 Accidental Clasts

Kimberlites host a significant range of types and proportions of accidental clasts, giving them a distinct, inequigranular texture. Dawson (1980) classified the clasts by their different origins:

1. The country rock surrounding the kimberlite, including lithologies which may have been totally eroded away since kimberlite emplacement (e.g. Venetia, Premier and many others).

2. Shallow-level crustal and/or metamorphic material, for example basement garnet granulites at Letlhakane.

3. Mantle material, including xenoliths and xenocrysts.

2.3.1.1 Mantle Xenoliths

Terrestrial volcanic rocks frequently contain mantle xenoliths (Hansteen et al., 1998), but they are particularly common in kimberlites (e.g. Dawson (1980) and references in Nixon (1973)). Kimberlites host a range of xenoliths that fall into three principal categories; (i) peridotites and pyroxenites, (ii) eclogites and (iii) metasomatised nodules including glimmerites (Fig. 2.5b), and MARID (mica, amphibole, rutile, ilmenite, diopside and zircon) xenoliths (Dawson, 1980). Mantle xenoliths in kimberlites are relatively unaltered and characteristically rounded. The types of xenoliths within individual pipes from the same kimberlite cluster can vary. For example Orapa hosts proportionally more eclogites (Shee & Gurney, 1979) whereas Letlhakane, only 40km away, hosts more peridotites (Stiefenhofer et al., 1997). Letlhakane contains a suite of mantle nodules which are interpreted

as representing progressive mantle metasomatism from garnet peridotites to phlogopite peridotites and wehrlites (Stiefenhofer, 1993; Stiefenhofer et al., 1997; van Achterbergh et al., 2001). Disintegrated mantle xenoliths produce a range of discrete grains and small microxenoliths of peridotitic and eclogitic affinities. At Letlhakane olivine, garnet, chrome-diopside, ilmenite and phlogopite xenocrysts predominate. Proportions of included mantle xenoliths vary between kimberlite bodies, and can be as high as 50% (Cox et al., 1973), although an average of 2% is more common (Dawson, 1980). Mantle xenoliths provide an important window into the composition of the mantle and can also be used as real samples for the testing of physical processes which are believed to take place within the upper mantle (Markwick & Downes, 2000; Stiefenhofer et al., 1997). A good review of mantle xenoliths in kimberlites can be found in Dawson (1980); Nixon (1995) and all volumes of the International Kimberlite Conference.

2.3.1.2 Megacrysts

Megacrysts are a suite of large, monomineralic ($\geq$10 mm) anhedral crystals (Gurney et al., 1979; Mitchell, 1986b; Shee & Gurney, 1979). They include olivine, garnet, clinopyroxene, orthopyroxene, phlogopite, ilmenite and zircon. Inclusions of one megacryst in another rarely occur (Fig. 2.5a and c). Megacrysts can be separated into two compositional groups; Cr-rich and Cr-poor (Eggler et al., 1979; Gurney et al., 1979; Harte & Hawkesworth, 1986). Compositions of the Cr-rich suite are similar to mantle peridotites found in kimberlites, and are therefore considered to be porphyroclasts of disaggregated lherzolites and non-cognate with the kimberlite melt (Nixon, 1973), in other words they are xenocrysts. Cr-poor megacryst compositions are significantly different from compositions of mantle xenoliths and the debate continues regarding their origin; a good review of these arguments is given in Shee & Gurney (1979) and Nowell et al. (2004).Their wide compositional variation, especially in Mg/Mg+Fe and Ca/Ca+Mg and increasing Fe contents with decreasing temperatures (derived from clinopyroxene geothermometry e.g. Gurney et al. 1979; Nixon 1973), implies they formed by crystal fractionation from a melt (Eggler et al., 1979; Harte & Hawkesworth, 1986). Eggler et al. (1979) and Pasteris et al. (1979) noted how inclusions and intergrowths in megacrysts are compositionally similar, supporting the interpretation

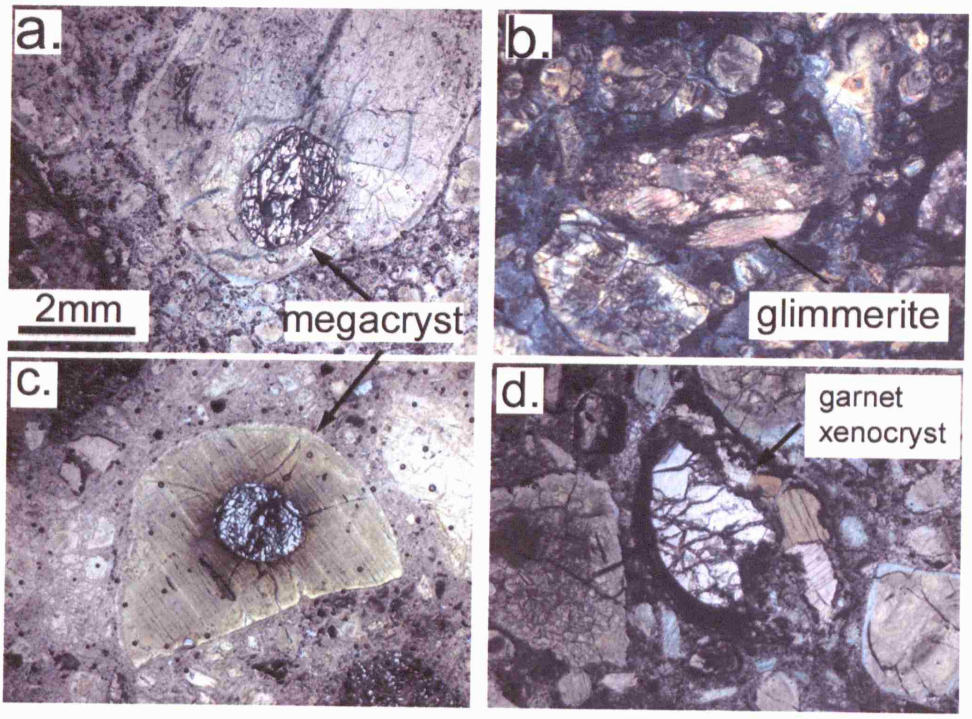

Figure 2.5: Photomicrographs of mantle-derived minerals from Letlhakane. (a) Garnet inclusion in a serpentinised olivine megacryst. (b) Glimmerite nodule. (c) Garnet inclusion in broken pyroxene. (d) Metasomatised garnet lherzolite xenolith.

that these minerals coexisted in equilibrium. The wide range of Cr-poor compositions at temperature ranges between 200-300°C occur with small changes in pressure, which complicates their petrogenesis.

The non-genetic term macrocryst will be given to anhedral crystals of any origin as recommended by Clement & Skinner (1985).

2.3.1.3 Olivine

Olivine is the most abundant mineral in most (Group I) kimberlite bodies (Skinner & Clement, 1979), however a paradox occurs regarding its origin. Olivine in kimberlites is present in two forms; (i) small (leq0.5 mm) subhedral to euhedral and (ii) larger (0.5-10 mm) anhedral grains with common fractured surfaces. As a first approximation it is logical that small, euhedral grains are primary ground-

mass phases and the larger, rounded anhedral grains are disaggregated mantle xenoliths. However, larger, euhedral olivines are also present in some kimberlites and can sometimes define a porphyritic texture (Mitchell, 1986b). Therefore, are all olivines primary to the kimberlite melt, or are a proportion of the larger grains both xenocrystal and phenocrystal? This is complicated further because compositions of olivine phenocrysts and xenocrysts overlap. For clarity during this thesis large olivine grains will be called 'macrocrysts' as recommended by Clement et al. (1984).

2.3.1.4 Diamonds

Terrestrial diamonds have two major parageneses; (i) products of shock pressures produced during meteorite impacts (French, 1998) and (ii) primary mantle minerals sampled and brought to the surface by ultramafic magmas, predominantly kimberlites and subordinately lamproites. Primary mantle diamonds are either found *in situ* in kimberlite bodies or as alluvial and marine deposits from erosion of their hosts. They are also found as inclusions within mantle xenoliths entrained by kimberlites, which represent the source rocks which they formed in (Bulanova, 1995; Gurney, 1986). Diamonds are classified by their source (peridotitic or P-type and eclogitic or E-type), their habit (Gurney 1986 gives a good summary of diamond forms) and their nitrogen content (Type I and Type II; nitrogen present and absent respectively). Dating studies of diamonds and their inclusions has revealed a dichotomy in their ages; P-type diamonds have been dated between 3.0 - 3.3 Ga and E-type diamonds between 990 - 1670 Ma (Bulanova, 1995).

The formation of most diamonds takes place at pressures between 40-60 kbar and temperatures between 1000-1300^{o}C, corresponding to depths between 150-200 km (Bulanova, 1995). They have two major growth mechanisms. Gem-quality stones and euhedral cores of more irregular habits grew slowly in near equilibrium conditions under carbon saturation, and have carbon isotope δ^{13}C values between -4 to -23 parts per thousand. Irregular rims or coats around octahedra and polycrystalline diamonds grew rapidly in more saturated conditions (Bulanova, 1995) and have δ^{13}C between -5 to -8 parts per thousand (Tomlinson et al., 2005). These latter stones have been linked with the kimberlite emplacement event reinforced by close Sr isotope contents of diamond and kimberlite at

Mbuji Maya in the DRC (Gurney, 1986). Tomlinson et al. (2005) rejected this model however on account of different large ion lithophile elements (LILE) and Ti contents between kimberlite and diamond "phenocrysts".

Mineral inclusions are a common feature in diamonds. The most abundant inclusions are sulphides, orthopyroxene, olivine, garnet, chromite and clinopyroxene. Olivine and chromite are exclusive to P-type diamonds (Gurney, 1986). Mineral inclusions completely enclosed in the diamond are perfectly preserved and therefore provide a direct window into compositions and dynamics of the mantle at the time of growth. For example, Deines & Harris (2004) studied $\delta^{13}C$ isotopes in inclusions of diamonds from both Orapa and Letlhakane and showed that Letlhakane hosts more P-type to E-type diamonds, the reverse of Orapa, a relationship which is matched by the mantle xenolith content (Section 2.3.1.1). Small divergences in diamond $\delta^{13}C$ content between Letlhakane and Orapa lead Deines & Harris (2004) to conclude that there are km-scale heterogeneities in petrology and carbon isotope distribution. This could either be a lateral or a vertical variation.

2.3.1.5 Country Rock Fragments

The amount and type of included country rock fragments varies between and within individual kimberlites. The type varies according to the regional stratigraphy. Letlhakane and Orapa were both emplaced through the Karoo stratigraphy and contain fragments of mudstones, sandstones and basalt, and the Archaean granite basement. Included crustal fragments are typically unaltered in diatreme facies kimberlite and altered in the root zone (Clement & Skinner, 1985; Clement, 1975; Dawson, 1971). This implies different temperatures of emplacement: cool, relatively unreactive kimberlite in the diatreme compared with hot and reactive kimberlite in the root zone Dawson & Hawthorne (1970). McFadden (1977) calculated emplacement temperatures in the region of $300^{o}C$ from palaeomagnetic thermal remanence studies of country rock fragments from De Beers, Duitoitspan, Finsch and Wesselton. Letlhakane, a predominantly diatreme-facies kimberlite, unusually contains many altered country rock fragments, often with reaction haloes where they have reacted with the erupting magma. This observation seems to question Clement's interpretations.

Sparks et al. (2006), Wagner (1914, 1971) and Barnett (2004) noted how country rock fragments cluster at the margins of the Venetia pipe in massive or layered country rock-rich breccias. These marginal breccias can contain up to 100% country rock fragments, but more often contain fewer fragments in a *kimberlitic* cement. Within a pipe, country rock fragment abundance and size can define diffuse layering. Size varies from sand-size up to 200-300 m (Clement, 1975; Mitchell, 1986a). Large blocks of country rock are found within the diatreme either as brecciated masses of multiple blocks or as one large massive block called a "floating reef" (Clement, 1975; Clement & Reid, 1989; Wagner, 1914, 1971), seen for example at Kimberley (Hawthorne, 1975). The blocks have retained their original stratigraphic layering, which indicates minimal disruption as they have slumped into the pipe.

Country rock fragments range in shape from well-rounded to angular clasts, indicative of their emplacement (Leahy, 1997); the degree of roundness indicates the amount of reworking and abrasion, possibly from multiple cycles of ejection and slumping back into the pipe (Fisher & Schmincke, 1984). The location of country rock fragments within a pipe can be at deeper or shallower depths than their original *in situ* location in the wall rock stratigraphy (Clement, 1975; Dawson, 1980). For example a 10 m block of granite basement was displaced to a greater height within the Orapa A/K1 pipe (Field et al., 1997). At Letlhakane basalt occurs up to 650 m below the Stormberg basalt stratigraphic position, and granite lapilli several hundred metres above its original location.

2.3.2 Juvenile Lapilli

A juvenile clast is a pyroclast derived from the magma, where a pyroclast is a product of an explosive volcanic activity (Fisher & Schmincke, 1984). Kimberlites, like other volcanic rocks, frequently contain rounded juvenile fragments ranging in size from a few millimetres to 8 cm (Danchin et al., 1975). These clasts are also called magmaclasts (Field & Scott Smith, 1999), nucleated autoliths (Danchin et al., 1975) and pelletal lapilli (Mitchell, 1986b). It is important to distinguish between genetically different juvenile clasts to fully understand their different origins, and what these tell us about the evolution of the kimberlite body

especially regarding multiple episodes of kimberlite eruption (Eccles et al., 2004). For clarity of terminology throughout this thesis, the non-genetic classification in Table 2.6 was used.

2.3.3 The Kimberlite Groundmass

The kimberlite groundmass is complicated by the variable mineralogy between and within individual bodies and issues concerning the primary or secondary nature of calcite, serpentine and microlitic diopside. Clement & Skinner (1985) considered the groundmass to be the phase left after macrocrysts, mantle xenoliths and lithic fragments have been removed, except for small euhedral olivines which are considered part of the primary groundmass phase. Skinner & Clement (1979) defined the groundmass mineralogy (excluding olivine) as monticellite, serpentine, phlogopite, calcite, diopside, apatite and opaque minerals spinel and perovskite which occur in varying proportions between kimberlites. For clarity throughout the thesis a textural division has been implemented to differentiate between the fragmental nature of the interclast phase of a volcaniclastic kimberlite, which was called the matrix, and the homogeneous phase of a coherent kimberlite, which was called the groundmass.

2.4 Types of Kimberlite Deposits

This section summarizes the geological and petrographic characteristics of the different types of kimberlite deposit found worldwide, working from the surface downwards. Interpretation and emplacement mechanisms are discussed in Section 2.5.

2.4.1 Extrusive Kimberlite Lava

Extrusive kimberlites are extremely rare (Dawson, 1980, 1971) and very few examples have been documented, for example the Igwisi Hills in Tanzania (Dawson, 1980; Reid et al., 1975), Gross Brukkaros (Ferguson et al., 1975) and two pipes in Northern Angola (Skinner & Marsh, 2004). The Igwisi Hills lava has very rounded olivines set in a matrix of calcite laths, spinel, perovskite, apatite and chlorite

Clast	Average Size	Habit	Description
 Magma selvage	50 µm to 10 mm	Round to irregular	Core of olivine phenocryst, macrocryst, or country rock fragment with thin (<<0.25mm) very fine-grained, grey-brown, optically unresolvable phase ± perovskite and spinel ± microlitic diopside. Not always complete rim around grain.
Ghost lapilli 	>50 µm to 2-3 mm	Rounded to sub-rounded	Olivine phenocryst rimmed by <0.25mm thick zone of perovskite and subordinate spinel, ± microlitic diopside.
 Pelletal lapilli	0.5 to 5 mm	Round	Kernel of olivine enclosed by 0.25-1mm thick, altered rim of crystalline kimberlite with microphenocrysts of olivine ± phlogopite ± monticellite and perovskite and spinel.
 Cored juvenile lapilli	2 to 50 mm	Round to irregular	Crystalline lapilli of kimberlite with core of any accidental fragment (macrocrysts, mantle xenolith or country rock fragment). Crystals in rim tend to be larger (0.5 – 5 mm) than the rim of pelletal lapilli. Core can be off-centre.
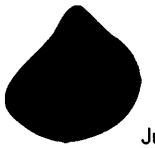 Juvenile lapilli	0.5 to 10 mm	Round to irregular	Rounded lapillus of coherent kimberlite with olivine phenocrysts (frequently altered), (often atoll) spinels, perovskite, ± monticellite and pools of carbonate.

Figure 2.6: Classification table of juvenile clasts.

in an amorphous, predominantly calcite with subordinate serpentine, base (Dawson, 1994). Meimechites are also considered to be the equivalent of a kimberlite lava (Butakova and Egorov, 1962 (*cited in* Dawson (1980)), Trofimov (1970), Dawson & Hawthorne (1970) and Mitchell (1986b)). Meimechites produce flows up to 1.5 km thick, and therefore extrusive kimberlites could be quite extensive. However, they have mostly been disputed as kimberlites on the grounds of their petrography (Dawson, 1980).

2.4.2 Pyroclastic Kimberlite

Pyroclastic kimberlite (PK) deposits which are located outside the pipe are also limited in occurrence, although Hawthorne's model of a kimberlite pipe (Hawthorne (1975)) suggests the presence of a tuff ring similar to those seen around maar volcanoes (Lorenz, 1975, 1979). There are very rare examples cited in the kimberlite literature. One is of an extra-vent pyroclastic flows at a pipe near Kasama in Mali (Dawson, 1980). Zonneveld et al. (2004) and Zonneveld et al. (2006) argue that some kimberlites, including the Star and 140/141 kimberlites, from the Fort a la Corne cluster in Saskatchewan, Canada, are completely preserved bodies with extra-vent pyroclastic airfall deposits. The general paucity of pyroclastic flows peripheral to kimberlite pipes, however, is probably a consequence of erosion of poorly consolidated tuffs which has resulted in poor preservation within the geological record. Pyroclastic kimberlites are more frequently associated with kimberlite craters and the pipe infill of Class 2 pipes (Section 2.2), e.g. the 140/141 kimberlite at Fort a la Corne in Canada (Berryman et al., 2003).

2.4.3 Epiclastic Kimberlite

Epiclastic processes are diverse in volcanic terranes and include grain flows, rockfalls, particle creep and avalanches (Cas & Wright, 1988). The processes take place in between phases of activity and after eruptions have ceased. They are predominantly the result of gravitational stabilisation of newly formed structures and are therefore an important mechanism in kimberlite crater infilling. Epiclastic deposits are an amalgam of reworked volcaniclastic kimberlites with entrained

country rock fragments. They are typically, but not exlusively, located within kimberlite craters, for example the Tokapal kimberlite, Bastar District, in India (Mainkara et al., 2004), Orapa in Botswana (Field et al., 1997) and Mwadui in Tanzania (Stiefenhofer & Farrow, 2004). Epiclastic kimberlites are also poorly preserved in the geological record for the reasons discussed for pyroclastic kimberlites. Hawthorne (1975) interpreted epiclastic kimberlites as extrusive volcaniclastic kimberlite tuff-rings which have collapsed under gravitational instability or have been washed back into the pipe. This process has been suggested for epiclastic kimberlite deposits at the Tokapal, Orapa and Mwadui kimberlites. The crater at Orapa is widely cited becuase it is an excellent example of a preserved crater with epiclastic kimberlite. It is infilled with debris flows, avalanches, and grain flow deposits from an intermittently collapsing tuff ring (Field et al., 1997). Shale beds at Orapa indicate a post-emplacement crater lake (Field et al., 1997). Lorenz (1975, 1979) makes an analogy between kimberlite pipes and maar volcanoes, in which case crater lakes were probably a common feature of kimberlite pipes. However, the absence of craters at most kimberlites challenges this idea, and suggests that they are not always formed during kimberlite eruption.

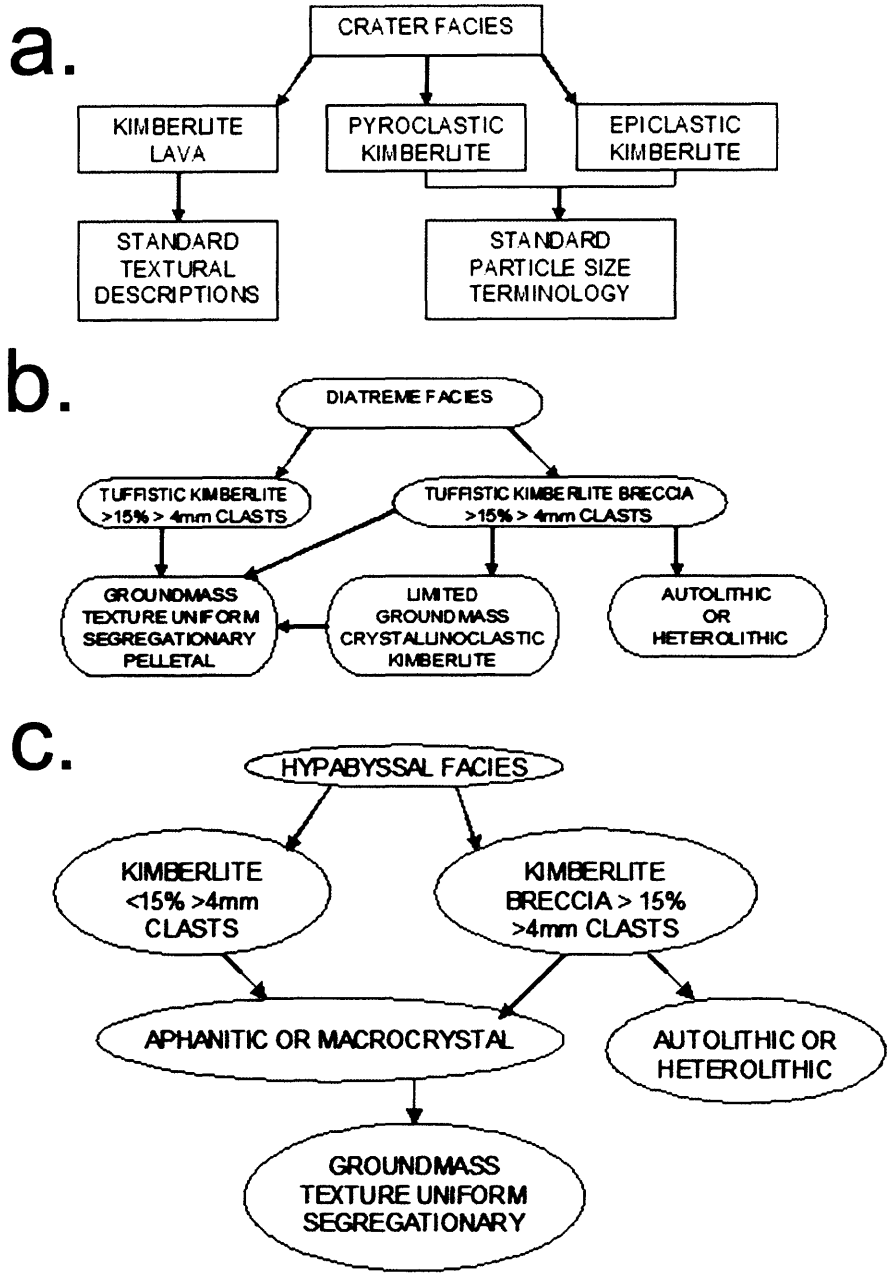

Figure 2.7: Kimberlite classification flow diagram. (a) Crater facies textural classification. (b) Diatreme facies textural classification. (c) Hypabyssal facies textural classification. (After Mitchell (1986b); modified from Skinner & Clement (1979) and Clement & Skinner (1985).)

2.4.4 Volcaniclastic Kimberlite

The term volcaniclastic is non-genetic and applied to volcanic aggregates with a fragmental texture, irrespective of the mode of emplacement (Cas & Wright, 1988). Pyroclastic and epiclastic kimberlites would also come under this umbrella term (Sparks et al., 2006). Volcaniclastic kimberlite (VK) avoids genetic confusion of kimberlite deposits where the mode of emplacement is not known or uncertain. For example, kimberlites characteristic of those found in the diatreme (Clement & Skinner, 1985) have undergone substantial alteration which may have destroyed their original textures (Walters et al., 2006). The kimberlite associated with the diatreme is also called a tuffistic kimberlite breccia (TKB) a term which was introduced by Clement & Skinner (1985, 1979) and is analagous with the term used to describe the Swabian Albs deposits (Reynolds, 1954). TKB is a very specific term where $\geq$15% of the rock is comprised of $\geq$4 mm sized "incorporated xenoliths and cognate kimberlite fragments..." (Clement & Skinner, 1985) (Fig. 2.7b). This includes unaltered country rock fragments and xenoliths that are not metasomatised (Clement & Skinner, 1985). Tuffistic is a genetic term which means an intrusive breccia, which does not apply to all kimberlites (Sparks et al., 2006). Instead of TKB, volcaniclastic kimberlite (VK) will be used in this thesis to describe the massive, fragmental kimberlite characteristic of most of the deposits at Letlhakane described in Chapter 3.

The textural classification scheme of TKB described above does not follow classic volcanological classification (c.f. Cas & Wright 1988). VK does follow this classification which facilitates comparison between kimberlites and other volcanic rocks. This is important to further the understanding of kimberlite eruptions because more is known about how other volcanic magmas erupt (Sparks et al., 2006). Figure 2.8 summarises the characteristics of a VK deposit into crustal, mantle, juvenile and alteration products. Olivine macrocrysts and phenocrysts are frequently pseudomorphed by serpentine and/or carbonate and/or talc. VK often has a fine-grained, cryptocrystalline interclast matrix comprised predominantly of groundmass phases (Fig. 2.8) set in a base dominated by microlitic diopside and serpentine, analagous with the 'cementing' phase described for a TKB by Clement & Skinner (1985, 1979). VK often contains porphyritic juvenile

clasts (Section 2.3.2) which impart a pelletal texture on the deposit (Mitchell, 1986b). Groundmass perovskites and spinels often have a random distribution throughout the interclast matrix (Haggerty, 1975), but can form clusters around olivine phenocrysts (Mitchell, 1986b). VK has an overall homogenous and massive appearance, although country rock fragment content varies throughout and defines crude layering (Section 2.3.1.5). More rarely emplacement processes segregate fine-grained material into bands and align elongate components (Clement & Reid, 1989). Sparks et al. (2006) divided VKs into massive or MVK and layered or LVK based on the structure of the deposit. A single pipe can contain several individual, texturally discernable VK lithofacies, e.g. Dawson (1980); Hawthorne (1975) and Clement & Reid (1989).

2.4.5 Coherent Kimberlite

Coherent kimberlite (CK) is a dark, dense rock with a more homogeneous, non-fragmental texture. The term coherent was introduced at the 2006 Kimberlite Emplacement Workshop by Ray Cas. It is also called hypabyssal (e.g. Clement & Skinner 1985 or magmatic kimberlite (e.g. Sparks et al. 2006), but these are terms which closely relate to the formation of the rock which is uncertain. The specific features of this rock type, as summarised by Skinner & Marsh (2004), include uniform and coherent textures with rare segregations, a higher proprtion of unaltered olivine (than TKB) and frequently altered country rock fragments. The groundmass is comprised of olivine, monticellite and occassionally phlogopite and apatite phenocrysts, and homogenously distributed spinel and perovskite set in a base of calcite and serpentine (Clement & Reid, 1989; Hetman et al., 2004; Skinner & Marsh, 2004).

The term hypabyssal kimberlite (HK) was used by Clement & Skinner (1985, 1979) to describe a kimberlite which crystallised directly from the melt without undergoing the gas-charged fluidisation processes proposed by Clement (*op. cit.*) for the formation of the TKB. HK defined by Clement & Skinner (1985) has a very specific texture. A hypabyssal kimberlite and hypabyssal kimberlite breccia are divided where the latter contains "≥15 vol% macroscopically visible fragments" (Clement & Reid (1989); Fig. 2.7c). Fragments derived from country rock have

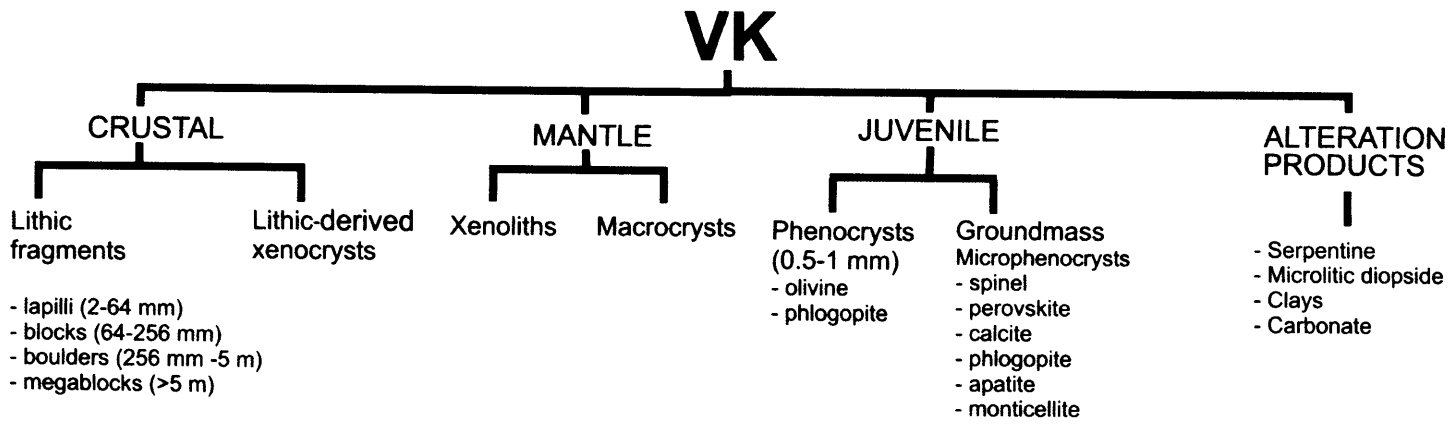

Figure 2.8: Volcaniclastic kimberlite classification flow diagram applied to this thesis. *(Courtesy of M. Field, pers. comm.)*

frequently been metasomatised. Microscopically (i) aphanitic, (ii) macrocrystic, and (iii) segregationary kimberlites are terms used by Clement & Skinner (1985) to texturally distinguish between kimberlite with (i) negligible macrocrysts ($\geq$0.5 mm), (ii) macrocrysts (predominantly of olivine) which produce an inequigranular texture, and (iii) distinct irregular segregations of serpentine with or without calcite.

More recently a new textural subdivision was introduced which marks the transition between TKB and HK. This texture was first reported by Field & Scott Smith (1998) at the Kamfersdam pipe near Kimberley in South Africa, and developed further by Hetman et al. (2004) and Skinner & Marsh (2004) after recognition of this textural transition in many global kimberlite bodies. This transition occurs in zones up to 10 m thick and is marked where segregations within the HK begin to coalesce and microlitic diopside (not seen in HK) begins to form patchy clusters (Field & Scott Smith, 1998; Skinner & Marsh, 2004). It is interpreted as the point where volatiles begin to exsolve so leading to explosive fragmentation and the formation of the TKB (Skinner & Marsh, 2004). Put more simply it is a frozen-in "degassing front" (Field & Scott Smith, 1998).

Sparks et al. (2006) proposed an alternative interpretation of coherent kimberlite deposits; they suggested that they are agglutinated and welded clastogenic deposits. Welding is described as "postdepositional compaction of hot pyroclastic deposit under its own weight." (Wolff & Sumner, 2000). Agglutination on the other hand is "instantaneous flattening of hot, soft pyroclasts upon landing" (Wolff & Sumner, 2000) or the kinetic mechanism by which clasts instantaneously adhere together on depostion (Capaccioni & Cuccoli, 2005). The resultant deposit is an agglutinate or spatter pile; particle outline is in part retained" (Wolff & Sumner, 2000). Wolff & Sumner (2000) add that both welding and agglutination are a continuum of one another. These are common process in terrestrial volcanic rocks (Capaccioni & Cuccoli, 2005; Cas & Wright, 1988; Fisher & Schmincke, 1984; Sparks et al., 1999). These two processes are accomodated in low viscosity melts(Wolff & Sumner, 2000), such as kimberlites. Although most published reports of welded deposits generally occur extra vent, they have also been reported from other volcanic pipes (Kano et al., 1997). Welding and agglutination is fundamentally influenced by accumulation rate of hot, plastic magmatic fragments

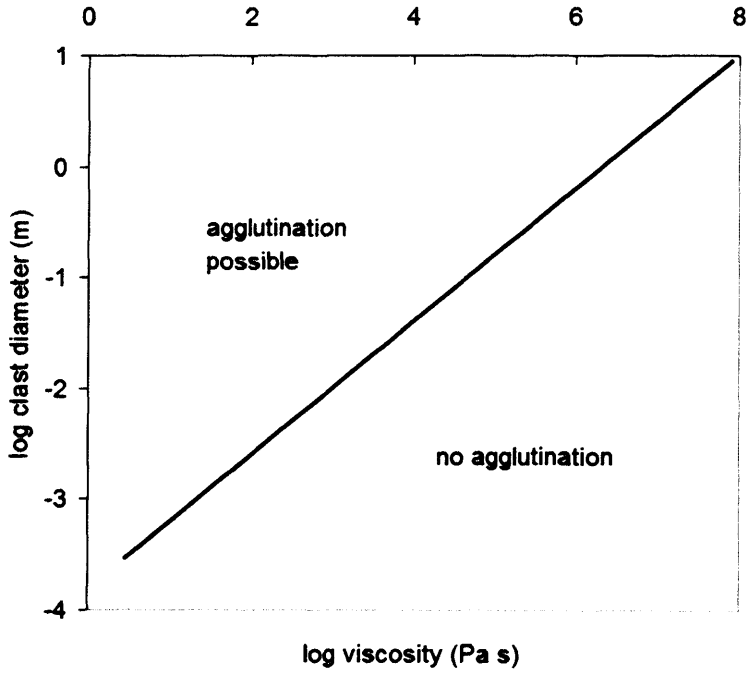

Figure 2.9: Plot of viscosity of the melt versus clast diameter to demonstrate the potential of welding in a volcanic rock. From (Wolff & Sumner, 2000).

where the freshly erupted deposit is buried before it has a chance to cool (Wolff & Sumner, 2000). Welding and agglutination adequately explains the occurrence of gradational transitions from this coherent kimberlite to the more fragmental VK (e.g. Tait et al. 2006), and why coherent kimberlites are found as irregular bodies towards the upper levels of the pipe. It seems feasible from Figure 2.9 that welding could take place during kimberlite emplacement.

The term CK was used during this thesis to describe the competent, typically dark, kimberlite deposits which have a coherent texture in thin section particularly. This was to avoid genetic confusion when describing these rocks.

2.4.6 Kimberlite Classification

There have been many classification schemes proposed for kimberlites which have raised significant debate regarding the primary or secondary nature of some con-

stituents, namely serpentine, calcite and microlitic diopside. Skinner & Clement (1979) and Mitchell (1986b) believe serpentine is a primary or late-stage groundmass phase, but this has been recently contested by Sparks et al. (2006) and Stripp et al. (2006) who demonstrate that serpentine is stable $\leq$500°C and X_{CO_2} $\leq$0.06 (Section 2.6). Skinner & Marsh (2004) proposed the exsolution of volatiles during emplacement favours stability of diopside as a primary crystallising phase. Again Stripp et al. (2006) show through mineral equilibria and thermodynamic calculations that diopside is a post-emplacement hydrothermal metamorphic product. Clement & Skinner (1979) pioneered the idea that kimberlite texture is related to location within the pipe, for example microlitic diopside is only found in the diatreme (Section 2.2, Fig. 2.7). However, Field et al. (1997) noted the presence of microlitic diopside within the crater facies at Orapa, and suggested that kimberlite textures cannot be assigned to zones within the pipe in this way. The preferred method for this thesis was to describe the features of the rocks in the field followed by petrographic study, and this led to interpretation and the suggestion of emplacement processes.

2.5 Kimberlite Emplacement Models

The sections above have discussed the major characteristics of kimberlite bodies. To summarise, these were:

1. Kimberlites are confined to localities on ancient continental crust, on both ancient cratons and younger mobile belts.

2. Kimberlites form provinces such as the Orapa and Letlhakane cluster. Certain kimberlites have been emplaced at the same time forming clusters in the geological record.

3. Co-existence of pipes with 'blind-intrusions', sills and dykes at the same elevation.

4. A paucity of extrusive kimberlite lavas, tuff-rings or peripheral pyroclastic deposits.

5. The co-existance of a wide range of kimberlite types within one pipe and between individual kimberlite bodies, which do not conform to an idealised model.

6. The wide range of types and abundance of entrained mantle and crustal fragments and thorough mixing of all components in the pipe.

7. Transport of dense, mantle xenoliths to the surface.

8. Variable abundances and compositions of groundmass and matrix components.

9. Variable thermal or metamorphic effects on included country rock fragments.

10. Evidence for emplacement temperatures as low as 300 °C (McFadden, 1977).

Any model proposing kimberlite emplacement must explain these observations. This section (2.5) presents a review of the main emplacement models proposed to date.

Kimberlites probably ascended to the surface by propagation of magma through a complex array of dykes along crustal weaknesses (Basson & Viola, 2004; Dawson, 1980; White et al., 1995). This is plausible as it is a common terrestrial process (Gudmundsson & Loetveit, 2005; Watanabe et al., 1999). Kimberlite magmas are believed to be very low viscosity melts (0.1 - 1 Pa s (Sparks et al., 2006)) and can therefore move through fractures easily. According to crack-propagation models it takes a kimberlite ~14 hours to ascend from depths of 150 km to the surface (Gregoire et al., 2006). The occurrence of dykes, sills and blind intrusions at the same locality presents an interesting phenomenon; why did some intrusions produce pipes and others fail to? Good examples of these 'composite' kimberlite occurrences are at the Wesselton and the De Beers pipes at Kimberley (Clement & Reid, 1989; Shee, 1985). The Wesselton pipe has a complex geometry and is comprised of a main pipe with an irregular root zone and a "blind" intrusion which is surrounded by a contact breccia (Clement & Reid, 1989; Shee, 1985). The De Beers pipe has a complex root zone which is also associated with a contact

breccia (Clement & Reid, 1989). The Duitoitspan pipe has a complex pipe geometry consisting of an intricate root zone with many branches and blind intrusions within close proximity of the Bultfontein pipe which has a pipe that progresses directly into a feeder dyke with no evidence of a root zone. Trofimov (1970) also talked about composite diatremes, sills and dykes co-exist in the Siberian shield.

There are essentially four main models of kimberlite emplacement; (i) intrusive fluidisation model of Dawson (1971), (ii) the embryonic pipe formation model of Clement (1982), Clement & Reid (1989), modified by Skinner & Marsh (2004, 2006), (iii) the Sparks et al. (2006) model of dynamic explosive kimberlite eruptions, and (iv) the phreatomagmatic model of Lorenz (1975).

Intrusive Fluidisation

Dawson (1971) suggested that the presence of multiple intrusions in a single kimberlite pipe and undisturbed masses of country rocks (floating reefs) precluded earlier ideas that kimberlites explosively bored out their diatremes. Instead he proposed the features seen in many southern African pipes were consistent with a model whereby gas-charged magma ascended rapidly (400 m/s close to the surface) towards the surface. Within 2-3 km, volatiles began to exsolve causing massive gas expansion. Strong adiabatic cooling was resposible for the large decrease in temperature and emplacement of a relatively cool material, explaining the paucity of thermal effects of entrained lithic fragments. The diatreme was formed after breakthrough of the surface from the feeder dyke depths of 2-3 km which created an explosion chamber. The fluidised crystal-rich kimberlite effectively drilled upwards producing the characteristic, smooth-sided diatreme typical of kimberlites. Processes proceeded past the point of eruption including later-stage formation of a tuff ring and crater and mass movement of unstable material.

Embryonic Pipe Formation

Clement & Reid (1989) based their dynamic model of kimberlite emplacement predominantly on subvolcanic processes which took place prior to the formation of the diatreme. They proposed that an extensive cycle of embryonic pipe formation took place as kimberlite magma ascended towards the surface and began

to exsolve its volatile content. Skinner & Marsh (2004) called this stage first and second boiling, according to processes of the same name in Cas & Wright (1988). The consequential large increase in pressure produced rapid volume expansion which caused subvolcanic brecciation and formed the explosion breccias seen at the Wesselton and De Beers pipes. A range of processes were reponsible for excavating the irregular geometries associated with the root zone (Hawthorne, 1975) including spalling, wedging and rock bursts (Clement & Reid, 1989). The effects were increased by the formation of 'gas caps' where volatiles coalesced ahead of the intruding magma and penetrated into local fractures already present in wall rocks. Trofimov (1970) and later Field & Scott Smith (1999) suggested that impermeable lithologies such as Karoo dolerite sills act as effective barriers to ascending kimberlite magmas. Volatile pressure builds up until it exceeds the confining lithostatic pressure and explosive breakthrough occurs (Field & Scott Smith, 1999). Clement (1982) (*cited in*; Clement & Reid 1989) adds that the irregular root zones were formed by many cycles of activity which are preserved in some bodies including the Wesselton pipe.

Formation of the diatreme was preceeded by breakthrough of the surface and formation of a shallow angled crater. Rapid depressurisation and a sudden upsurge of volatiles produced adiabatic expansion of gases which extended through the base of the crater into a large part of the embryonic pipe system (Clement & Reid, 1989). This stage is envisaged as a single, large explosion by Skinner & Marsh (2004) which produces shockwaves capable of explosively fracturing wall rocks. Gas-solid fluidized systems develop, although the fluidisation intensity would rapidly diminish and provide only a buffering effect to large fragments floating down into the diatreme (floating reefs). Clement & Reid (1989) hypothesise that between 1-5 discrete intrusions can comprise the diatreme facies, which are characterised by TKBs. Country rock fragments were incorporated into the ascending magma during embryonic pipe formation and from unstable wall rock collapses which were prevalent during the waning stages of the eruption when gas velocity declines and the fluidised system deflates. Gas streaming and "short-lived pneumatic transport" contribute to the mixed or "ordered" nature of TKB (Clement & Reid, 1989). The model proposes the formation of the diatreme was short-lived which culminated in the rapid crystallisation or quenching of vapour

phases as the interclast matrix. Although Clement & Reid (1989) suggested that diatreme formation is a short-lived process, they add that periods elapsed between eruptive phases. This is supported by the presence of epiclastic kimberlite within the diatreme zone at the Finsch and Wesselton pipes.

Dynamic Kimberlite Volcanism

An alternative theory by Sparks et al. (2006) suggests that dykes ascend to within tens of metres of the surface where explosive break through is triggered by a condition called 'choked flow'. During choked flow the magma supply rate (500 to 10^5 m^3/s) is greater than some critical value and exits the vent as an overpressured regime (Sparks et al., 2006). Hot, explosively fragmenting kimberlite magma cannot escape the vent fast enough so pressure at the point of exit is higher than the ambient atmospheric pressure of 1 atm. In the model, heat is lost by transfer to the wall rocks and by entrainment of country rock material. Decompression of the magma, once the surface has been broken, triggers rapid vesiculation of pyroclasts and the erupting material becomes very buoyant. Material is easily ejected and is excavated with the predicted intensity of a Plinian eruption. This process progressively widens the vent and develops a pipe geometry (Sparks et al., 2006). An overpressured regime is maintained at the surface until the vent widens past a critical point when the exit pressure is close to 1 atm (Sparks et al., 2006). The vent continues to widen as more material is excavated and unstable wall rocks collapse. Rock bursts occur at depth if material excavated from the forming pipe creates underpressure, forcing implosion of the pipe walls. This could explain country rock-rich breccias marginal to the pipe walls.

Davidson (1964); Kennedy and Nordlie (1968) (*cited in* Dawson (1980)) and Sparks et al. (2006) believe the pipe excavates downwards through the energetic ejection of material. In this model, as gas flow decreases and the pipe widens a condition will be reached when large material can no longer be excavated and the pipe begins to infill (see Figure 12 (b) in Sparks et al. 2006). It is possible that this stage can be compared to a column collapse during a Plinian-style eruption when the plume is no longer able to sustain the weight of large pyroclasts [1].

[1] Comment made by Ray Cas at the 2006 Kimberlite Emplacement Workshop

The pipe infill (VK) may therefore be the result of the chaotic column collapse (Brown *et al. in press*). This hypothesis explains why only crude structures occur in the restricted area of the pipe. The idea of a cavity being created which subsequently infills with fragmental deposits is similar to the emplacement model of Trofimov (1970). Trofimov (1970) suggested that a "pipe-like cavity" is produced by explosive eruptions which are triggered by volatile exsolution from a magma trapped by an impermeable cap of rock. This cavity subsequently infills with material falling back into the cavity from explosive pulses of activity. The fragmental fall back deposits include brecciated fragments of earlier, already lithified kimberlite (Trofimov, 1970).

Gas-flow through the kimberlite which is infilling the pipe, produces another stage in the pipe's development. Fluidisation is an engineering term for a process whereby the gas flux through a bed of particles is sufficient to mobilize them and the system behaves as if it were a fluid (Walters et al., 2006). A fluidised regime establishes when "at a particular rate of gas flow the bed *(of particles)* expands and the individual particles become free to move" (Reynolds, 1954). Fluidisation was first associated with volcanic rocks by Cloos (1941; *cited in* Reynolds (1954)) who described the Swabian Albe tuff deposits as the products of fluidisation. Dawson (1962; *cited in* Clement (1975)) first linked this process to kimberlites. Experimental work has recreated fluidised pipe structures by passing gas through a vent into an unconsolidated bed of particles (Gernon et al., 2006; Walters et al., 2006; Woolsey et al., 1975). Although these experiments have dimensional limitations compared with true kimberlite pipes, they demonstrate how fluidisation can effectively homogenise material within the pipe. These experiments have also illustrated how zones marginal to the wall rocks are relatively free from fluidisation, and this possibly explains the presence of marginal breccias discussed in Section 2.3.1.5. Fluidisation can also explain the downward transport of large country rock blocks (floating reefs) because a fluidised bed of particles is a quasi-dynamic system with a bulk friction of effectively zero (Clement & Reid, 1989; McCallum et al., 1975).

Phreatomagmatic Kimberlite Eruption

A third model, first proposed by Lorenz (1975) and developed further by Kurszlaukis et al. (1998) and Lorenz (1999), uses a phreatomagmatic trigger. A local source of water comes into contact with the rising kimberlite magma at depths of 200-300 m, where the pressure is low enough to allow the water to flash boil. On contact with the hot magma the water is initially insulated by a thin film of stable vapour of low heat conductivity called Leidenfrost phenomenon (Lorenz, 1999). Shock waves produced from volcanoseismicity during magma ascent disrupt and destroy this film so that water and magma make direct contact. Heat is rapidly transferred from the magma to the water, which catastrophically expands. The sudden increase in pressure exceeds the strength of the magma which undergoes brittle fragmentation. Superheated water injects into fractures within the fragmented magma, increasing the surface area of water-magma contact and elevating the degree of heat transfer. The water vapourises and the liquid-gas system decouples. This is the point at which eruption takes place.

In the phreatomagmatic model explosions are generated within the root zone and are controlled by magma-water interaction. The rapid water vapourisation fragments overlying magma and the surrounding country rock. The system rapidly cools as substantial country rock fragments are entrained (c.f. Sparks et al. 2006). Material is excavated by phreatomagmatic explosions which produce an "explosion chamber" that magma intrudes into (Lorenz, 1999). As explosions proceed and material is excavated, mass deficiencies develop and wall rock collapses occur. This process forms the diatreme as explosions take place with increasing depth. Collapsing tephra clouds will produce base surge deposits in the crater. Lorenz (1979, 1999) suggests the initial material which fills the diatreme is a clastic kimberlite deposit. Lithification takes place as deuteric and meteoric waters infiltrate the system and alter olivine. This process causes an increase in volume which is manifested as late stage slickensided faults within the kimberlite. Lorenz (1999) explains that the lack of volatile exsolution during eruption is supported by the lack of vesicles in most kimberlites.

2.6 Secondary Alteration

Kimberlites are notoriously altered rocks (e.g. Clement (1975); Mitchell (1986b); O'Brien & Tyni (1999); Skinner & Clement (1979)), therefore the effects of alteration on primary components is required to fully understand kimberlite emplacement. Alteration of olivine macrocrysts and phenocrysts by serpentinisation is significant (Mitchell, 1986b). The origin of the interclast groundmass and matrix phases have several interpretations. Secondary processes are clearly important in understanding kimberlite evolution, and this section will address kimberlite alteration processes and focus on the origin of the interclast phase.

Serpentine constitutes around 20 to 50 volume% of the matrix phase in most kimberlites (Skinner & Clement, 1979). Serpentine is an umbrella term under which a wide range of polymorphs and polytypes exist, including chrysotile, lizardite and antigorite (Deer et al., 1983; Mitchell, 1986b). Despite serpentine abundance in kimberlites, there have been few studies of their compositional range (Dawson, 1980; Mitchell, 1986b), except Berg (1986) and a recent paper by Stripp et al. (2006). Serpentine can be categorised by its paragenesis into three groups: (i) pseudomorphs of earlier minerals; (ii) veins or segregations in the matrix; (iii) prograde replacement products of earlier pseudomorphing serpentine (Dawson, 1980; Mitchell, 1986b). These textures are variable; serpentine pseudomorphing olivine has fibrous habits with undulose extinction, and serpentine within the groundmass shows a range from fibrous to spherulitic habits (Stripp et al., 2006). Matrix carbonate is subordinate to serpentine in most deposits. A few however, including the De Beers dyke and the Benfontein Sills which are referred to as calcite kimberlites, have up to 50 volume% carbonate (Jones & Wyllie, 1985; Skinner & Clement, 1979).

Mitchell (1986b) summarised the matrix phase of VK as extremely fine-grained or cryptocrystalline, dominated by serpentine, microlitic diopside and less frequently carbonate and phlogopite. Serpentine, carbonate and phlogopite form structureless pools as a pseudo-amorphous, interclast phase. Microlitic diopside, however, produces small (5-50 μm), lath-like microlites which radiate at the edge of olivines (Fig. 2.10) and flood the interclast matrix in some deposits. The origin of the amorphous or cryptocrystalline matrix phase has been interpreted

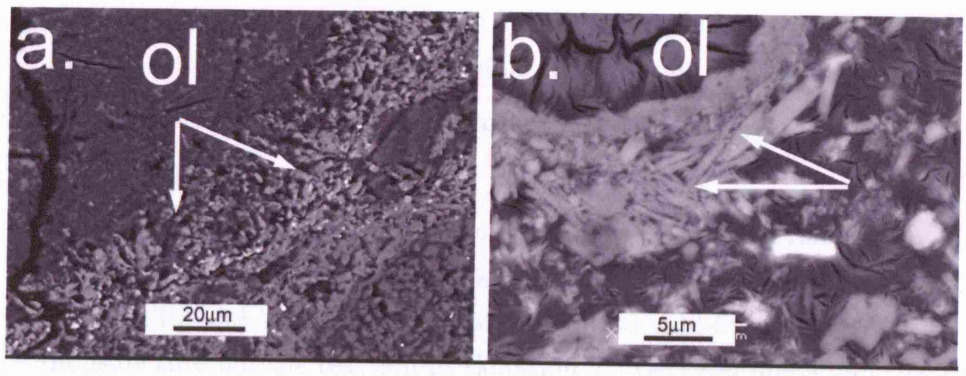

Figure 2.10: Backscatter electron images of interclast microlitic diopside at Letlhakane. White arrows point to diopside microlites radiating from the edge of olivine phenocrysts (ol). (b) Illustrates the mesh-like texture of matrix serpentine (darker grey phase below the diopside).

as: (i) crystallisation of late-stage residual kimberlite fluids (Le Roex et al., 2003; Skinner, 1986); (ii) liquid immiscibility of late-stage residual fluids rich in H_2O and CO_2 from melts with a silicate and carbonatitic nature (Clement, 1975); (iii) vapour phase crystallisation (Clement & Reid, 1989); (iv) as products of secondary alteration and hydrothermal metamorphism (Dawson, 1980; Stripp et al., 2006; Trofimov, 1970); (v) alteration of ash (Sparks et al., 2006).

Stripp et al. (2006) conducted an extensive study of samples collected from Venetia, South Africa and made some key observations and interpretations. It was concluded that fragmental, volcaniclastic kimberlites were originally clastic deposits with porosities between 20-30 volume% (Walters et al., 2006), which lithified following a series of "post-emplacement, sub-solidus hydrothermal metamorphism ($\leq$400 ^{o}C)" from the circulation of meteoric waters. Trofimov (1970) believed that residual gases and hydrothermal fluids were responsible for alteration including carbonatization, serpentiniztion and chloritization. Trofimov (1970) uses the term "autometamorphism" to describe the processes reponsible for chemical changes of the kimberlite filling diatremes. The stages of alteration outlined by Stripp et al. (2006) are summarised below.

1. Serpentinisation of olivine phenocrysts and macrocrysts, xenocrysts (from

country rock) and lithic fragments via the isovolumetric reaction given in Equation 2.1, which preserves original olivine grain boundaries.

$$2Mg_2SiO_4 + 1.613H_2O = 0.806Mg_3Si_2O_5(OH)_4 + 1.581MgO_{(aq)} + 0.387SiO_{2_{aq}} \quad (2.1)$$

2. Si^{4+} and Mg^{2+} are introduced into the fluid phase by the reaction in Equation 2.1 and combine with Ca^{2+} released from the serpentinisation of monticellite and lithic fragments to precipitate void-filling microlitic diopside through the reaction in Equation 2.2 between fluids and talc rims around serpentinised olivines. Titanite and hydro-andradite can also be produced at this stage, as seen at Venetia where they form intimate intergrowths with microlitic diopside.

$$Mg_3Si_4O_{10}(OH)_2 + Ca(OH)_{2_{aq}} = CaMgSi_2O_6 + 2Mg(OH)_2 + 2SiO_2 \quad (2.2)$$

3. Phyllosilicates (including serpentine and chlorite) crystallise at lower temperatures from Si^{4+} and Mg^{2+} produced from reaction 2.1, which can replace earlier lizardite pseudomorphs of olivine, suggesting that there were cycles of influx of meteoric waters.

4. Saponite forms in reducing environments from alkaline solutions towards the final stages of alteration.

Stripp et al. (2006) also demonstrated that alteration products at Venetia were influenced by the type of included country rock fragments. Widespread studies of this kind would improve our understanding of individual kimberlite pipes and aid the development of a more general model.

There is still a wide opportunity to study the alteration of kimberlites. The hypothesis presented above is just one suggestion. Counter-arguments to this suggestion include the interpretation that microlites crystallising in other volcanic systems are possible quench products in reponse to degassing as a magma ascends rapidly to the Earth's surface and decompresses (Sable et al., 2006), and therefore microlitic diopside in kimberlite is also a quench product (Clement & Reid, 1989).

2.7 Kimberlite Geochemistry

A fundamental study by Smith (1983) identified two compositionally distinct kimberlites in southern Africa; Group I, and 'micaceous' Group II kimberlites. Table 2.1 presents the isotopic data on which this division was based, although the same division was made based on mineralogical differences by Wagner (1914, 1971) who divided kimberlites into "basaltic" and "lamprophyric" kimberlites. Group I have low Sr and Nd relative to the bulk Earth indicating their undifferentiated source, whereas Group II are enriched in Sr and Nd, and low in Pb which relates to their slightly enriched source (Dawson, 1987). The major differences between the two groups of kimberlites are given in Table 2.1.

Kimberlites are low SiO_2 (between 25-35 wt%) potassic igneous rocks (Mitchell, 1986b; Sparks et al., 2006). Kimberlite geochemistry is a contentious issue because of their 'hybrid' nature (Dawson, 1971) discussed in Section 2.3. It is difficult to identify minerals which have crystallised as primary groundmass phases from the melt compared with those which are xenocrystic Dawson 1980; Mitchell 1986b. If the megacryst suite has crystallised from a protokimberlite melt the bulk melt composition would have evolved and a bulk rock geochemical analysis will not give the composition of the primitive kimberlite melt (Mitchell, 1986b). Furthermore, geochemical analyses are contaminated by country rock fragments, mantle xenoliths and secondary alteration products. Major elements have been influenced by olivine and spinel fractionation, modal mineralogy, contamination from entrained accidental material and secondary alteration (Mitchell, 1986b). Trace elements have also been affected by these processes with the exception of some immobile trace elements which are refractory and often unaffected by secondary alteration. Trace elements in kimberlites are classified into (i) *compatible* elements, including Cr, Ni and Co which have abundances similar to those in ultramafic rocks and *incompatible* elements, including Nb, Zr, Sr and REE which have abundances similar to carbonatites, melilitites and potassic lavas (Mitchell, 1986b; Wedepohl & Muramatsu, 1979). Kimberlites are enriched in LREE relative to HREE which is believed to be related to the degree of partial melting and composition of the source rock (Becker & Le Roex, 2006; Le Roex et al., 2003). Geochemical analysis forms an important part of this thesis by demonstrating

	Group I	Group II
Location	Widespread, global	Within a zone 400 x 1250 km between the Western Cape and Swaziland, confined to southern Africa
Age	Broad distribution of ages	115-200 Ma
Petrography	Olivine phenocrysts $\leq$0.5 mm	Olivine phenocrysts variable in size, phlogopite defining feature
Volatiles	CO_2 dominated	H_2O dominated
$^{86}Sr/^{86}Sr$	0.7033-0.7049	0.7074-0.7109
$^{206}Pb/^{207}Pb$	18.45-20.05	17.2-17.7
$^{143}Nd/^{144}Nd$	0.51271-0.51277	0.51208-0.51228
Source	Undifferentiated to slightly differentiated	Ancient enriched source

Table 2.1: Isotopic variation between Group I and Group II Kimberlites and their related source regions, from Skinner (1986); Smith (1983) and Dawson (1987).

how the bulk rock geochemistry of contaminated kimberlite samples can be used to characterise individual lithofacies within the pipe, as well as leading to an understanding of shallow-level petrogenesis and emplacement processes.

Chapter 3

The Geology of the D/K1 Kimberlite Pipe

3.1 Introduction

The study of historical explosive volcanic eruptions is usually undertaken by the observation and subsequent interpretation of their extra-vent deposits (e.g. Cas & Wright (1988); Fisher & Schmincke (1984) and references therein). Kimberlites present an alternative perspective. Exposed kimberlite outcrops are predominantly intra-vent because erosion has removed poorly consolidated volcanic deposits exterior to the vent (Section 2.2.1) and subsurface outcrops have been exposed through mining. There are very few similar studies made of deposits within other volcanic pipes (e.g. Kano et al. 1997; Stoppa 1996 and Kurszlaukis & Lorenz 1997). Consequently there is little data with which comparison with kimberlite pipes can be made. Kimberlite pipes have the potential to provide insight into conduit processes, therefore developing this field of volcanology (e.g. Brown *et al.*, *in press*).

D/K1 is a steep-sided volcanic pipe, analagous to the southern African Class 1 pipes discussed in Section 2.2. D/K1 is a geologically complex volcanic pipe, which is evident from previous studies of the internal geological variations (Section 3.2). The aim of this thesis was to characterise the internal geological variations at D/K1. This chapter presents the geological and petrographical criteria used to differentiate the D/K1 pipe into six texturally distinct major lithofacies associations. Non-genetic terminology was used throughout which was discussed in

Chapter 1 and is summarised in Section 3.4. The approach taken for this chapter was to systematically describe the rocks in hand specimen and petrographically, and then to interpret the deposits and recommend an emplacement model.

3.1.1 Aims and Justifications

The previous geological model designed by J. Jakubec among others in 1996, divided the D/K1 pipe into four major kimberlite lithofacies (Fig. 3.2) based on variations in diamond grade and geological observations (Jakubec and Field, *pers. comm.*[1]). As excavation of the mine continued, differentiation between the lithofacies grew increasingly difficult because they became more similar in characteristics with increasing depth. This raised the question of how valid the model now was, which was imperative in deciding whether Letlhakane could continue to be economically productive in the future as an underground mine. Underground mining incurs greater production costs and planners and managers must be confident that they have the resources at depth to compensate for this (Dominy et al., 2002). A new delineation drilling project was undertaken between 2003-2005 for both the D/K1 and D/K2 pipes to investigate the nature of the kimberlite at depth and to update the geological models.

3.2 Review of Old D/K1 Model

There are no detailed published accounts of the geology of the Letlhakane kimberlite in the scientific literature. The only previous detailed studies of the D/K1 Pipe were published as internal reports by De Beers Consolidated Mines Ltd. Stiefenhofer (1993) conducted an extensive study into a suite of mantle xenoliths from Lethlakane, but he did not focus on the host kimberlite. In this respect, much of the following section is collected from these unpublished reports and I thank the authors for their permission to use them.

D/K1 was divided into three major kimberlite lithofacies, LM1, LM2 and a basalt-rich breccia unit during the mid-1980s (Fig. 3.1). Prior to this the only distinction was between diatreme facies "TKB" and basalt breccia (e.g.Skinner &

[1]Comments made during a discussion at the 2006 Kimberlite Emplacement Workshop, Saskatoon, Canada.

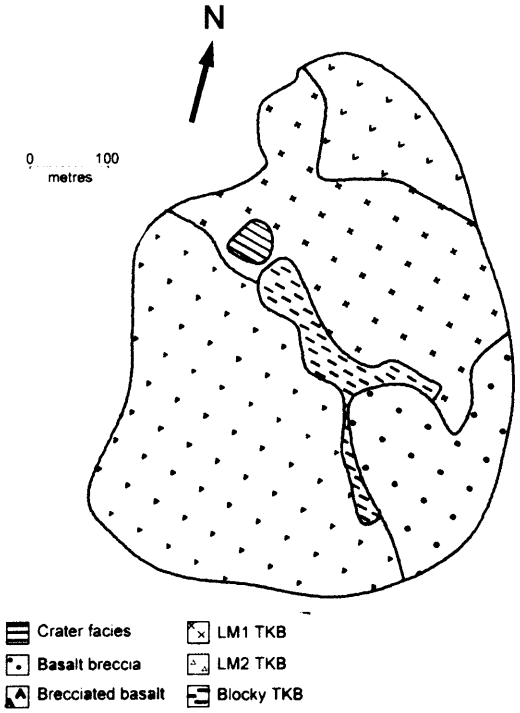

Figure 3.1: Schematic illustrating the surface of D/K1 from Field (1988b). The two major kimberlite lithofacies, LM1 and LM2 are separated by a zone of increased proportion of basalt blocks, and remnants of a crater facies.

Clement 1978 and Harper 1981). Field (1988a) instigated the LM1/LM2 divide noting that LM1 contained a lower proportion of accidental basalt fragments and more abundant phlogopite macrocrysts than in LM2 ($\leq$2%; McClenaghan, 1989 *cited in* Stiefenhofer 1993). Both lithofacies contained poorly developed pelletal lapilli, although their textures were described as pelletal or segregationary. They both contained altered olivine macrocrysts and phenocrysts, phlogopite, garnet and ilmenite macrocrysts, fragments of basalt and mantle peridotite xenoliths. In thin section pelletal lapilli are composed of coarse kernels of olivine and phlogopite set in a fine-grained rim of spinel, perovskite and probable serpentinised monticellite (Field, 1988c). The inter-lapilli matrix is made of fine-grained clinopyroxene (diopside) microlites and pale green serpentine, with some samples abundant in chlorite alteration.

In between LM1 and LM2 is a zone with an increased concentration of basalt

blocks called the "blocky TKB" (Fig. 3.1). Field (1988a) noted that LM1 truncated LM2, indicating its younger age. Variations within LM1 and LM2 were often noted. Field (1991) recorded six different textural varieties including a transitional diatreme-hypabyssal kimberlite with fresh olivine cores and baked lithics, and a contaminated hypabyssal kimberlite with a uniform distribution of groundmass components.

The Southern Basalt Breccia (Fig. 3.2) is composed of two parts; a lower unit which is dark brown and competent, clast-supported and massive, and an upper unit which "drapes" over the lower unit and is matrix-supported and layered (Field, 1988a; Stiefenhofer, 1993). The contact between the wall rock and the basalt breccia varies in dip from 45° to sub-vertical. Shallower angles resemble the geometry of a flared crater (Hawthorne, 1975). Field (1988a) observed other samples as probable crater facies kimberlite described as (i) a fine-grained, gritty kimberlite with a brown, "turbid" clay-rich matrix, and (ii) a well-bedded, possible epiclastic kimberlite.

Between 1988 and 1998, LM2 was divided in two; LM2W and LM2E. LM2W resembles LM1 but has a higher country rock fragment content and diffuse layering towards the contact with BBR. LM2E is a less competent, paler and more altered kimberlite, similarly enriched in country rock fragments and quite distinct from LM1 and LM2W. The mine model shown in Figure 3.2 was built using these four kimberlite lithofacies. Delineation drilling at Letlhakane in the early 1990s (Field, *pers. comm.*) reached depths of ~400 m elevation. The model was extrapolated downwards and it was interpreted that LM1, LM2W and LM2E split into three "trouserlegs" at an elevation of 570 m. BBR was modelled to a depth of ~560 m elevation where it pinches out. The other three lithofacies were extrapolated to depths of ~380 m elevation.

Recent updates to the geological model divide D/K1 into four kimberlite lithofacies, although the distribution and geometries of the units have changed (Lebani & Khango 2005; Fig. 3.3). The model of Lebani & Khango (2005) has recently been adjusted as a result of this study. Principally, the BBR lithofacies does not extend as far into the pipe as indicated in their model, and VK2 is divided into two separate lithofacies as shown in Figure 3.3.

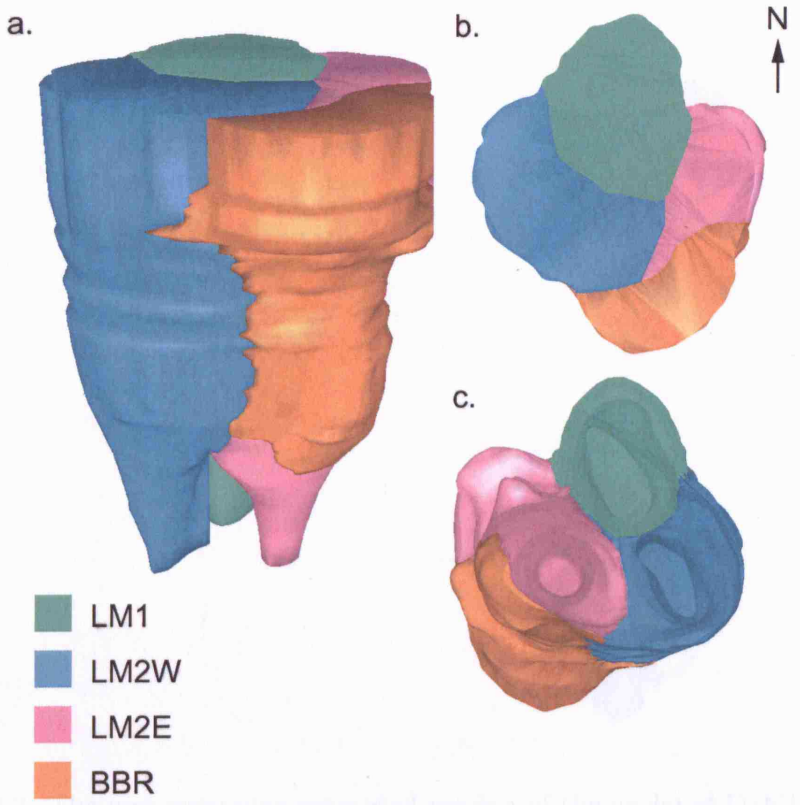

Figure 3.2: The old computer-generated D/K1 model by J. Jakubec. (a) Main ore body looking from the side on. (b) Birds-eye view. (c) Looking from the bottom up to see the three pipes splitting at depth.

3.3 Methods

Delineation drilling took place at Letlhakane between July 2003 and August 2005. In total 81 holes were drilled for geological and geotechnical modelling (Lebani & Khango, 2005), of which 34 targeted D/K1 and were logged during this study. Drill core logs were collected using the templates in Appendix A (on the enclosed CD), and all drill core logs are presented on the enclosed CD. The proportion of country rock fragments was collected using the method recommended in an internal De Beers report by Stiefenhofer et al. (2004). A code was used to log the grain size, clast or matrix support, sorting and the structure (Table 3.3). Four face maps were collected and are presented in Appendix A on the enclosed CD.

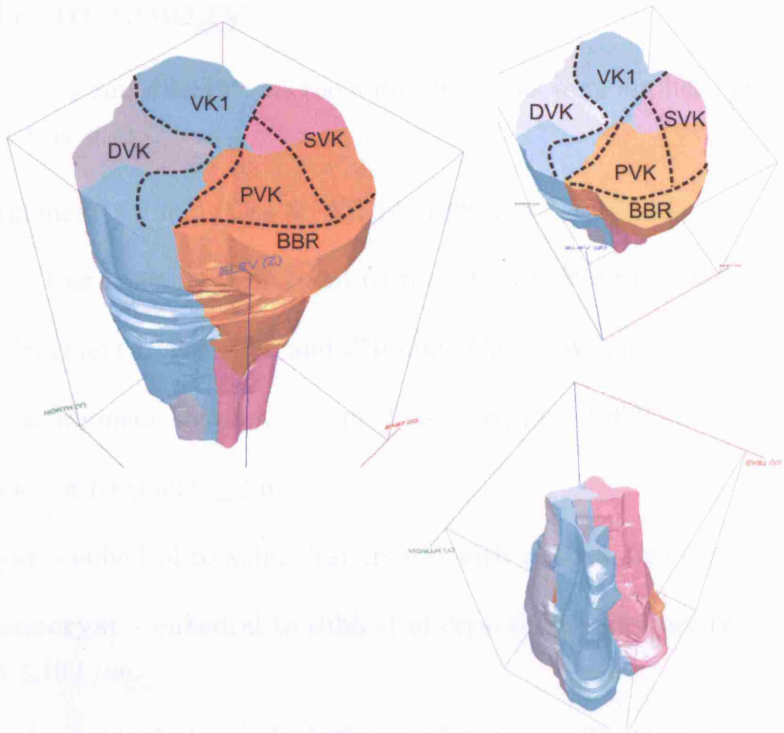

Figure 3.3: The new computer-generated version of the updated D/K1 model by Lebani & Khango (2005). The inverted image illustrates how in the model the D/K1 pipe does not split in 'trouserlegs' at depth.

Table 3.1: Core logging code

Grain size	c	coarse (5-≥30 mm)
	m	medium (1-5 mm)
	f	fine (≤1 mm)
support	c	clast-supported
	m	matrix-supported
sorting	p	poorly
	w	well
structure	m	massive
	b	bedded

Image Analysis

Appendix C outlines the criteria used to determine grain size distribution through quantitative image analysis.

3.4 Terminology

To ensure consistent observations the following terms were applied systematically throughout this study:

Ash - a frgament $\leq$2 mm (Cas & Wright, 1988).

Lapillus - a fragment between 2 and 64 mm (Cas & Wright, 1988).

Block - a fragment between 64 and 256 mm (Cas & Wright, 1988).

Boulder - a fragment 256 mm to 2 m (Cas & Wright, 1988).

Megablock - a fragment $\geq$2 m.

Phenocryst - euhedral to subhedral crystal with at least two euhedral faces.

Microphenocryst - euhedral to subhedral crystal with at least two euhedral faces $\leq$100 μm.

Macrocryst - subhedral to anhedral crystal $\leq$10 mm (Section 2.3.1.2).

Xenocryst - anhedral crystal from a disaggregated lithic (crustal) fragment (Cas & Wright, 1988).

Megacryst - subhedral to anhedral crystal $\geq$10 mm (Section 2.3.1.2).

Mantle xenolith - fragment of mantle rock including eclogites and peridotites; as observed by Stiefenhofer (1993).

Juvenile lapillus - cognate clast of kimberlite, possibly a crystallised fragment from an earlier eruption phase, defined in Section 2.3.2.

Lithic - accidental country rock fragment.

Coherent - dark, dense, competent kimberlite described in Section 2.4.

Volcaniclastic - volcanic aggregate with a fragmental texture, irrespective of the mode of emplacement, described in Section 2.4.

Alteration haloes - halo of altered, often pale kimberlite surrounding lithic lapillus or block.

Fragmental - term used to describe a heterogeneous interclast texture comprised of small lithic lapilli and ash, phenocrysts and microphenocrysts set in a base including one or a combination of serpentine, phlogopite and calcite. Ususally characterised by a pelletal or pseudo-pelletal texture.

Non-fragmental - term associated with the homogeneous, more uniform texture of a coherent kimberlite characterised by a groundmass phase of olivine phenocrysts and oxide microphenocrysts in a mesostasis of any one or a combination of serpentine, calcite and phlgopite. Does not contain pelletal or pseudo-pelletal textures.

Matrix - interclast phase in volcaniclastic kimberlite.

Groundmass - mesostasis phase in a coherent kimberlite and of juvenile clasts; cements microphenocrysts, phenocrysts and macrocrysts in these rocks.

3.5 The Geology of the D/K1 Pipe

This section describes the geological characteristics of the six major kimberlite lithofacies associations of D/K1 defined by structure, lithic clast size and abundance, olivine grainsize and abundance, and alteration. Table 3.5 summarises the main geological and petrological characteristics of each major lithofacies association, and Figures 3.4 and 3.5 present some representative logged sections from the D/K1 pipe.

	VK1	DVK	PVK	SVK	BBR	CK
Colour	Dark grey	Very dark grey	Pale-dark grey	Pale grey-brown	Light grey-brown	Very dark grey-black
Ol Content (vol%)	30-40	50	30	30	10-20	60
Av. ol size (mm)	3	2	4	5	3	3
Ol alt.	Completely serpentinised	Fresh-serpentinised	Completely serpentinised	Completely serpentinised	Completely serpentinised	Fresh with Ca-rich rims
Av. lithic content (vol%)	12	10	8	15	60-≥90	7
Lithic fragment size; max. av.	10 mm, 2 mm	20 mm, 2 m	300 mm, 10 mm	20 mm, 2 m	200 mm, 10 m	100 mm, 10 mm
Lithic Alt.	Few alteration haloes	Metamorphosed and alteration haloes	Metamorphosed (?)	Unaltered	Unaltered-oxidised	Metamorphosed
Texture	Ghost lapilli, pseudo-pelletal	Ghost lapilli; pseudo-pelletal	Pelletal and juvenile lapilli	Pelletal and juvenile lapilli	Ghost lapilli and rare pelletal lapilli	Coherent, non-fragmental
IM or GM phase	Fine microlites and serpentine	Coarser microlites, serpentine and rare calcite	V. fine-grained microlites and serpentine	V. fine-grained microlites, serpentine, calcite and phlogopite	Serpentine and microlites	calcite, serpentine, oxides and phlogopite
Structure	Massive to crudely layered	Massive to crudely layered	Massive to crudely layered	Massive to crudely layered	Massive to crudely layered	Massive

Table 3.2: Summary table of the main characteristics of the major D/K1 lithofacies; VK1, DVK, PVK, SVK, BBR and CK which are described in Section 3.5 below. (Ol - all olivines (macrocrysts, phenocrysts and microphenocrysts); IM - interclast matrix; GM - groundmass; Alt - alteration; Av. average; Max. - maximum; v - very)

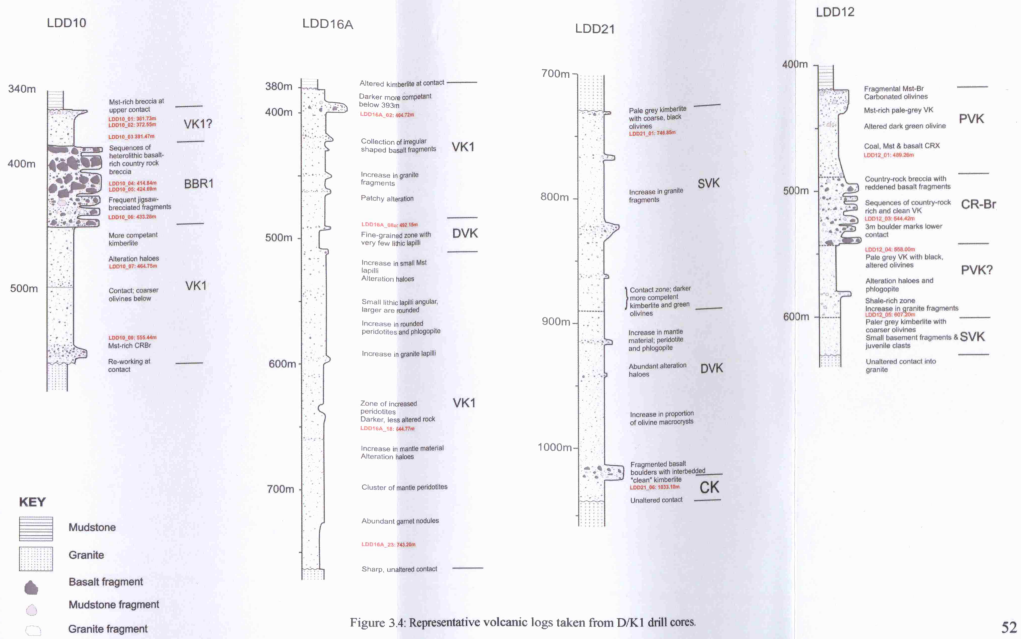

Figure 3.4: Representative volcanic logs taken from D/K1 drill cores.

Figure 3.4: Representative volcanic logs from D/K1 drill cores.

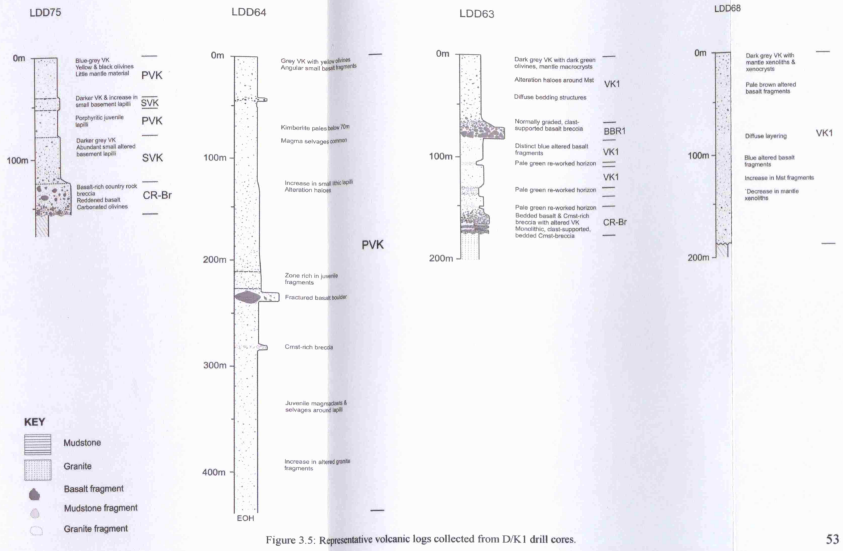

Figure 3.5: Representative volcanic logs collected from D/K1 drill cores.

Figure 3.5: Representative volcanic logs from D/K1 drill cores.

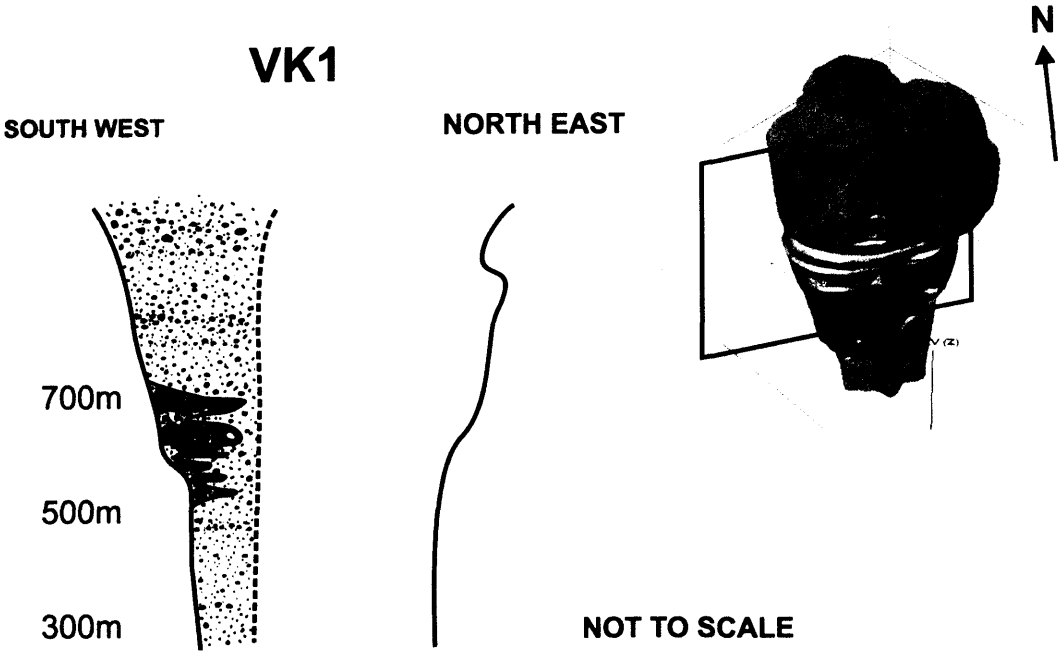

Figure 3.6: Schematic illustrating the large scale features of VK1; country rock breccias, and crude layering. (Model of D/K1 is shown to illustrate the location of the cross section.)

3.5.1 VK1

VK1 is located from the north to the south-west of the D/K1 pipe (Fig. 3.3), and is comprises of predominantly massive to crudely layered volcaniclastic kimberlite and country rock breccias, in addition to a layered country rock breccia and one bedded VK horizon (Fig. 3.6). VK1 is greater than 600 m thick and extends from the present day mine surface to below the known extent of the D/K1 pipe.

3.5.1.1 Country rock breccias (CRBr)

There are two country rock rich breccia lithofacies within VK1 (not part of the BBR lithofacies described later).

BBr1

BBr1 is a poorly sorted, crudely layered breccia with $\geq$90 vol% lithic content. It is located within the south-west of VK1 between 730 and 665 m elevation (Fig.

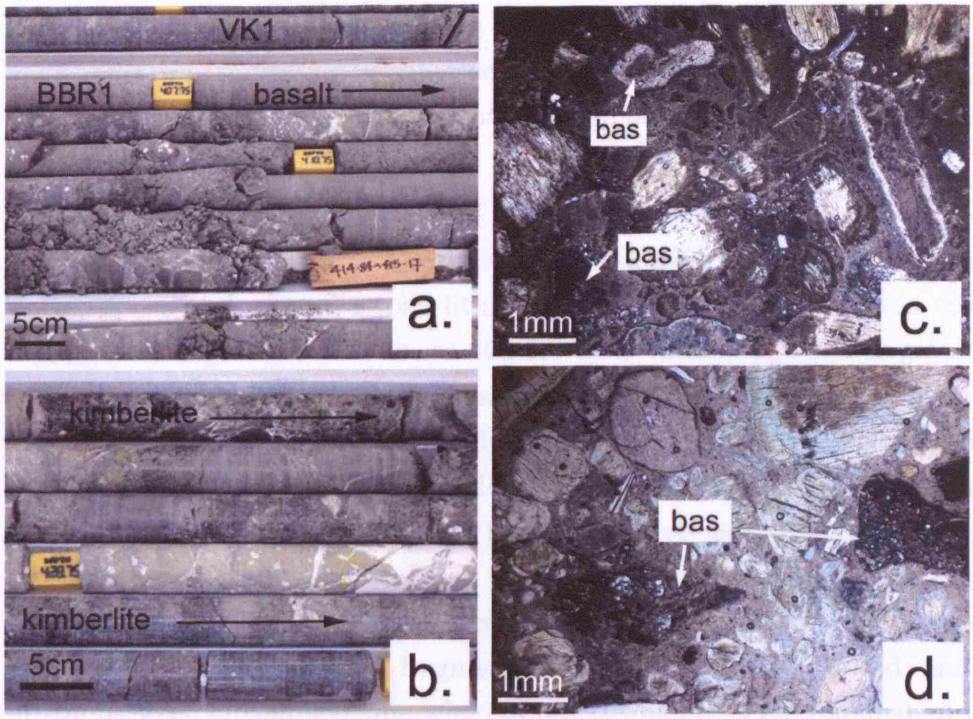

Figure 3.7: (a) and (b) Photographs of drill core sections from BBr1 illustrating the block-rich nature of this breccia. Jigsaw-textured fractures (referred to later in the text) are shown in the lower image. (c) and (d) Photomicrographs illustrating small accidental basalt (bas) lapilli, the upper example very altered, with olivine macrocrysts and phenocrysts in a fine-grained altered clay-rich cement.

3.6). It forms 2-10 m thick sequences dominated by lithic blocks and boulders interbedded with lithic-poor volcaniclastic kimberlite characteristic of VK1 (Fig. 3.6). Lithic clasts are $\geq$95% basalt, with subordinate granite and mudstone. They range in size from 2-3 mm up to 10 m; only basalt fragments form blocks greater than 2 m. Occasionally, large megablocks ($\geq$10 m) have jigsaw-textured fractures which are cemented by calcite (Fig. 3.7). Lithic clasts are angular to sub-rounded. They are found in mixed lithologies; for example, amygdaloidal and non-amygdaloidal basalt clasts are juxtaposed. The upper contact is marked by a large basalt megablock of 10 m diameter in drill core LDD10 (Appendix A).

BBr1 is predominantly clast-supported, however, an interclast matrix is sparsely distributed throughout the rock which comprises of small, angular lithic clasts,

pseudomorphs of olivine macrocrysts (10-20 vol% of the matrix), phlogopite and xenocrysts of pyroxene set in a microcrystalline cement of microlitic diopside and serpentine and rare pools of calcite at the edge of grains (Fig. 3.7c and d).

Carbonaceous mudstone breccia (CMST-Br)

The CMST-Br is a clast to matrix supported kimberlite breccia. Matrix supported zones comprise ~25 vol% lithic lapilli set in a dark olive-green coloured, clay-rich matrix. It occurs between 665-630 m elevation, adjacent to granite wall rock and marginally below the Tlhabala Formation mudstone stratigraphy. It was intersected by drill cores LDD63 and LDD73 (Appendix A). Layering is defined by clast-supported horizons interbedded with fine-grained, lithic-poor horizons, with a thickness between 20-40 cm (Fig. 3.8). There is a weak grain alignment of ~30° at the upper contact. The lithic population is comprised of 50% carbonaceous mudstone (CMST) and coal lapilli, 25% mudstone (MST) and 25% basalt. CMST, coal and MST fragments are angular (Fig. 3.8c and d) and range in size between 50 and 500 mm, whereas basalt fragments are rounded and range between 80 and 400 mm. The matrix is composed of olivine macrocrysts which have been carbonated to a white colour or serpentinised to a black coloured mineral, small lithic lapilli, phlogopite and xenocrysts of pyroxene set in a clay-rich base with occasional pools of calcite between grains.

3.5.1.2 Volcaniclastic Kimberlite

Massive Volcaniclastic Kimberlite (VK1)

There are two constituent massive volcaniclastic kimberlite lithofacies within VK1. The first, which is called VK1a, is the most volumetrically abundant ($\geq$95%) volcaniclastic kimberlite lithofacies of the VK1 body. It fills the VK1 area of the pipe from the south-west to the north not occupied by BBr1 or VK1b (Fig. 3.13). VK1a is massive to crudely layered with layering defined by concentrations of lithic fragments (Fig. 3.6) which comprise ~12 vol% of the rock on average, and varies between $\leq$1 vol% and 29 vol%. Crude layers vary in thickness from $\leq$2 m to $\geq$10 m and are defined by both increases and decreases in lithic content. These layers are particularly prevalent in the northern lobe of VK1a.

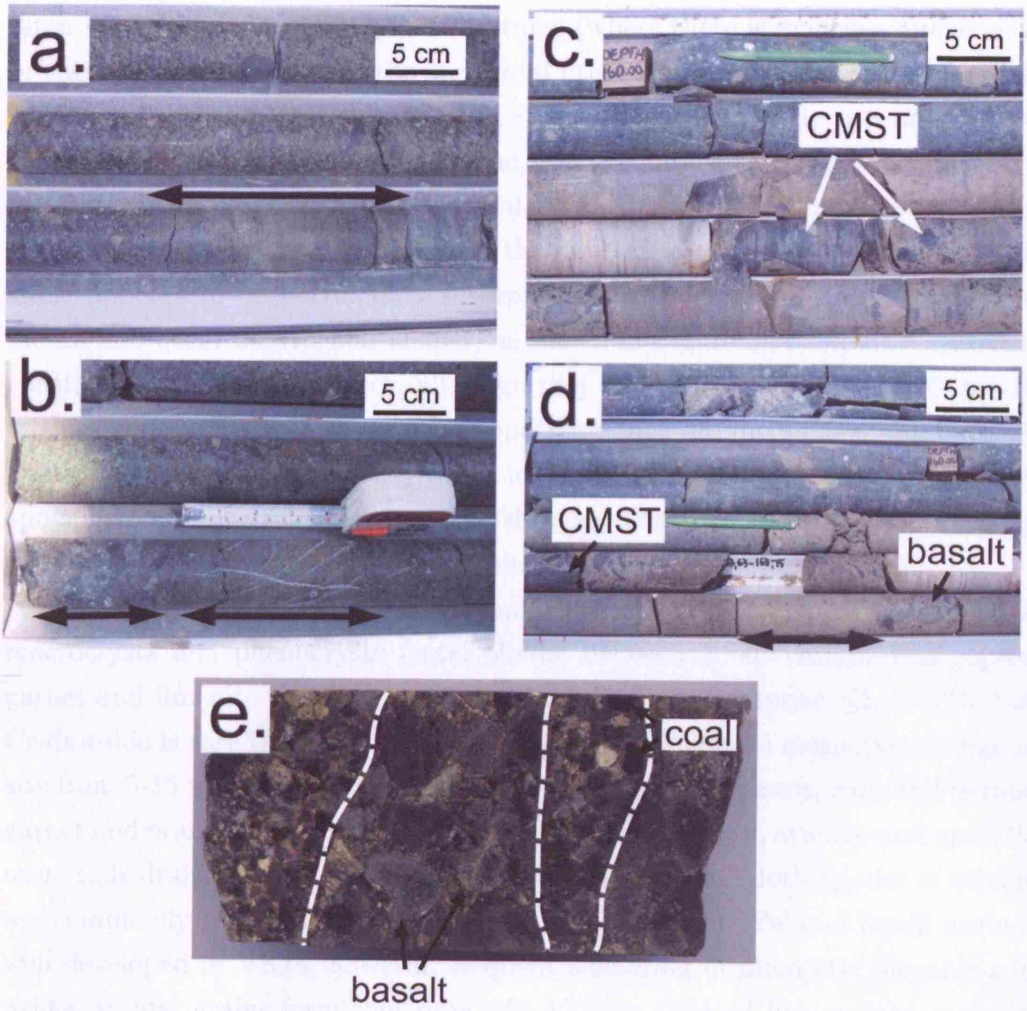

Figure 3.8: Drill core photographs of CMST-Br illustrating the structure of this unit. Black arrows indicate individual sequences. (a) and (b) fine-grained and coarse-grained layers from drill core LDD63. (c) and (d) illustrate the angular, CMST lapilli-rich nature of this breccia. (e) Polished drill core section illustrating individual layers marked by dashed white lines.

The lithic population is dominated by basalt throughout VK1a by 90 vol% on average. Granite and mudstone fragments are subordinate (~10%) and sandstone is very rare (≤1 vol%). The shape of lithic fragments varies with size; lapilli ≤20 mm are typically angular whereas lapilli and blocks ≥ 20 mm are more rounded. Lithic alteration also varies with grain size. Basalt lapilli and blocks ≥50 mm

often show contact metamorphism textures (where there is evidence of chemical or thermal reaction between the accidental lithic and the surrounding kimberlite; Figures 3.9a) and 3.12e. Basalt lapilli $\leq$50 mm are completely metamorphosed which has produced a distinct, pale blue/grey coloured clast. Zones within VK1a are rich in lithic lapilli with alteration haloes (Fig 3.9c and d) where there has been chemical or thermal reaction between the kimberlite and lithic fragment. Mudstone appears to be particularly susceptible to this process. Basalt lapilli and blocks also occur as irregular shapes, as shown in Figure 3.9b. Mantle xenoliths constitute $\sim$1 vol% of the rock, although they can comprise up to 5 vol% in $\sim$10 m thick zones. The mantle xenolith population includes lherzolites, harzburgites and subordinate eclogites. They range in size from 15-250 mm and are generally sub-spherical, very rounded 'egg'-like shapes. The rims have been affected by alteration and the cores typically remain fresh.

The matrix consists of fine lithic lapilli and ash-sized fragments, and olivine macrocrysts and phenocrysts (total olivine between 30-40 vol%). Phlogopite, garnet and ilmenite macro- and megacrysts combined comprise $\leq$1-5 vol%, but Cr-diopside is rare (Fig. 3.9c and f). Garnet and phlogopite megacrysts range in size from 5-15 mm in diameter. Two types of garnet are present; ruby-red pyrope garnet and orange pyrope. Olivine macrocrysts are 3 mm on average and up to 20 mm. Euhedral olivine phenocrysts are typically $\leq$1 mm. Both species of olivine are completely replaced by serpentine (Fig. 3.9c and f). Pelletal lapilli are not well developed in VK1a, however, frequent clustering of microlitic diopside and oxides around grains form thin rims $\sim$20-100 μm thick of fine-grained material which creates a pseudo-pelletal texture. These will be referred to as ghost-lapilli (Fig. 3.11d). The interclast matrix phase is dominated by microlitic diopside, which is finely disseminated between clasts as well as forming fringes and clusters. The base is predominantly amorphous serpentine and rare irregular patches of calcite (Fig. 3.9c). There is a paucity of discrete oxides within the matrix, this applies to both perovskite and subordinate spinel. They are more commonly located at the edge of olivine phenocrysts. There are zones located close to the wall rock and kimberlite with increased lithic fragment content which are more heavily altered (Fig. 3.12). These zones have gradational contacts with the dark

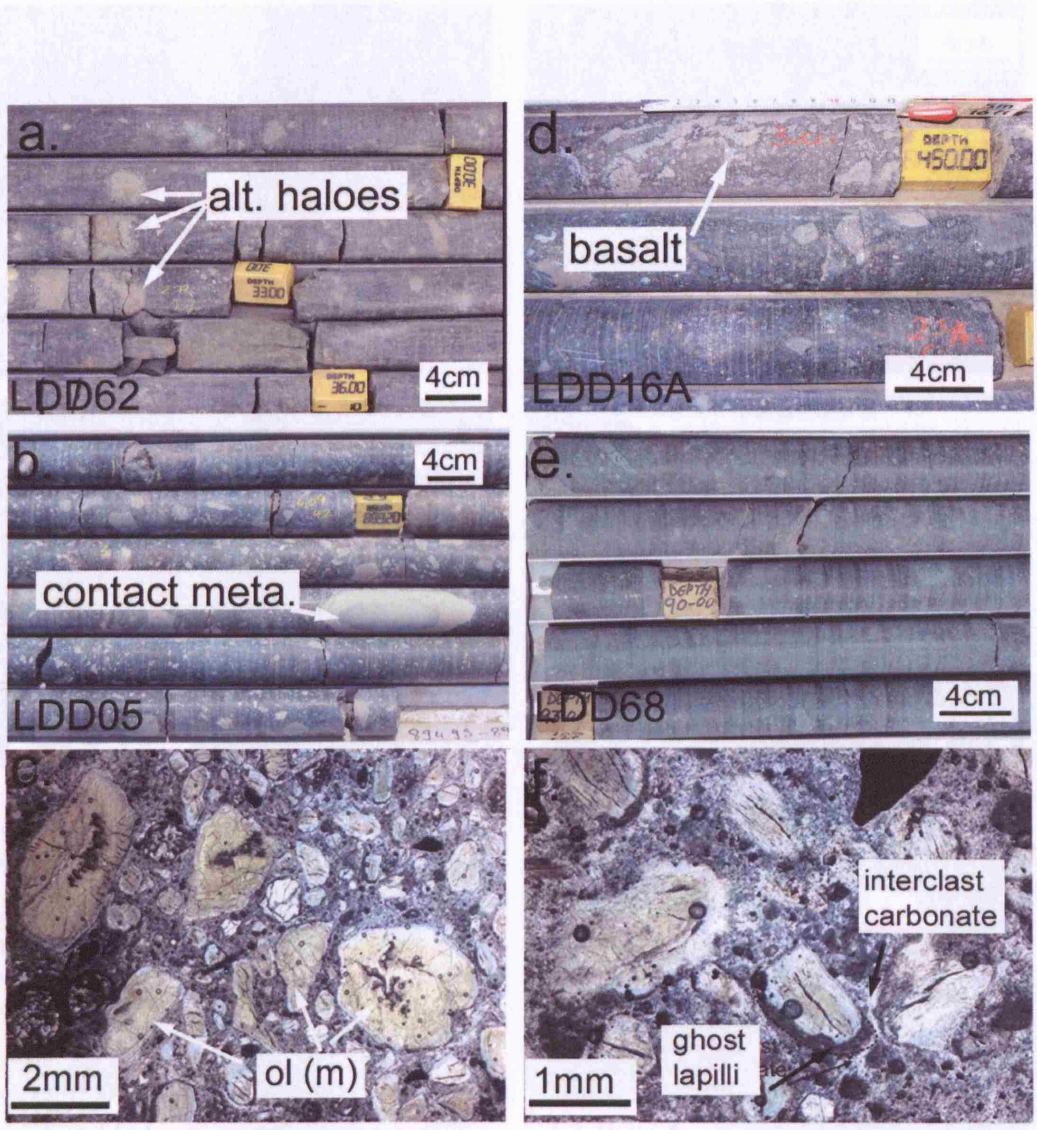

Figure 3.9: Drill core photographs and photomicrographs of volcaniclastic kimberlite from VK1a. (a) Alteration haloes around mudstone lapilli. (b) Contact metamorphism in rounded basalt block. (c) Photomicrograph of olivine macrocrysts in VK1 (ol(m)). (d) Irregular, dissolved shape of an included basalt fragment. (e) Crude layer of lithic poor kimberlite. (f) Photomicrograph of ghost lapilli and interclast pools of calcite.

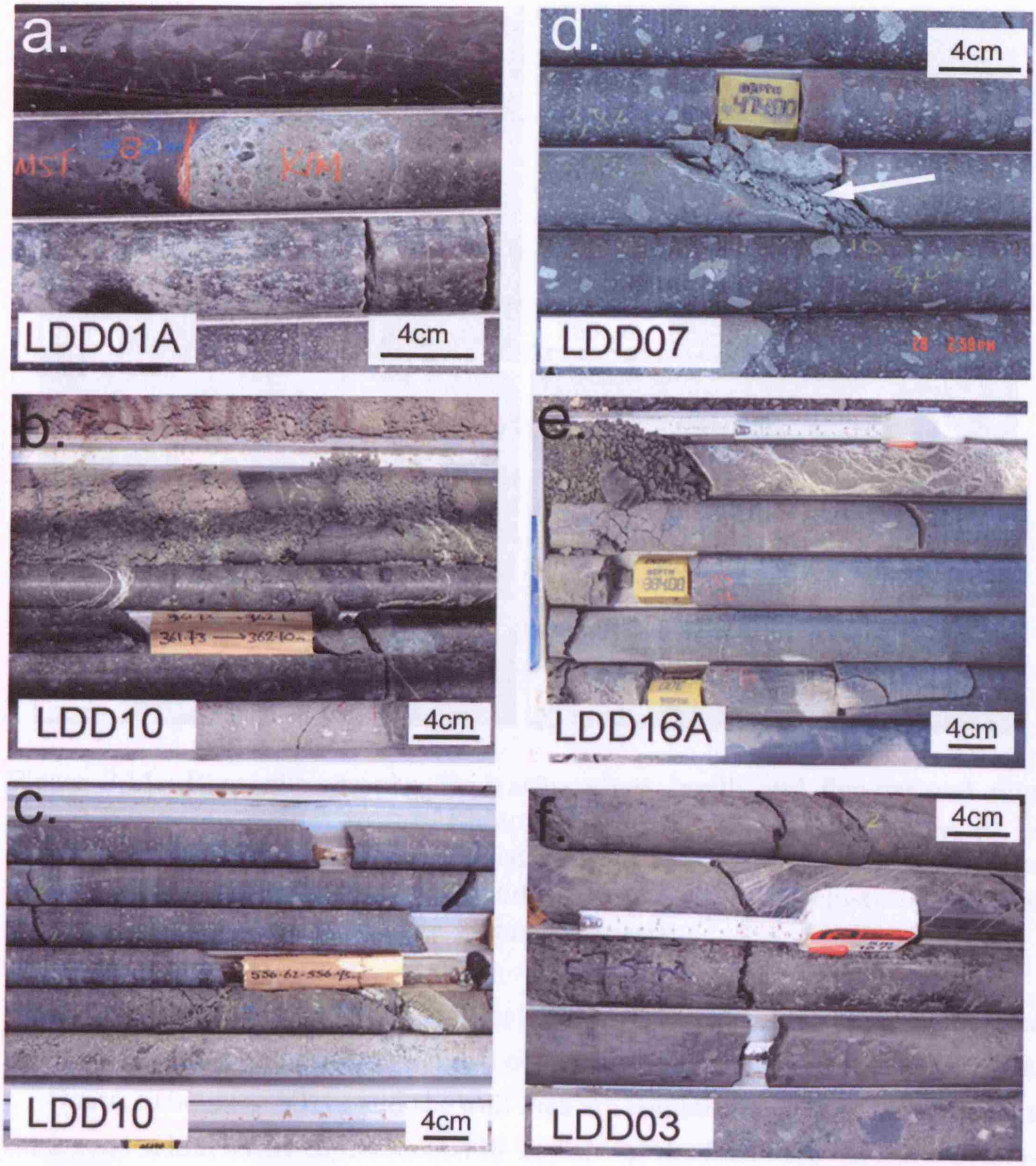

Figure 3.10: Drill core sections of contacts between VK1a and the wall rock. (a) Diffuse bedding in a fine-grain kimberlite. (b) Fine-grain kimberlite interbedded with mudstone and calcite marking joints. (c) and (d) Altered kimberlite with calcite-bounded faults and 'cataclastic' (see text) kimberlite marked by the white arrow in (c). (e) Brecciated wall rock with a calcite cement. (f) Mudstone-rich breccia (CMST-Br).

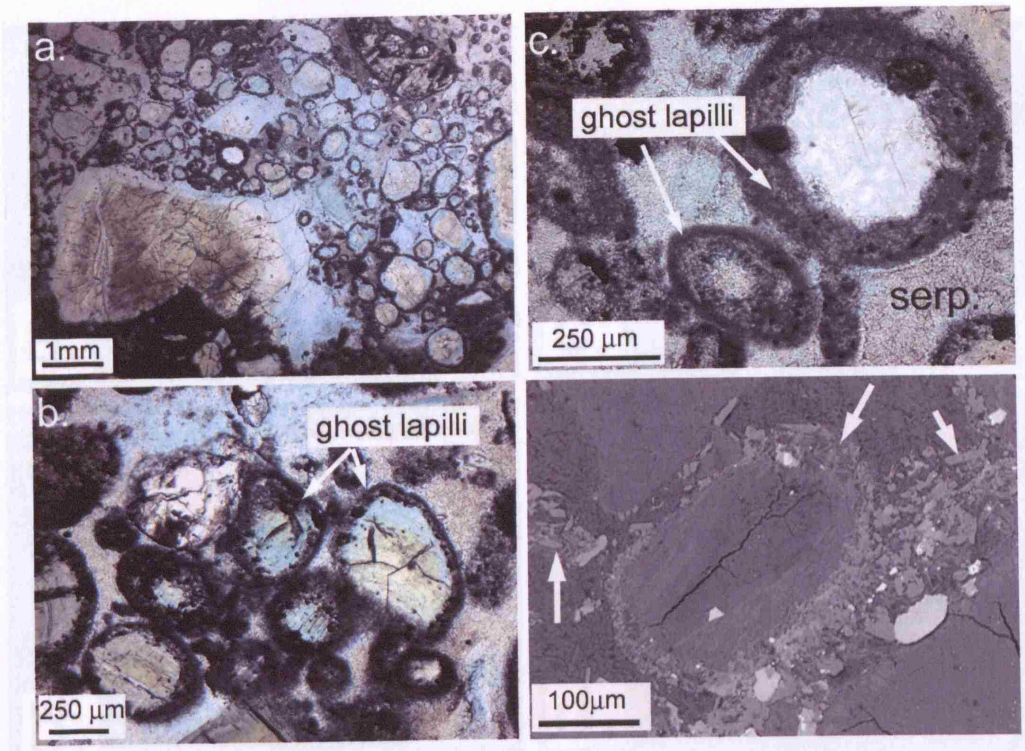

Figure 3.11: Photomicrographs illustrating ghost lapilli and fine-grained rims from VK1a samples. (a) to (c): Photomicrographs of samples LDD16A_02 illustrating ghost lapilli and fine-grained rims (serp. - serpentine). (d) Electron backscatter image of microlitic diopside (white arrows) clustering around an olivine phenocryst and discrete within the matrix.

VK1a. In thin section the interclast matrix phase of these heavily altered zones is almost optically unresolvable, and is composed of clay and microlitic diopside.

Contacts between VK1a and the wall rock are commonly marked by a 0.25-3 m thick zone of kimberlite characterised by any one of the following: (i) diffuse layering; (ii) lithic fragments set in a fine-grain, very weathered, clay-rich kimberlite; (iii) extensive alteration, including the presence of carbonated olivine macrocrysts; (iv) joint surfaces covered with 'cataclastic' kimberlite which is a very fine-grained kimberlite that is interpreted here as being produced by movement along a fault; (v) a zone of carbonaceous mudstone-rich breccia; (vi) brecciated wall rock with a calcite cement (Fig. 3.10).

The second type of volcaniclastic kimberlite, VK1b, is located at the northern

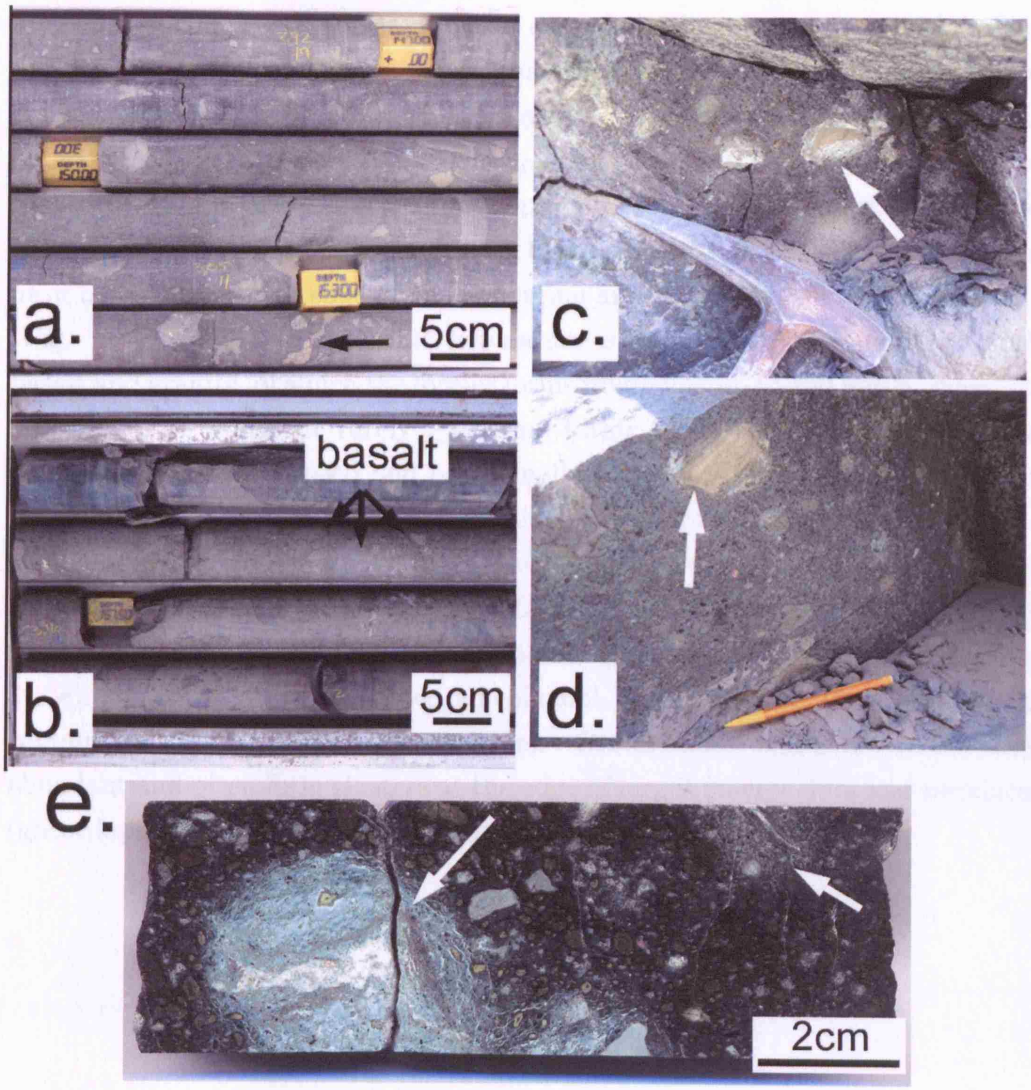

Figure 3.12: Drill core sections of bleached kimberlite within VK1a. (a) - (c) Lighter kimberlite matrix containing lithics with dark rims. (d) Basalt-rich breccia in a pale grey, fine-grained kimberlite. (e) Polished drill core section of alteration halo around an irregular lithic fragment.

contact with the wall rock (Fig. 3.13). It was intersected by drill cores LDD08, LDD11A and LDD23A at approximately 400 m elevation (Fig. 3.13a). However, pit sample LMS58 is classified as the same lithofacies using bulk rock geochemistry

in Chapter 6 (Fig. 6.1), which implies it extends to the current excavated surface of the mine. VK1b is a green coloured massive volcaniclastic kimberlite with ~30 vol% olivine macrocrysts and on average 10 vol% lithic content, and abundant mantle macrocrysts (other than olivine) and xenoliths. Olivine macrocrysts are of the order of 2 mm in size and are totally pseudomorphed and often zonally altered (Fig. 3.13d and e). The small ($\leq$1 mm) olivine phenocrysts and microphenocrysts have been completely replaced by serpentine and have remnant euhedral habits (Fig. 3.13 d and e). The lithic population is dominated throughout by both basalt and granite, of which the former forms fragments up to 450 mm in diameter and the latter which are rarely $\geq$10 mm. Lithic lapilli are mostly $\leq$5 mm and completely metamorphosed and occasionally have alteration haloes. There is a notable increase in clays within alteration haloes around lithic lapilli. Mantle xenoliths are altered and also display reaction rims. Macrocrysts are relatively abundant compared to other D/K1 lithofacies. The interclast matrix has a patchy texture produced by 'clumps' of amorphous clays and patches of calcite (Fig. 3.13e). Textures which resemble ameoboidal porphyritic lapilli in the matrix contain olivine phenocrysts (Fig. 3.13e). Groundmass oxides are moderately abundant and often form clusters at the edge of larger macrocrysts and necklaces (ghost lapilli) around olivine phenocrysts.

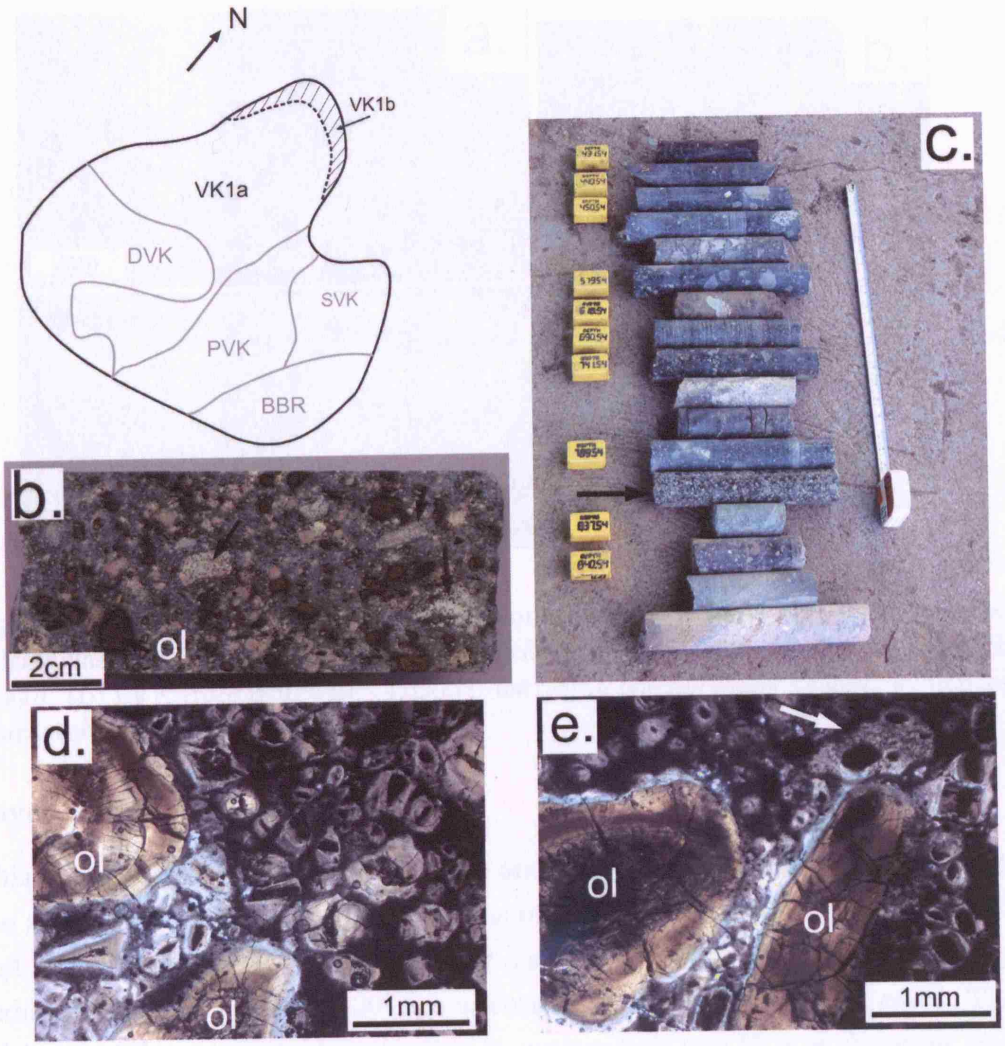

Figure 3.13: (a) Location of VK1b within VK1 on a plan view at 400 m elevation within the D/K1 pipe. (b) Polished drill core section from drill core LDD23A showing an olivine macrocryst (ol) with dark rim and black arrows point to metamorphosed granite lapilli. (c) Drill core sections from LDD11A illustrating the distinct difference of VK1b highlighted by the black arrow. (d) and (e) Photomicrographs showing zonally altered olivine macrocrysts and phenocrysts (ol) and the patchy nature of the interclast matrix. White arrow in (e) points towards a texture which resembles an ameoboidal porphyritic lapillus.

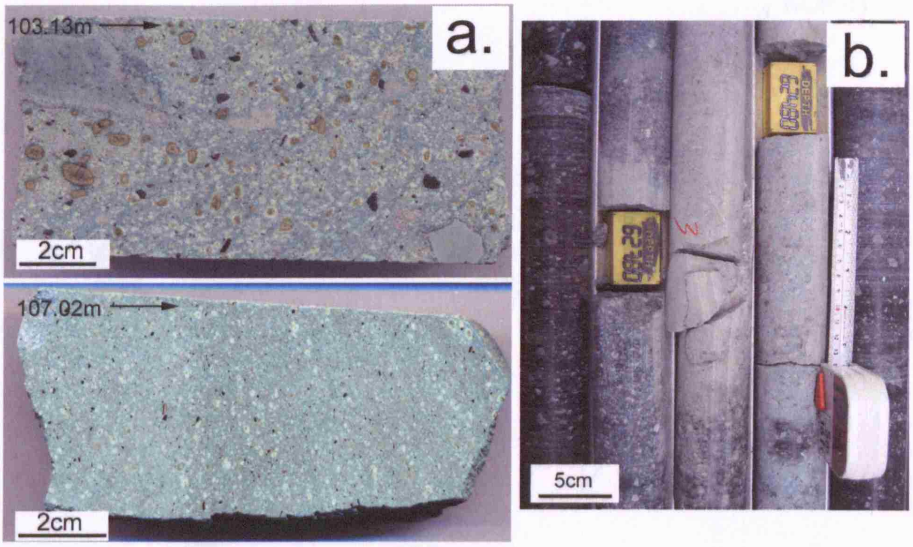

Figure 3.14: (a) Polished drill core sections from drill core LDD63 of layered volcaniclastic kimberlite in VK1. Downhole drilling depths are shown on each image. (b) LVK from drill core LDD03 illustrating the normally graded sequences characteristics of this lithofacies.

Layered Volcaniclastic Kimberlite

This lithofacies is volumetrically small and occurs around 690 m elevation in the south-west of the D/K1 pipe. It was only intersected by drill cores LDD03 and LDD63 (Appendix A). It has a very distinctive pale green matrix with thin, bedded layers which dip at $\sim 30^{o}$ (no orientation; dip taken from drill core). The thickness of the unit varies between 2 m in one borehole and 12 m in the other, and it is interbedded with VK1. Individual normally graded layers are ~10-50 mm and are defined by altered olivine macrocryst abundance (Fig. 3.14). Alteration of the lithofacies is extensive and has affected the surrounding kimberlite (Fig. 3.14a).

3.5.2 Dark Volcaniclastic Kimberlite (DVK)

The dark volcaniclastic kimberlite (DVK) is a massive volcaniclastic deposit characterised by a competent, dark grey to black coloured matrix with abundant fresh and serpentinised olivine macrocrysts (~50 vol%) and variable (≤1-25 vol%) lithic

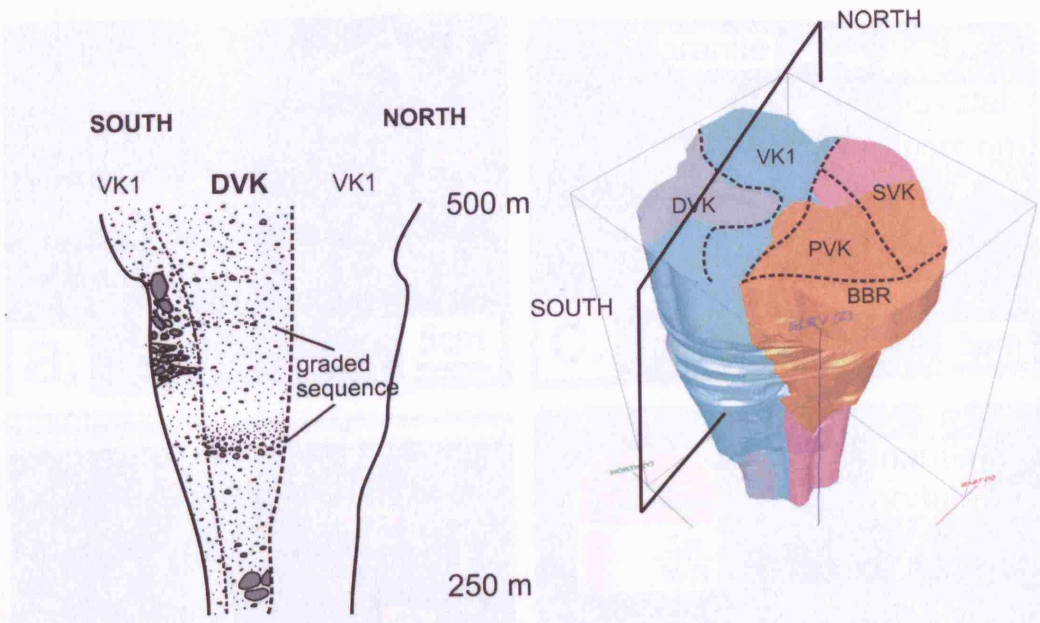

Figure 3.15: Schematic illustrating the large scale features of DVK; massive to crudely layered sequences, and the contact zone marked by country rock breccias to the south. (Model of D/K1 is shown to illustrate the location of the cross section.)

clast abundances. Crude layers are defined by reverse to normally graded sequences between 2-15 m thick of increasing lithic lapilli content. Average lithic content is 10 vol%. DVK forms an irregular lobate geometry surrounded by VK1 to the north, east and south, and the country rock to the west (Fig. 3.15). Basalt lapilli and blocks dominate the lithic population, constituting approximately 80%, with subordinate granite (15%) and mudstone (5%), but no sandstone was observed. Lithic lapilli and blocks are typically angular to subrounded, with an average size of 20 mm in diameter, and a maximum of 1.64 m. Lithic fragments have often been metamorphosed (Fig. 3.16c and d) and are often surrounded by an alteration halo. However, there is a region ~10 m thick between 260-250 m elevation with several jigsaw-textured fragmented basalt boulders between 0.5-1.7 m in diameter. These basalt boulders are around 650 m below their original stratigraphic position in the Stormberg sequence. Olivine-rich mantle xenoliths comprise 1-5 vol%. They are typically rounded and range between 10-100 mm in diameter (Fig. 3.16d).

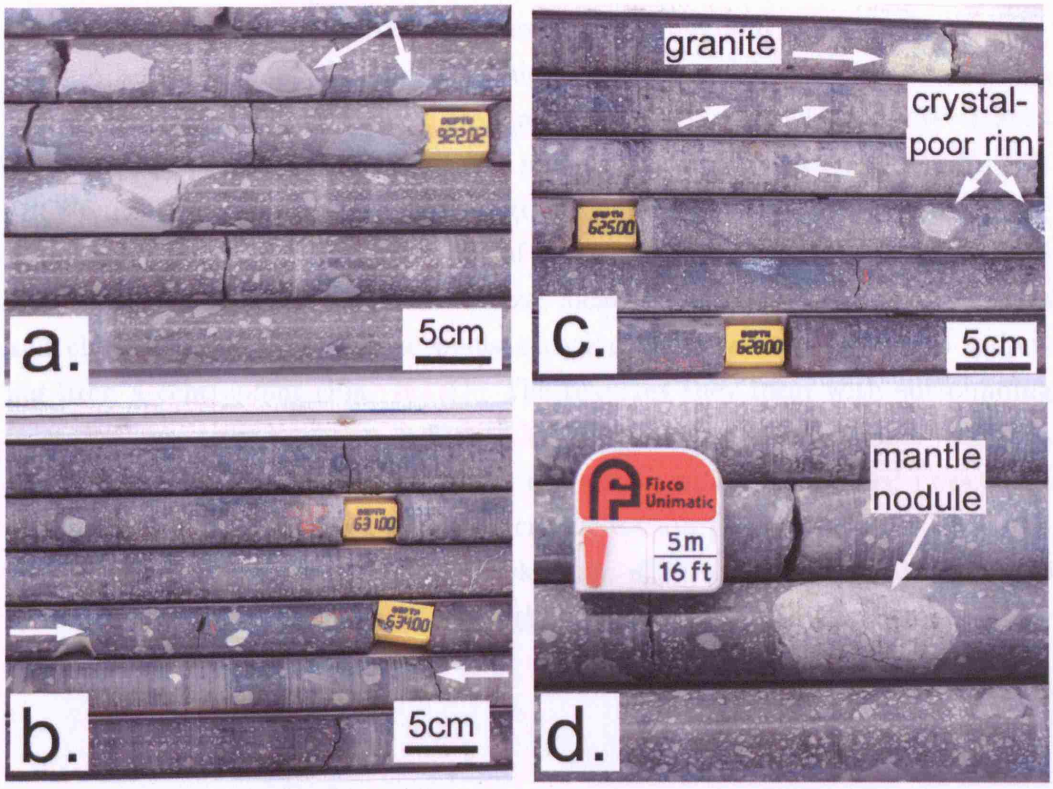

Figure 3.16: Representative photographs of textures from DVK drill core sections. (a) Typical DVK texture with abundant fresh olivine macrocrysts in a dark grey matrix. Arrows point to metamorphosed basalt. (b) Zone of macrocryst-poor DVK between the arrows. (c) Photo illustrates crystal-poor rims around country rock fragments and granite lapilli with an alteration halo. Single arrows point towards patchy distribution of olivine macrocrysts. (d) Rounded mantle nodule.

DVK contains ~50 vol% olivine macrocrysts (~2 mm in diameter) and phenocrysts (≤0.2 mm), phlogopite and garnet macrocrysts (1-2 vol%). The interclast matrix of DVK is comprised of the aforementioned olivine phenocrysts, oxide microphenocrysts of spinel and perovskite, and a cryptocrystalline base of serpentine, microlitic diopside and calcite. Olivines have a patchy distribution throughout the lithofacies. There is a zone at an elevation between 500-350 m elevation intersected by drill cores LDD22 and LDD24 (Appendix A) where lithic lapilli have rims ~5 mm thick which are poor in olivines (Fig 3.16b). Olivine macrocrysts generally have fresh cores and serpentinised rims (Fig. 3.17b and c),

although the abundance of fresh olivines varies throughout the unit, both vertically (observed from drill cores) and laterally (observed in the mine exposure). Olivine phenocrysts have a subtle grain alignment in places, which is investigated and discussed in Appendix C. Interclast microlitic diopside is coarser than in VK1 (10-30 μm) and widespread, located at grain boundaries and between grains. Calcite comprises approximately 1-3 vol% of the interclast matrix and forms irregular patches between 100μm to 1 mm in size, located in between adjoining crystals and clasts (Fig. 3.17a). These pools occasionally have acicular grains radiating from a centrepoint (Fig. 3.17f). The textures they form with surrounding clasts is interesting, as shown in Figure 3.17a where calcite infills triple-junctions between clasts. This texture resembles cementing which has infilled pore space and not textures produced by volatile crystallisation (Brown et al., 2006). Oxide microphenocrysts spinel and perovskite are $\leq$100 μm and typically nucleate at olivine grain boundaries producing ghost lapilli and a pseudo-segregationary texture (Fig. 3.17e).

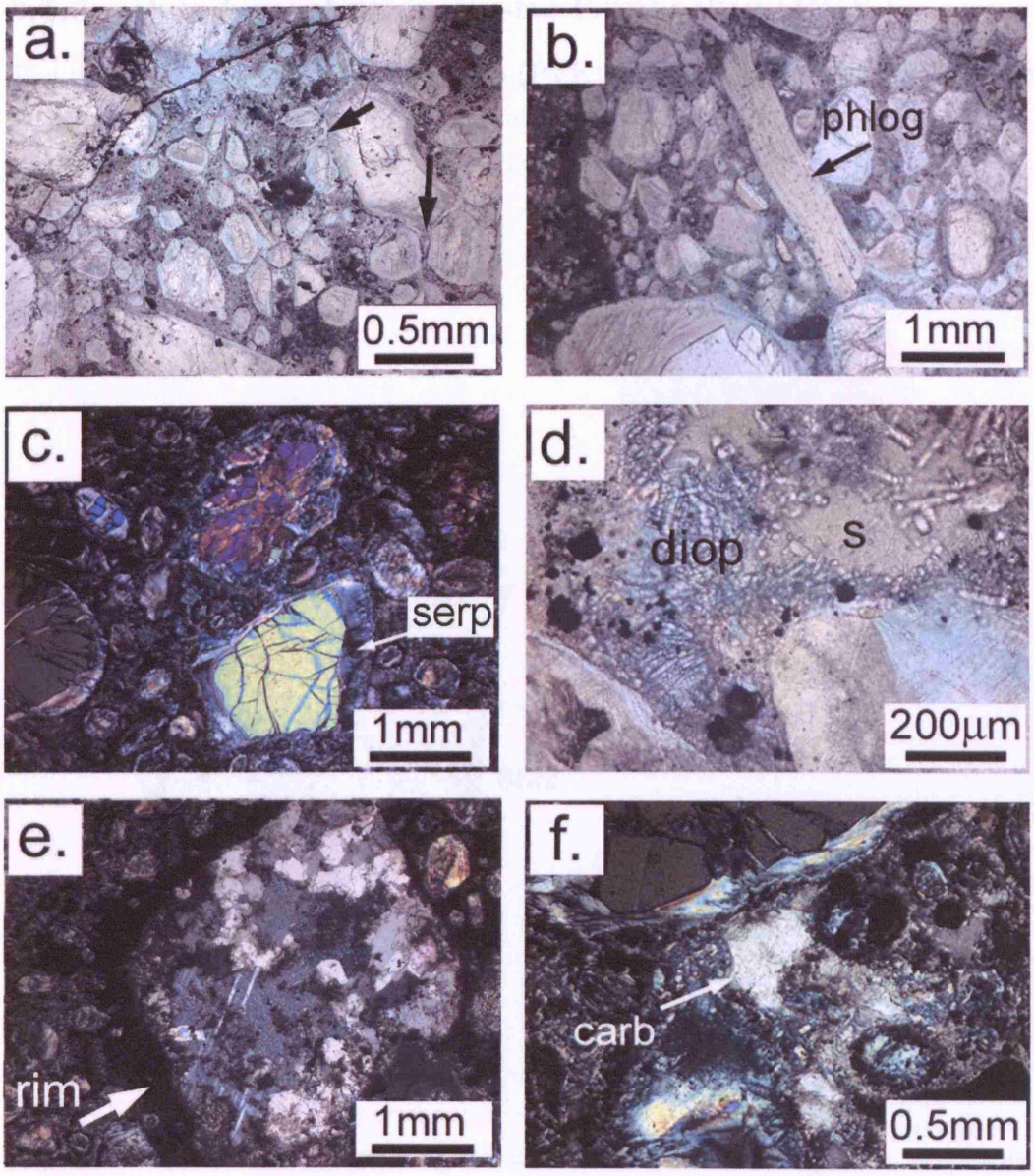

Figure 3.17: Photomicrographs of DVK textures. (a) Illustration of agglutinated textures where three grains meet, highlighted by the black arrows. (b) Large phlogopite macrocryst (phlog). (c) Crossed-polarised light photomicrograph of olivine macrocrysts with fresh cores and altered rims (mottled grey, low birefringence phase; serp.). (d) Groundmass phases of microlitic diopside (diop), dark brown and black, euhedral oxides and pools of amorphous, yellow serpentine (s). (e) Pseudomorphed granite lapilli with a thin rim of a dark, optically unresolvable phase. (f) Crossed-polarised light photomicrograph of a pool of calcite with acicular grains (carb) radiating from the edge of an olivine, and with concave habit.

3.5.3 Pale Grey Volcaniclastic Kimberlite (PVK)

The pale grey volcaniclastic kimberlite (PVK) is located within the east of the D/K1 pipe (Fig. 3.18). It is predominantly a pale grey coloured massive volcaniclastic lithofacies with a country rock-rich breccia.

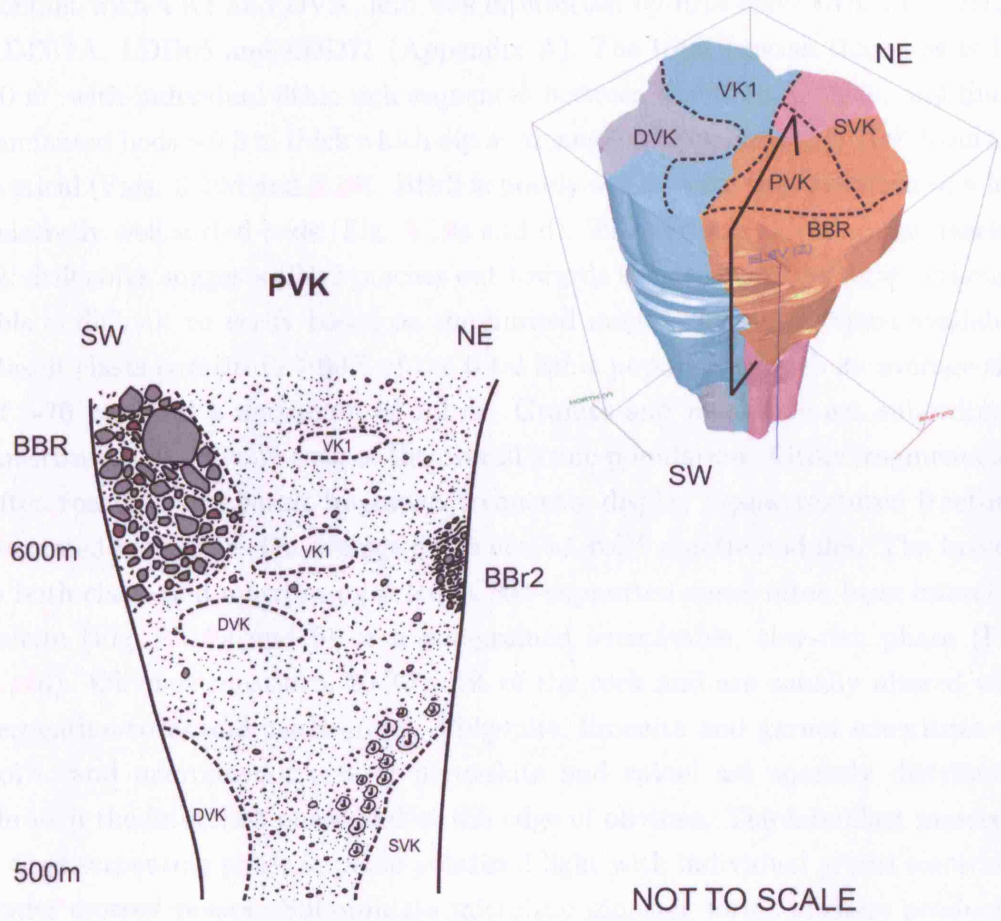

Figure 3.18: Schematic illustrating an interpretation of the structure and large-scale features of PVK, including both BBR and BBr2. Lenses of VK1 and DVK are shown on the cross-section, and represent an undulating contact or mixing of large juvenile megablocks. (Model of D/K1 is shown to illustrate the location of the cross section.)

Basalt-rich breccia (BBr2)

BBr2 is a heterolithic, basalt-rich breccia with up to 80 vol% lithic fragments and a light green coloured kimberlite matrix (Fig. 3.19). It is located internally within the D/K1 pipe as a sub-unit of PVK between 570 and 500 m elevation, close to the contact with VK1 and DVK, and was intersected by drill cores LDD15, LDD22, LDD11A, LDD65 and LDD71 (Appendix A). The total breccia thickness is 15-30 m, with individual lithic-rich sequences between 4 and 10 m thick, and finely laminated beds $\leq$0.5 m thick which dip at an angle of approximately 100^o from the vertical (Figs. 3.19d and 3.18). BBr2 is poorly sorted with the exception of a few relatively well sorted beds (Fig. 3.19a and d). The variable thickness intersected by drill cores suggests BBr2 pinches out towards the centre of the pipe, although this is difficult to verify based on the limited number of intersections available. Basalt clasts constitute $\geq$90% of the total lithic population, with an average size of $\sim$70 mm and a maximum of 1.2 m. Granite and mudstone are subordinate constituting $\sim$1-2 vol% each of the overall lithic population. Lithic fragments are often rounded and basalt fragments frequently display jigsaw textured fractures cemented by calcite. On average there are $\sim$4 vol% mantle nodules. The breccia is both clast- and matrix-supported. Clast-supported zones often have interclast calcite (Fig. 3.19a and b) or a fine-grained irresolvable, clay-rich phase (Fig. 3.19d). Olivines constitute 20-30 vol% of the rock and are zonally altered with serpentine cores and calcite rims. Phlgopite, ilmenite and garnet constitute $\leq$1 vol%, and microphenocrysts of perovskite and spinel are sparsely distributed through the interclast phase and at the edge of olivines. The interclast matrix is a clear serpentine phase in plane-polarized light with individual grains resolvable under crossed polars. Subordinate microlitic diopside forms clusters producing a patchy-texture to the matrix. Microlites also radiate away from the edge of olivine grains which produces a thin $\leq$30 μm selvage rim or a ghost lapilli that also contain oxide microphenocrysts (Fig. 3.19c and f).

Massive Pale Grey Volcaniclastic Kimberlite (mPVK)

The dominant massive to crudely layered volcaniclastic kimberlite deposit of PVK has 30-40 vol% dark green to black coloured altered olivine macrocrysts and an

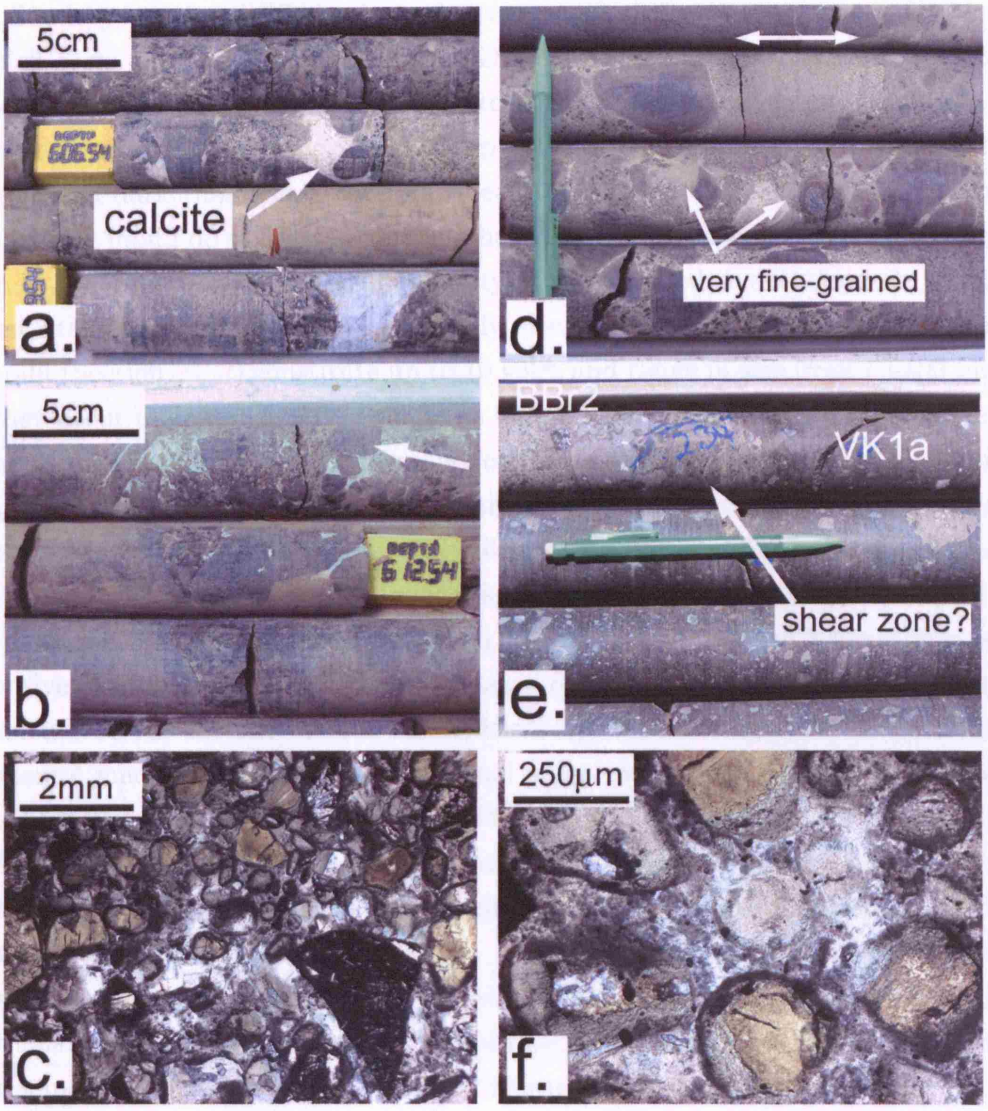

Figure 3.19: (a) and (b) Photographs of drill core sections from BBr2. White arrows point to interclast calcite. (c) and (f) Photomicrographs illustrating the calcite-rich interclast matrix phase and thin rims around olivine. (d) Photo of drill core illustrating a fine-grained, bedded sequence (white doublehead arrow). (e) Basal shear zone marks the contact with VK1a (BBr2 on the left at the top of the photo and VK1a on the right).

average lithic fragment content of about 8 vol% (Fig. 3.20). Crude layers are defined by varying lithic contents between 4-30 vol% over sequences 10-20 m thick (e.g. drill cores LDD12 and LDD76 in Appendix A). The lithic population is dominated by basalt ($\geq$90% of total lithics) with subordinate mudstone, carbonaceous mudstone, granite and up to 10 % sandstone. Lithic lapilli often have thin dark rims where there has been contact metamorphism (Fig. 3.20b), but these lapilli do not have alteration haloes. Lithic sizes are 10 mm on average and $\leq$300 mm maximum and they are typically rounded to subrounded. Mantle xenoliths are rare ($\leq$1 vol%) and totally altered. Cored and non-cored juvenile lapilli (Section 2.3.2) constitute up to 10 vol% and range in size from 10-300 mm. They occur in zones 20-170 m thick (as intersected by drill cores) close to either the contact with SVK, or the lower regions close to the wall rock. Cored juvenile lapilli are typically rounded and have lithic cores (Fig 3.20c and f), or in one case an altered mantle xenolith core. Juvenile lapilli have more irregular shapes and resemble kimberlite from SVK (which is described below).

Olivine macrocrysts (4-15 mm) and phenocrysts ($\leq$0.5 mm) have been extensively altered and often have serpentine cores and calcite rims. Other components of the mPVK include small lithic lapilli and xenocrysts of pyroxene, ilmenite macrocrysts, and perovskite and spinel microphenocrysts set in an interclast matrix of patchy serpentine and microlitic diopside. A large abundance of all olivines have a 10-50μm thick fine-grained rim comprising of oxide and olivine microphenocrysts, serpentine and microlitic diopside. Crystalline pelletal lapilli have thicker rims of $\geq$50 μm to $\leq$1 mm which are comprised of altered groundmass mineralogy including olivine phenocrysts in addition to another type of small, euhedral grains, probably replaced monticellite and microphenocrysts of spinel and perovskite (Fig. 3.21d). The interclast matrix phase of mPVK is predominantly serpentine and microlitic diopside which has a patchy distribution between clasts. Although PVK is predominantly a pale grey coloured rock, there is a continuum to a rock type with a darker grey colour, however, no mineralogical differences were observed between these two different types.

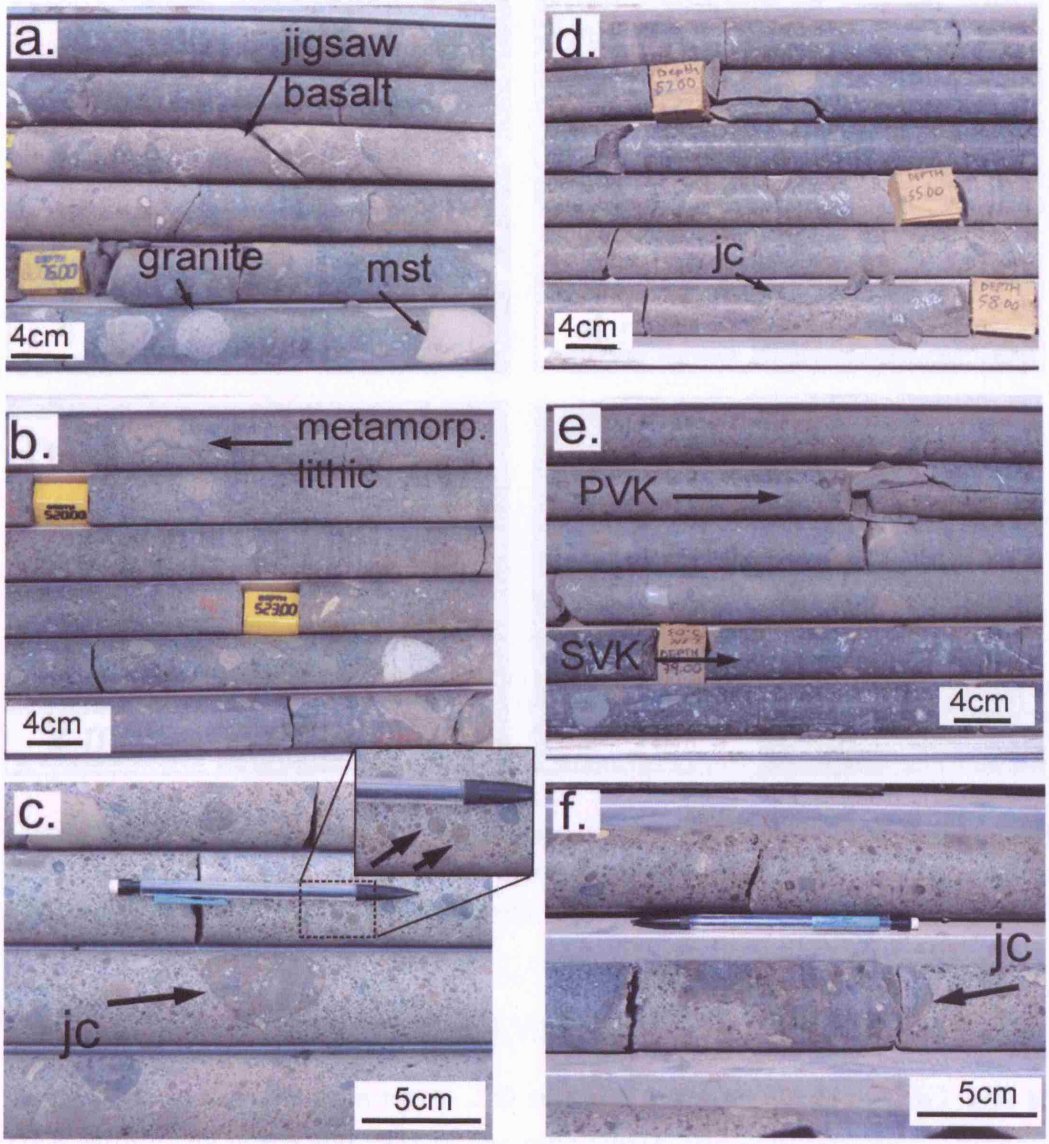

Figure 3.20: Photographs of drill core sections from PVK. (a) Jigsaw-fragmented and an amygdaloidal basalt, granite and mudstone (mst) fragments. (b) Metamorphosed lithic lapilli. (c) and (d) Round cored juvenile clasts (jc). (e) Drill core section illustrating the difference between PVK and SVK. (f) Irregular juvenile clasts (jc).

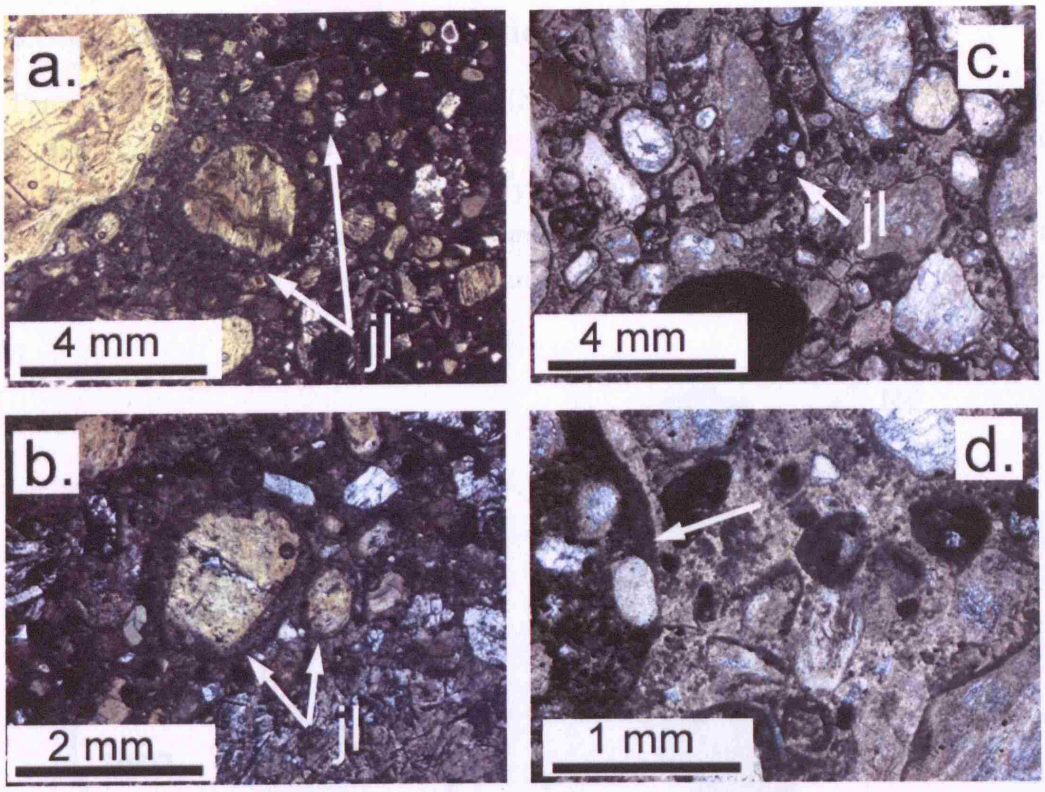

Figure 3.21: Photomicrographs of thin sections from PVK. (a) and (b) cored juvenile lapilli (jl). (c) asymmetric cored juvenile lapilli. (d) The fine-grain matrix of PVK. Arrow points to close-up of juvenile lapilli from (c), with altered possible monticellite.

Contacts from PVK to DVK and VK1

There is a 'transition' zone up to 150 m thick between PVK to VK1 and to DVK within the north and west of the pipe where drill core intersects fluctuate between these lithofacies. The actual contact is often sharp characterised by a rare alteration texture manifested by bleaching of the matrix, and a small increase in lithic content. The contact is more obvious between sub-unit BBr2 and VK1a (Fig. 3.19e). Rounded juvenile blocks of VK1 were observed in PVK.

3.5.4 Speckled Volcaniclastic Kimberlite (SVK)

The speckled volcaniclastic kimberlite (SVK) is massive and located in the east of the pipe, adjacent to PVK (Fig. 3.22). It is characterised by small 5-15 mm altered and angular granite lapilli and yellow-brown altered olivine macrocrysts (~30 vol%) set in a light grey to dark brown coloured matrix. The granite lapilli give the lithofacies a speckled appearance. Crudely defined beds are typically

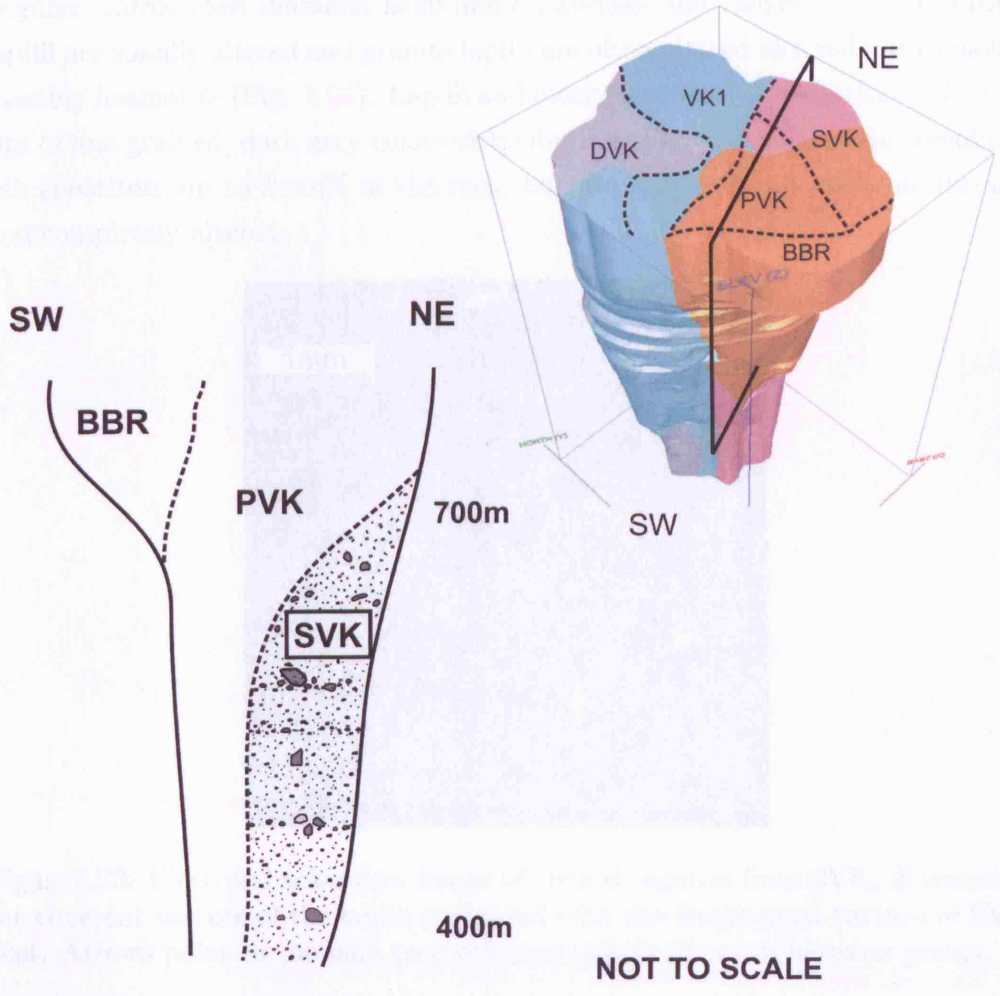

Figure 3.22: Schematic illustrating the interpreted structure and large-scale features of SVK and its relationship with other lithofacies. (Model of D/K1 is shown to illustrate the location of the cross section.)

normally graded with lithic content varying from 2 to ≥50 vol% in sequences 2-5 m thick. Lithic content is on average 15 vol% of the rock. Lithic lapilli are predominantly basalt (≥80% of the lithic population). Granite lapilli are a defining feature of this lithofacies and constitute ≤10 vol% of the rock, which is the highest abundance within D/K1. Mudstone and carbonaceous mudstone combined comprise 10% of the lithic population and sandstone ~1%. Basalt and mudstone lapilli and blocks are mostly rounded, whereas granite lapilli are angular. Lithic clast diameter is 20 mm on average and ranges to ≥2 m. Lithic lapilli are zonally altered and granite lapilli are often altered to a red/pink colour; possibly heamatite (Fig. 3.24). Lapilli and blocks frequently have a thin (1-5 mm) rim of fine-grained, dark grey coloured kimberlite (Fig. 3.24d). Mantle xenoliths can constitute up to 5 vol% of the rock, but are rare with ≤1 vol% on average and completely altered.

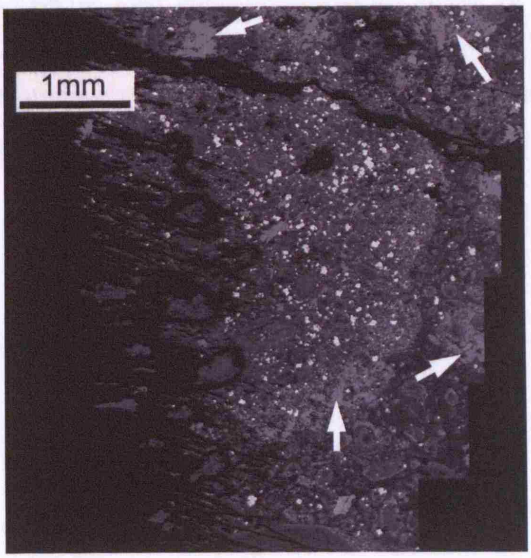

Figure 3.23: Electron backscatter image of juvenile lapillus from SVK, illustrating the coherent texture of the lapilli compared with the fragmented texture of SVK host. Arrows point to the pale grey coloured calcite phase in between grains.

Olivine phenocrysts ($\leq$1.5 mm) and macrocrysts have been totally serpentinised and have a $\sim$25-50μm thick rim of fine-grained serpentine and microlitic diopside with perovskite and subordinate spinel microphenocrysts (Fig. 3.25c-e). In places olivine phenocrysts are aligned. There are very few mantle-derived macrocrysts (phlogpite, garnet or chrome-diopside) in SVK. Pelletal lapilli are in similar abundance to PVK (Section 3.5.3). The rims of juvenile lapilli are texturally different to the other volcaniclastic kimberlite lithofacies described for D/K1 and they closely resemble the mineralogy and texture of the groundmass in CK, described below (Fig. 3.23). Patches of ash-sized, olivine-poor material were observed which gives the rock a patchy or mottled texture (Fig. 3.24). The interclast matrix of SVK is comprised of a fine-grained base of serpentine, microlitic diopside, calcite and phlogopite (Fig. 3.25). Microlitic diopside often coagulates into patches in between olivine and other components (Fig. 3.25a). The amorphous base phase also contains irregular pools of phlogopite and calcite, the latter typically fill spaces in between clasts (Figs. 3.25d, e and 3.24). Interclast oxides are predominantly perovskite which also nucleate at the edge of olivine phenocrysts producing ghost lapilli (Fig. 3.25d and e).

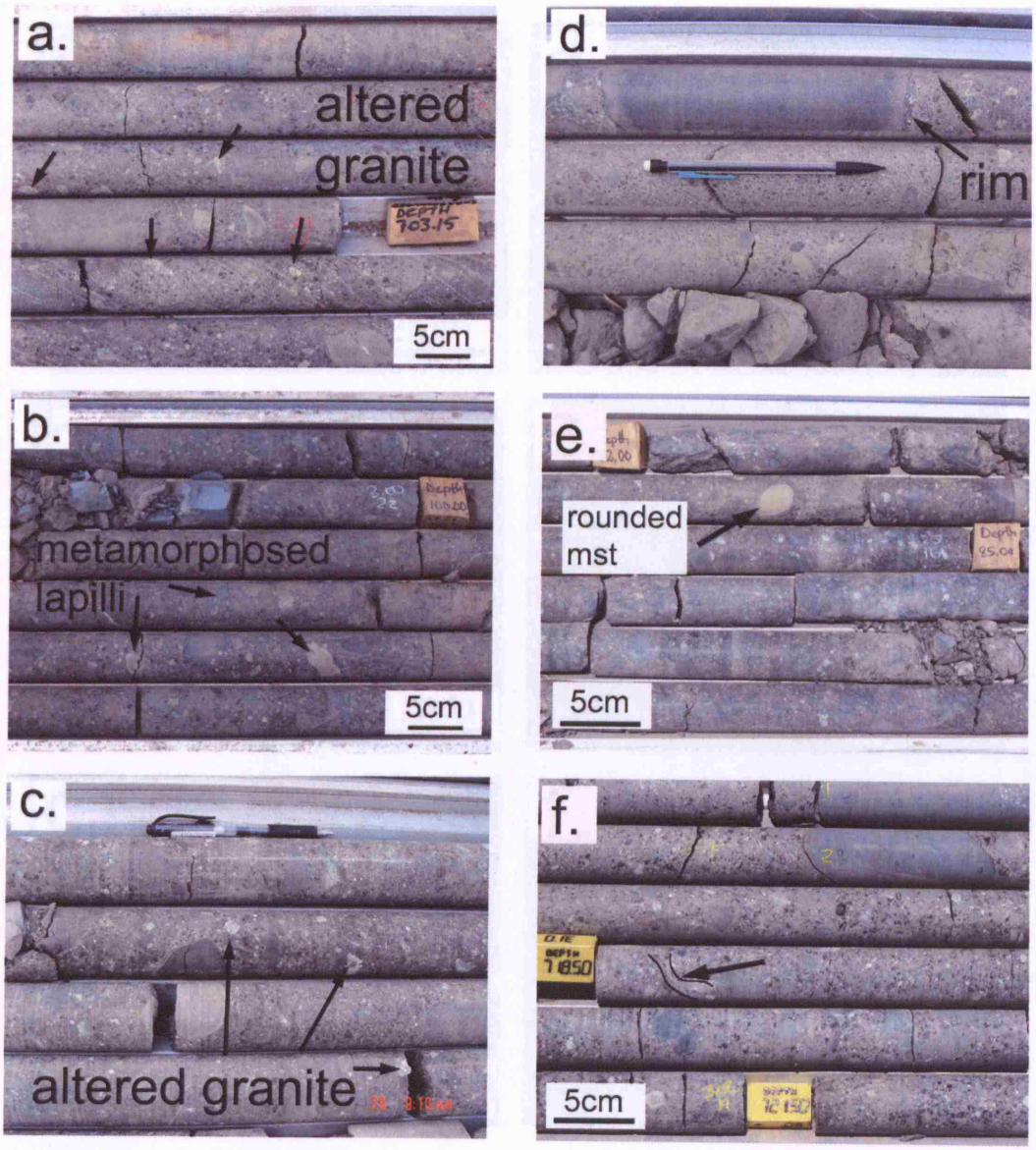

Figure 3.24: Representative photographs of SVK drill core sections. (a) and (c) Arrows point to altered, angular granite lapilli. (b) Arrow highlights metamorphosed basalt lapilli. (d) Arrow points to a dark grey coloured, crystalline rim around basalt block with white, carbonated olivines. (e) Very rounded mudstone lapilli. (f) Arrow points to fine-grained, olivine-free interclast phase.

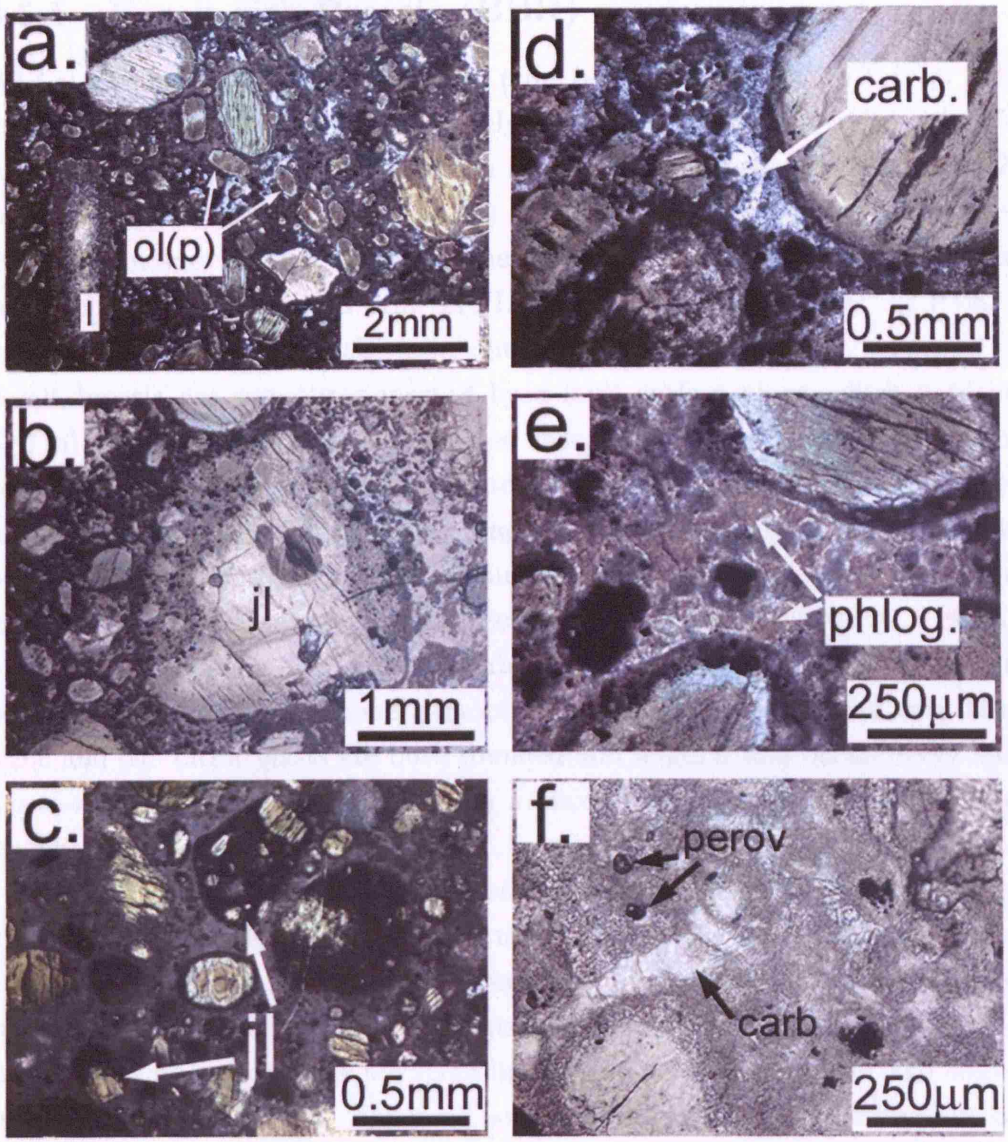

Figure 3.25: Photomicrographs of thin sections from SVK. (a) General view of aligned altered olivine phenocrysts (ol(p)), macrocrysts, and lithic lapilli (l) in an altered, fine-grained matrix. (b) Cored juvenile lapilli with kernel of anhedral olivine xenocryst. (c) Round juvenile lapilli (jl). (d) Interclast calcite (carb.). (e) Possible interclast phlogopite and magma selvages around olivine phenocrysts. (f) Microlitic diopside, pools of calcite (carb) and groundmass perovskite (perov).

3.5.5 Basalt-rich Breccia (BBR)

BBR is located in the south-east of the pipe, between VK1 and PVK (Fig. 3.3). It is a poorly sorted, massive to crudely layered heterolithic breccia with ≥55 vol% lithic lapilli to megablocks ≥10 m in diameter. BBR has on average 10-20 vol% of altered olivine macrocrysts set in a light brown-grey coloured altered interclast matrix. Crudely layered sequences are 5-10 m thick with interbedded volcaniclastic kimberlite. In drill core LDD12 (Fig. 3.4; Appendix A) PVK is interbedded with BBR. In the mine outcrop, individual layers or 'packages' of basalt breccia are sometimes marked by a fault surface along which boulders (≥2 m) above and below are aligned (see Face Map 3; Appendix A). The lobate geometry of these packages is highlighted by pathways for groundwater shown in Figure 3.27, and upper packages drape over the packages below. The lithic population of BBR is ≥90% basalt, including abundant amygdaloidal basalt and oxidised basalt which are not often observed in other lithofacies (Fig. 3.26a-d). Mudstone, granite and sandstone are subordinate constituting ≤10% of the total population, although mudstone is more abundant close to the wall rock (Fig. 3.26c and d). Lithic clasts are both rounded and angular and occasionally have jigsaw-fit textures. Basalt clasts reach a maximum size of 10 m, and have an average diameter of 200 mm.

The interbedded kimberlite is composed of a combination of lithic lapilli (typically oxidised mudstone lapilli) (≤10 mm) and totally altered whitish olivine macrocrysts 3 mm in diameter with rims of microlitic diopside and oxide microphenocrysts. Lithic derived xenocrysts of pyroxene and mantle derived macrocrysts of garnet and ilmenite are sporadically distributed throughout and constitute ≤2 vol% of the matrix. The interclast phase is a relatively homogeneous pale brown-coloured interclast matrix, which is difficult to resolve optically. The matrix is composed of serpentine and microlitic diopside. Oxide microphenocrysts are erratically distributed throughout the matrix, and cluster at the edge of olivines. Pelletal lapilli are rare with ≤0.1% of rock and are altered. The kimberlite is clast supported and poorly sorted close to the wall rock and it is dominated by small (3-5 mm) lithic lapilli with ≤5 vol% altered olivine macrocrysts (Fig. 3.26c).

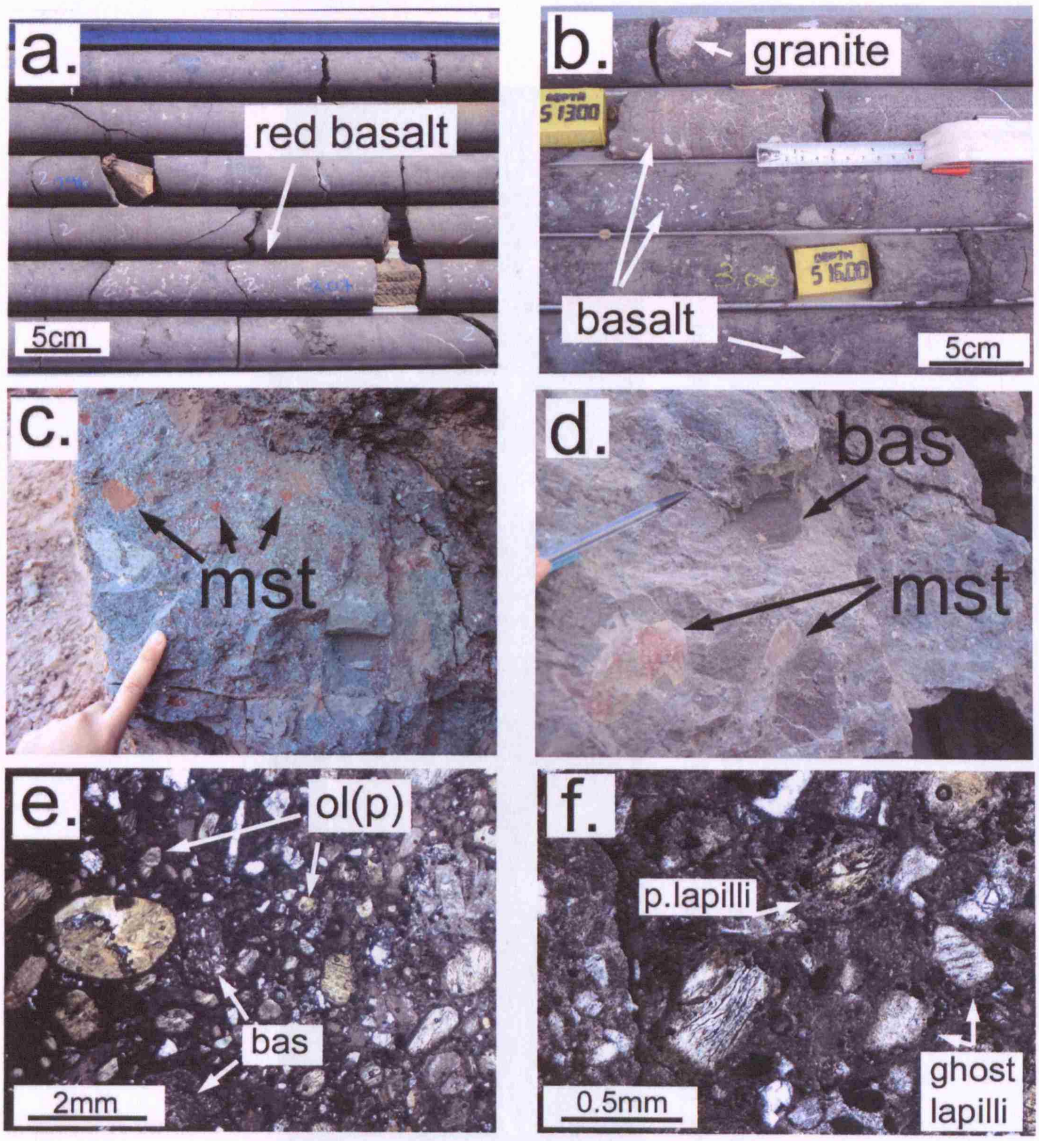

Figure 3.26: Photographs and photomicrographs of sections from BBR. (a) and (b) Drill core sections showing oxidised, amygdaloidal basalt boulders unique to this lithofacies, and (b) granite lapilli. (c) and (d) Photographs of BBR in the mine, illustrating oxidised mudstone lapilli and blocks and basalt set in a green coloured interclast matrix. (e) Photomicrograph of BBR illustrating the highly fragmental texture including small, altered basalt lapilli (bas) and olivine phenocrysts (ol(p)) and (f) pelletal (p. lapilli) and ghost lapilli set in a fine-grained clay-rich interclast matrix.

Figure 3.27: Photograph of BBR outcrop in the mine. Groundwater which has seeped through a more porous package of breccia highlights the structure of this unit. Dashed white lines mark individual packages.

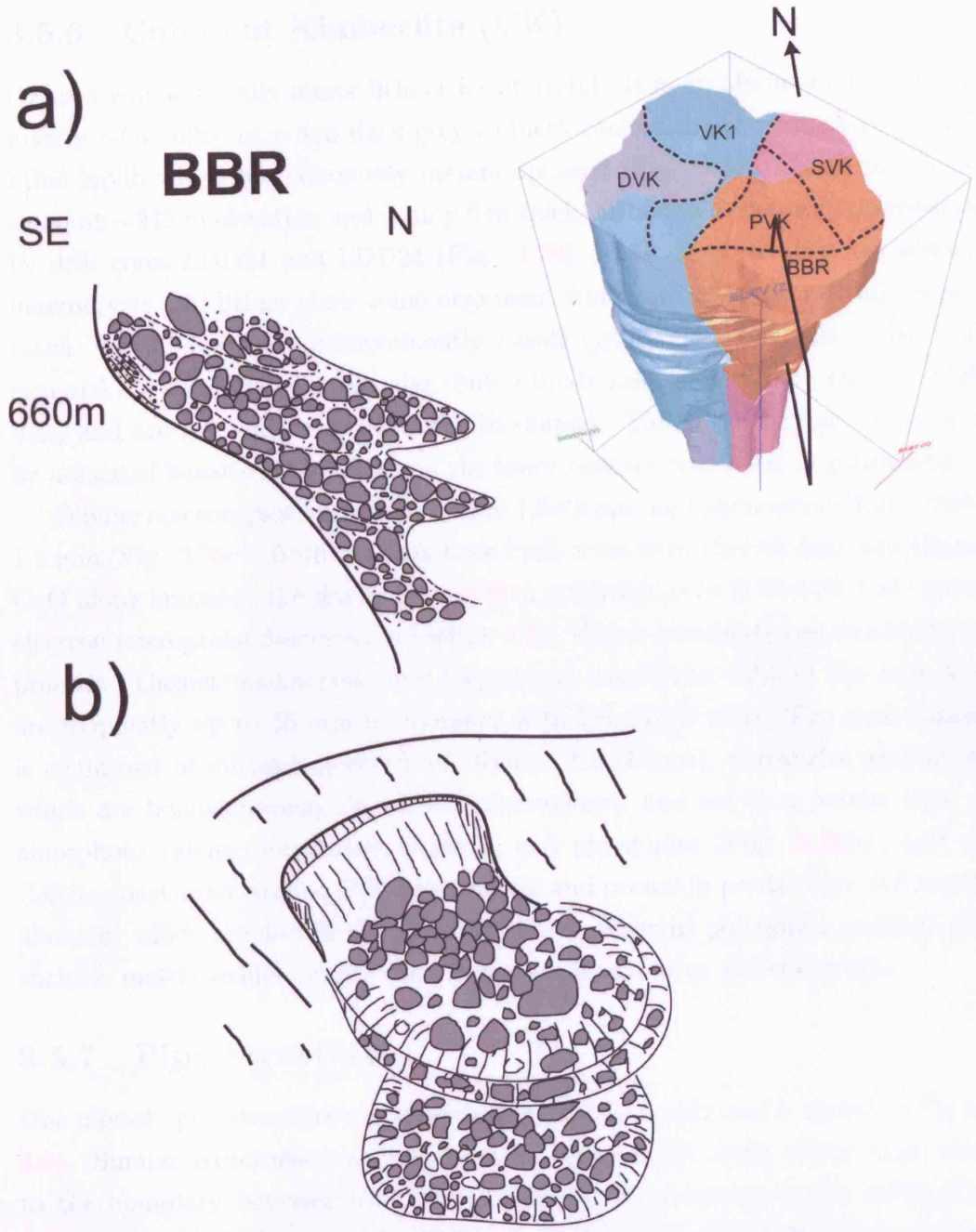

Figure 3.28: (a) Schematic illustrating the structure and large-scale features of BBR (model of D/K1 is shown to illustrate where the cross section was taken). (b) Cartoon model of mass movement processes adapted from Cas & Wright (1988).

3.5.6 Coherent Kimberlite (CK)

CK is a volumetrically minor lithofacies at D/K1. It is an olivine-rich (approximately ~60 vol%) coherent dark grey to black rock with approximately 7 vol% lithic lapilli which are commonly metamorphosed (Fig. 3.30a). The unit is located at ~245 m elevation and is only 6 m thick, although it was only intersected by drill cores LDD21 and LDD24 (Fig. 3.29). It is massive, although olivine macrocrysts and lithics show some alignment which are near to vertically orientated. Lithic lapilli are predominantly basalt (≥80% of total), which are ≤50 mm and are subrounded to angular. Subordinate granite lapilli are smaller (≤30 mm) and are generally angular and lath-shaped. The upper contact is marked by a zone of basalt-rich breccia and the lower contact into DVK is gradational.

Olivine macrocrysts range in size from 1.5-12 mm and phenocrysts from ≤0.5-1.5 mm (Fig. 3.30c). Both varieties have fresh cores with Ca-rich rims and higher CaO along cracks in the grains (Fig. 3.30d; analysed to be 0.96 wt% CaO using electron microprobe described in Section 4.5). This is interpreted as an alteration product. Garnet macrocrysts and megacrysts constitute ~2% of the rock and are frequently up to 15 mm in diameter with kelyphitic rims. The groundmass is composed of microphenocrysts of olivine (200-500μm), perovskite and spinel which are homogeneously distributed throughout, and set in a patchy base of amorphous calcite, serpentine, chlorite, and phlogopite (Fig. 3.30b,c, and e). Calcite constitutes around 5% of the matrix and occurs in pools about 0.5 mm in diameter which are devoid of any other phases, whereas phlogopite poikilitically encloses matrix oxides (Fig 3.30e). There are no ghost or pelletal lapilli.

3.5.7 Pipe Structures

One pipe-shaped structure was observed during this study and is shown in Figure 3.31. Similar structures have been seen in the same location of the pipe, close to the boundary between VK1, DVK and within proximity of the BBR (Fig. 3.31), by Field & Scott Smith (1998), J. Stiefenhofer and P. Kesebonye (*pers. comm.*). This pipe is ≥12 m (bench height) high and 1-2 m wide, and contain poorly sorted rounded to sub-angular lapilli and blocks of basalt (80-95 vol%), and rare (≤1 vol%) altered olivine and unaltered ilmenite macrocrysts. There are

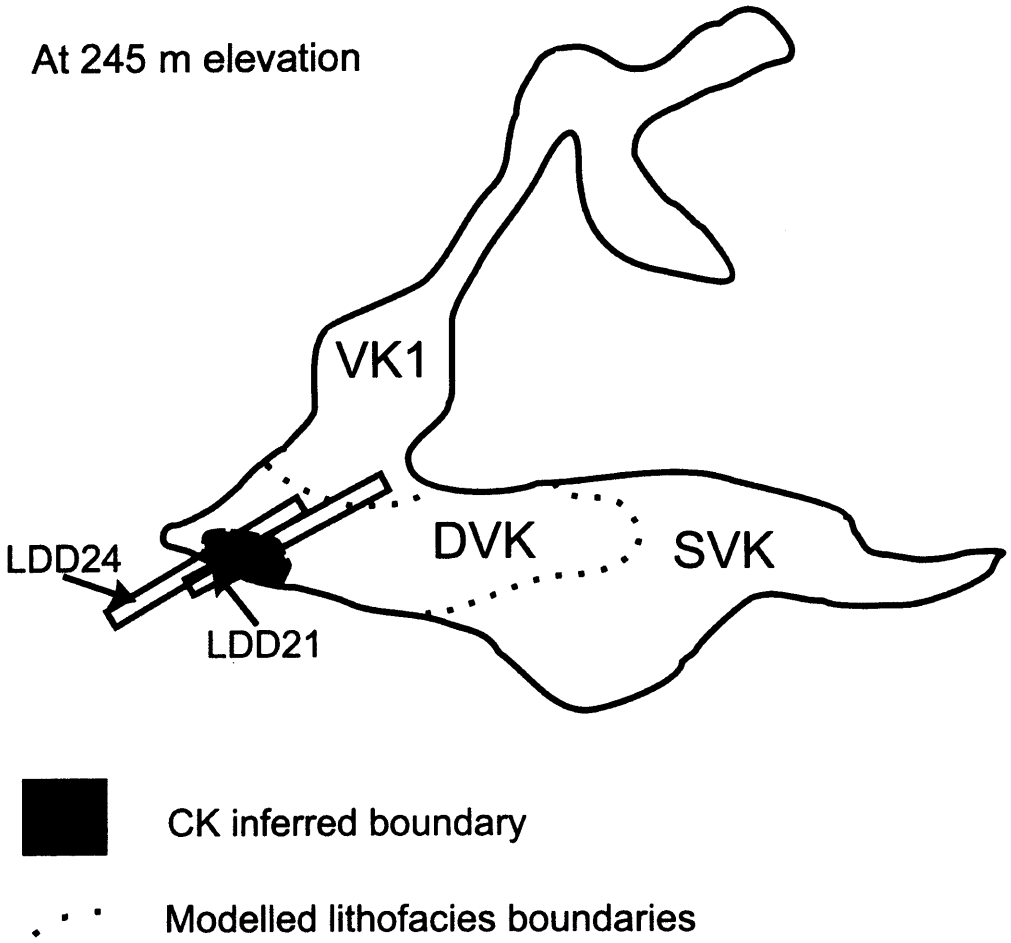

Figure 3.29: Schematic illustrating the location of CK on plan section of the D/K1 pipe.

a paucity of ash-sized components. The interclast cement is poorly consolidated and comprised of patchy calcite and a clay-rich, muddy, pale-green coloured slurry.

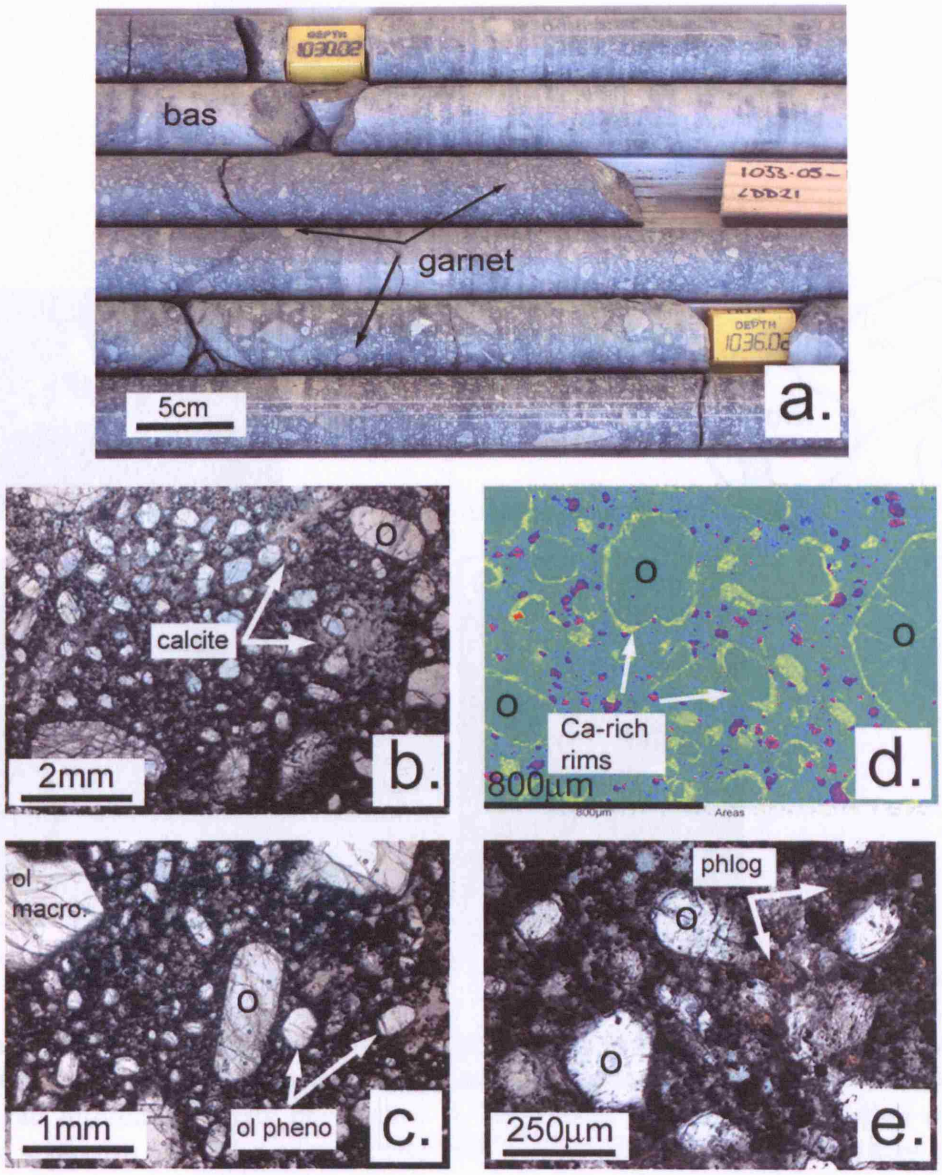

Figure 3.30: Drill core photographs and photomicrographs of CK sections. (a) Drill core showing large, fresh olivine macrocrysts, rounded garnets with dark kelyphitic rims and country rock contamination including basalt (bas). (b) General view of CK showing irregular calcite segregations in the matrix. (c) General view of CK demonstrating the size difference between olivine macrocrysts (ol macro) and phenocrysts (ol pheno). (d) False colour image of olivines with Ca-rich rims illustrated by the yellow phase[2] (e) Poikilitic matrix phlogopite (phlog). (o - olivine.)

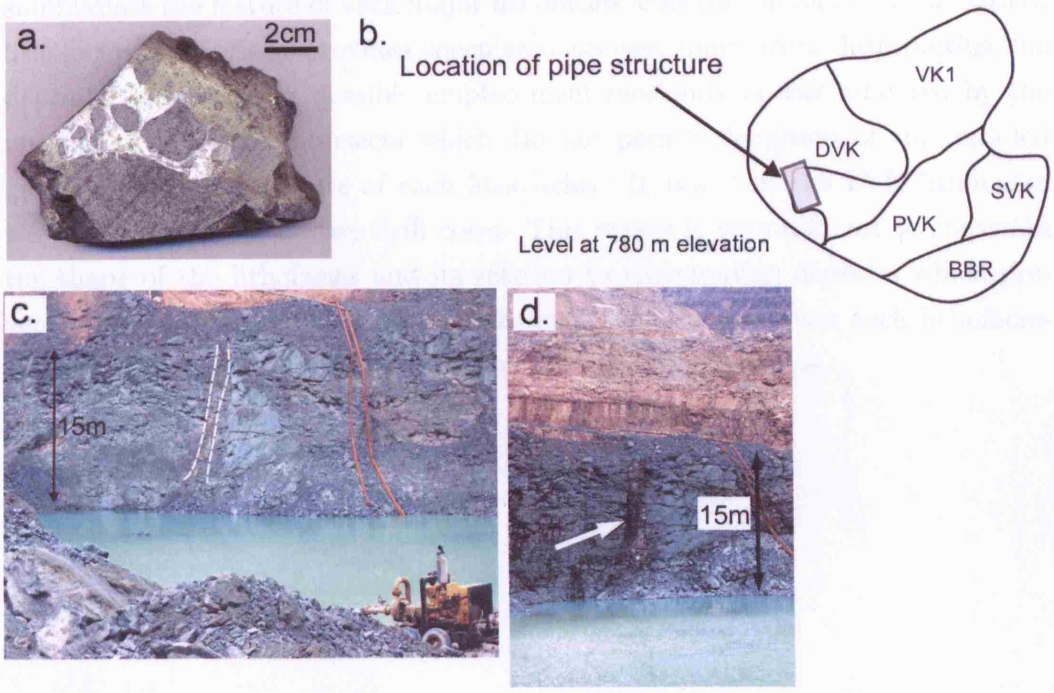

Figure 3.31: Photograph of the one pipe structure within VK1. (a) Sample collected from the pipe illustrating the angular to rounded shapes of basalt lapilli and an interclast matrix dominated by secondary calcite. (b) Location of the pipe structure on a plan view of the D/K1 pipe. (c) and (d) Photograph of the pipe structure in the mine outcrop.

3.6 Discussion

The D/K1 pipe can be divided into six texturally distinct major kimberlite lithofacies associations; VK1, DVK, PVK, SVK, CK and BBR. Additional subdivisions were made of DVK, PVK and VK1 into smaller lithofacies of country rock-rich breccias, and massive and layered volcaniclastic kimberlites. Table 3.3 summarises the feature of each major lithofacies associtation and its constitutent lithofacies, and briefly provides speculated process summaries. Interpreting the deposits and assigning possible emplacement mechanisms was hindered by the number of drill core intersects which did not permit definition of the detailed geometry and architecture of each lithofacies. In one case the LVK lithofacies was only intersected by two drill cores. This makes it very difficult to constrain the shape of the lithofacies and its relation to surrounding deposits which prevent accurate interpretation. The discussion below summarises each lithofacies and provides an interpretation based on the available evidence.

Major Lithofacies Association	Constituent Lithofacies	Description	Interpretation
VK1	BBr1	Poorly sorted, crudely layered basalt-rich breccia.	Gravitional collapse of wall rock producing an avalanche deposit.
	CMST-Br	Clast to matrix supported country rock breccia, dominated by CMST and MST fragments and sorted in places.	Cohesionless grain flow deposit.
	VK1a	Dark grey massive to crudely layered volcaniclastic kimberlite with pipe structures. Volumetrically most significant lithofacies within VK1.	Deposits produced from a dynamic, explosively eruptive system which produced fragmental textures. Quarried out VK1b.
	VK1b	Green coloured massive volcaniclastic kimberlite with abundant mantle xenoliths.	Deposits produced from a dynamic, explosively eruptive system which produced fragmental textures. Older than VK1a.
	LVK	Pale green layered volcaniclastic kimberlite. Volumetrically smallest lithofacies within VK1.	Intraclast of a bedded pyroclastic unit.
DVK		Dark grey, massive to crudely layered volcaniclastic kimberlite with fresh olivine macrocrysts and metamorphosed lithic lapilli. Contains interclast calcite.	Deposits produced from an explosively eruptive system which produced spatter that welded on deposition.
PVK	BBr2	Crudely layered to finely laminated basalt rich breccia. Clast and matrix supported with occasional muddy matrix.	Grain flow deposit with a muddy/slurry substratum related to the emplacement of PVK.
	mPVK	Massive to crudely layered pale to dark grey volcaniclastic kimberlite with porphyritic juvenile lapilli which resemble SVK.	Deposits from a dynamic, explosively eruptive system whereby plastic magma pellets were incorporated and preserved.

Major Lithofacies Association	Constituent Lithofacies	Description	Interpretation
SVK		Massive to crudely layered pale grey volcaniclastic kimberlite characterised by small, angular and altered granite lapilli. Contains porphyritic juvenile lapilli and interclast calcite and phlogopite.	Deposits produced from an explosively eruptive, dynamic eruptive system which produced a fragmental texture. This phase of eruptions introduced a new generation of granite fragments into the pipe.
BBR		Heterolithic, poorly sorted, massive-bedded basalt-rich breccia.	Deposits from mass movement processes including avalanches and debris flows triggered by gravitationally unstable wall rock collapses.
CK		Fresh olivine macrocryst-rich, dark grey to black massive kimberlite with rare metamorphosed lithic lapilli. Coherent, homogeneous groundmass phase with calcite, phlogopite and groundmass oxides.	Consistent with Clement & Skinner (1985) classification of a macrocrystsic hypabyssal kimberlite except the presence of basalt fragments. Speculate this is a late-stage kimberlite magma which was passively emplaced.

Table 3.3: Major characteristics and interpretations of all major lithofacies associations and their constituent minor lithofacies.

3.6.1 Interpretation

VK1

VK1 is composed of (i) two country rock-rich breccias, one with a kimberlite interclast matrix and one clast and matrix supported, (ii) two texturally distinct, poorly sorted, massive volcaniclastic kimberlites, and (iii) one layered volcaniclastic kimberlite. Close examination of VK1 has demonstrated that this is a heterogeneous deposit. Variations are principally in the form of diffuse layering which was defined by variable lithic fragment content. The presence of the two VKs indicates multiple eruptive phases, where the predominant VK1a cross-cuts VK1b. VK1a is therefore the younger deposit (Fig. 3.13a). The fine bedding of the LVK is not seen anywhere else at D/K1. LVK may be an intraclast of bedded pyroclastic kimberlite derived from a section of a tuff-ring which collapsed into the pipe. This fragment was able to sink through the pipe relatively undisturbed. A mechanism for this non-disruptive down-rafting is given by Clement & Reid (1989); McCallum et al. (1975) and Woolsey et al. (1975); fluidised beds establish quasi-frictionless systems through which fragments can sink without significant attrition from other particles.

The poorly sorted nature of BBr1 characterised by basalt megablocks suggest that this is an avalanche deposit, probably triggered by a number of gravitationally unstable wall rock collapses (Cas & Wright, 1988; Takarada et al., 1999). Interbedding between BBr1 and volcaniclastic kimberlite VK1a suggests that the wall rocks were collapsing simultaneously with the kimberlite eruption. The clast supported layers observed in the CMST-Br are indicative of cohesionless grain flow mechanisms, similar to scree slope deposits on the flanks of volcanoes (Cas & Wright, 1988) and the grain flow deposits at Orapa (Field et al., 1997).

Alteration haloes around lithic lapilli show a chemical reaction where volatiles are drawn out of the clast and react with the surrounding kimberlite. This process was probably a result of meteoric fluids percolating through the clastic deposit and leaching mobile elements from olivine and xenocrysts which produced an alkaline fluid (Section 2.6; Stripp et al. 2006). Irregular-shaped basalt lapilli, as shown in Figure 3.9d, appear to have reacted with a hot, fluid phase which has dissolved away the original morphology of the fragment. This occurred before the

deposit settled as the reaction has not extended into the surrounding kimberlite. The proposed reaction is probably not temperature related beacuse there were no other indications of heating effects on the clasts, for example re-crystallisation at the edges. Chemical dissolution provides a more favourable explanation for this texture. Zones within VK1 had variable alteration, which was manifested by a change in colour of the kimberlite and an optically unresolvable clay-rich interclast matrix. The zones of increased alteration are generally associated with elevated lithic fragment contents which would increase the porosity and facilitate percolation by secondary fluids.

DVK

DVK is also a massive to crudely layered kimberlite. The presence of basalt blocks and megablocks ~650 m deeper than their original stratigraphic position may suggest a volume deficit in the pipe during eruption which infilled with rock fall deposits (i.e. Brown *et al.*, *in press*). This is not a new idea and was proposed by Trofimov (1970) for Siberian kimberlite pipes including Udachnaya. Jigsaw-textured fractures in these blocks imply shear stresses during their transport within the pipe, which indicates that the rock falls may have developed into flows at some stage (Reubi & Hernandez, 2000). Alternatively, these blocks sank to these depths through a quasi-frictionless fluidised system established towards the later stages of an eruption, which was discussed by Clement & Reid (1989). In this case jigsaw fractures probably developed as fragments made contact with the pipe floor.

The maximum lithic size derived from explosive activity rarely exceed 600 mm in the DVK, and the shapes of lithic fragments range from rounded to angular. Maximum clast size is a function of explosive intensity and smaller lapilli indicate more energetic explosive fragmentation. Juxtaposition of angular and rounded lithic lapilli and blocks suggests mixing between phases of eruptions with varying explosive intensities. Mixing may have taken place during fluidisation. Rounded fragments are interpreted as having had significant interaction with other clasts through repeated ejection and fall-back into the vent, and therefore indicate a longer emplacement history (Fisher & Schmincke, 1984). Rounding can also

be caused by thermal or chemical spalling of wall rocks before diatreme formation, however there was no evidence to support pre-eruptive processes or embryonic pipe formation at D/K1 (Clement & Reid 1989, Brown *et al.*, *in press*). Crystal-poor rims around lithic lapilli are unique to DVK (Fig. 3.16c). They are interpreted as rapidly cooled magma-derived glassy rims that adhered to the lithic lapilli during eruption and have subsequently devitrified and been altered (Fig. 3.17e). The metamorphosed textures of most lithic lapilli indicate elevated emplacement temperatures which sustained a more reactive environment in the erupting kimberlite. An increase in the rate of accumulation of freshly erupted, hot material can elevate the overall temperature of a deposit. This is believed to be the case for the DVK, as discussed further below.

The dark-coloured, competent nature of the DVK lithofacies and its gradational contacts with VK1 are similar to the characteristics of the transitional Tuffistic Kimberlite Breccia (TKtB) and transitional Hypabyssal Kimberlite (HKt) at the Gahcho Kuè pipes in Canada, described by Hetman et al. (2004). These rocks are interpreted as transition phases between diatreme facies TKBs and root zone facies HKs. They are formed by "in situ textural modification" in the magma as it approaches the surface and volatiles exsolve (c.f. Clement & Reid (1989)) which disrupts the magma and produces patchy pelletal textures juxtaposed with coherent magmatic textures. Field & Scott Smith (1999) summarised the textures as "frozen degassing fronts" (Hetman et al., 2004). The DVK lithofacies is characterised by a pseudo-pelletal texture dominated by ghost-lapilli in an interclast matrix of serpentine, diopside microlites and patchy calcite. There is a paucity of well developed juvenile lapilli. The interclast matrix phases, paticularly calcite, have filled spaces in between clasts (Fig. 3.17a). This textures resembles pore-fill which took place after the deposition of the clasts. The interclast calcite is therefore interpreted as secondary alteration pore-fill, not a product of vapour phase crystallisation based on the textural evidence. This observation is consistent with the arguments of Stripp et al. (2006). Calcite forms distinct pools forming 'triple junctions' in between clasts which resemble welded textures in volcanic rocks (e.g. Sruoga et al. (2004) and BBrown et al. (2006)). Therefore, DVK was produced by subaerial deposits of explosively fragmenting magma not by intrusive kimberlite breccias. This is supported by the observed crude layering.

The extensively metamorphosed lithic fragments of DVK imply that this phase of eruption had a higher accumulation rate; rapidly buried freshly erupted material could not cool the same higher rate as other deposits which accumulated more slowly (Wolff & Sumner, 2000). The freshly formed and buried hot spatter welded and agglutinated together on deposition (Capaccioni & Cuccoli, 2005; Head & Wilson, 1989; Sumner et al., 2005; Wolff & Sumner, 2000). The altered lithic fragments that occur in the DVK deposits suggest slower rates of cooling that allow longer lasting reactions between entrained clasts and the cooling melt. Elevated rates of accumulation can also lead to welding and agglutination (Capaccioni & Cuccoli, 2005; Wolff & Sumner, 2000). The textures occurring in the DVK deposits include infill of pore spaces between clasts producing 'triple junctions' of calcite and/or serpentine. These textures are consistent with those described at Venetia by Brown et al. (2006). Welding and agglutination reduces pore space and therefore porosity (Wolff & Sumner, 2000). Olivine phenocrysts and small macrocrysts are completely altered in the DVK, whereas alteration has only invaded the rims of larger olivine macrocrysts. This suggests that the alteration environment leading to serpentinisation was not as aggressive as it was in VK1 where most olivines are completely pseudomorphed by serpentine. As there were fewer pore spaces, hydrothermal and or meteoric fluids could not easily percolate through this deposit. The coarser nature of diopside microlites may also be a function of cooling rates; the more slowly cooled DVK deposits with fewer cations available (due to less alteration) to precipitate diopside favour fewer, but larger crystals. The process of welding has also been used to interpret the textures of the Victor kimberlite in Canada (Webb et al., 2004).

PVK

BBr2 within the PVK lithofacies is interpreted as a debris flow deposit due to its overall poor sorting, open framework and basal shear zone (Fig. 3.19e). The inter-clast mud-like or slurry pore fill phase and fine laminate layers suggests a water-rich medium acted as an efficient lubricant, enabling rapid transport from the pipe walls. Juvenile and lithic lapilli in this unit also support the suggestion that it is a reworked volcaniclastic kimberlite.

The relatively small size of lithic lapilli in the PVK (≤300 mm) and their sub-rounded to rounded shapes can be explained by extensive recycling of the deposit, possibly through repeated ejection and fall-back into the vent (Fisher & Schmincke, 1984). Thin dark rims around lithic lapilli (Fig. 3.20b) resemble metamorphic textures produced by interaction with the freshly erupted kimberlite. However, this eruptive enrivonment was not as reactive as VK1 or DVK because reactions between the lithic fragments and kimberlite host are scarce.

Exotic juvenile lapilli (from a different kimberlite lithofacies) at PVK are significant in understanding the sequence of emplacement. Juvenile lapilli are characteristic of many kimberlite bodies (Mitchell, 1986b). At Victor, in Canada, Webb et al. (2004) speculated that juvenile lapilli were produced by magmatic fire fountaining, similar to the spatter described by Sumner et al. (2005) . This process can be applied to pelletal lapilli where a core of olivine or country rock fragment is surrounded by a magmatic selvage. Larger (≥1 cm) porphyritic juvenile lapilli resemble SVK and VK1, and smaller (≤1 cm) lapilli are similar to the coherent texture of CK. Their formation was preceeded by crystallisation of an earlier phase of kimberlite. These porphyritic juvenile lapilli are thought to be autoliths of an exotic kimberlite which was probably quarried out by the younger PVK eruption. The rounded shapes of the lapilli either indicate that they were recycled within the eruptive regime or that they were semi-molten and plastic when they were erupted. The close proximity of the juvenile lapilli-rich zone to the lower contact with SVK suggests that they were excavated as one of the first phases of eruption which formed the PVK.

SVK

The large-scale structure of SVK is similar to that of PVK with better defined crude layers (Fig. 3.22). However, there are no country rock breccias associated with this lithofacies indicating that it is derived exclusively of explosive volcanic processes and not by gravitationally-induced wall rock slumps and rock falls. Distinct rounding of lithic lapilli (but not granite) demonstrates recycling during the history of the eruptive event, as discussed above. Angular granite lapilli present a problem to this interpretation. The characteristic population of granite lapilli in the SVK may be explained by eruption through a diverted vent. This

eruption excavated a new generation of basement granite which was incorporated into the erupting kimberlite as lithic fragments. Diversion of the vent could have been caused by the blocking of the original vent by large country rock slumps (Sparks et al., 2006), or by a crystallised magmatic plug.

The alignment of olivine pheocrysts is also related to emplacement mechanisms. Grain alignment in kimberlites is attributed to fluidisation by Clement & Reid (1989); McCallum et al. (1975) and Gernon et al. (2006). Small juvenile lapilli with coherent textures are considered to be fragments of a earlier crystallised kimberlite. The fine-grained interclast phase, illustrated in Figure 3.25f, appears to have segregated in between individual SVK lapilli. The texture is interpreted as post-emplacement, secondary pore infill (Stripp et al., 2006).

BBR

The BBR lithofacies is the largest country rock breccia at D/K1 and it seems to have created a scar or backcut into the geometry of the pipe (Fig. 3.3). Poorly sorted fragments of country rock lapilli, blocks, boulders and megablocks indicate mass movement processes including avalanches, slides and debris flows which were probably triggered by gravitational instability of the wall rocks. They have collapsed simultaneously with kimberlite eruptions based on interbedding with PVK kimberlite (e.g. Sparks et al. 2006). Avalanche and debris flow deposits are characterised by: (i) megablocks up to 10 m in diameter in avalanche deposits; (ii) a muddy interclast substratum in debris flows (Fig. 3.26c). The deposit described as an epiclastic kimberlite in Section 3.2 is probably a shear zone at the base of a debris flow. The lobate shape of individual breccia packages is consistent with mass movement processes illustrated in Figure 3.26c (Cas & Wright (1988); ch. 10). Massive, poorly sorted avalanche deposits represent the bulk of the BBR lithofacies. Subordinate debris flows are confined to close proximity of the wall rock (Figs. 3.26c and 3.28b). The bowl-shaped geometery of the BBR lithofacies which cuts back into the wall rock (Figs. 3.18 and 3.28) is consistent with a collapse scar. The emplacement of BBR probably took place as the PVK was forming based on its associations. There was also mixing with lower lithologies which is evident from inclusions of granite and olivine, garnet and ilmenite macrocrysts.

CK

This coherent, dark, competent rock with metamorphosed lithic lapilli, abundant fresh olivine macrocrysts and groundmass calcite is consistent with the Clement & Skinner (1985) classification of a macrocrystic hypabyssal kimberlite. However, gradational contacts with volcaniclastic kimberlite above contest this classification; sharp, chilled contacts may be expected if emplacement of a hot, late-stage magma intruded into a cool deposit (e.g. Cas & Wright 1988). Furthermore, pepperites may form if hot magma intruded into an unconsolidated deposit (e.g. McClintock et al. 2002; Skilling 2006). The gradational contacts of CK are similar to textures described by Field & Scott Smith (1999); Hetman et al. (2004); Skinner & Marsh (2004) which are interpreted as transition zones between degassed kimberlite which has explosively fragmented and kimberlite which has been emplaced as an effusive eruption and volatiles have precipitated by vapour phase crystallisation. However, this model implies that kimberlites were emplaced as intrusive breccias, but basalt lapilli at these depths in the CK are not consistent with the intrusive model. This mechanism cannot explain how lithic fragments derived from lithologies ~650 m higher came to be included in the 'intrusive' CK. An alternative explanation for the coherent or hypabyssal kimberlite is proposed by Sparks et al. (2006). They suggest dark, coherent deposits are welded volcaniclastic kimberlites, which was discussed for the DVK lithofacies above. This could be a mechanism for the formation of CK but it is not possible to verify becuase the only study of the unit was from drill core sections. In a welded deposit you would expect to see features such as cooling joints (Cas & Wright, 1988). There is not sufficient evidence to completely exclude the magmatic intrusion interpretation either.

Pipe Structures

The characteristics of the pipe structure located close to the VK1-DVK contact can be interpreted as either (i) localised fluidisation pipe where gas streaming has elutriated fine ash and small lapilli (Clement & Reid, 1989; Gernon et al., 2006), or (ii) as vertical rafts of basalt fragments. Vertical structures with a high concentration of a particular lithic type could have been produced if a large crack

had formed in the pipe which was infilled by a subsequent wall rock collapse. Subsequent alteration precipitated a carbonate-rich material which cemented between the basalt boulders and blocks. It is difficult to see how the fragments became so rounded by this process. The alternative interpretation, however, can explain this feature. Lithic lapilli and blocks were rounded by exfoliation from a turbluent, gas-solid system established in the fluidised "cell" within the pipe (Clement & Reid, 1989). Similar pipe structures have been observed at Letseng in Lesotho and Orapa in Botswana by Gernon et al. (2006) which have been interpreted as "gas-segregation pipes". It is not obvious why fluidisation of this intensity was localised within this zone of the D/K1 pipe. It is possible that other pipe-structures have not been recognised or not yet exposed in the mine. Alternatively, some mechanism was responsible for concentrating gas streaming here. Gernon et al. (2006) explained that these structures formed during the waning stages of an eruption as gas-flow rates diminished. Gernon (*op. cit.*) also suggested that large lithic lapilli can concentrate gas segregations. The pipe at D/K1 is located within proximity of the BBr1 lithofacies which may have provided the required sites for gas nucleation. Therefore we can predict to see more pipes associated with country rock breccias as greater depths of the D/K1 kimberlite pipe are exposed.

3.6.2 Interclast Matrix

There is consistency between the interclast matrix phases of all volcaniclastic kimberlite lithofacies at D/K1. This phase predominantly consists of olivine, spinel and perovskite phenocrysts in a fine-grained base of serpentine and microlitic diopside which produces a patchy-texture. Extensive alteration of olivine (macrocrysts and phenocrysts) and the absence of discrete groundmass oxides within the matrix, combined with the patchy, cryptocrystalline serpentine and microlitic diopside base are consistent with the observations and interpretations of Walters et al. (2006) and Stripp et al. (2006). The ubiquitous paucity of discrete oxide phenocrysts within the interclast phase is consistent with observations by Walters et al. (2006). They suggest it represents the elutriation of ash-size particles into the gas phase of a fluidised system. The textures of the interclast

matrix at D/K1 are in agreement with the hydrothermally produced pore fill products of Stripp et al. (2006), which are discussed in Section 2.6. Although there is wide variability of calcite abundance in the matrix, it typically forms irregular pools up to 1 mm in diameter with characteristic shapes typified in Figure 3.17f. Brown *et al.* (*in press*) discussed how these textures are not consistent with the "segregations" proposed by Clement & Skinner (1985), but are probably a pore-filling cement between agglutinated lapilli. The calcite textures at D/K1 agree with this hypothesis, and are analagous with other terrestrial welded volcanic deposits, e.g. Sruoga et al. (2004).

The degree of alteration varies between and within lithofacies, and is interpreted as a function of the porosity of the freshly deposited material. Zones of bleached kimberlite in VK1 were often located adjacent to regions of elevated lithic content where porosity was higher and meteoric fluids could easily percolate through the deposit. On the contrary, DVK contains abundant fresh olivine macrocrysts, suggesting a lower porosity which is consistent with the welded hypothesis; reduced porosity as a result of welding will lower the permeability and inhibit percolation of meteoric fluids. The amount of alteration within the DVK lithofacies varies vertically and laterally, suggesting the degree of welding was variable. Lateral variation in welding intensity is indicative of volatile resorption processes, as disucssed by Sparks et al. (1999). However, it is probable that a combination of welding mechanisms took place which were controlled by the temperature and the rate of accumulation of pyroclasts (Head & Wilson, 1989).

3.7 Conclusion

The D/K1 pipe is a geologically and petrographically complex body composed of at least six texturally distinct major kimberlite lithofacies associations. The deposits do not fully represent the entire history of the formation of the pipe as the remaining lithofacies were probably produced during the waning stages of the whole eruption event. The initial, most violently eruptive pipe-forming events either completely ejected all associated pyroclasts which were deposited away from the vent, or subsequent eruptions quarried out these older deposits. The eruptive environment was evidently very dynamic and multiple processes were

taking place simultaneously including explosive pulses of eruptive activity, mass movement of gravitiationally unstable wall rocks, and fluidisation. Remnants of other processes include the LVK lithofacies in VK1. This intraclast may indicate the presence of a crater at D/K1 which collapsed or was washed back into the pipe during a later phase of activity. The timing of the formation of CK remains inconclusive. If it is assumed to be a magmatic plug, it was probably intruded after DVK and could have been responsible for diverting the ascending new pulse of magma which erupted as SVK.

Chapter 4

Spinel Mineral Chemistry

4.1 Introduction

The aim of this chapter was to use spinel compositions to test the hypothesis that spinels behave discretely between kimberlite lithofacies showing that the D/K1 kimberlite originated from more than one magma batch. The data from these results was also used as petrogenetic and geochemical indicators to understand the shallow level petrogenesis of the kimberlite magma(s).

Spinels are ubiquitous groundmass minerals in kimberlites (Chakhmouradian & Mitchell, 2001; Haggerty, 1975; Jones & Wyllie, 1985; Mansun et al., 2004; Mitchell, 1979; Mitchell & Clarke, 1976; Naidoo et al., 2004; Pasteris, 1983; Shee, 1985; Tompkins & Haggerty, 1985). Spinels were chosen for analysis because their compositions are sensitive to ambient conditions as they crystallise from a melt, which makes them good petrogenetic and geochemical indicators (Irvine, 1965). The aims of this chapter were (i) to understand to what extent groundmass spinel compositions can be used to fingerprint individual kimberlite lithofacies, (ii) to understand how compositional variability is controlled by spinel paragenesis, (iii) to use spinel compositional variability to understand changing conditions in the melt as the kimberlite ascended towards the surface, and (iv) to design a model of spinel crystallisation in relation to other groundmass phases. This is the most extensive study of groundmass spinel compositions at the Letlhakane D/K1 pipe, and a comparison with other kimberlite bodies was made to further understand kimberlite petrogenesis.

4.2 Previous Work

Irvine (1965, 1967) carried out a detailed study of spinel mineral chemistry, focussing in particular on how spinel composition provides a record of pressure, temperature, oxygen fugacity, and and changing melt composition and co-crystallisation with other phases. Numerous studies since then have realised the importance of spinel as an indicator of complex petrogenetic processes in ultramafic rocks. For example, Allan et al. (1988) studied the systematics between Cr-spinel compositions and the composition of the melt, and Shane (1998) used Fe-Ti spinel compositions to fngerprint individual fallout lithofacies from the Taupo Volcanic Zone in New Zealand. An excellent review of spinel trends in terrestrial rocks is given by Barnes & Roeder (2001).

Spinels are particularly important in kimberlites as they remain one of the few primary phases not modified by secondary alteration (e.g. Pasteris 1983). Furthermore, complex zoning within individual grains can be used to trace changing conditions in the melt (e.g. Tompkins & Haggerty 1985). Haggerty (1973, 1975) observed how spinel compositions in themselves are not uniquely "kimberlitic", but their zoning patterns and compositional trends are. Careful separation of samples from individual intrusions within the same kimberlite body by Mitchell & Clarke (1976) at Peuyuk in Canada, Mitchell (1979) at Tunraq in Canada, Pasteris (1983) at De Beers in South Africa, and Naidoo et al. (2004) at Koffiefontein in South Africa demonstrated that spinel compositions and textures are specific to certain kimberlite lithofacies within a single body. The source of these compositional heterogeneities remains contentious: Mitchell & Clarke (1976) propose a link between composition and decreasing pressure in a fractionating melt, and Mitchell (1979) believes spinel compositions differed at Tunraq either due to different degrees of partial melting, differentiation under high pressure, or small-scale compositional heterogeneities of the source rocks. Pasteris (1983) prefers the hypothesis that individual root zone kimberlites at the De Beers pipe represent a succession of melt phases from a single, fractionating melt.

Representative spinel compositions from several kimberlite bodies are given in Table 4.2, which demonstrates the variability between kimberlites.

Wt % oxide	1	2	3	4	5	6	7	8	9	10	11	12
TiO_2	0.10	0.63	9.17	21.51	22.59	3.00	16.70	1.91	9.30	5.55	2.36	19.47
Al_2O_3	36.82	17.31	10.69	5.99	7.80	4.80	8.70	1.33	0.14	1.84	49.32	12.53
Cr_2O_3	26.88	46.44	25.03	3.97	0.86	55.40	2.40	58.50	1.16	15.36	2.56	0.97
FeO	10.55	15.36	20.52	23.45	27.22	17.20	23.20	16.49	29.64	43.46	14.38	26.96
Fe_2O_3	4.76	7.18	19.78	24.56	25.60	10.40	32.20	10.00	52.16	31.83	9.74	14.48
MnO	9.15	0.34	0.47	1.21	0.45	0.40	0.50	1.11	1.45	0.71	0.29	1.04
MgO	17.46	12.80	13.33	18.06	16.80	11.10	15.70	10.61	5.46	3.11	20.32	23.20
Total	98.03	100.36	98.99	98.72	101.32	99.30	99.30	99.95	99.30	101.90	98.97	98.65
Mol % end member spinel molecules												
$MgAl_2O_4$	60.60	30.60	16.70	8.10	10.30	3.20	12.00	2.50	0.20	2.90		
Mg_2TiO_4	0.30	2.10	27.00	40.20	34.30	10.40	31.90	6.80	14.90	7.00		
Mn_2TiO_4	-	-	0.50	1.80	0.60	-	0.70	-	2.30	1.20		
Fe_2TiO_4	-	-	-	13.70	22.10	-	11.70	-	8.70	8.30		
$MnCr_2O_4$	0.40	0.90	0.50	-	-	1.00	-	3.00	-	-		
$MgCr_2O_4$	11.60	23.80	-	-	-	34.40	-	38.30	-	-		
$FeCr_2O_4$	19.60	30.40	25.80	3.60	0.80	32.60	2.20	31.60	1.10	16.00		
Fe_3O_4	7.50	12.20	29.60	32.70	31.90	18.20	42.20	17.80	72.70	64.90		

Table 4.1: Worldwide spinel compositions from Mitchell 1986b. Macrocrysts: 1,2 Aluminous magnesian chromite (AMC) from Tunraq. Magmatic Trend 1: 3 Titanian magnesian aluminous chromite (TIMAC) from Peuyuk B; 4 Magnesian ulvöspinel magnetite (MUM) from Peuyuk; MUM from Wesselton; 5 MUM from Benfontein Sills; 6 Titanian magnesian chromite (TMC); 7 MUM from Tunraq. Magmatic Trend 2: 8,9 Bellsbank; 10 Zagadochnaya; 11,12 Pleonaste from the De Beers Dyke.

4.3 Spinels in Kimberlites

Spinels have cubic-close packed (CCP) crystal structures with alternating layers of octahedral and octahedral-tetrahedral polyhedra. They have the general formula of AB_2O_4, where A and B represent tetrahedral and octahedral sites respectively (Waychunas, 1991). The particular cation occupying each site controls the crystal lattice; *normal* spinels contain more cations in the 'B' site (e.g. spinel, $MgAl_2O_4$ and chromite, $Fe^{2+}Cr_2O_4$), and *inverse* spinels contain an equal share between the 'A' and 'B' sites (e.g. magnetite, $Fe^{3+}[Fe^{3+}Fe^{2+}]O_4$ and ulvöspinel, $Fe^{2+}[Fe^{3+}Ti]O_4$) (Haggerty, 1991b). The cation distribution is sensitive to ambient conditions during melt fractionation, and oxygen fugacity (fO_2), magma composition, pressure and temperature can therefore be inferred from the spinel composition (e.g. Allan et al. 1988; Ballhaus et al. 1991; Irvine 1965; Kamenetsky et al. 2001; Sack & Ghiorso 1991a,b).

Kimberlites host a wide range of spinel solid solutions which can be summarised into the following eight end-member compositions (Mitchell, 1986b):

$MgCr_2O_4$	magnesiochromite
$FeCr_2O_4$	chromite
$MgAl_2O_4$	spinel
$FeAl_2O_4$	hercynite
Fe_3O_4	magnetite
$MgFe_2O_4$	magnesioferrite
Fe_2TiO_4	ulvöspinel
Mg_2TiO_4	magnesian ulvöspinel

Chromite, magnesiochromite and spinel represent the early formed compositions, which proceed towards increased Fe- and Ti-rich ulvöspinel and magnetite at the expense of Cr and Al (Haggerty, 1975).

Spinels in kimberlite occur as macrocrysts as well as phenocrysts. Spinel macrocrysts are characteristically aluminous-magnesian-chromites, spinels and hercynites (Haggerty, 1975; Mitchell & Clarke, 1976). They are typically 0.1-0.5 mm in diameter (Mitchell, 1986a) and have rounded habits, which either resulted from resorbtion due to disequilibrium with the kimberlite melt (Mitchell, 1986b), or mechanical abrasion during kimberlite ascent and emplacement (Mitchell &

Clarke, 1976). Some spinel macrocrysts originated from disaggregated mantle nodules, as their compositions are comparable with spinels within lherzolite xenoliths and alpine peridotites (Mitchell, 1986b). Spinels are also associated with the megacryst suite (Section 2.3.1.2), which potentially crystallised as phenocrysts from a protokimberlite melt (Gurney et al., 1979; Mahotkin et al., 2000; Nowell & Pearson, 1998). Groundmass spinel phenocrysts in kimberlites on average range between 0.001-0.1 mm in diameter (Mitchell, 1986a), and typically display complex zoning (Haggerty, 1975). Mitchell (1986b) defined the following major trends of kimberlitic spinel compositions, which are summarized on the modified multicomponent spinel prisms in Figure 4.1:

1. **Magmatic Trend 1**; spinel compositions evolve from titanian-magnesian-aluminous-chromites (TIMAC) or titanian-magnesian-chromites with 1-12 wt% TiO_2 with increasing Ti and Fe^{3+}/Fe^{2+} with a simultaneous decrease in Cr towards magnesian-ulvöspinel-magnetites (MUM).

2. **Magmatic Trend 2**; spinel compositions trend from aluminous-magnesian-chromites (AMC) by increasing Fe^{2+}/Fe^{2+}+Mg with a subsequent increase in Ti to titanian-magnesian-chromites (TMC) to titanian-chromites (TC) and ultimately to ulvöspinel-magnetites.

4.3.1 Atoll Spinels

Atoll spinels are a textural type of groundmass spinel commonly found in kimberlites, although they are not exclusively kimberlitic (Armstrong et al., 1997). They have a euhedral to subhedral core which is often zoned, surrounded by a 'lagoon' of groundmass mesostasis (serpentine) which are enclosed by a rim of Fe-rich ulvöspinel or magnetite (Mitchell & Clarke, 1976) which parallels the shape of the core (Armstrong et al., 1997). Atoll spinels are associated with coherent or hypabyssal kimberlite in dykes, sills and root zones of kimberlite pipes (Mitchell, 1986b). Armstrong et al. (1997) makes one reference to atoll spinels within diatreme facies kimberlite, however to date this texture within this kimberlite type is unique.

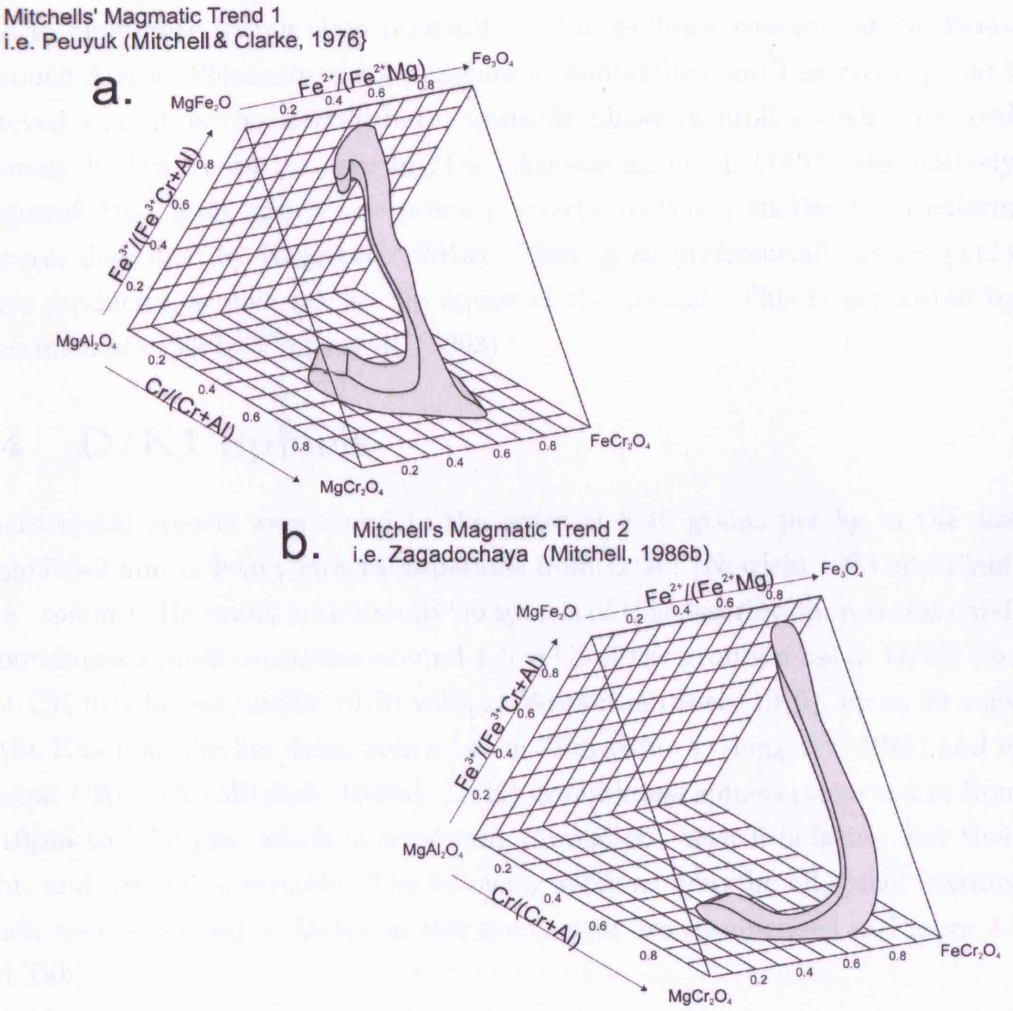

Figure 4.1: Oxidised spinel prisms illustrating (a) Mitchell's Magmatic Trend 1 with spinel compositions from Peyuk (Mitchell & Clarke, 1976), and (b) Magmatic Trend 2 with spinel compositions from Zagadochnaya (Mitchell, 1986b).

The formation of atoll spinels remains poorly understood. Mitchell & Clarke (1976) propose that a less stable spinel phase surrounding the chrome-rich core was resorbed after crystallisation of the iron-rich atoll rim. Pasteris (1983) found pleonaste (Mg-Fe-Al-spinel) as an intermediate phase between atoll cores and rims in kimberlite within close proximity of the wallrock contacts at De Beers in South Africa. Pleonaste is not common in kimberlites and Pasteris (*op. cit.*) believed that it is the intermediate, unstable phase of atoll spinels, resorbed in many bodies by an increase in fO_2. Armstrong et al. (1997) alternatively suggested that atoll spinels are primary growth features, similar to cruciform textures described by Haggerty (1991a). They grow preferentially along {111} plane producing arrowheads at the apices of the crystal. This is supported by experimental work by Faure et al. (2003).

4.4 D/K1 Spinels

Macrocrystal spinels were found in the order of 8-40 grains per kg in the size range 0.5-2 mm in heavy mineral separates from D/K1 (Nowicki 1993 and Field, *pers. comm.*). However, in this study no spinels of this description were observed. Groundmass spinels constitute around 1-5 vol% of the groundmass at D/K1 (except CK lithofacies), unlike 10-20 vol% at Wessleton (Shee, 1985), up to 30 vol% at the Koidu kimberlite dyke, Seirra Leone (Tompkins & Haggerty, 1985) and in general 1-30 vol% (Mitchell, 1986a). D/K1 groundmass spinels range in size from $\leq$ 10μm to $\geq$50 μm, which is consistent throughout each lithofacies, but their habit and texture is variable. The following sections describe all spinel textures which were identified at D/K1 in this study, and are summarised in Figure 4.2 and Table 4.4.

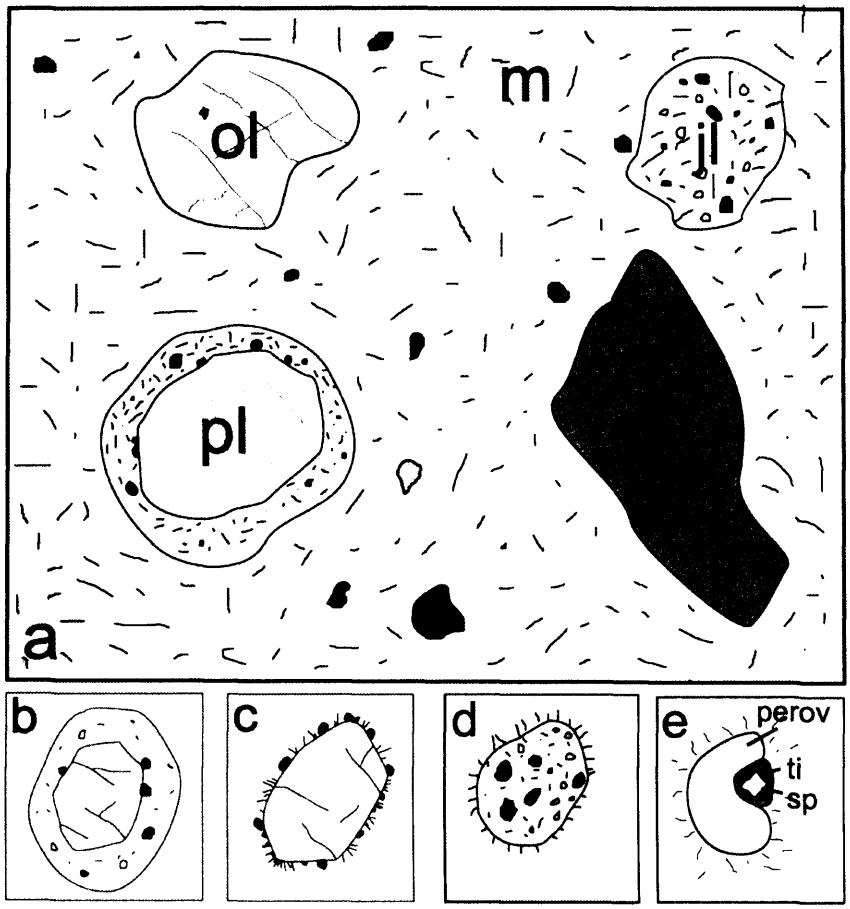

Figure 4.2: Schematic diagram of spinel (small black grains) textures identified at D/K1. (a) General view of a kimberlite texture at ~x100 magnification (m - matrix; ol - olivine macrocryst (with spinel inclusion); l - lithic clast; pl - pelletal lapilli; jl - juvenile lapilli)). (b) pelletal lapilli where spinels are contained within the groundmass of the lapilli rim. (c) ghost-lapilli where spinels are found at the edge of olivines. (d) porphyritic juvenile lapilli with small groundmass spinels. (e) spinel in association with perovskite (sp - spinel; ti - titanite; perov - perovskite).

Sample	Ghost-lapilli		Pelletal lapilli		Magmaclast		Matrix		Inclusion		Occurrence	Size (μm)
	simp.	atoll	simp.	atoll	simp.	atoll	simp.	atoll	perov	ol-pheno	ol-macro	
LDD10_01	X	x	-	-	-	-	**X**	**X**	-	-	-	Well resorbed	20-50
LDD10_02	**X**	-	-	-	-	-	X	X	-	-	-	Well resorbed	20-50
LDD10_03	**X**	-	-	-	-	-	**X**	X	-	-	x	Moderately resorbed	20-50
LDD10_04	**X**	-	-	-	-	-	**X**	x	x	-	-	Moderately resorbed	20-50
LDD10_05	**X**	-	-	-	-	-	**X**	x	x	-	-	Frequently resorbed	20-50
LDD10_06	**X**	x	-	-	-	-	X	**X**	-	-	x	Resorbed atoll rims	20-60
LDD10_07	**X**	-	-	-	-	-	**X**	X	-	-	x	Resorbed atoll rims	20-60
LDD10_09	**X**	x	-	-	-	-	-	x	-	-	X	Frequently resorbed	20-50
LDD16A_02	**X**	-	-	-	-	-	-	x	-	-	-	Frequently resorbed	20-50
LDD16A_08	**X**	-	-	-	-	-	-	X	x	x	-	Euhedral	20-50
LDD16A_18	**X**	-	-	-	-	-	X	x	x	-	-		
LDD16A_23	**X**	-	-	-	-	-	X	x	x	x	-	Resorbed atoll rims	20-60
LDD12_01	X	-	**X**	-	-	-	X	-	-	-	-	Few atolls	30- 60
LDD12_03	-	X	-	X	x	X	X	X	-	-	x	Preserved atolls in PL.	20-100
LDD12_04	X	x	-	x	-	-	**X**	x			X	Moderately resorbed	20-50
LDD12_05	x	-	-	-	-	-	x	**X**	-	-	-	Frequently resorbed	20-50
LDD21_01	x	-	**X**	-	X	-	-	-	-	-	-	Mod resorbed	20-70
LDD21_06	-	-	-	-	-	-	X	**X**	-	x	-	Well preserved	20-80

Table 4.2: Summary of petrographic textures from each sample. **X** - abundant (50-75% of all spinels); X - moderately abundant (20-50%); x - rare ($\leq$20%).

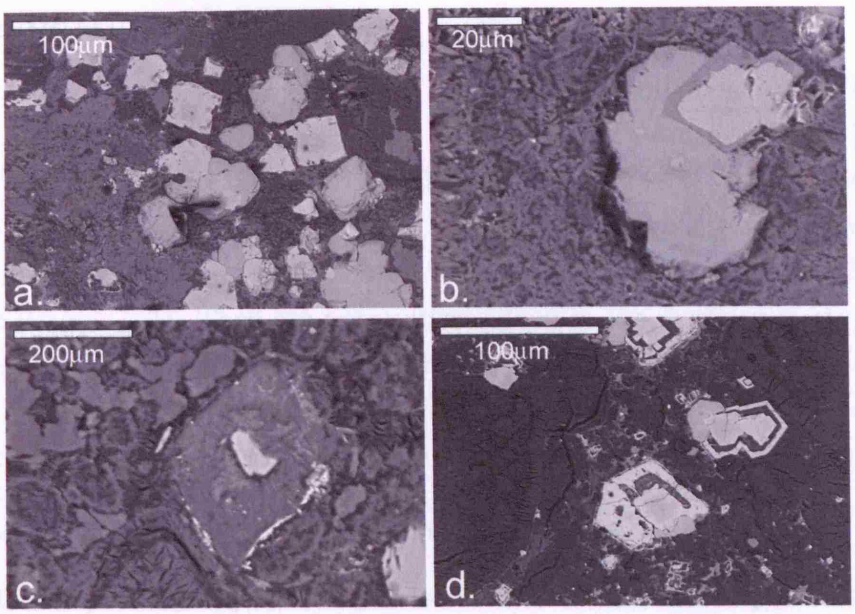

Figure 4.3: Back scattered electron images of discrete groundmass spinels. (a) Cluster of discrete, euhedral groundmass spinels (paler grey grains). (b) Euhedral spinel (smaller, paler grey grain) with perovskite and an interconnecting zone of titanite (darker grey phase). (c) Resorbed groundmass atoll spinel. (d) Cluster of groundmass atoll spinels; zoning is shown where the core is darker grey than the rim. (All backscatter images were taken using Jeol 773 Superprobe at UCL. Bright albedos in these images represent minerals with a higher atomic numbers, for example metal, sulphides and oxides.)

Discrete Groundmass Spinels

Discrete groundmass spinels are $\leq$10 μm up to 40 μm and typically display euhedral habits (Fig. 4.3). They often exhibit resorbtion textures, although this varies between lithofacies, and ranges from near-perfect euhedral grains to smaller, anhedral, corroded grains (Fig. 4.3 a and c). VK1 contains the most abundant resorbed groundmass spinel textures and CK hosts well preserved discrete groundmass spinels. Occasionally these spinels occur in clusters (Fig. 4.3 a), but rarely grouped together in chains.

Groundmass Atoll Spinels

Atoll spinels from D/K1 are typically around 40 μm in diameter. They are well preserved within the CK lithofacies and in the groundmass of some juvenile lapilli within volcaniclastic kimberlite lithofacies (Fig. 4.4a-c). Atoll spinels were also found as discrete grains within the interclast matrix phase of volcaniclastic kimberlites (Fig. 4.4d, e and f), where they are not usually observed (Mitchell 1986b; Section 4.3.1). They are not well preserved in the kimberlites studied for this thesis. They often have very thin rims which are occasionally replaced by another phase (darker grey phase in Figure 4.4d and e). These spinels also have asymmetric growth textures (Fig. 4.4c and e).

Groundmass Spinels with Perovskite

Groundmass spinels are occasionally associated with groundmass perovskite. The perovskite forms a horseshoe shape around the spinel, which is often cubic, and a zone of titanite occurs at the interface between spinel and perovskite which copies the cubic habit of the spinel (Fig.4.3b). Similar relationships are reported at Wessleton by Shee (1985). These are discussed in Chapter 5.

Spinels within Pelletal Lapilli

At D/K1 groundmass spinels were contained within the rims of crystalline pelletal lapilli (Fig. 4.5b), within juvenile porphyritic lapilli (Fig. 4.5d) and at the edge of olivine phenocrysts forming ghost lapilli (Fig 4.5a). Spinels within pelletal lapilli are often small, between 30 μm and $\leq$10 μm, euhedral grains, or resorbed, irregular grains. Atoll spinels contained within the groundmass of porphyritic juvenile clasts and in the rims of pelletal lapilli are the largest spinels seen during this study, up 100 μm in diameter.

Inclusions in Olivine

Spinels hosted in olivine phenocrysts and macrocrysts at D/K1 are shown in Figure 4.6. They are very small (often $\leq$ 10 μm) and typically euhedral, except where alteration has taken place, which is evident by the extensive alteration of their host olivine.

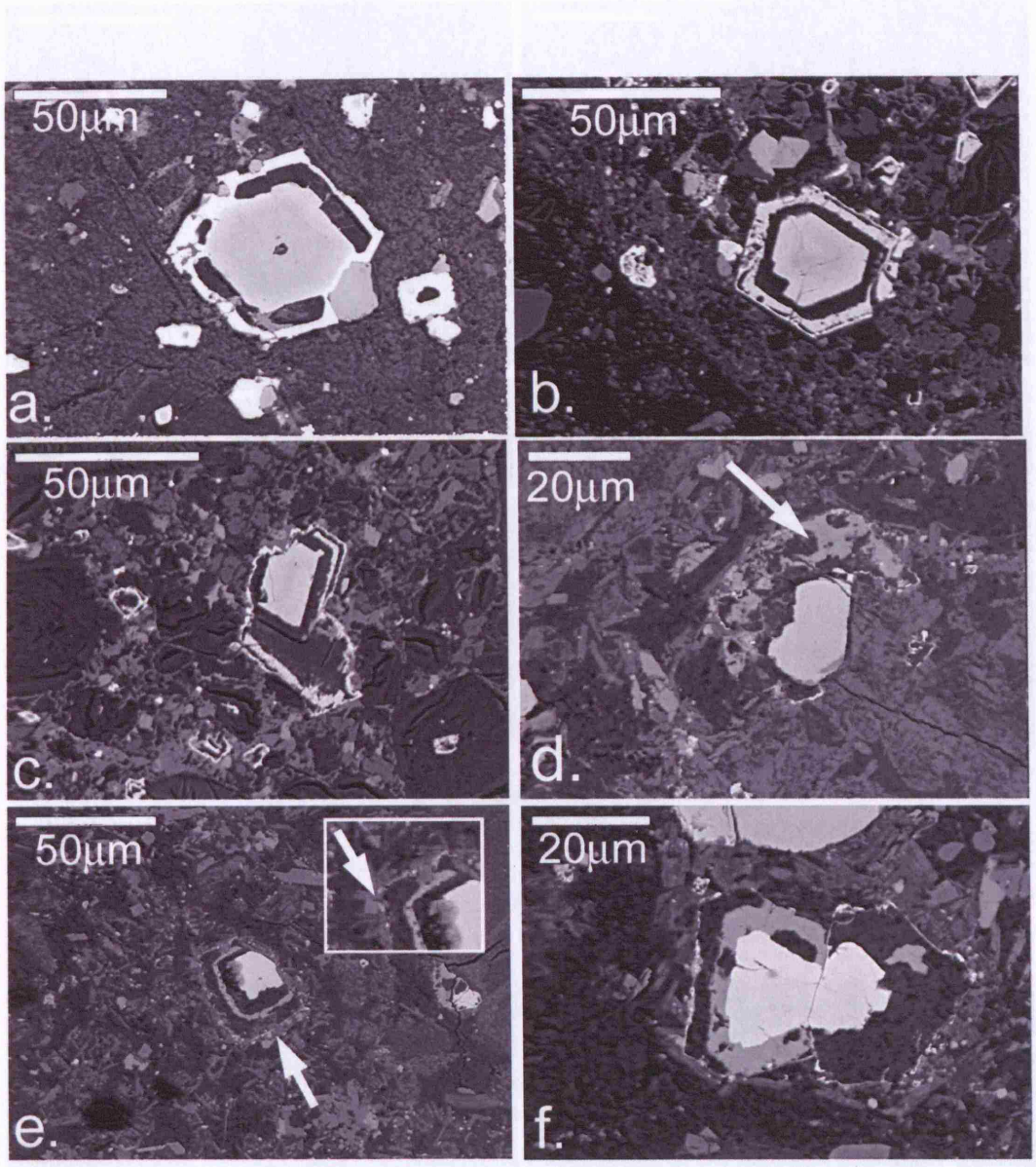

Figure 4.4: Back scattered electron images of atoll spinels from D/K1. (a) A well preserved atoll spinel from the CK lithofacies. (b) and (c) Well preserved atoll spinels contained within juvenile lapilli. (d), (e) and (f) are discrete groundmass atoll spinels within the VK1 volcaniclastic kimberlite, from D/K1. White arrows in (d) and (e) are highlighting a replacement phase, discussed in the text.

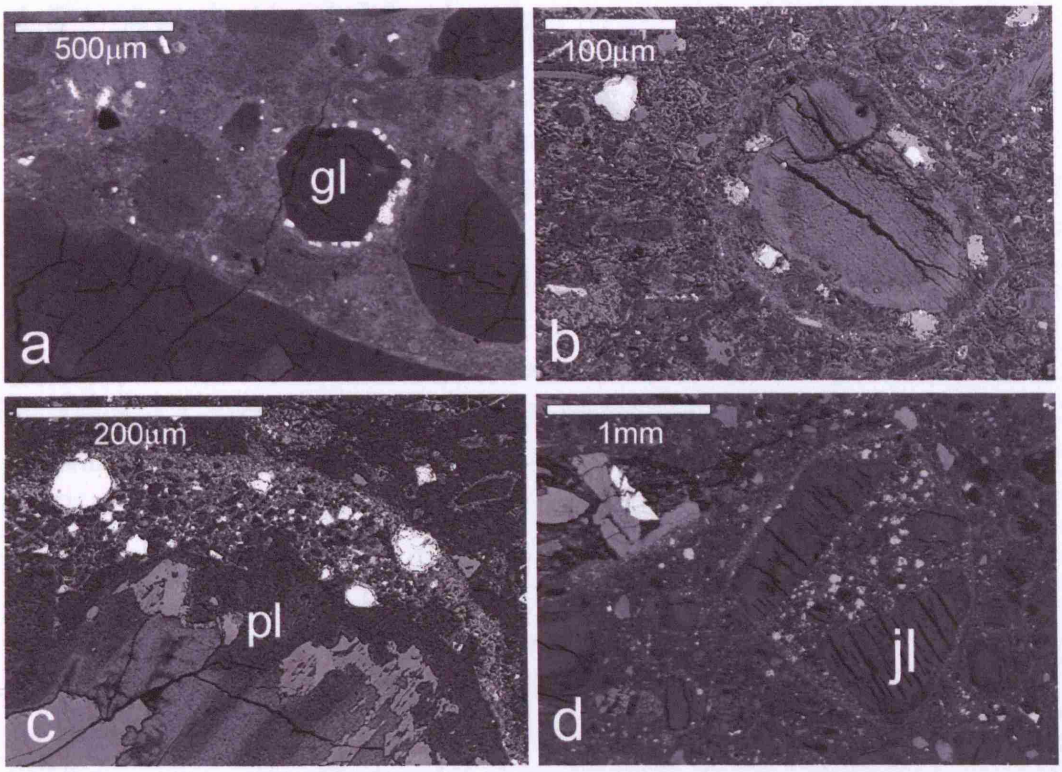

Figure 4.5: Back scattered electron images of spinels (pale/white grains) within pelletal lapilli and juvenile clasts. (a) and (b) Ghost lapilli (gl); olivine phenocryst with oxide halo. (c) Pelletal lapilli (pl) with relatively coarsely crystalline kimberlite surrounding olivine core. (d) Juvenile clasts; rounded fragment of exotic kimberlite containing atoll spinels.

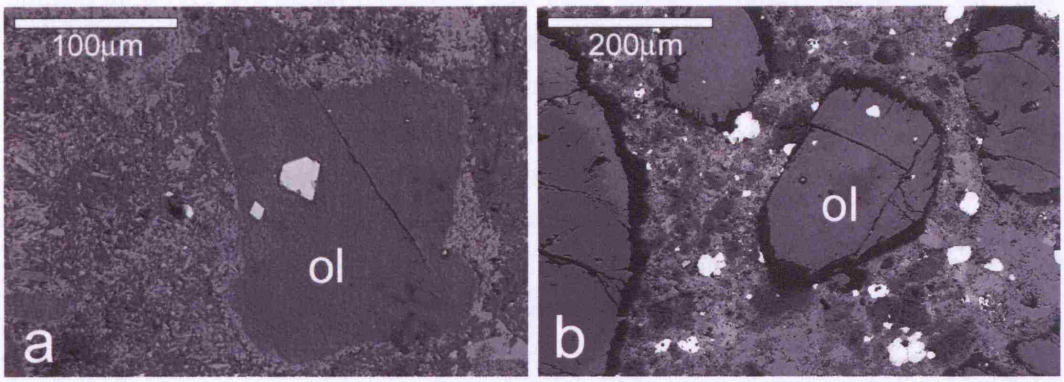

Figure 4.6: Back scattered electron images of spinel (pale grains) inclusions in olivine (darker grey host) (a) macrocryst and (b) phenocryst.

4.5 Analytical Methods

Over 700 groundmass spinel compositions were analysed from eighteen kimberlite samples collected during field visits to Letlhakane. The samples were considered representative of each lithofacies based on their mapped geology from drill core logging (Table 4.4).

Spinel analyses were carried out using polished, carbon coated microprobe sections on a Jeol 733 Superprobe with an Oxford Instrument ISIS energy dispersive system at Birkbeck College. The minimum magnification was 40μm and maximum is 3 x 106 μm and the beam diameter of 2 μm was used for individual mineral analyses. Oxide weight percentages of SiO_2, TiO_2, Al_2O_3, Cr_2O_3, FeO, MnO, MgO and CaO were measured. All iron was analysed as FeO and recalculated stoichiometrically. Data was collected at 15 kV for 100 second count-time. Data is corrected using a SEMQuant (ZAF4) program. Before measurements were taken the beam was calibrated using Specpure© cobalt metal (99.99% Co) and profile standardisation materials. The standards and the reproducibility of the data are listed in Appendix B. 80 analyses were also made using a Cameca SX50 wave dispersive spectrometer at the Natural History Museum to account for interfering Cr and Mn lines (Appendix B).

Frequently spinel totals were low. This could not be rectified by checking the quality of the polish and ensuring that analyses did not overlap two mineral phases. There are several possibilities for the acquisition of low totals: (i) many spinels at D/K1 are small ($\leq$20μm) and have resorbed edges which are very difficult to polish to a completely flat surface; (ii) all kimberlite samples have been altered, producing hydrous minerals, which may possibly influence the composition of the spinels. All analyses were collected under the same conditions and therefore the results are considered to be a measure of the true spinel composition. The results were recalculated into cation proportions as recommended by Pasteris (1982). Analyses with $\geq$ 0.15 Si and/or Ca cation proportions (cpu) were discarded to ensure only pure spinel compositions were interpreted.

4.6 Presentation of the Data

The majority of published spinel compositions from kimberlite bodies are presented on triangular spinel prism diagrams as shown in Figure 4.1, and projections of selected faces of these diagrams particularly Cr/Cr+Al versus Fe^{2+}/Fe^{2+}+Mg (e.g. Haggerty 1991b; Pasteris 1982). Barnes & Roeder (2001) recommended using bivariate plots of Fe^{3+}/Fe^{3+}+Al+Cr versus Fe^{2+}/Fe^{2+}+Mg, Ti versus Fe^{2+}/Fe^{2+}+Mg and a ternary plot of Fe^{3+}, Cr and Al. For comparison with the global kimberlitic spinel dataset Figure 4.8 presents D/K1 spinel compositions on these conventional plots. However, the aim of studying groundmass spinel mineral chemistry at D/K1 was to identify discernible compositional trends for each kimberlite lithofacies. These trends were most definitive on simple bivariate plots of Al versus Cr and Fe^{3+} versus Ti. Therefore they were used in the sections below to illustrate spinel compositional variations between lithofacies.

4.7 Spinel Mineral Chemistry

Table 4.7 shows the mean and standard deviations of all D/K1 spinel compositions and spinel compositions analysed from each lithofacies. Tables 4.7.1 to 4.7.5 present representative spinel compositions from each lithofacies. Figures 4.8, 4.9 and 4.10 show all of the analysed D/K1 spinel compositions on the conventional plots discussed above. The earlier formed spinels at D/K1 are titanian-aluminous-magnesian-chromites (TIMAC, c.f. Mitchell 1986b), with Cr ~8 cpu and Al ~4.5 cpu, which plot at the base of the spinel prism. There is a continuous compositional trend towards the magnesian-ulvöspinel-ulvöspinel-magnetite (MUM) series at the apex of the spinel prism. This is the typical kimberlitic spinel trend of increasing Ti and Fe at the expense of Cr and Al with approximately constant $Fe^{2+}/(Fe^{2+}+Mg)$ of ~0.5 (e.g. Armstrong et al. 1997; Haggerty 1975; Mitchell 1979; Mitchell & Clarke 1976; Tompkins & Haggerty 1985), and is consistent with the Magmatic Trend 1 of Mitchell (1986b). D/K1 spinels are all titaniferous; only rare grains have less than 5 wt% TiO_2 and the maximum value recorded was 22.23 wt% TiO_2. These compositions are similar to those from Peuyuk (Mitchell & Clarke, 1976) except for a paucity (~0.1%) of Ti-free magnetites within the

D/K1 spinel set. Figure 4.19 presents groundmass spinel compositions from this study with spinels contained within mantle xenoliths from Stiefenhofer (1993). There is a strong Al-enrichment of the mantle-derived spinels, although a few D/K1 groundmass compositions overlap the field defined by Stiefenhofer's data.

There is a degree of overlap between spinel compositions from all the D/K1 pipe (Figs. 4.9 and 4.10). However, the locus ($\geq$90% of analyses) of each set of spinel compositions divided according to lithofacies highlights more unique trends which are discussed in the sections below. The predominant trends in the two cation plots used in Figures 4.12 to 4.16 are illustrated in Figure 4.11 and are referred to throughout the descriptions below.

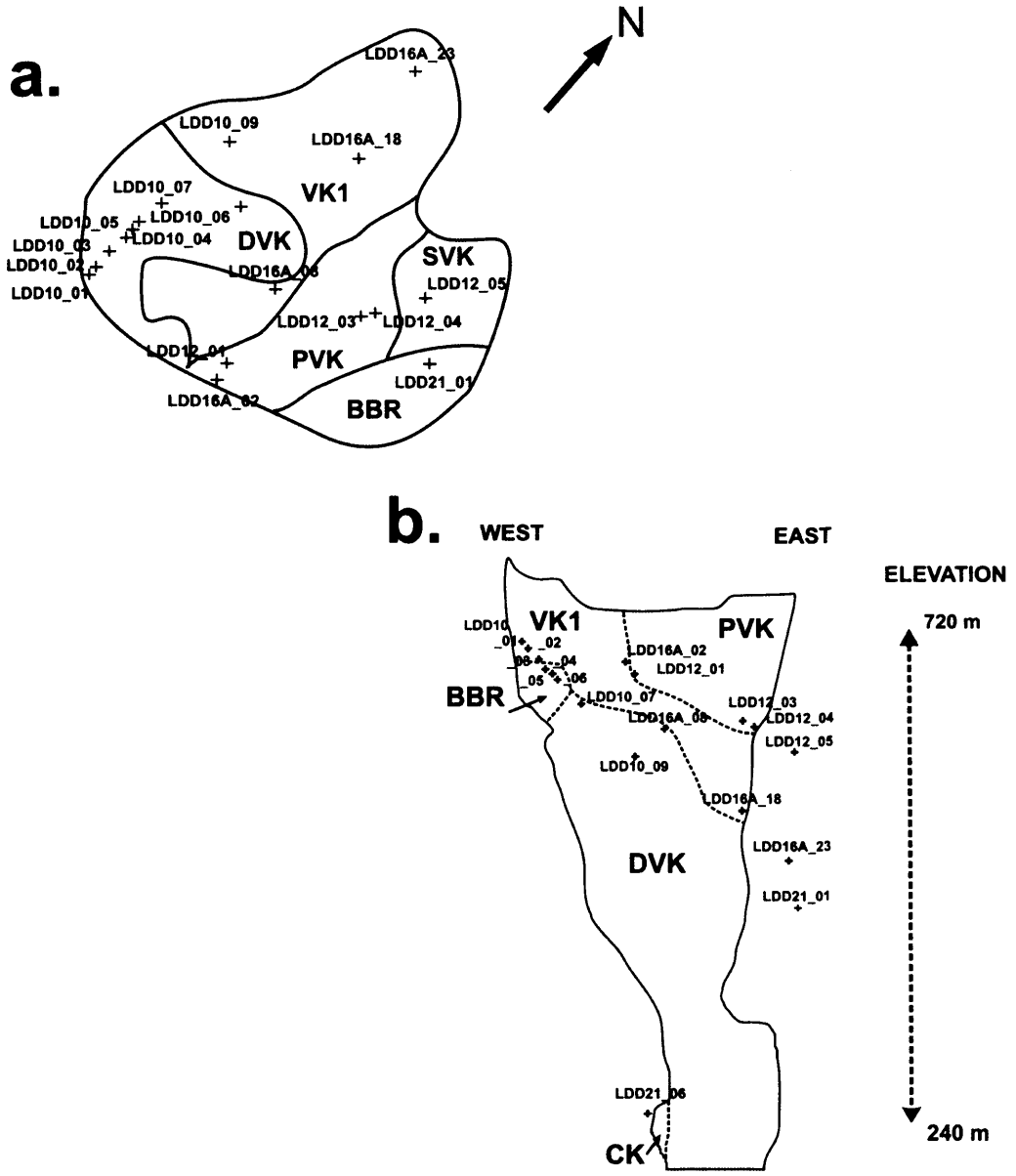

Figure 4.7: The location of samples analysed for spinel compositions. (a) Plan view to show spatial distribution of samples. (b) Projected 2D view down the kimberlite pipe to give a representation of the depth variation of the samples. (N.B. Samples outside of pipe outline are actually within the pipe but they are outside the pipe limits in this cross section.)

		SiO_2	TiO_2	Al_2O_3	Cr_2O_3	FeO*	MnO	MgO	CaO
All D/K1	mean	0.25	10.04	6.44	24.37	42.45	0.52	10.48	0.18
(N=639)	std dev	0.10	4.31	3.08	16.70	14.83	0.28	2.21	0.13
VK1	mean	0.24	9.12	5.80	29.26	39.84	0.58	10.24	0.19
(N=175)	std dev	0.10	4.08	2.23	15.91	14.75	0.31	1.86	0.13
BBr1	mean	0.25	11.92	4.90	23.30	42.81	0.48	10.41	0.19
(N=131)	std dev	0.10	4.30	1.09	15.01	10.00	0.15	1.36	0.10
DVK	mean	0.23	9.98	4.42	18.17	51.15	0.73	8.35	0.14
(N=95)	std dev	0.09	3.86	2.51	16.93	17.07	0.38	2.62	0.13
PVK	mean	0.25	10.76	7.71	20.43	43.04	0.34	11.93	0.21
(N=148)	std dev	0.11	4.18	2.69	17.39	13.71	0.16	1.03	0.13
SVK	mean	0.25	9.01	8.92	28.03	39.29	0.49	10.03	0.19
(N=52)	std dev	0.10	4.54	3.47	15.83	16.24	0.25	3.02	0.11
CK	mean	0.37	6.54	11.31	31.45	33.49	0.49	12.09	0.14
(N=38)	std dev	0.08	3.00	3.79	14.33	15.59	0.19	1.97	0.13

Table 4.3: Mean and standard deviation of all D/K1 spinels and divided by lithofacies (FeO* - all iron was analysed as FeO; N - number of analyses).

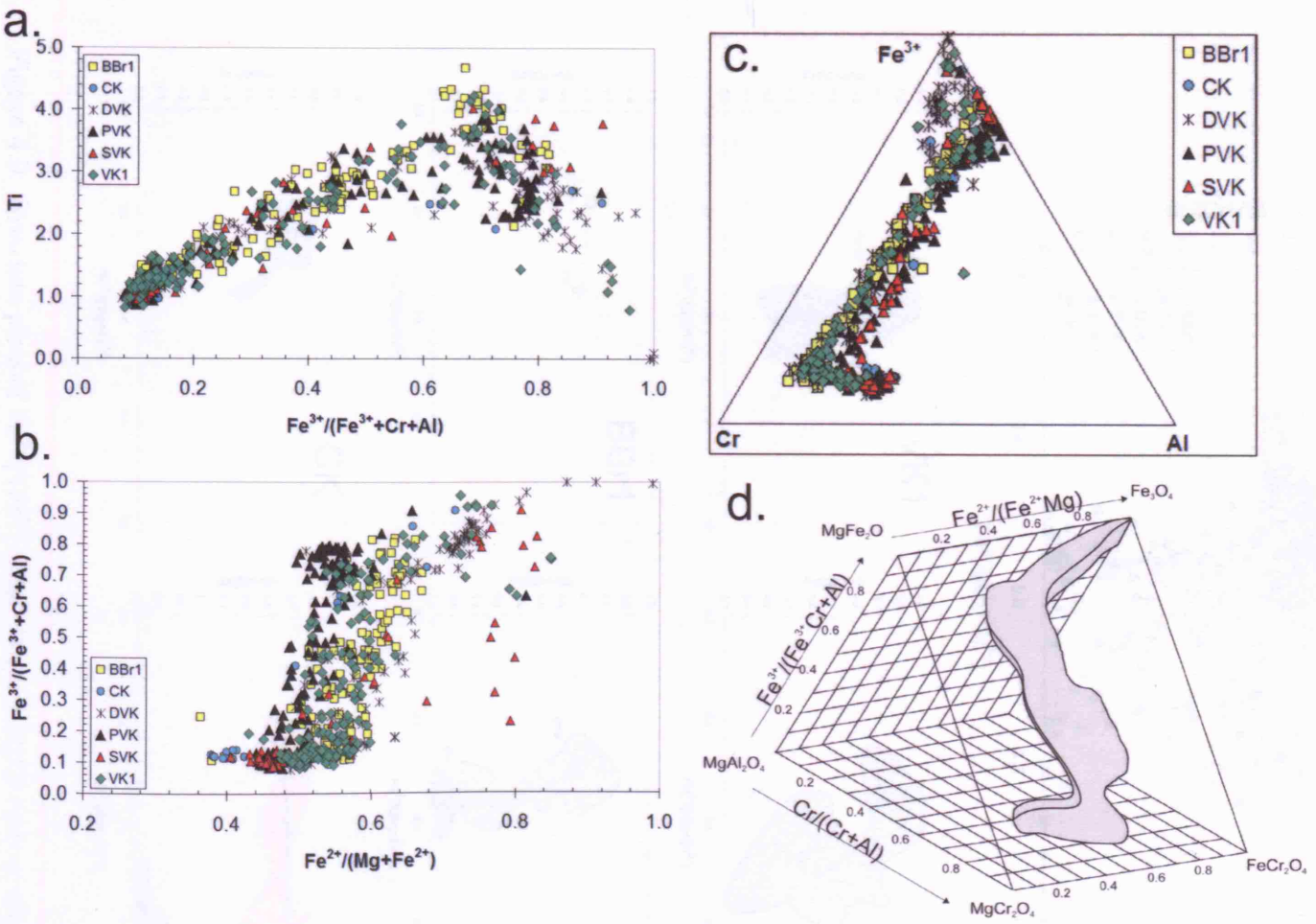

Figure 4.8: Standard plots representing all D/K1 spinel compositions. Core to rim analyses are shown on each plot to illustrate direction of compositional zoning. (a) Ti^{4+} versus $Fe^{3+}/Fe^{3+}+Cr+Al$; (b) $Fe^{3+}/Fe^{3+}+Cr+Al$ versus $Fe^{2+}/Fe^{2+}+Mg$; (c) Triangular plot of Fe^{3+}, Cr^{3+} and Al^{3+}; (d) oxidised spinel prism illustrating the locus ($\geq$90% of analyses) of all D/K1 spinel compositions.

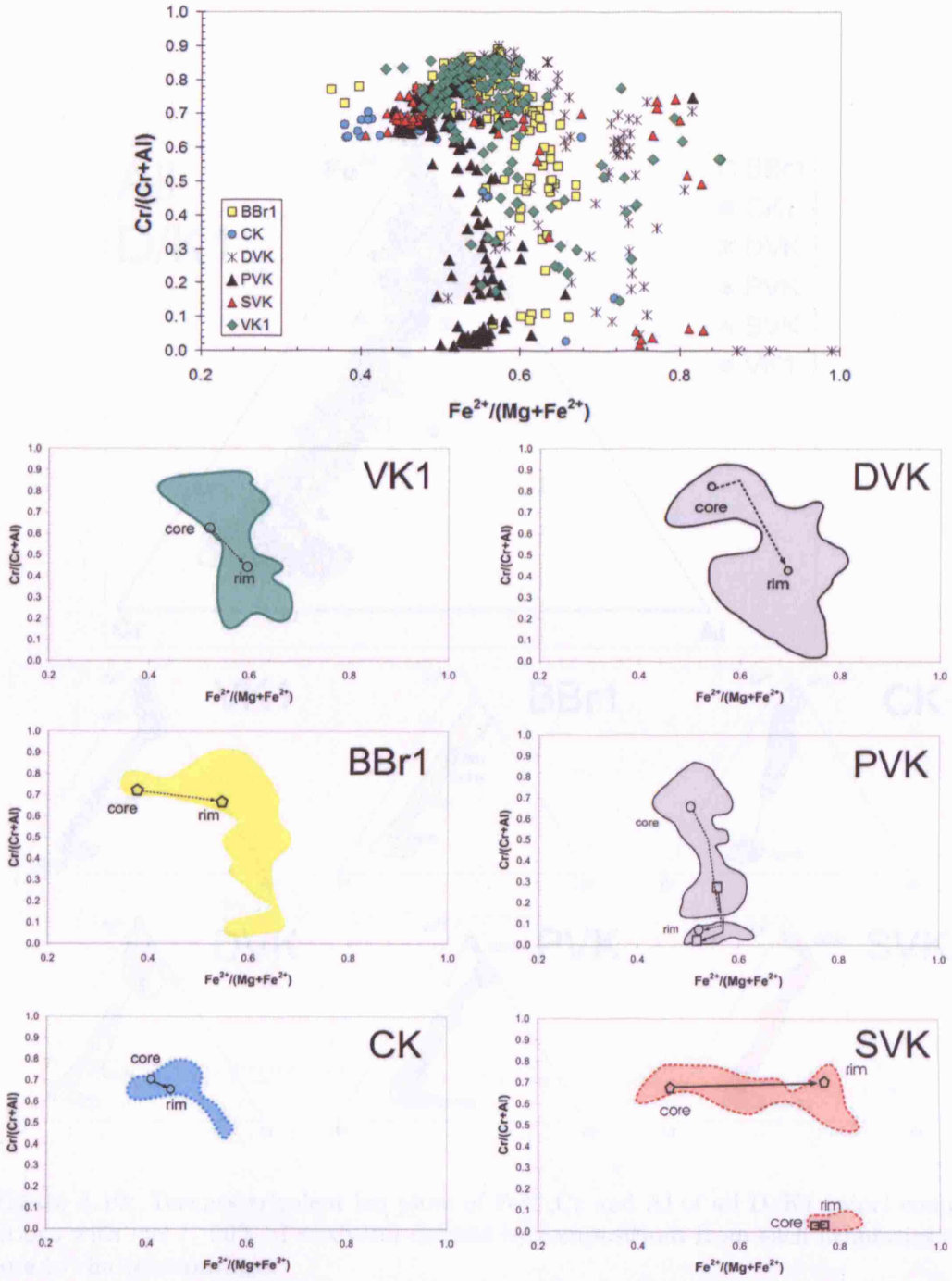

Figure 4.9: Bivariate plots of $Fe^{2+}/(Fe^{2+}+Mg)$ versus (Cr/Cr+Al) of all D/K1 spinel compositions with loci ($\geq$90% of analyses) defined by compositions from each lithofacies and core to rim relationships.

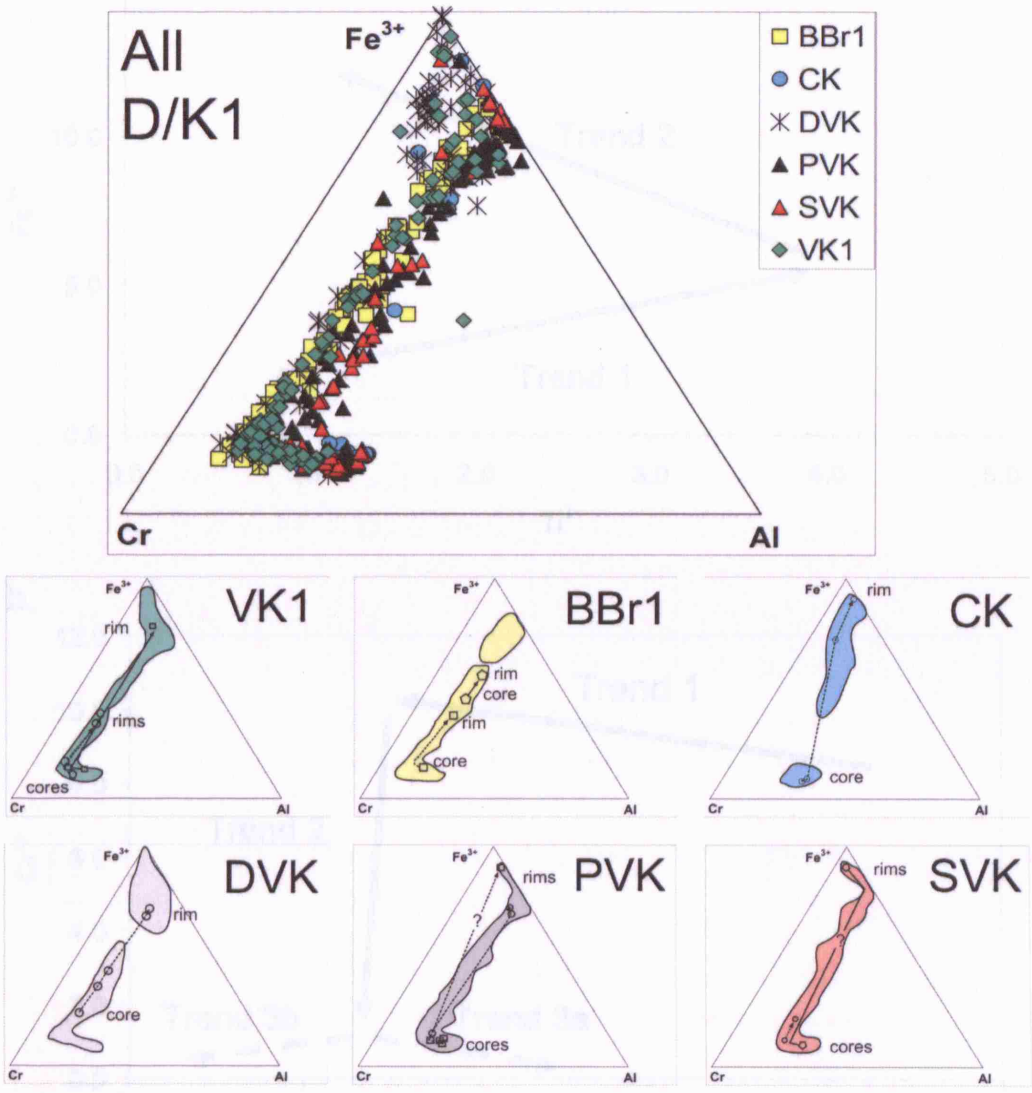

Figure 4.10: Ternary trivalent ion plots of Fe^{3+},Cr and Al of all D/K1 spinel compositions with loci ($\geq$90% of analyses) defined by compositions from each lithofacies and core to rim relationships.

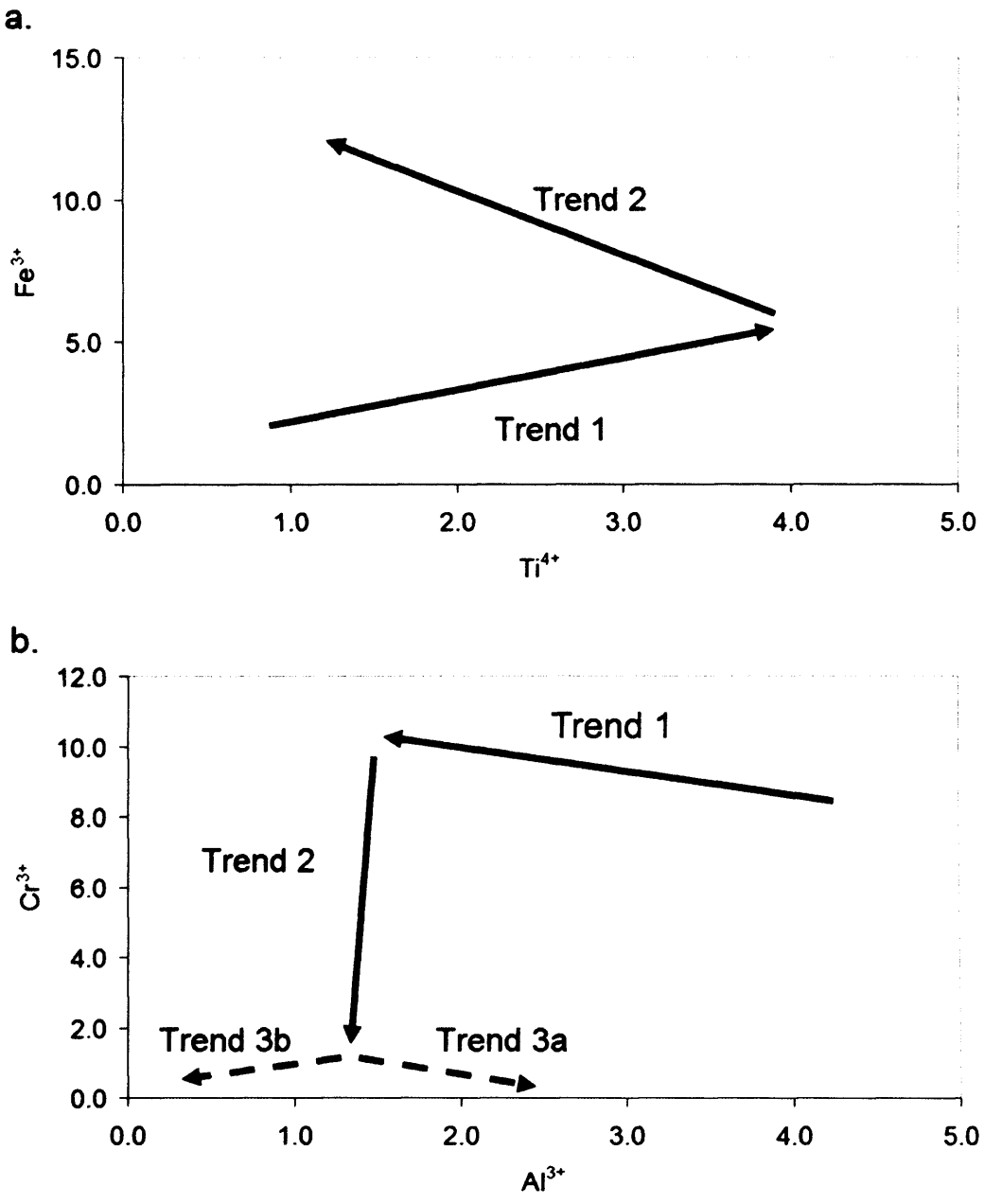

Figure 4.11: Predominant trends defined by all D/K1 spinels.

4.7.1 VK1

Figures 4.8,4.9 and 4.10 demonstrate that VK1 spinels follow Mitchell's Magmatic Trend 1 defined by an decrease in Cr and Al with an increase in Ti and Fe^{3+} (Mitchell, 1986b). Although there is considerable compositional overlap between spinels from the six samples analysed, there are some more distinct trends.

Samples LDD10_01 and LDD10_03 are characterised by early formed spinels with Al content of $\leq$2.5 cpu which is low compared to other VK1 samples which have $\geq$3 cpu. Spinels from sample LDD16A_23 has consistently higher Al and Cr content and unlike other VK1 spinels, they do not evolve to a Cr content of lower than 2 cpu. The majority of VK1 spinels do not show Trends 3a or 3b (Fig. 4.11b) except sample LDD10_01 which shows two analyses belonging to Trend 3a which are aluminous magnesioferrites. Trend 3b is strongly defined by spinels from sample LDD16A_02 which also have a distinctive Trend 2 in Figure 4.12b of increasing Fe^{3+} with decreasing Ti, which represents compositions from the ulvöspinel to magnetite series and is not shown by other VK1 spinels. Spinels analysed from Sample LDD16A_02 also have higher $Fe^{2+}/(Fe^{2+}+Mg)$ up to 0.8, and Fe^{3+} $\geq$12 cpu (Fig. 4.12b).

Figure 4.12c and d show VK1 spinel compositions plotted according to paragenesis. Compositions of spinel inclusions in olivine phenocrysts are confined to Trend 1 of Figure 4.11a and b. Spinels contained within the rims of ghost-lapilli have comparatively low Al content of $\leq$3.5 cpu, and contain compositions with the lowest Al content of $\leq$0.5 cpu and the highest Fe^{3+} of $\geq$13 cpu of all analysed VK1 samples.

	1 c MA	2 c MA	3 i MA	4 r MA	5 i MA	6 c MA	7 c IP	8 c IP	9 c IP	10 r M	11 c GA	12 c GL	13 c GL	14 i GL	15 i IP	16 c GL	17 c MP
Wt% Oxide																	
SiO_2	0.5	0.5	0.2	0.2	0.1	0.2	0.3	0.3	0.3	0.4	0.2	0.2	0.2	0.2	0.2	0.2	0.2
TiO_2	20.9	19.8	7.2	13.5	13.2	10.4	5.1	4.8	4.7	4.7	15.7	9.5	5.6	5.9	9.2	8.2	7.8
Al_2O_3	4.3	4.4	10.8	4.5	4.4	5.0	13.2	12.5	14.3	15.0	5.4	5.4	7.8	5.8	4.9	5.5	5.1
Cr_2O_3	5.0	4.5	41.1	24.1	28.2	26.3	41.3	41.6	40.5	38.6	9.0	34.0	43.2	43.2	35.2	38.4	40.4
FeO	32.5	31.4	23.5	27.2	27.1	23.5	19.4	18.7	19.1	17.7	29.0	24.1	21.8	22.8	23.8	22.5	22.7
Fe_2O_3	25.8	28.2	7.3	16.9	15.8	22.5	8.0	8.2	7.1	8.7	31.1	14.7	8.7	10.1	12.6	11.9	10.1
MnO*	0.9	0.6	0.6	0.1	0.5	0.8	0.5	0.3	0.4	0.2	0.4	1.1	0.9	0.7	0.5	0.6	0.8
MgO	12.3	12.4	10.8	10.9	11.1	11.6	12.7	12.6	12.4	13.5	11.6	10.4	9.8	9.2	10.4	11.0	9.9
CaO	0.3	0.5	0.3	0.1	0.2	0.3	0.0	0.0	0.0	0.1	0.4	0.2	0.1	0.2	0.0	0.0	0.5
Total	102.5	102.3	101.8	97.5	100.6	100.6	100.5	99.0	98.8	98.8	102.8	99.4	98.2	98.1	96.8	98.2	97.4
Cation proportions (calculated to 32 O)																	
Si	0.1	0.1	0.1	0.1	0.0	0.1	0.1	0.1	0.1	0.1	0.1	0.1	0.1	0.1	0.1	0.0	0.0
Ti	4.1	3.9	1.4	2.8	2.7	2.1	1.0	0.9	0.9	0.9	3.1	1.9	1.2	1.2	1.9	1.7	1.6
Al	1.3	1.4	3.3	1.5	1.4	1.6	4.0	3.8	4.3	4.5	1.7	1.7	2.5	1.9	1.6	1.8	1.7
Cr	1.0	0.9	8.4	5.3	6.0	5.6	8.3	8.5	8.3	7.8	1.9	7.3	9.3	9.4	7.8	8.3	8.9
Fe(iii)	5.1	5.6	1.4	3.5	3.2	4.5	1.5	1.6	1.4	1.7	6.2	3.0	1.8	2.1	2.6	2.4	2.1
Fe(ii)	7.1	6.9	5.1	6.3	6.1	5.3	4.1	4.1	4.1	3.8	6.4	5.5	5.0	5.3	5.6	5.1	5.3
Mn	0.2	0.1	0.1	0.0	0.1	0.2	0.1	0.1	0.1	0.0	0.1	0.3	0.2	0.2	0.1	0.1	0.2
Mg	4.8	4.9	4.2	4.5	4.5	4.6	4.8	4.9	4.8	5.2	4.5	4.2	4.0	3.8	4.3	4.5	4.1
Ca	0.1	0.1	0.1	0.0	0.1	0.1	0.0	0.0	0.0	0.0	0.1	0.1	0.0	0.1	0.0	0.0	0.1
Mol % end-members																	
$MgAl_2O_4$	16.8	17.1	14.6	18.1	17.6	19.8	26.0	25.4	28.2	29.9	20.9	21.5	16.0	23.5	20.2	22.2	11.6
Mg_2TiO_4	21.7	21.9	17.6	19.1	19.1	19.1	12.9	12.5	12.0	12.1	18.2	15.5	14.8	11.9	16.7	16.7	17.9
Mn_2TiO_4	1.2	0.8	-	0.2	0.7	1.1	-	-	-	-	0.6	1.6	-	1.0	0.7	0.8	-
Fe_2TiO_4	28.7	26.3	-	15.9	13.8	6.1	-	-	-	-	20.2	7.1	-	2.3	6.5	3.5	-
$MnCr_2O_4$	-	-	0.8	-	-	-	1.4	0.8	1.3	0.5	-	-	2.8	-	-	-	1.7
$MgCr_2O_4$	-	-	4.5	-	-	-	5.7	7.2	5.0	7.1	-	-	2.7	-	-	-	1.2
$FeCr_2O_4$	6.5	5.9	56.8	32.9	37.6	34.9	50.3	52.4	50.0	47.7	11.7	45.6	55.4	59.1	48.2	51.5	58.1
Fe_3O_4	25.2	28.0	5.6	13.9	11.2	18.8	3.7	1.7	3.5	2.7	28.3	8.7	8.3	2.2	7.7	5.3	9.5

Table 4.4: Representative spinel compositions from VK1 samples. (GA - atoll spinel contained within ghost lapilli; GL - simple spinel contained within ghost lapilli; IM - spinel inclusion within olivine macrocryst; IP - spinel inclusion contained within olivine phenocryst; M - discrete spinel within the interclast matrix; MA - discrete atoll spinel within the interclast matrix; MP - spinel associated with perovskite within the interclast matrix; c - core; i - intermedtiate; r - rim.)

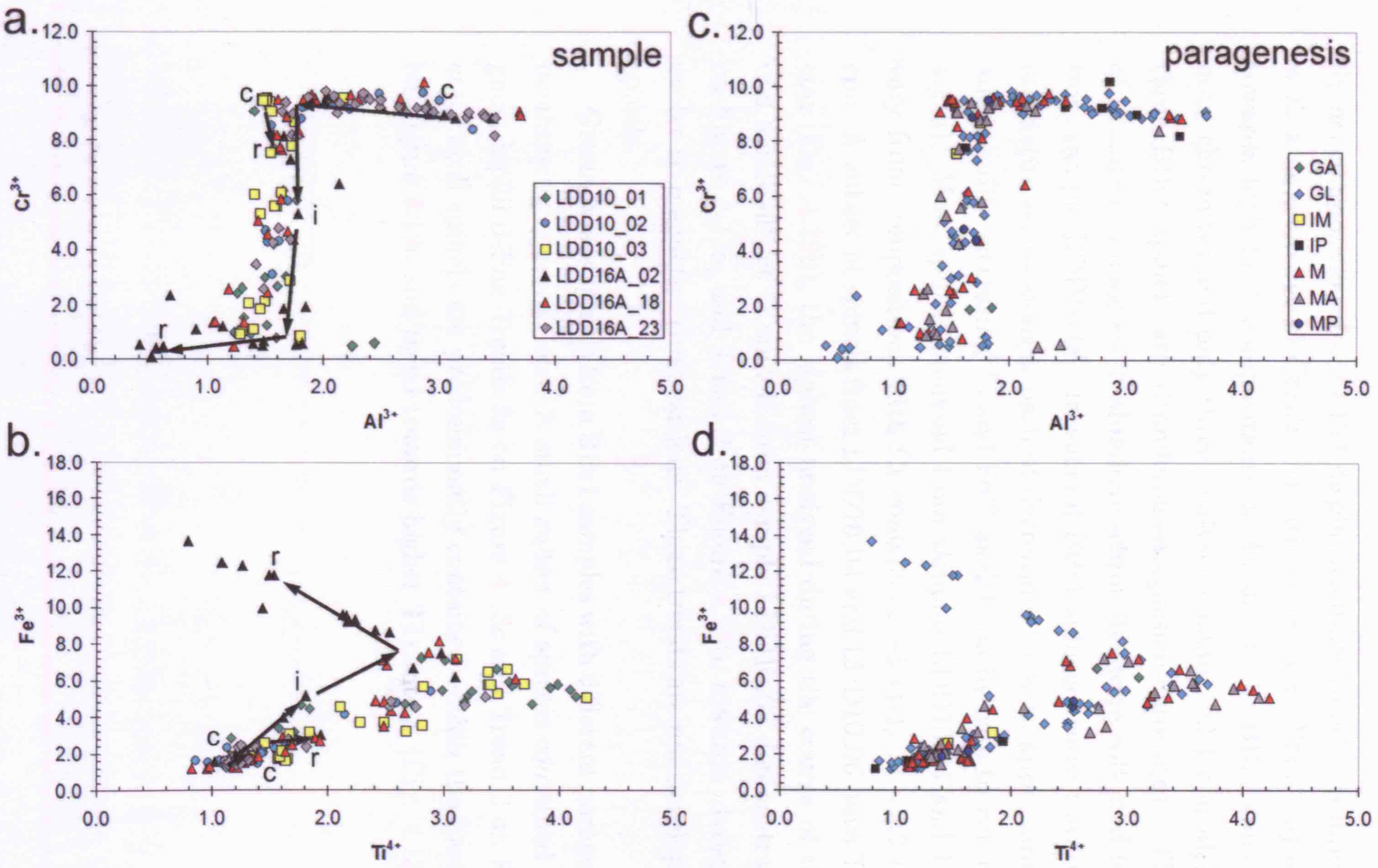

Figure 4.12: Bivariate plots of spinel compositions from VK1. (a) and (c) Cr versus Al divided by sample and paragenesis respectively. (b) and (d) Fe^{3+} versus Ti divided by sample and paragenesis respectively. (GA - atoll spinel contained within ghost lapilli; GL - simple spinel contained within ghost lapilli; IM - spinel inclusion within olivine macrocryst; IP - spinel inclusion contained within olivine phenocryst; M - discrete spinel within the interclast matrix; MA - discrete atoll spinel within the interclast matrix; MP - spinel associated with perovskite within the interclast matrix.)

4.7.2 BBr1

Spinel compositions from BBr1 display a similar trend to compositions from VK1, with a larger range of Cr/Cr+Al ratio (Figs. 4.8. They 4.9) and do not extend towards high Fe^{3+} compositions on Figure 4.10. BBr1 spinels are not aluminous chromites and only three analyses contain $\geq$2.4 cpu at high Cr contents; these BBr1 spinels are titaniferous-magnesian-chromites. The three analyses of titaniferous-magnesian-aluminum-chromites were collected from a single grain from sample LDD10_06. In general BBr1 spinels evolve towards the ulvöspinel-magnetite series along a path of decreasing Cr with approximately constant Al, and steadily increasing Ti and Fe^{3+} as defined by core to rim relationships (Fig. 4.13a). Most spinels analysed from samples LDD10_04 and LDD10_05 did not vary from compositions with Cr content of $\sim$1 cpu, Ti $\sim$3.2 cpu, and Fe^{3+} $\sim$6 cpu. A subset of spinels from LDD10_04 and LDD10_06 have Ti contents of 4.68 cpu (Fig. 4.13b), the highest analysed during the course of this study. A second small subset of spinels from sample LDD10_06 demonstrate both Trend 3a on Figure 4.13a, and Trend 2 on Figure 4.13b, towards ulvöspinels, but do not evolve to magnetite compositions. These trends are not developed by other BBr1 spinels.

Groundmass spinels from BBr1 samples with different paragenesis have broadly overlapping compositions. A small subset of spinels contained within the rim of ghost-lapilli define Trends 3a on Figure 4.13c and Trend 2 on Figure 4.13d. Discrete atoll spinels are predominantly contained within the lower half of Trend 2 on Figure 4.13c and trend towards higher Ti content (Fig. 4.13d).

	1	2	3	4	5	6	7	8	9	10	11	12	13	14	15	16	17
	c	c	r	c	r	c	c	r	r	c	r	c	r	c	r	c	r
	GL	GL	M	M	M	M	M	M	M	M	M	MP	MP	M	M	MA	MA
Wt% Oxide																	
SiO_2	0.2	0.1	0.4	0.4	0.4	0.4	0.2	0.2	0.2	0.4	0.3	0.3	0.2	0.2	0.2	0.3	0.3
TiO_2	6.1	7.1	13.6	14.4	14.9	14.4	7.2	6.8	6.9	6.4	6.7	9.2	8.0	13.1	13.1	12.8	13.1
Al_2O_3	6.9	5.3	4.8	4.7	4.2	4.6	5.5	5.3	5.5	4.8	4.7	5.0	4.9	5.1	5.5	5.5	5.5
Cr_2O_3	44.6	44.4	17.5	18.2	12.6	16.7	44.3	44.0	44.3	39.9	37.7	36.1	39.3	28.1	26.0	20.9	19.1
FeO_x	21.8	23.1	29.4	30.8	31.4	29.2	23.3	22.4	22.9	22.7	22.4	24.2	23.4	27.3	25.9	24.5	24.4
Fe_2O_3	7.1	7.8	27.0	23.1	27.3	23.1	6.9	7.5	7.3	12.9	15.8	13.3	11.9	14.0	17.6	23.9	24.7
MnO*	0.3	0.4	0.6	0.5	0.4	0.5	0.3	0.5	0.3	0.7	0.6	0.7	0.8	0.6	0.5	0.2	0.3
MgO	10.2	9.9	10.6	9.9	9.5	10.3	9.9	9.7	9.9	9.6	10.0	10.2	9.8	10.8	12.1	12.9	13.0
CaO	0.2	0.1	0.2	0.2	0.3	0.2	0.2	0.3	0.2	0.1	0.1	0.4	0.4	0.2	0.1	0.4	0.4
Total	97.4	98.3	103.9	102.2	100.8	99.3	97.7	96.6	97.3	97.5	98.2	99.3	98.8	99.5	101.0	101.3	100.9
Cation proportions (calculated to 32 O)																	
Si	0.1	0.0	0.1	0.1	0.1	0.1	0.1	0.0	0.0	0.1	0.1	0.1	0.1	0.1	0.1	0.1	0.1
Ti	1.3	1.5	2.7	2.9	3.1	3.0	1.5	1.4	1.4	1.3	1.4	1.9	1.7	2.7	2.6	2.5	2.6
Al	2.2	1.7	1.5	1.5	1.4	1.5	1.8	1.8	1.8	1.6	1.5	1.6	1.6	1.6	1.7	1.7	1.7
Cr	9.7	9.7	3.6	3.8	2.7	3.6	9.7	9.7	9.7	8.8	8.2	7.8	8.5	6.0	5.4	4.4	4.0
Fe(iii)	1.5	1.6	5.3	4.6	5.6	4.8	1.4	1.6	1.5	2.7	3.3	2.7	2.5	2.9	3.5	4.7	4.9
Fe(ii)	5.0	5.3	6.4	6.9	7.2	6.7	5.4	5.2	5.3	5.3	5.2	5.5	5.4	6.2	5.7	5.4	5.4
Mn	0.1	0.1	0.1	0.1	0.1	0.1	0.1	0.1	0.1	0.2	0.1	0.2	0.2	0.1	0.1	0.0	0.1
Mg	4.2	4.1	4.1	4.0	3.9	4.2	4.1	4.0	4.1	4.0	4.1	4.2	4.0	4.4	4.8	5.1	5.1
Ca	0.0	0.0	0.1	0.1	0.1	0.0	0.1	0.1	0.0	0.0	0.0	0.1	0.1	0.1	0.0	0.1	0.1
Mol % end-members																	
$MgAl_2O_4$	14.42	10.97	18.38	18.28	16.87	18.43	11.19	11.25	11.41	19.45	19.20	20.02	20.12	20.33	21.29	21.21	21.47
Mg_2TiO_4	16.24	18.55	16.59	15.42	15.56	16.89	18.92	18.29	18.36	14.85	16.00	16.13	15.21	16.99	19.14	21.24	21.31
Mn_2TiO_4	-	-	0.78	0.76	0.53	0.75	-	-	-	1.02	0.93	1.03	1.19	0.91	0.64	0.31	0.48
Fe_2TiO_4	-	-	16.01	19.86	21.87	19.26	-	-	-	0.83	0.40	6.49	4.41	15.51	12.61	10.33	10.94
$MnCr_2O_4$	1.05	1.28	-	-	-	-	0.90	1.42	0.81	-	-	-	-	-	-	-	-
$MgCr_2O_4$	3.47	1.74	-	-	-	-	1.07	2.01	1.90	-	-	-	-	-	-	-	-
$FeCr_2O_4$	59.84	59.18	22.55	23.87	16.86	22.42	59.55	59.83	60.12	54.47	51.20	48.81	53.84	37.59	33.86	27.30	24.97
Fe_3O_4	4.98	8.27	25.68	21.81	28.32	22.27	8.38	7.22	7.40	9.39	12.28	7.52	5.22	8.67	12.46	19.60	20.83

Table 4.5: Representative spinel compositions from BBr1 samples. (See Fig. 4.12 for paragenesis abbreviations. c - core; i - intermediate; r - rim.)

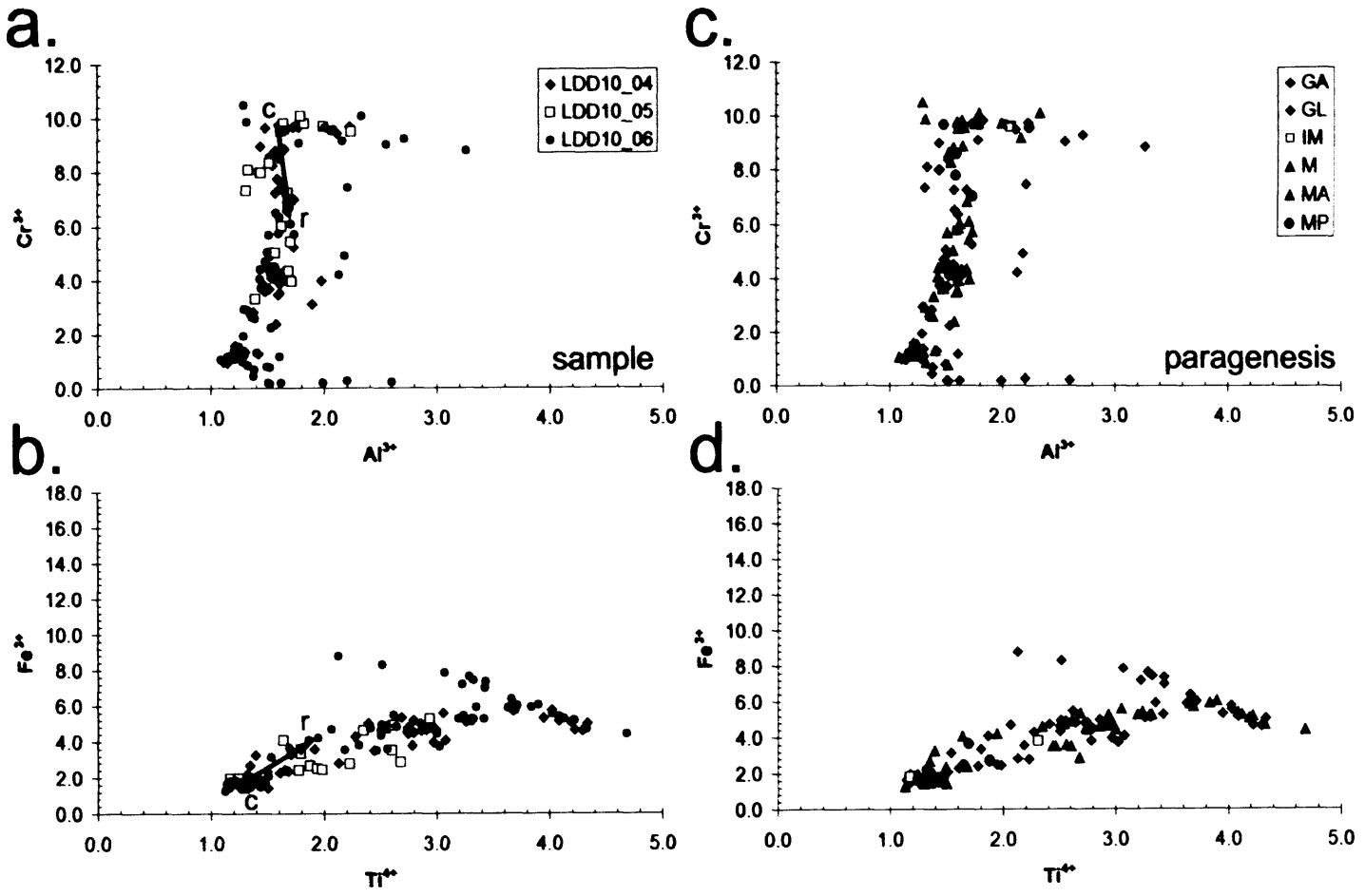

Figure 4.13: Bivariate plots of spinel compositions from BBr1. (a) and (c) Cr versus Al divided by sample and paragenesis respectively. (b) and (d) Fe^{3+} versus Ti divided by sample and paragenesis respectively (see Fig. 4.12 for paragenesis abbreviations.).

4.7.3 DVK

Figure 4.8,4.9 and 4.10 shows that spinel compositions from DVK define a broad range in both Cr/Cr+Al and Fe^{2+}/Fe^{2+}+Mg space relative to other D/K1 lithofacies. Core to rim relationships demonstrate the Magmatic Trend 1 of Mitchell (1986b). On Figure 4.10 DVK spinels cluster into two groups separated by a gap towards elevated Fe^{3+} content. Core to rim analyses from the same grain span across this gap. DVK spinels contain the highest Fe^{3+} content of 15.88 of all D/K1 spinels analysed during the course of this study. Only spinels analysed from sample LDD10_09 are aluminous chromites, and these range to an Al-content of ~4 cpu. Spinels from sample LDD16A_08 range from Al of $\leq$2.2 cpu and spinels from sampe LDD10_07 show an even lower Al content. DVK spinel compositions from sample LDD10_09 define Trend 3a and sample LDD10_07 define Trend 3b (c.f. Fig. 4.11b) on Figure 4.14a. However, one core to rim analysis from sample LDD10_07 forms a trend across the base of the plot from aluminous-ulvöspinel to ulvöspinel-magnetite, illustrated on Figure 4.14a. This is an anomaly and does not reflect the normal trend. Sample LDD10_09 hosts the rare few examples of magnetite analysed from D/K1 kimberlite during the course of this study (Fig. 4.14b). There is a gap from ulvöspinel at Fe^{3+} of 11 cpu to these magnetites at Fe^{3+} of 16 cpu.

Spinels contained within olivine phenocrysts are confined to titaniferous-magnesian-chromite compositions (Figs. 4.8d and 4.14c). Spinel inclusions in olivine macrocrysts are characterised by lower Al and Cr content ($\leq$7.5 and 1.6 cpu respectively). They define both Trend 3a and 3b on Figure 4.14c. Spinels belonging to Trend 3b are almost pure magnetites which were contained within an unusual crystalline inclusion shown in Figure 4.20. Both simple and atoll spinels discrete within the groundmass define a trend from titaniferous-magnesian-chromites towards the ulvöspinel-magnetite series, defined by core to rim relationships. This trend crosses the entire range of the D/K1 dataset. The sudden change from Trend 1 to Trend 2 on Figure 4.14d is not recorded in one single grain; core to rim relationships are confined to either Trend 1 or Trend 2.

	1 r GL	2 i GL	3 i GL	4 r GA	5 c GA	6 c MA	7 r MA	8 i MA	9 r MA	10 c GL	11 c GP	12 r GP
Wt% Oxide												
SiO_2	0.34	0.25	0.22	0.39	0.23	0.15	0.12	0.28	0.22	0.16	0.16	0.25
TiO_2	10.46	6.16	5.52	6.18	4.88	10.73	5.69	6.4	9.52	6.16	6.69	7.01
Al_2O_3	6.14	9.8	12.84	7.49	12.64	5.91	4.88	6.17	4.85	5.13	4.26	3.67
Cr_2O_3	31.07	42.79	41.17	42.96	42.22	30.96	44.89	43.63	23.47	44.76	43.56	41.53
FeO_x	22.5	20.2	19.6	20.8	19.7	24.7	22.6	22.1	26.7	21.6	21.5	22.0
Fe_2O_3	16.31	7.68	7.08	9.40	5.31	14.8	9.8	8.4	23.7	7.57	8.48	9.70
MnO*	0.40	0.28	0.22	0.82	0.18	0.45	1.44	0.22	0.86	0.44	0.44	0.69
MgO	12.86	12.18	12.48	11.31	11.59	11.13	8.7	10.42	8.5	9.77	9.77	9.33
CaO	0.11	0.06	0.05	0.07	0	0.12	0	0	0.1	0.16	0.33	0.34
Total	100.2	99.4	99.2	99.4	96.8	98.9	98.1	97.6	98.0	95.7	95.2	94.5
Cation proportions (calculated to 32 O)												
Si	0.09	0.07	0.06	0.10	0.06	0.04	0.03	0.08	0.06	0.05	0.04	0.07
Ti	2.08	1.22	1.08	1.24	0.98	2.19	1.19	1.32	2.01	1.31	1.43	1.52
Al	1.91	3.03	3.92	2.36	3.97	1.89	1.60	2.00	1.61	1.70	1.43	1.25
Cr	6.50	8.88	8.43	9.07	8.89	6.64	9.89	9.48	5.22	9.98	9.80	9.47
Fe(iii)	3.25	1.52	1.38	1.89	1.06	3.02	2.05	1.73	5.02	1.61	1.82	2.10
Fe(ii)	4.98	4.43	4.25	4.64	4.40	5.59	5.27	5.08	6.28	5.09	5.12	5.31
Mn	0.09	0.06	0.05	0.19	0.04	0.10	0.34	0.05	0.20	0.11	0.11	0.17
Mg	5.07	4.77	4.82	4.50	4.60	4.50	3.61	4.27	3.56	4.11	4.15	4.01
Ca	0.03	0.02	0.01	0.02	0.00	0.03	0.00	0.00	0.03	0.05	0.10	0.10
Mol % end-members												
$MgAl_2O_4$	23.75	19.85	25.50	15.37	25.66	23.59	19.95	24.73	19.27	11.11	18.00	15.64
Mg_2TiO_4	19.59	15.93	13.99	16.19	12.65	16.30	12.52	14.05	13.92	17.02	17.10	17.34
Mn_2TiO_4	0.56	-	-	-	-	0.64	2.11	0.32	2.05	-	0.67	1.06
Fe_2TiO_4	5.68	-	-	-	-	10.39	0.21	2.00	9.28	-	0.26	0.68
$MnCr_2O_4$	-	0.81	0.63	2.43	0.53	-	-	-	-	1.37	-	-
$MgCr_2O_4$	-	5.36	4.61	5.49	4.29	-	-	-	-	4.20	-	-
$FeCr_2O_4$	40.31	54.66	51.91	53.97	54.83	41.45	61.56	58.66	42.93	61.58	61.69	59.41
Fe_3O_4	10.11	3.39	3.36	6.55	2.04	7.63	3.64	0.23	12.55	4.72	2.29	5.89

Table 4.6: Representative spinel compositions from DVK samples. (See Fig. 4.12 for paragenesis abbreviations. c - core; i - intermedtiate; r - rim.)

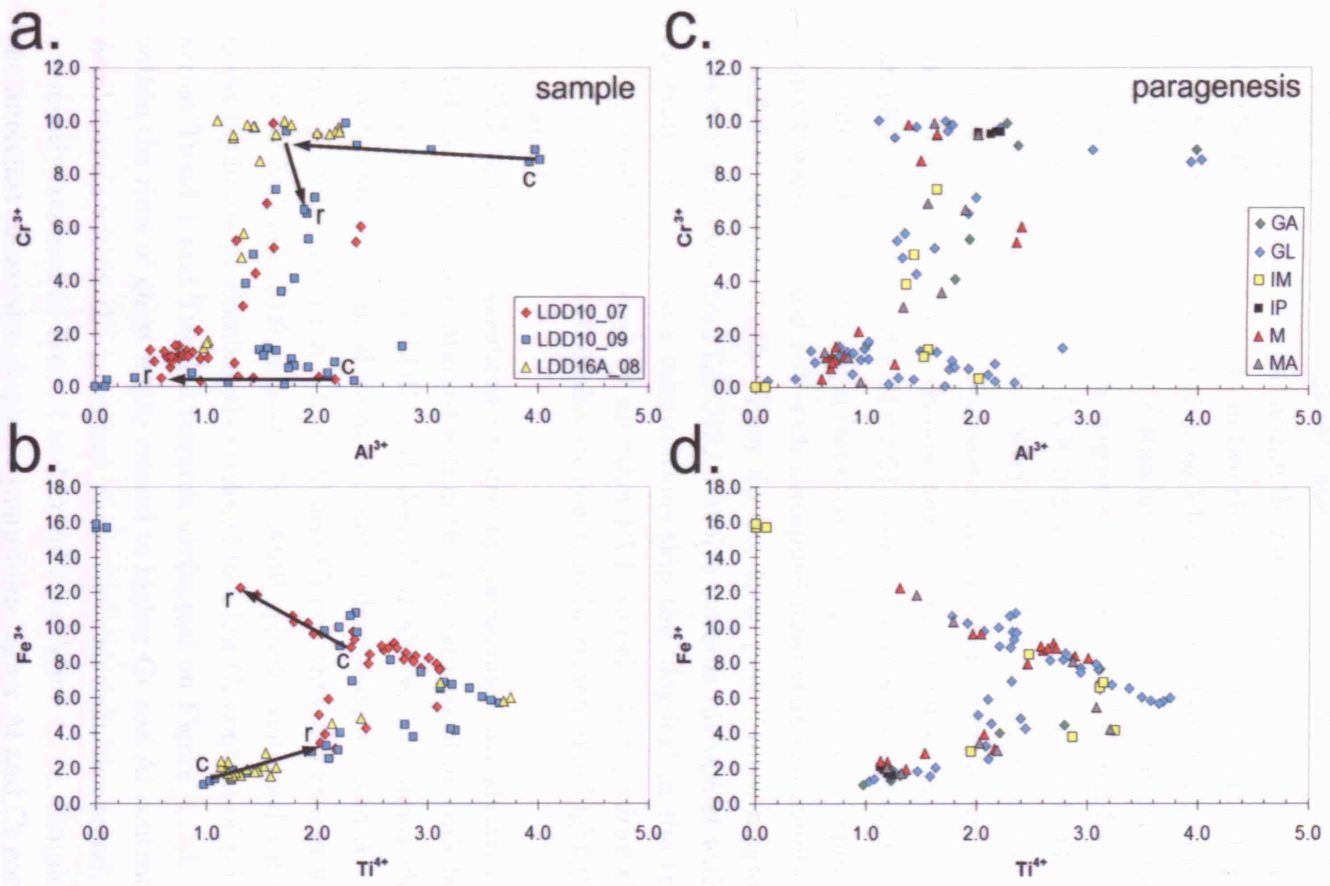

Figure 4.14: Bivariate plots of spinel compositions from DVK. (a) and (c) Cr versus Al divided by sample and paragenesis respectively. (b) and (d) Fe^{3+} versus Ti divided by sample and paragenesis respectively (see Fig. 4.12 for paragenesis abbreviations).

4.7.4 PVK

Figures 4.8,4.9 and 4.10 illustrate how spinel compositions from PVK overlap the predominant D/K1 trend although they are enriched in Mg. On Figure 4.9 spinels from the PVK lithofacies form two clusters; one predominant cluster very similar to the trend defined by spinels from VK1, with an additional group at lower Al and Cr contents. PVK spinels are aluminous chromites with an Al content up to 4.50 cpu (Fig. 4.15a). Trend 2 on Figure 4.15a is subtly different for each of the three samples analysed from the PVK lithofacies. Sample LDD12_03 contains spinels with the highest Al content (4.50 cpu) of all PVK spinels analysed. They decrease in Cr with a concomitant decrease in Al. This produces a curve for Trend 2 (c.f. Fig. 4.11b) which has a shallow angled trend relative to other D/K1 spinels. Samples LDD12_01 and LDD12_04 define a similar trend which evolves from an Al content of 2.5 and 2.0 cpu respectively (Fig. 4.15a). PVK spinel compositions evolve towards Ti- and Fe^{3+}-rich ulvöspinel-magnetite end-members along Trend 1 and 2 on Figure 4.15b. They do not form pure Ti-free magnetite. A small subset of analyses from LDD12_03 evolve towards ulvöspinel with more rapidly increasing Fe^{3+}. These compositions skip the 'dog-leg' in the trend on Figure 4.15b, which is followed by all other PVK spinels. Compositional changes from core to rim of individual grains are generally incremental as highlighted on Figures 4.15a and b.

PVK spinel compositions divided by parageneses are shown on Figure 4.15c and d. Atoll spinels contained within the groundmass of juvenile lapilli define the same trend as sample LDD12_03 described above; aluminous chromites which evolve towards ulvöspinel along a trend of decreasing Cr and Al. Simple spinels within juvenile lapilli jump from Al and Cr contents of 3.25 and 9.22 cpu respectively to 2.05 and 3.09 respectively. Atoll spinels contained within the rims of ghost lapilli are predominantly confined to a low Cr content of $\leq$5.0 cpu and cut-across Trend 1 and Trend 2 towards ulvöspinel on Figure 4.15d. Simple spinels within the rims of ghost lapilli extend to higher Cr and Al contents (Fig. 4.15a). Atoll spinels within the interclast phase show no definitive trend, although they are mostly confined to Trend 1 and Trend 2 on Figure 4.15c. Simple spinels within the interclast phase also display a jump from higher Al and Cr contents of Trend

2 to low Al and Cr on Trend 3a (Fig. 4.15c). Inclusions in olivine phenocrysts are predominantly confined to Trend 1 on Figures 4.15c and completely confined to Trend 1 on 4.15d.

	1	2	3	4	5	6	7	8	9	10	11	12	13	14	15	16	17	18
	c	i	c	r	c	r	r	i	i	c	r	c	i	i	c	c	r	c
	M	M	M	M	P	P	P	P	P	P	MA	PA	PA	PA	PA	IP	IP	IP
Wt% Oxide																		
SiO_2	0.2	0.4	0.2	0.3	0.5	0.5	0.3	0.4	0.5	0.3	0.2	0.1	0.2	0.2	0.3	0.2	0.2	0.3
TiO_2	8.3	9.0	6.5	6.7	5.7	5.7	6.5	5.3	9.5	5.2	11.1	5.4	10.1	5.0	4.7	5.3	5.2	6.6
Al_2O_3	7.4	8.1	8.0	7.5	12.7	11.4	9.3	10.8	7.1	13.5	6.2	10.1	7.6	14.0	13.1	10.0	13.7	7.6
Cr_2O_3	35.5	32.7	40.0	42.4	39.4	40.0	39.2	42.6	34.4	41.5	28.1	42.1	25.0	39.4	40.7	42.5	39.4	41.7
FeO_x	21.5	21.5	20.9	21.1	20.2	20.1	18.8	18.8	22.4	19.4	22.4	18.8	21.5	18.4	18.5	18.8	18.3	21.5
Fe_2O_3	11.7	15.9	10.5	8.0	7.4	7.6	9.1	6.5	13.8	6.2	17.0	9.1	20.6	7.3	7.1	7.8	7.2	7.9
MnO*	0.4	0.5	0.3	0.4	0.4	0.6	0.5	0.6	0.4	0.4	0.6	0.3	0.7	0.4	0.3	0.1	0.2	0.1
MgO	11.5	13.1	11.2	11.2	12.1	11.8	12.6	12.2	12.8	12.4	12.6	12.2	12.8	12.6	12.2	12.1	12.7	10.9
CaO	0.1	0.2	0.1	0.0	0.1	0.1	0.0	0.1	0.0	0.0	0.1	0.1	0.1	0.2	0.1	0.1	0.2	0.2
Total	96.4	101.3	97.7	97.7	98.3	97.9	96.4	97.4	100.9	98.8	98.3	98.3	98.6	97.5	97.1	97.0	97.0	96.9
Cation proportions (calculated to 32 O)																		
Si	0.0	0.1	0.0	0.1	0.1	0.1	0.1	0.1	0.1	0.1	0.0	0.0	0.1	0.1	0.1	0.1	0.1	0.1
Ti	1.7	1.8	1.3	1.4	1.1	1.1	1.3	1.1	1.9	1.0	2.3	1.1	2.0	1.0	0.9	1.1	1.0	1.4
Al	2.4	2.5	2.5	2.4	3.9	3.6	3.0	3.4	2.2	4.1	2.0	3.1	2.4	4.3	4.1	3.2	4.3	2.5
Cr	7.7	6.7	8.6	9.1	8.2	8.4	8.4	8.9	7.1	8.5	6.0	8.8	5.3	8.1	8.5	9.0	8.2	9.0
Fe(iii)	2.4	3.1	2.1	1.6	1.5	1.5	1.9	1.3	2.7	1.2	3.4	1.8	4.1	1.4	1.4	1.6	1.4	1.6
Fe(ii)	4.9	4.7	4.7	4.8	4.4	4.5	4.2	4.2	4.9	4.2	5.1	4.2	4.8	4.0	4.1	4.2	4.0	4.9
Mn	0.1	0.1	0.1	0.1	0.1	0.1	0.1	0.1	0.1	0.1	0.1	0.1	0.2	0.1	0.1	0.0	0.0	0.0
Mg	4.7	5.1	4.5	4.5	4.7	4.7	5.1	4.8	5.0	4.8	5.1	4.8	5.1	4.9	4.8	4.9	5.0	4.5
Ca	0.0	0.0	0.0	0.0	0.0	0.0	0.0	0.0	0.0	0.0	0.0	0.0	0.0	0.0	0.0	0.0	0.1	0.1
Mol % end-members																		
$MgAl_2O_4$	29.8	23.9	16.5	15.5	24.9	22.8	19.4	22.4	26.8	26.7	30.7	28.3	27.0	21.2	28.0	15.7	15.6	22.4
Mg_2TiO_4	14.4	23.2	17.1	17.5	14.2	14.6	17.4	14.1	17.3	13.1	17.2	13.0	12.4	14.4	13.4	17.5	16.1	15.2
Mn_2TiO_4	0.5	0.3	-	-	-	-	-	-	0.6	-	0.4	-	-	-	-	-	-	-
Fe_2TiO_4	6.4	21.0	-	-	-	-	-	-	5.0	-	9.3	-	-	-	-	-	-	-
$MnCr_2O_4$		-	0.9	1.2	1.0	1.7	1.6	1.8	-	1.1	-	1.1	1.0	0.4	0.6	0.2	0.2	1.8
$MgCr_2O_4$		-	3.9	4.0	3.4	3.9	6.0	6.7	-	4.7	-	4.9	5.9	7.5	5.2	3.2	4.9	4.1
$FeCr_2O_4$	48.0	4.4	52.7	55.3	49.3	50.0	50.2	53.9	43.8	51.8	31.7	49.8	52.0	56.2	50.5	56.1	57.5	50.3
Fe_3O_4	0.8	27.2	8.9	6.4	7.1	7.1	5.3	1.2	6.5	2.6	10.6	3.0	1.7	0.2	2.2	7.1	5.7	6.1

Table 4.7: Representative spinel compositions from PVK samples. (JL - spinel contained within the groundmass of a juvenile lapilli; JA; atoll spinel contained within the groundmass of a juvenile lapilli; P - spinel contained within the rim of a cored pelletal lapilli; c - core; i - intermedtiate; r - rim. See Fig. 4.12 for other paragenesis abbreviations.)

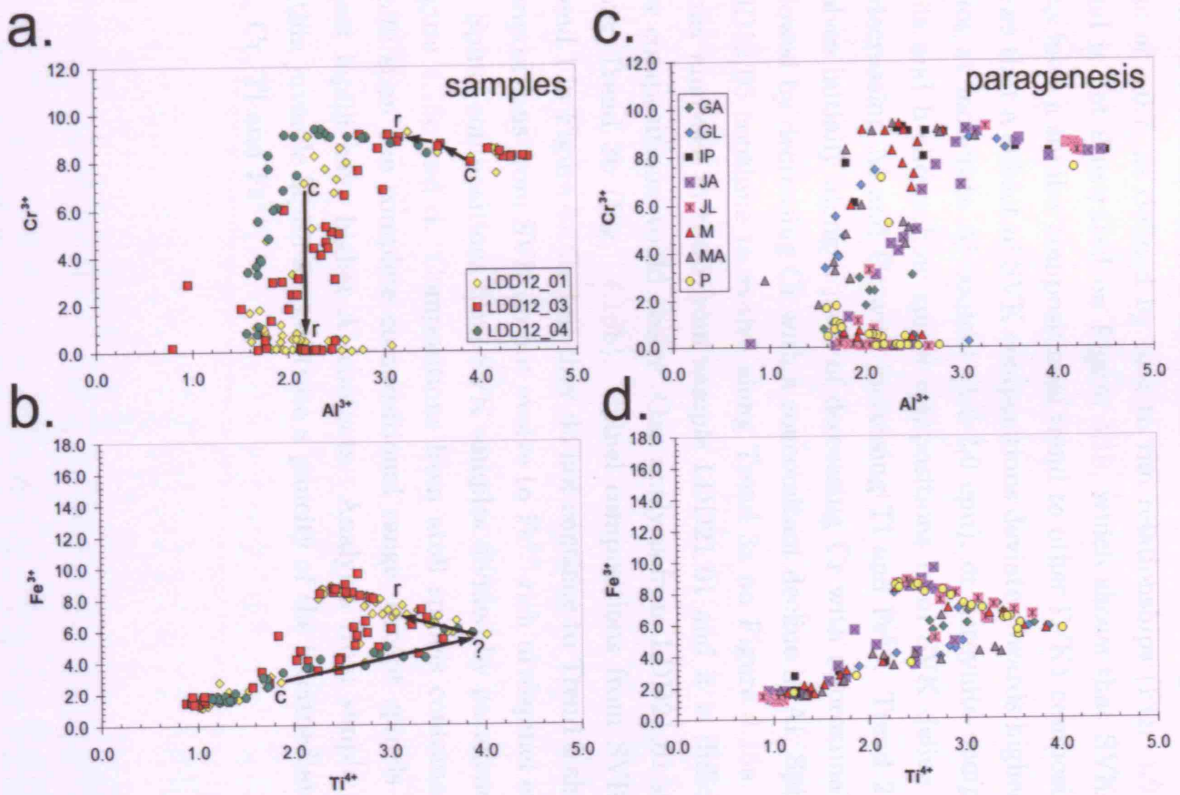

Figure 4.15: Bivariate plots of spinel compositions from PVK. (a) and (c) Cr versus Al divided by sample and paragenesis respectively. (b) and (d) Fe^{3+} versus Ti divided by sample and paragenesis respectively. (JL - spinel contained within the groundmass of a juvenile lapilli; JA; atoll spinel contained within the groundmass of a juvenile lapilli; P - spinel contained within the rim of a cored pelletal lapilli; see Fig. 4.12 for other paragenesis abbreviations.)

4.7.5 SVK

Spinels analysed from SVK define two clusters of compositions on Figure 4.9. Both clusters demonstrate an increase in Fe^{2+}/Fe^{2+}+Mg at a constant Cr/Cr+Al ratio of ~0.7, as defined by core to rim relationships (Fig. 4.9). This different trend is not illustrated on Figure 4.10, which shows that SVK spinel compositions have a similar compositional trend to other D/K1 compositions. Figure 4.9 shows that a subset of SVK compositions deviate towards higher Fe^{2+}/Fe^{2+}+Mg ratios at moderate Al content (1.0-2.0 cpu), or hercynite compositions. Figure 4.16a and b shows how spinel compositions from SVK define the D/K1 trend of decreasing Al and Cr with increasing Ti and Fe^{3+}. Trend 2 on Figure 4.16a evolves initially along a path of decreasing Cr with approximately constant Al, followed by decreasing Cr with a concomitant decline in Al. Spinels from sample LDD12_05 continue to evolve along Trend 3a on Figure 4.16a. There are fewer spinel analyses in total from sample LDD21_01 and it is difficult to determine how compositions would evolve. One analysis from LDD21_01 suggests evolution along Trend 3b (Fig. 4.16b). Spinel compositions from SVK define a strong Trend 1 in Figure 4.16b, but they do not continue to Trend 2 showing that spinel compositions from SVK do not evolve to Fe^{3+}-rich ulvöspinel endmembers.

Spinel compositions from SVK samples divided by paragenesis are shown on Figure 4.16c and d. Compositions from atoll spinels contained within juvenile lapilli span the complete compositional range, except spinels contained within ghost lapilli have higher Al contents. Analyses from simple spinels contained within juvenile lapilli demonstrate a paucity of the intermediate compositions in Al, Cr, Ti and Fe^{3+}.

	1	2	3	4	5	6	7	8	9	10	11	12	13	14	15
	c	r	c	r	c	c	i	r	c	r	c	i	i	r	c
	P	P	P	P	P	M	M	M	M	M	M	M	M	M	M
Wt% Oxide															
SiO_2	0.5	0.3	0.2	0.2	0.2	0.2	0.1	0.2	0.3	0.3	0.3	0.2	0.2	0.2	0.2
TiO_2	5.3	5.7	5.4	11.6	5.0	11.4	6.8	5.1	5.6	5.5	6.0	10.4	5.3	5.5	11.8
Al_2O_3	9.7	9.4	11.7	6.2	12.5	7.2	8.2	12.5	12.6	11.8	9.6	7.6	10.4	13.2	8.0
Cr_2O_3	38.1	42.6	40.4	16.1	42.5	25.2	42.0	41.0	39.7	41.1	43.3	30.1	43.2	41.5	25.0
FeO_x	11.3	9.4	9.0	26.3	6.9	17.1	9.3	7.6	6.8	7.0	7.5	15.0	6.7	7.2	18.2
Fe_2O_3	22.6	18.5	17.8	33.7	19.4	26.1	19.5	17.9	18.9	18.3	19.0	22.6	18.7	19.2	25.3
MnO*	0.9	0.3	0.1	0.8	0.4	0.6	0.4	0.5	0.4	0.4	0.4	0.5	0.3	0.4	0.4
MgO	9.4	12.8	13.1	5.8	12.1	10.4	12.3	12.7	12.1	12.6	12.6	12.4	12.0	12.7	12.0
CaO	0.2	0.2	0.1	0.2	0.1	0.2	0.3	0.2	0.3	0.2	0.3	0.2	0.2	0.1	0.2
Total	97.9	99.3	97.8	100.9	99.1	98.5	98.9	97.6	96.7	97.1	98.8	99.2	97.1	99.9	101.1
Cation proportions (calculated to 32 O)															
Si	0.1	0.1	0.0	0.1	0.1	0.0	0.0	0.1	0.1	0.1	0.1	0.1	0.0	0.1	0.0
Ti	1.1	1.1	1.1	2.4	1.0	2.3	1.3	1.0	1.1	1.1	1.2	2.1	1.1	1.1	2.3
Al	3.1	2.9	3.6	2.0	3.8	2.3	2.6	3.9	3.9	3.7	3.0	2.4	3.3	4.0	2.5
Cr	8.2	8.8	8.4	3.5	8.7	5.4	8.8	8.5	8.3	8.6	9.0	6.3	9.1	8.4	5.2
Fe(iii)	2.3	1.9	1.8	5.5	1.4	3.5	1.9	1.5	1.4	1.4	1.5	3.0	1.4	1.4	3.6
Fe(ii)	5.1	4.1	3.9	7.8	4.2	5.9	4.3	3.9	4.2	4.1	4.2	5.0	4.2	4.1	5.5
Mn	0.2	0.1	0.0	0.2	0.1	0.1	0.1	0.1	0.1	0.1	0.1	0.1	0.1	0.1	0.1
Mg	3.8	5.0	5.1	2.4	4.7	4.2	4.9	5.0	4.8	5.0	4.9	4.9	4.8	4.9	4.7
Ca	0.1	0.1	0.0	0.1	0.0	0.1	0.1	0.0	0.1	0.1	0.1	0.1	0.1	0.0	0.0
Mol % end-members															
$MgAl_2O_4$	19.4	25.2	19.8	24.3	25.3	25.2	29.1	17.2	25.9	24.5	19.8	29.7	26.0	30.9	24.7
Mg_2TiO_4	13.4	13.1	15.1	14.4	2.3	12.9	12.0	18.0	13.3	14.4	16.0	16.0	13.8	13.9	13.6
Mn_2TiO_4	-	-	-	-	1.2	-	0.8	-	-	-	-	0.8	-	0.6	-
Fe_2TiO_4	-	-	-	-	26.8	-	16.3	-	-	-	-	9.4	-	14.6	-
$MnCr_2O_4$	2.6	0.6	1.0	0.4	-	1.1	-	1.3	1.4	1.1	1.1	-	1.3	-	1.3
$MgCr_2O_4$	0.7	7.7	9.0	8.1	-	5.4	-	5.9	6.9	6.2	7.1	-	5.1	-	6.1
$FeCr_2O_4$	48.0	53.2	54.3	52.2	22.1	53.5	34.0	54.5	52.0	52.8	55.6	39.6	51.2	32.4	51.6
Fe_3O_4	15.9	0.3	0.8	0.6	22.3	1.9	7.8	3.1	0.5	0.9	0.4	4.6	2.6	7.6	2.6

Table 4.8: Representative spinel compositions from SVK samples (see Fig. 4.15 for paragenesis abbreviations. c - core; i - intermedtiate; r - rim).

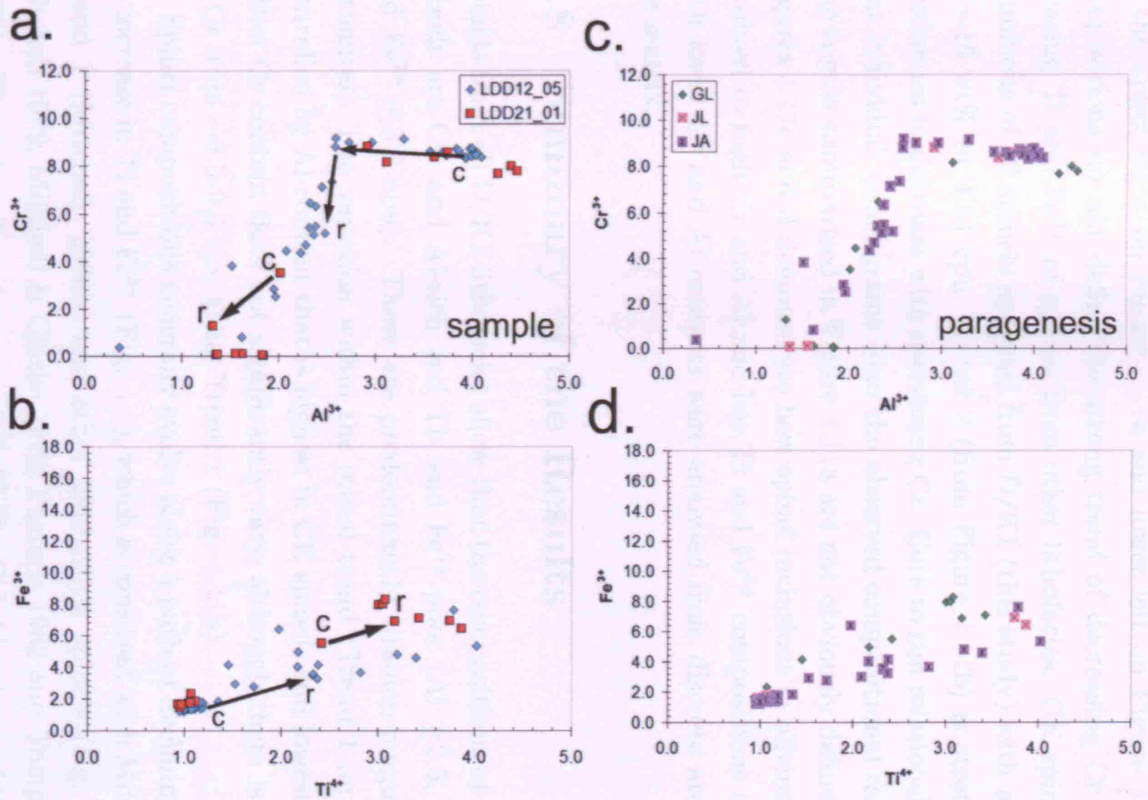

Figure 4.16: Bivariate plots of spinel compositions from SVK. (a) and (c) Cr versus Al divided by sample and paragenesis respectively. (b) and (d) Fe^{3+} versus Ti divided by sample and paragenesis respectively. (See Fig. 4.15 for paragenesis abbreviations).

4.7.6 CK

Figures 4.8,4.9, 4.10 and 4.17 demonstrate that spinels analysed from the CK lithofacies are predominantly titanian-aluminous-magnesian-chromites confined to the upper right on Figure 4.17a and lower left on Figure 4.12b. CK spinel compositions do not define the strong trend of decreasing Cr and Al with increasing Ti and Fe^{3+} of spinels from other lithofacies. CK spinels are the most aluminous of all spinels analysed from D/K1 (this study) with a maximum value of ~16 wt% or 4.51 cpu. Trend 2 (from Figure 4.11b) is stretched as both Al contiunues to decrease with decreasing Cr. Core to rim relationships demonstrate that individial spinel grains span the observed compositional range (Fig. 4.17a). The trends summarised in Figure 4.11a are not obviously defined by CK spinels. Figures 4.17c and d demonstrate how spinel inclusions in olivine phenocrysts are confined to high Cr and Al and low Ti and Fe^{3+} compositions and compositions with lower Cr and Al contents were analysed from discrete atoll spinels within the matrix.

4.8 Summary of the Results

Spinels from all D/K1 lithofacies show that the compositions of early crystallised spinels are Cr- and Al-rich and Ti- and Fe^{3+}-poor (Al $\geq$2.5, Cr $\geq$8.5, Ti $\leq$2 and Fe^{3+} $\leq$3.5 cpu). These are predominantly titanian-magnesian-aluminous-chromites. The variation within the initial trend (Trend 1 on Figure 4.11b) is controlled by Al-content that is highest in CK spinels and lowest in BBr1 spinels. Initial Cr content does not significantly vary, although there is a small increase of Cr from ~8.5-9.5 cpu along Trend 1 (Fig. 4.11b).

Spinel compositions generally evolve along a path of declining Al and Cr with an increase in Ti and Fe^{3+} (Fig. 4.8), which is consitent with Mitchell's Magmatic Trend 1 (Mitchell, 1986b) and other kimberlitic spinels (e.g. Haggerty 1975; Mitchell 1979; Mitchell & Clarke 1976; Pasteris 1982 and Tompkins & Haggerty 1985). There is a broad range of Fe/Fe^{3+}+Cr+Al values which are consistent with the observations of Barnes & Roeder (2001). However, Fe^{2+}/Fe^{2+}+Mg also demonstrates an important definition between lithofacies despite having a small

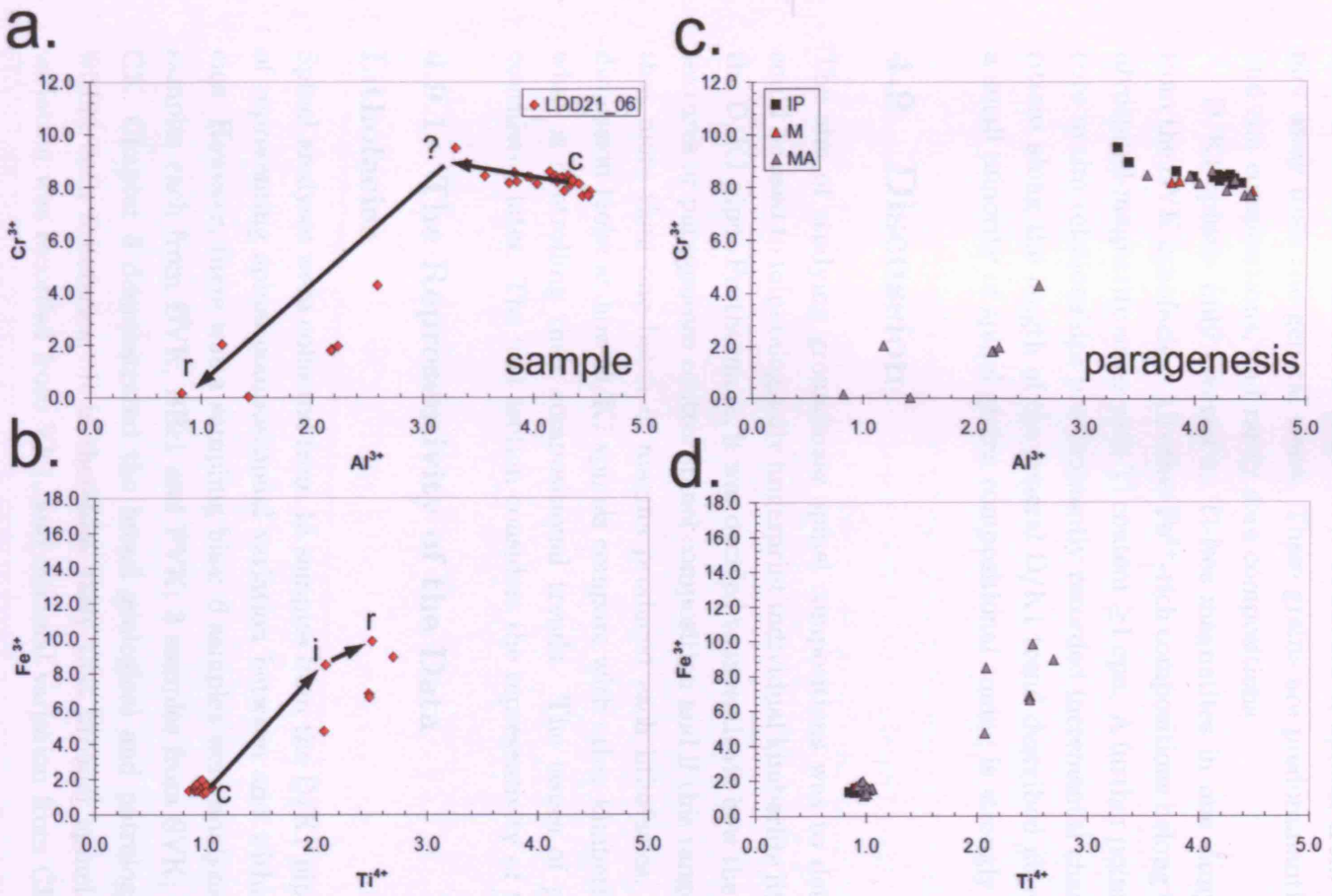

Figure 4.17: Bivariate plots of spinel compositions from CK. (a) and (c) Cr versus Al divided by sample and paragenesis respectively. (b) and (d) Fe^{3+} versus Ti divided by sample and paragenesis respectively (see Fig. 4.12 for paragenesis abbreviations).

range in values throughout. PVK spinels are the most magnesian whereas DVK spinels are the most ferric (Fig. 4.8). A subset of spinels from SVK and VK1 plot away from the general trend. These grains are predominantly intermediate and rim compositions, and rarely core compositions.

D/K1 spinels only evolved to Ti-free magnetites in one sample, LDD10_09 from the DVK lithofacies. All other Fe^{3+}-rich compositions belong to the magnesian-ulvöspinel-magnetite series with Ti content $\geq$1 cpu. A further point to note is that core to rim relationships predominantly recorded incremental changes in compositions along the length of the general D/K1 trend described above, although in a small minority of spinel grains compositional zoning is strongly developed.

4.9 Discussion

The aim of studying groundmass spinel compositions was to determine if they could be used to mineralogically fingerprint individual kimberlite lithofacies within the D/K1 pipe. Furthermore, it was decided to investigate how the range of spinel textures or parageneses control spinel composition and if this range demonstrates that more than one batch of magma produced each lithofacies. The following discussion looks at how D/K1 spinels compare with other kimberlite bodies, and what is controlling their compositional trends. The issues of paragenesis are considered later. The first section considers the representivity of the data.

4.9.1 The Representivity of the Data

Lithofacies

Spinel analyses were collected from 18 samples from the D/K1 pipe with the aim of representing spinel compositional variation between and within each lithofacies. However, there was a sampling bias: 6 samples were analysed from VK1; 3 samples each from DVK, BBr1 and PVK; 2 samples from SVK; 1 sample from CK. Chapter 3 demonstrated the broad geological and petrological variability within each lithofacies. It is therefore likely that broader spinel compositional variation was recorded from VK1, and minimal variation from CK based on the

number of samples analysed. For the purposes of the interpretation and discussion of the data below it is assumed that the samples analysed are representative of each lithofacies.

Zoning and Paragenesis

Another aim of this study was to understand how spinel compositional variability was controlled by the paragenesis of the spinel grain. Analyses from core to rims were measured where grains were large enough, but it is possible that all areas of all grains were not equally analysed and therefore the data may not be completely representative of all spinel compositions at D/K1. Every attempt was made to analyse all areas of all grains where grain size permitted. Furthermore, the dataset contains $\geq$620 analyses which is statistically large. It is assumed that from these extensive results that all compositional variations from core to rim were sampled. However, factors such as resorbtion or alteration may have removed certain compositions that may only be preserved in rare cases.

The representation of spinel paragenesis is complicated by the preservation of each spinel texture within the samples analysed. Figure 4.18 illustrates the proportion of spinel paragenesis analysed from each lithofacies. Every effort was made to measure compositions from all spinels found within each sample, therefore the proportions shown on Figure 4.18 are considered representative of the parageneses within each lithofacies. This statement has important implications on how spinel paragenesis influences spinel compositions, and is discussed below.

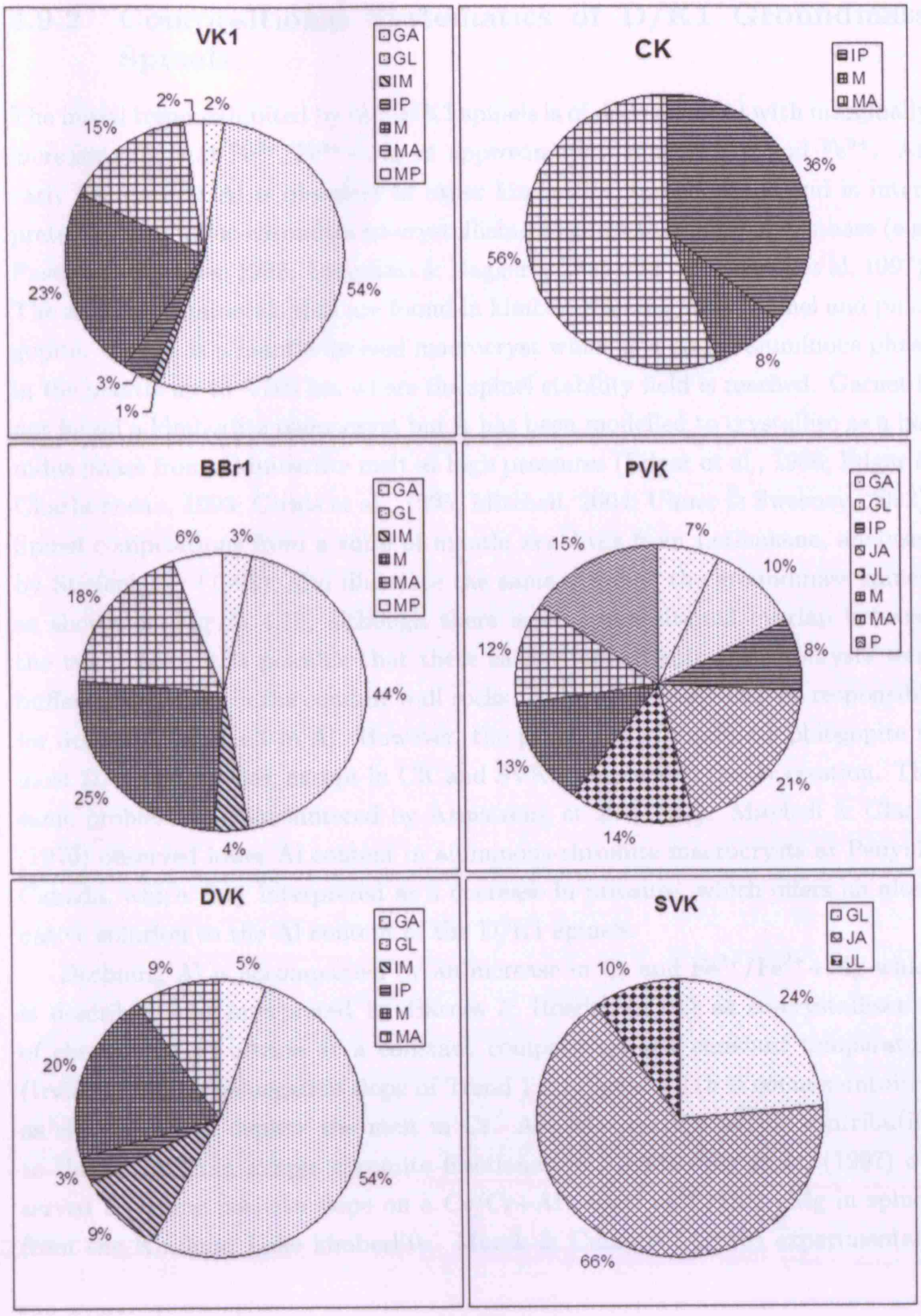

Figure 4.18: Pie charts showing the percentage of each spinel texture analysed from each lithofacies. (See Fig. 4.12 for paragenesis abbreviations.)

4.9.2 Compositional Systematics of D/K1 Groundmass Spinels

The initial trend exhibited by the D/K1 spinels is of decreasing Al with marginally increasing Cr and Fe^{2+}/Fe^{2+}+Mg at approximately constant Ti and Fe^{3+}. An early decrease in Al is observed in other kimberlitic spinel trends and is interpreted as aluminous-chromites co-crystallising with another aluminous phase (e.g. Pasteris 1983; Shee 1985; Tompkins & Haggerty 1985 and Armstrong et al. 1997). The aluminous minerals that are found in kimberlites are garnet, spinel and phlogopite. Garnet is a mantle-derived macrocryst which is a stable aluminous phase in the mantle up to ~100 km where the spinel stability field is reached. Garnet is not found a kimberlite phenocryst but it has been modelled to crystallise as a liquidus phase from a kimberlite melt at high pressures (Edgar et al., 1988; Edgar & Charbonneau, 1993; Girnis et al., 1995; Mitchell, 2004; Ulmer & Sweeney, 2002). Spinel compositions from a suite of mantle xenoliths from Letlhakane, analysed by Stiefenhofer (1993), also illustrate the same trend as the groundmass spinels as shown on Figure 4.19, although there is no compositional overlap between the two types. It is possible that these earlier formed spinel macrocrysts were buffered by garnet in the conduit wall rocks. Phlogopite could also be responsible for depleting the melt in Al. However, the paucity of groundmass phlogopite in most D/K1 lithofacies, except in CK and SVK, complicates this suggestion. The same problem was encountered by Armstrong et al. (1997). Mitchell & Clarke (1976) observed lower Al content in aluminous-chromite macrocrysts at Peuyuk, Canada, which they interpreted as a decrease in pressure, which offers an alternative solution to the Al content of the D/K1 spinels.

Declining Al is accompanied by an increase in Cr and Fe^{2+}/Fe^{2+}+Mg which is described and interpreted by Barnes & Roeder (2001) as co-crystallisation of chromite with olivine at a constant composition and constant temperature (Irvine, 1967). The negative slope of Trend 1 on Figure 4.11b is counter-intuitive as chromites will deplete the melt in Cr. Another factor must be contributing to this trend than simple chromite fractionation. Armstrong et al. (1997) observed the same positive slope on a Cr/Cr+Al versus Fe^{2+}/Fe^{2+}+Mg in spinels from the Kirkland Lake kimberlite. Murck & Campbell (1986) experimentally

determined that Cr content will increase in spinel with increasing temperature. It may therefore be suggested that the latent heat of crystallisation from the simultaneous precipitation of another phase, olivine or phlogopite for example, was capable of raising the temperature sufficiently to lower the partition coefficient of Cr in spinel. Other suggestions for the observed increase in Cr content in spinels include: (i) non-ideality within the spinel solid solution (Barnes & Roeder, 2001); (ii) a decrease in Mg-content of the melt controlled by olivine crystallisation which stabilises spinels with higher Cr at higher Fe^{2+}/Fe^{2+}+Mg ratios (Armstrong et al., 1997); (iii) a sharp decrease in Al content which forces spinels to substitute more Cr into the octahedral site (Armstrong et al., 1997); (iv) rapid non-equilibrium crystallisation of spinel as the kimberlite is making its ascent towards the surface (Armstrong et al., 1997). Compositions of spinel inclusions in olivine phenocrysts support the suggestion that co-crystallisation of olivine affects Cr content in spinels, as shown on Figure 4.17c.

The subtle distinction in Fe^{2+}/Fe^{2+}+Mg ratios between lithofacies is significant because it reflects the primitive composition of the melt and may show that spinels crystallised from melts with different starting compositions. This was also demonstrated in hypabyssal kimberlite within the root zone at the De Beers pipe by Pasteris (1983) and the Wesselton pipe by Shee (1985). They interpreted the differences in Fe^{2+}/Fe^{2+}+Mg ratios as increased degrees of fractionation from the same parent melt. Within the D/K1 pipe the trend is from CK-PVK-SVK-VK1 & BBr1-DVK in terms of increasing Fe^{2+}/Fe^{2+}+Mg ratios, suggesting that CK and PVK are the least evolved melts. This implies that these lithofacies were erupted first if this was a simple, one-stage process of a single fractionating melt. This is not consistent with the geological observations and emplacement model proposed in Section 7.4.1 which suggests VK1 and DVK were erupted before PVK and SVK. However, at Wesselton Shee (1985) showed that a compositionally more evolved sill is transected by a compositionally more primitive pipe. Therefore, the degree of melt evolution based on Fe^{2+}/Fe^{2+}+Mg ratios cannot be used to place the emplacement sequence of the lithofacies within the D/K1 pipe.

The intermediate compositions of D/K1 spinels evolve along a path of decreasing Cr with increasing Ti, Fe^{2+} and Fe^{3+} at approximately constant Al and Mg content (Fig. 4.8). This is the standard 'kimberlitic trend', as it was termed by

Barnes & Roeder (2001), who interpreted it as a crystallisation trend caused by spinel co-precipitating from a melt with olivine. Olivine crystallisation depletes the melt in Mg and to a lesser extent Cr and enriches it in Fe and Ti. This forces spinel compositions towards ulvöspinel endmembers. Cr in kimberlites is predominantly fractionated into chromites at an early stage during groundmass crystallisation (Tompkins & Haggerty, 1985), which will also increase the concentration of Fe and Ti in the residual melt. Iron is preferentially partioned into spinel with falling temperature (Irvine, 1965). Armstrong et al. (1997) suggested that the kimberlitic trend is also influenced by an increase in the ferrous iron component from the oxidation of ferric iron, which pushes compositions towards ulvöspinel-magnetite endmembers as illustrated by Trend 2 on Figure 4.11a.

The more evolved spinel compositions are characterised by the Ti- and Fe^{3+}-rich ulvöspinel-magnetite series. Very few grains from D/K1 proceed to Ti-free magnetite, which is also a characteristic of the Kirkland Lake kimberlite (Armstrong et al., 1997), the fissile micaceous kimberlite at Tunraq (Mitchell, 1979), and 'phase C' spinels at Peuyuk (Mitchell & Clarke, 1976). The distinctive 'kick' in the trend shown on Figure 4.11a is a consequence of crystallisation of Cr-poor magnetites. Brod et al. (2005) interpreted it as an increase in the magnetite component at the expense of the ulvöspinel component as Al and Cr become unavailable. Within spinels from the D/K1 kimberlite pipe this strong inflection towards magnetite with decreasing Ti-content may be accentuated by co-crystallisation with perovskite. A similar interpretation was made by Shee (1985) for spinels from the Wesselton kimberlite. Shee (1985) also attributed falling Ti content to a decrease in pressure, suggesting that Ti-free magnetite crystallised at lower pressures possibly after the kimberlite had been emplaced. The more evolved spinel compositions demonstrate two distinct trends in the field of Cr versus Al, illustrated on Figure 4.11b. Trend 3a increases in Al, and Trend 3b decreases in Al at very low Cr content. Spinels which define Trend 3a are more deficient in Fe^{3+} than spinels which define Trend 3b (e.g Fig. 4.14a and b). This indicates that Al is preferentially substituting into the spinel at the expense of Fe^{3+}, which may be a feature of localised zones in the melt with lower fO_2. Alternatively, increasing Al (and Mg) at low Cr content may indicate a new generation of phlogopite crystallisation (Pasteris, 1983).

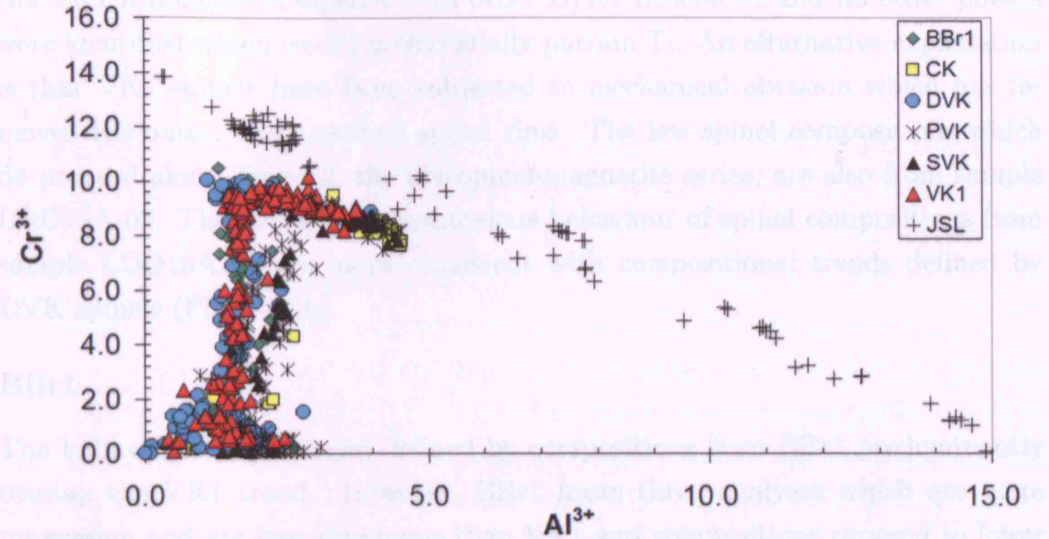

Figure 4.19: Cr versus Al for D/K1 spinels with spinel compositions from the suite of mantle xenoliths at Letlhakane (JSL) (Stiefenhofer, 1993).

The Letlhakane D/K1 groundmass spinels are notably Ti-rich and very few analyses had $\leq$5 wt% TiO_2. The groundmass assemblage was dominated by perovksite which also suggests a strong influence of Ti on the Letlhakane kimberlite. It is possible that the liquidus phases were continually saturated in Ti and therefore Ti-free magnetite was never stabilised on the liquidus.

4.9.3 Lithofacies-specific Compositional Systematics

VK1

VK1 spinel compositions cover the full extent of the compositional range defined by all D/K1 spinels (Fig. 4.9) to a Cr/Cr+Al ratio of ~0.15. Figure 4.12a shows that the few grains which evolved to lower Cr/Cr+Al ratios were analysed from sample LDD16A_02. Figure 4.12b shows that most VK1 spinel compositions plot along Trend 1 but not Trend 2. The lack of Trend 2 on Figure 4.12b is ambiguous because it suggests that another phase was preferentially partioning Ti from the melt over spinel. However, perovskite has a similar abundance in

the VK1 lithofacies compared with other D/K1 lithofacies and no other phases were identified which would preferentially partion Ti. An alternative explanation is that VK1 spinels have been subjected to mechanical abrasion which has removed the outer, more evolved spinel rims. The few spinel compositions which do proceed along Trend 2, the ulvöspinel-magnetite series, are also from sample LDD16A_02. The consistently anomalous behaviour of spinel compositions from sample LDD16A_02 are more consistent with compositional trends defined by DVK spinels (Fig. 4.14b).

BBr1

The bulk of the spinel trend defined by compositions from BBr1 predominantly overlap the VK1 trend. However, BBr1 hosts three analyses which are more magnesian and are less aluminous than VK1 and compositions proceed to lower Cr/Cr+Al ratios (Fig. 4.9). Lower Al compositions suggest that either spinels crystallised from a melt initially depleted in Al, or these earlier spinel compositions became unstable in later, more evolved residual liquids and have been resorbed. The latter argument may be related to the amount of country rock fragments entrained within the BBr1 kimberlite, which can produce chemical disequilibrium through reactions between the melt and lithic clast (Pasteris, 1983). However, country rock fragments are not altered in this lithofacies and it is unlikely that any reactions between melt and lithic took place. Therefore this mechanism cannot explain the observed depletion in Al. The three analyses with elevated Mg content are all from the same grain which is possibly exotic to the BBr1 lithofacies and probably a macrocryst. Spinels from sample LDD10_06 are distinct in that they evolve to the lowest Cr/Cr+Al ratios ($\leq$1.0) and produce a strong Trend 3a (c.f. Figure 4.11b). This trend is similar to that defined by spinels from the DVK lithofacies (Fig. 4.9). Furthermore, spinel compositions from LDD10_06 evolve along Trend 2 (ulvöspinel-magnetite series) whereas other BBr1 spinels do not. This trend is also strongly defined by spinels from the DVK lithofacies. This is an important observation as it shows that this basalt-rich breccia contains grains derived from both VK1 and DVK. This is consistent with the observations of bedding within this unit made in Section 3.5 and implies mixing between lithofacies after emplacement.

DVK

Spinel compositions from DVK samples show the widest compositional spread across Fe^{2+}/Fe^{2+}+Mg ratios. DVK spinels do not evolve to the very low Cr contents observed in other D/K1 lithofacies, which may be related to an elevated temperature of this unit compared with other lithofacies. This is consistent with the interpretations made in Chapter 3 that DVK is a welded volcaniclastic kimberlite. As discussed above Cr will partition more easily into spinel at higher temperatures (Murck & Campbell, 1986). In general DVK spinels evolve from a lower Al content, similar to BBr1 spinels. Only three analyses have Al contents $\geq$2.5 cpu from sample LDD10_09. Excluding these three samples the similarity of this trend with BBr1 spinels may suggest the kimberlite from the basalt breccia unit is more associated with DVK than VK1, which develops the interpretations made in the section above (Section 4.9.3).

Spinel compositional trends are divided at low Cr content and demonstrate both Trend 3a and Trend 3b on Figure 4.14b. Spinels along Trend 3a have higher Ti contents and lower Fe^{3+} contents than those along Trend 3b. This indicates that localised deficiencies in Fe^{3+} in the melt were compensated by increased substitution of Al. Three analyses from DVK are Ti-free magnetites. These grains were located within an unusual crystalline inclusion contained in an olivine macrocryst (Fig. 4.20), and are interpreted as exotic compositions because magnetites were not observed in any other D/K1 sample. However, the compositions are not consistent with a mantle-derived olivine macrocryst.

PVK

PVK spinel compositions are slightly enriched in Al and Mg which probably derives from the composition of the parent melt (e.g. Pasteris 1983). Spinel compositions from samples LDD12_01 and LDD12_03 define a trend of decreasing Cr with decreasing Al. This suggests that the influence of a co-crystallising aluminous phase was less in PVK than in VK1 and DVK because spinel compositions from PVK continue to partition Al as compositions evolve towards magnesian-ulvöspinel. An alternative explanation is that the co-crystallising Al phase became a stable liquidus phase at lower temperatures (at lower Mg content Pasteris

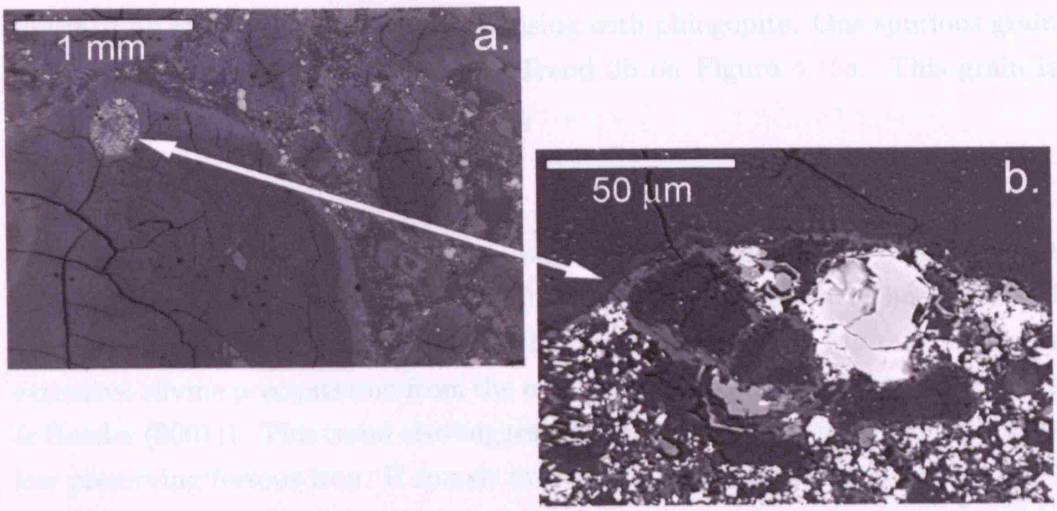

Figure 4.20: Electron backscatter images of a large, crystalline and very unusual inclusion in an olivine macrocryst from LDD10_09. (The lower image (b) is an enlargement of the upper image (a).)

1983) for the VK1 and DVK magmas. Mg has preferentially partitioned into the groundmass spinels of PVK over Fe^{2+} and Fe^{3+}. Elevated Mg content may be a result of higher temperature during spinel crystallisation (Pasteris, 1983), or a decrease in the amount of olivine precipitating from the melt (Agee et al., 1982). Petrographic descriptions of PVK in Section 3.5 indicate that macrocrystal olivines are more abundant than phenocrysts so a decrease in olivine precipitation may be plausible. It is difficult to constrain crystallisation temperatures in kimberlite melts for the reasons discussed in Section 4.9.5.

A subset of spinel compositions from PVK samples define a trend which cuts across the distinctive kink between Trends 1 and 2 on Figure 4.15b controlled by more rapidly increasing Fe^{3+}. Fe^{3+} is generally associated with higher fO_2 (e.g. Mitchell & Clarke (1976); Pasteris (1983) and Armstrong et al. (1997)), therefore these unusual spinel compositions may represent localised zones of higher fO_2 perhaps caused by the entrainment of more oxidised crustal fragments.

More evolved spinels from PVK proceed along Trend 3a on Figure 4.15a and do not evolve to the higher Fe^{3+} compositions on Figure 4.15b. As discussed above, this late stage enrichment in Al prevents significant partitioning of Fe^{3+}

and may be related to spinel co-crystallising with phlogopite. One spurious grain from sample LDD12_03 evolves along Trend 3b on Figure 4.15a. This grain is discussed below in terms of paragenesis.

SVK

Spinel compositions from SVK evolve along a path of increasing Fe^{2+}/Fe^{2+}+Mg at an approximately constant Cr/Cr+Al; from aluminous chromite to hercynite and ulvöspinel, but not towards magnetite. Increasing Fe^{2+}/Fe^{2+}+Mg ratio indicates extensive olivine precipitation from the melt which enriches it in Fe^{2+} (e.g. Barnes & Roeder (2001)). This trend also suggests the oxidation state remained relatively low preserving ferrous iron. If spinels precipitated from a melt saturated in Fe^{2+} and deficient in Fe^{3+} they will be confined to compositions represented within the right hand side within the base of the spinel prism (Fig. 4.8d.). This trend is similar to that described by Mitchell (1979) for the massive micaceous kimberlite at Tunraq, and is more consistent with the early compositions from Mitchell's Trend 2 (Mitchell, 1986b). Mitchell (1986b) suggests this trend is the result of extensive crystallisation of groundmass phlogopite prior to the crystallisation of most groundmass spinels. SVK contains phlogopite as an interclast phase located between clasts as an amorphous phase (Section 3.5). This could support Mitchell's hypothesis but it assumes that phlogopite is a primary groundmass phase, which is not clear from the petrography.

CK

Spinel compositions from CK define the smallest compositional range of all the lithofacies. This range is characterised by high Al and Mg and low Fe^{2+}, Fe^{3+} and Ti abundance. Therefore compositions predominantly cluster in the 'early formed' titanian-aluminous-magnesian-chromite endmembers. Very few spinels evolved towards ulvöspinel-magnetite endmembers, suggesting that they crystallised from a melt which did not fractionate the significant amount of olivine required to drive spinel compositions towards ulvöspinel endmembers. This is not supported by petrographic observations as CK contains abundant olivine

phenocrysts (Section 3.5). Alternatively, the melt from which these spinels crystallised had elevated Al content, but this is not supported by bulk rock geochemistry (Chapter 6). The set of spinel compositions from CK predominantly define a small group marginally separated from most other D/K1 compositions (Fig. 4.9). It is possible that these spinels are macrocrystic and are therefore not primary groundmass phases. Mitchell & Clarke (1976) provide another explanation for the same trend in a subset of Peuyuk spinels; they suggested that a late-stage carbonate-rich fluid depleted the residual silicate melt in volatiles that precluded reactions between the early formed spinels and residual liquids. Groundmass carbonate is more abundant within the CK lithofacies than other D/K1 lithofacies, and therefore this mechanism is a possible explanation for the primitive nature of CK spinels.

4.9.4 Paragenesis-specific Compositional Systematics

Within the D/K1 spinel dataset there is no clear separation of compositional trend according to spinel paragenesis, except for spinel inclusions in olivine phenocrysts. This observation is important as it implies that spinel crystallisation and growth were taking place over a wide range of changing melt compositions and conditions. There are compositional trends that occur within individual lithofacies. This is very important as it supports the suggestion that some lithofacies are composed of more than one batch of magma.

Atoll Spinels

The various proposed origins of atoll spinels were outlined in Section 4.3.1 and can be summarised as (i) the result of a resorbed phase of a less stable spinel composition, or (ii) a primary growth feature. Atoll spinels occur as discrete grains within the interclast matrix of diatreme facies volcaniclastic kimberlite at D/K1 (Fig. 4.4d, e, and f), as well within the groundmass of the coherent kimberlite (CK) and the groundmass of juvenile lapilli (Fig. 4.4a, b, and c). The presence of groundmass atolls in volcaniclastic kimberlite contradicts the statement of Mitchell (1986b) who claims that atoll spinels are a feature of hypabyssal kimberlite associated with root zones, dykes and sills. Armstrong et al. (1997)

referred to atoll spinels within diatreme facies at the Kirkland Lake kimberlite as "rarely occurring", but do not provide a petrological explanation for this observation. The cores of groundmass atoll spinels are more magnesian than their 'simple' spinel counterparts suggesting that they crystallised from more primitive melt compositions. This is consistent with the compositional trends defined by Mitchell & Clarke (1976) where atoll cores are early formed TIMACs and rims evolve towards ulvöspinel and magnetite. The rims of atoll spinels at D/K1 were frequently ≤ 2 μm which made analysis of their compositions very difficult, perhaps explaining the absence of magnetite from these compositional trends. These very thin rims appear to have been replaced by titanite.

Groundmass atolls are occasionally partly enclosed by perovskite (Fig. 5.2). This was also observed by Chakhmouradian & Mitchell (2000) who interpreted it as the result of co-crystallisation of perovskite with the more evolved magnetite atoll rim. Figure 4.4e shows a very interesting relationship between an atoll spinel within the interclast matrix of sample LDD10_06 (BBr1). The spinel core is only partially surrounded by an atoll rim. The rest of the grain is surrounded by phlogopite microlites suggesting they grew simultaneously with the atoll spinel rim.

The largest and most well preserved atoll spinels are contained within the groundmass of juvenile lapilli from sample LDD12_03 of the PVK lithofacies (Fig. 4.4b and c). Figure 4.21 illustrates two contrasting compositional trends from atoll spinels contained within two individual juvenile lapilli. In JL01 spinels evolve along Trend 3b compared with JL02 which contains spinels that evolve along Trend 3a (Fig. 4.21). Every attempt was made to analyse all areas of all grains, so it is assumed that these results are representative of the real trends. This is a significant observation because it suggests that the PVK lithofacies contains spinels that were derived from at least two batches of magma. The juvenile lapilli from which these spinel analyses were collected are both rounded (Fig. 4.21) indicating that they were plastic when incorporated into the kimberlite. The clasts are interpreted as droplets of an earlier, crystallised, but still molten magma. This pattern of constrasting spinel compositional trends was also observed in the DVK lithofacies defined by simple spinels contained within the rims of ghost lapilli (Fig. 4.14c) and in spinels contained within juvenile lapilli from

the SVK lithofacies (Fig. 4.16c). They show that these lithofacies were also built up from more than one batch of magma.

Spinel Inclusions in Olivine

Spinel inclusions in olivine define two trends based on whether they are included in an olivine phenocryst or an olivine macrocryst. Inclusions in phenocrysts are predominantly confined to TIMAC compositions whereas inclusions in macrocrysts include ulvöspinel and magnetite compositions. It is unusual that spinel inclusions in olivine macrocrysts are of such evolved compositions; in general they are of more primitive compositions e.g. Barnes & Roeder (2001) so this is an important observation. It is possible that the more primitive spinel inclusions in olivine phenocrysts have been buffered from reacting with more evolved kimberlite fluids, but inclusions contained within olivine macrocrysts have not. Olivine macrocrysts are frequently fractured, which could have provided a path for late stage kimberlitic fluids (Fe^{3+}- and Ti-rich) and post-emplacement meteoric fluids to make contact with the included spinels (e.g. Fig. 3.11a).

Discrete Groundmass Spinels

Figure 4.18 presents the proportions of spinel textures analysed from each lithofacies (see Section 4.9.1). The proportions define a paucity of discrete groundmass spinels in all lithofacies except CK. Walters et al. (2006) suggested that the lack of spinels as discrete grains within the interclast phase is a good indication that volcaniclastic kimberlites contain very little ash-sized material in the original clastic deposit shortly after eruption. Subsequent hydrothermal alteration has infilled the pore spaces solidifying the rock and producing the interclast phase rich in serpentine and microlitic diopside (Stripp et al., 2006). Section 3.5 characterises all D/K1 lithofacies as fragmental volcaniclastic kimberlites except CK, which has a more coherent, homogeneous texture. Therefore, the proportion of spinels as discrete interclast or groundmass grains is an indicator of the processes that occurred during eruption.

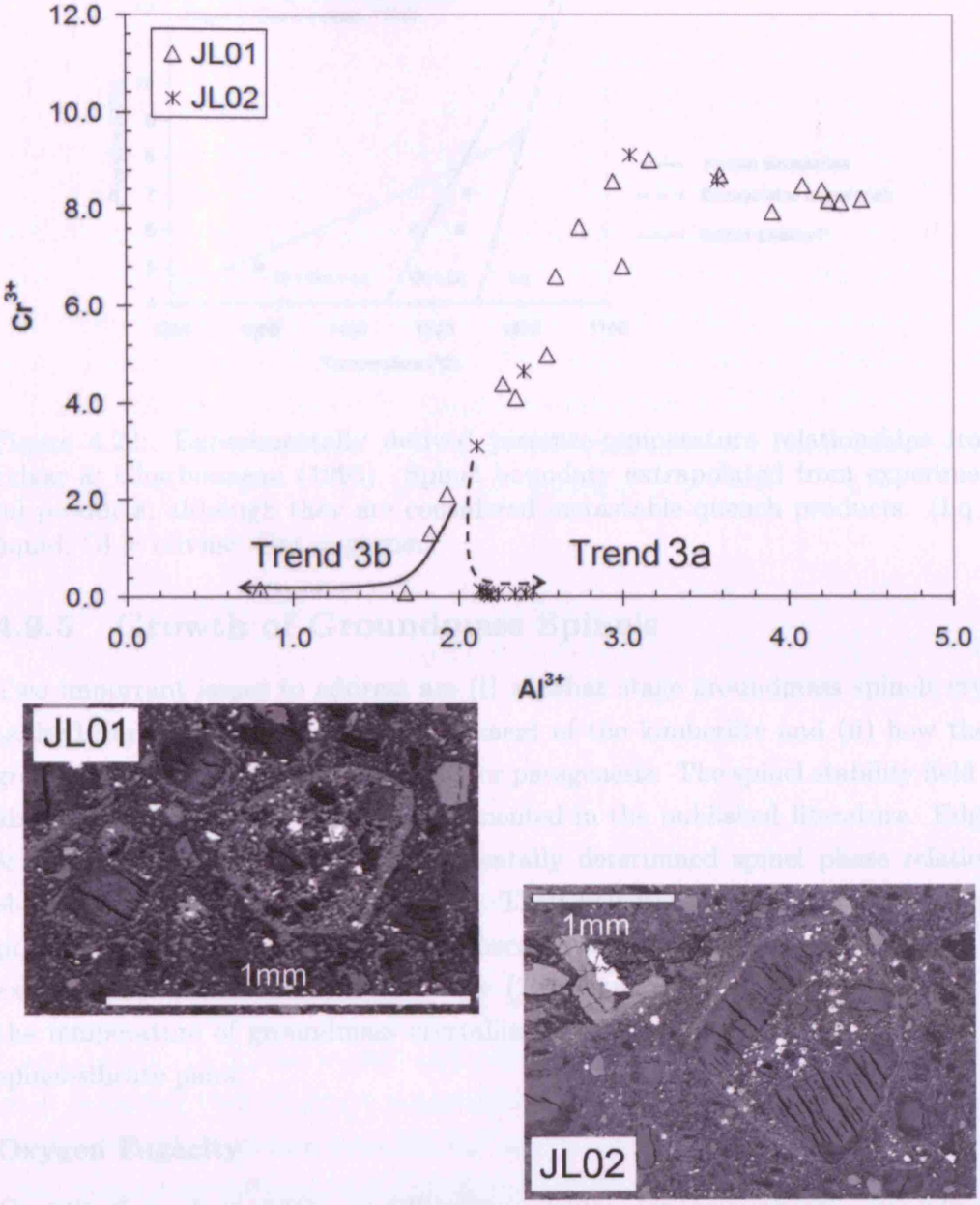

Figure 4.21: Bivariate plot of Al versus Cr for atoll spinels contained within two individual juvenile lapilli (backscatter electron image insets) from sample LDD12_03. Two contrasting compositional trends are illustrated.

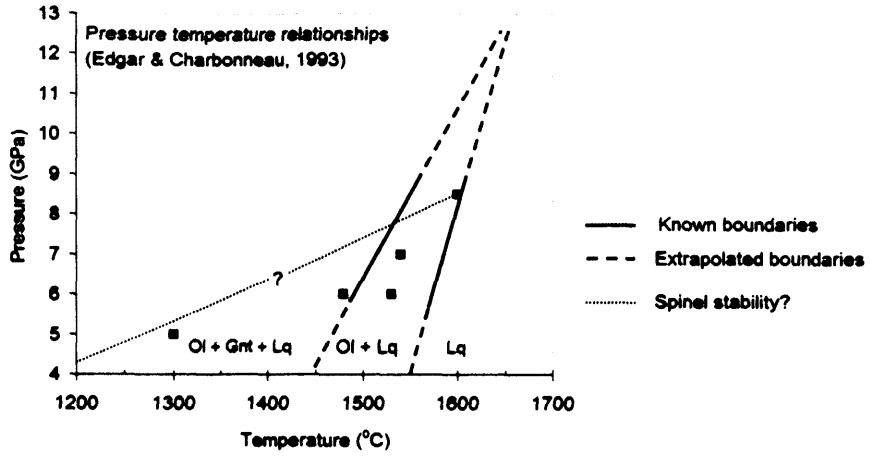

Figure 4.22: Experimentally derived pressure-temperature relationships from Edgar & Charbonneau (1993). Spinel boundary extrapolated from experimental products, although they are considered metastable quench products. (Lq = liquid; Ol = olivine; Gnt = garnet)

4.9.5 Growth of Groundmass Spinels

Two important issues to address are (i) at what stage groundmass spinels crystallised during ascent and/or emplacement of the kimberlite and (ii) how their growth varied between lithofacies and/or paragenesis. The spinel stability field in kimberlites is currently not well documented in the published literature. Edgar & Charbonneau (1993) have experimentally determined spinel phase relationships that are shown in Figure 4.22. They believed, however, that these are probably metastable quench products because they occur unsystematically in the experimental runs. Mitchell & Clarke (1976) and Mitchell (1986b) calculated the temperature of groundmass crystallisation between 600-800°C at fO_2 using spinel-silicate pairs.

Oxygen Fugacity

Quantitative values of fO_2 are difficult to calculate for the kimberlite groundmass because silicate-oxide pairs are frequently altered (Pasteris, 1983) and therefore it is not certain if they were in equilibrium (Shee, 1985). This is also true for Letlhakane spinels, with the exception of 16 analyses of spinel inclusions in olivine

phenocrysts collected from the CK lithofacies. fO_2 was determined using the oxygen barometer of Ballhaus et al. (1991) for spinel-olivine pairs. The application of this oxygen barometer assumes that: (i) the iron content of the olivine is $\leq$0.15 cpu, therefore it is only applicable to upper mantle assemblages; (ii) orthopyroxene is required to buffer silica activity, even though it is not present in equation 4.1; (iii) spinels crystallised above ~800°C, below which spinels become ordered and the size differences between trivalent cations produces non-ideality which is difficult to correct (Ballhaus et al., 1991). Points (ii) and (iii) are not consistent with groundmass spinels at D/K1, however the geobarometer is used to qualitatively assess fO_2 conditions. The oxygen barometer of Ballhaus et al. (1991) is defined in Equation 4.1 using a temperature of 525 K (~800°C) which is just within the boundaries of Mitchell's temperature of groundmass crystallisation (Mitchell, 1986b). The results are presented in Figures 4.23 and 4.24.

$$\Delta log\left(fO_2\right)^{(FMQ)} = 0.27 + 2505/T - 400P/T - 6log\left(X_{Fe}^{olv}\right)$$
$$-3200\left(1 - X_{Fe}^{olv}\right)^2/T + 2log\left(X_{Fe^{2+}}^{sp}\right) + 4log\left(X_{Fe^{3+}}^{sp}\right) + 2630\left(X_{Al}^{sp}\right)^2/T \quad (4.1)$$

Where: P - (GPa)
T - K
$X_{Fe^{3+}}^{sp} = Fe^{3+}/\Sigma Fe$
$X_{Al}^{sp} = Al/\Sigma R^{3+}$
$X_{Fe}^{olv} = Fe^{2+}/(Fe^{2+}/Mg)$ in olivine
$X_{Fe^{2+}}^{sp} = Fe^{2+}/(Fe^{2+}/Mg)$ in spinel

Figure 4.23 shows that fO_2 values for the spinel inclusions in olivine phenocrysts from D/K1 are slightly reduced relative to the FMQ buffer (Fig. 4.23). It is predicted that as spinel compositions evolve towards ulvöspinel and magnetite the fO_2 increases towards the magnetite-hematite buffer because these compositions crystallised later (based on petrographic relationships) at shallower levels in the upper mantle and lower crust. This same trend of increasing fO_2 with spinel crystallisation occurred in spinels from Wesselton (Shee, 1985). The range in fO_2 defined by the D/K1 spinel dataset is comparatively small. Mitchell & Clarke (1976) suggested that changing spinel compositions reflect decreasing

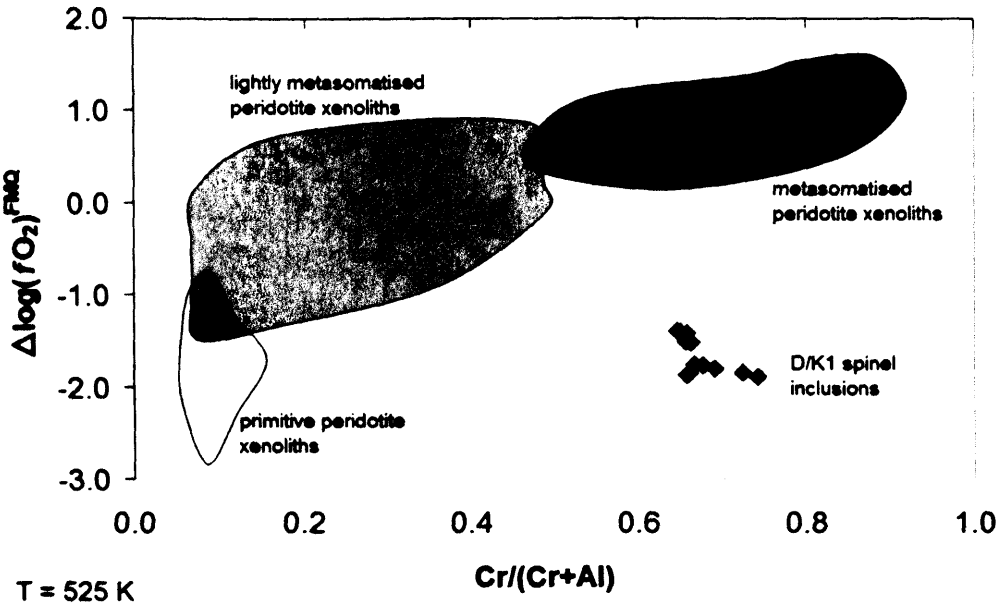

Figure 4.23: Results of calculated oxygen fugacity of spinel inclusions in olivine using the oxygen barometer of Ballhaus et al. (1991) versus Cr/Cr+Al. Representative fields for spinel lherzolite and harzburgite xenoliths are also shown for comparison. The mantle xenoliths illustrate increasing fO_2 with the degree of metasomatism (Ballhaus et al., 1991).

fO_2 as a direct result of falling temperatures along the quartz-fayalite-magnetite QFM buffer.

Pasteris (1983) used $Fe^{2+}/Fe^{2+}+Fe^{3+}$ versus $Fe^{2+}/Fe^{2+}+Mg$ as an alternative way to qualitatively present the relative variability in fO_2 within a single kimberlite body. Low $Fe^{2+}/Fe^{2+}+Fe^{3+}$ relates to high fO_2. Figure 4.24 shows that spinels from SVK crystallised under the lowest fO_2 and spinels from DVK crystallised under the highest fO_2. Shee (1985) related changes in the iron content of groundmass spinels to changes in the prevailing fO_2 which are related to the emplacement of the kimberlite. As the kimberlite approaches the surface volatiles will begin to exsolve and degas Clement (1975); Dawson (1971). Kimberlite magmas are assumed to be rich in CO_2 (e.g. Dawson 1980), which when degassed will dissociate and produce free oxygen capable of increasing the oxidation state of the melt (Shee, 1985). The compositional trends defined by the D/K1 spinel dataset (this study) are consistent with Shee's model. Shee's (op. cit.) conclu-

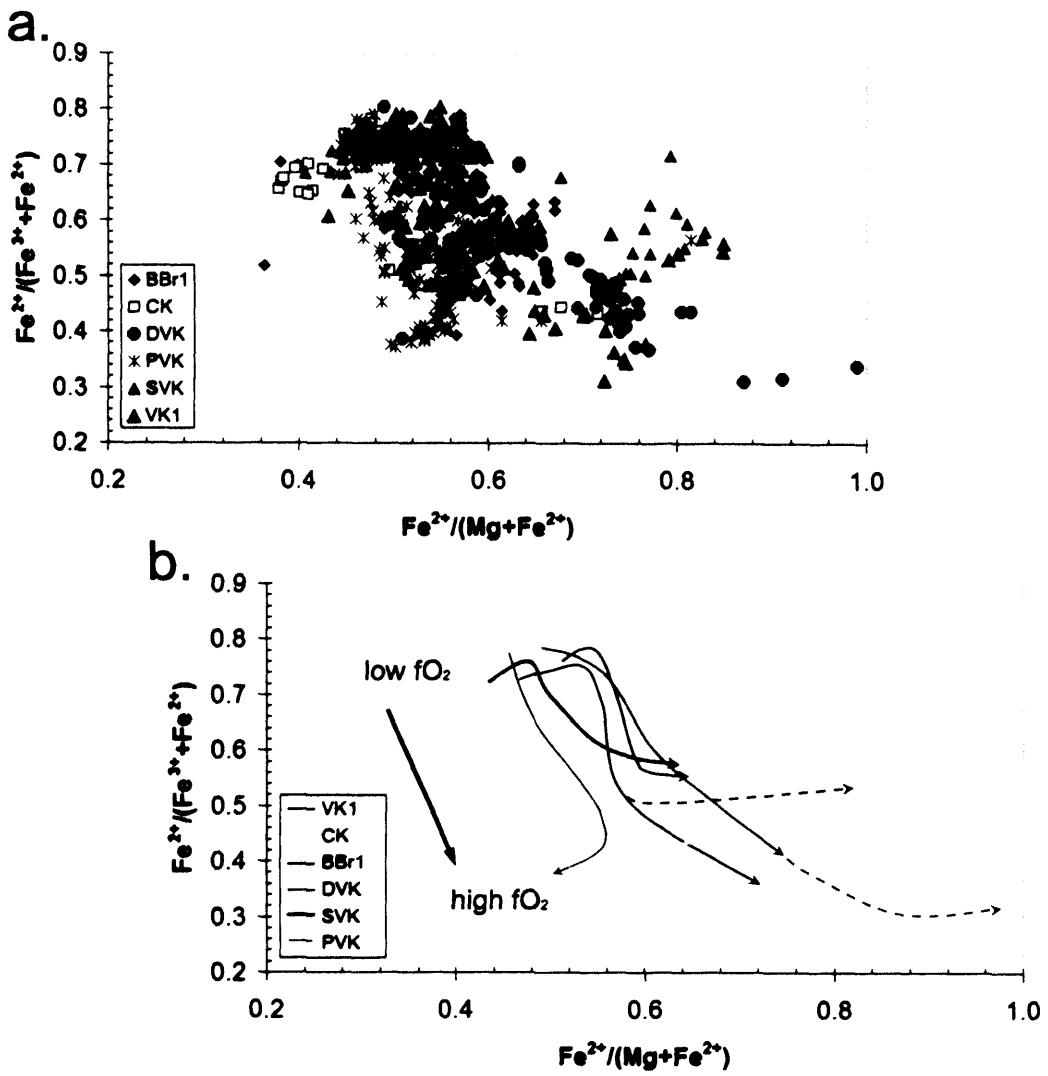

Figure 4.24: $Fe^{2+}/Fe^{2+}+Fe^{3+}$ versus $Fe^{2+}/Fe^{2+}+Mg$ showing the relative fO_2 of each lithofacies according to the method described by Pasteris (1983).

sions and the trends presented in Figure 4.24 indicate that groundmass spinel compositions can be used to qualitatively constrain different eruption conditions between individual lithofacies.

Groundmass Spinel Crystallisation

Nucleation and growth of crystals in magmas are key factors in understanding the mechanics and chemical evolution of a melt. Crystal size distribution and habit are related to kinetic processes within a melt and include (i) melt viscosity, (ii) the rate of diffusion of ions through the melt which is relative to the temperature, (iii) the degree of undercooling (Dunbar et al., 1995), (iv) the latent heat of crystallisation and how it is removed from the crystal-melt interface (Best, 2003), and finally (v) co-crystallisation with other phases (Roeder et al., 2006). Understanding how the rate of spinel growth is controlled by the rate of cooling is difficult in kimberlites because we do not fully understand at which point growth took place. Did spinels grow in the diatreme after eruption or did they grow in the precursor or feeder dyke during ascent towards the surface and were effectively quenched on eruption. It is unreasonable to compare models of kimberlites crystallisation with lava flows, lava lakes or plutons (Dunbar et al., 1995) as kimberlites were probably porous, clastic deposits immediately after they were erupted (Sparks et al., 2006; Walters et al., 2006), assuming this is the point at which the spinels crystallised.

The degree of spinel nucleation is high in kimberlite melts because they have contrasting atomic structures to the silicate liquids from which they crystallise (Best, 2003; Wada et al., 2004). The small size is dependent on solubility of Cr between the melt and crystallising spinel (Roeder et al., 2001); a spinel with 30-40 wt% Cr_2O_3 probably crystallised from a melt with only 0.02-0.06 wt% Cr_2O_3 (Roeder & Reynolds, 1991). Large nucleation densities produce many small crystals as the required elements for growth are quickly depleted from the melt. Spinels within the D/K1 kimberlite are consistent with this behaviour.

Compositional zoning from core to rim is predominantly incremental in the D/K1 spinels although some grains define compositions throughout the range defined by the collected dataset. Spinels are therefore presumed to have precipitated over a wide range of conditions in the melt. Early formed spinels must have been buffered from changing melt compositions, either from sluggish kinetics as temperature decreased and viscosity increased, or if these grains had been quenched.

There is no petrographic evidence however for quench textures in early formed spinels.

The subsets of spinel textures presents a paradox; small, euhedral or simple spinels do not show complex zoning, and larger, compared with atoll spinels that are frequently strongly zoned. Roeder et al. (2006) demonstrated that co-crystallisation of spinel and olivine at the cotectic during chaotic or turbulent tholeiitic basalt magma ascent produces many small euhedral spinels. A significant proportion of these grains were contained as inclusions in olivine phenocrysts. In contrast, there were fewer large spinels of which only a small number were included in olivine phenocrysts. From this, Roeder et al. (2006) concluded that during chaotic ascent there was significant physical interaction between rapidly growing spinels and olivines. Larger spinels however grew during periods of quiescence and therefore had little interaction with growing olivines. The spinel subsets at D/K1 are consistent with the model of Roeder et al. (2006). Poorly zoned, small, euhedral spinels are found as inclusions in olivine phenocrysts and as discrete grains within the groundmass. They are interpreted as having crystallised as the kimberlite magma ascended towards the surface. Complexley zoned spinels, including atoll spinels, grew during less chaotic conditions such as the passive emplacement proposed for the CK lithofacies in Section 7.4.1. The second statement is in agreement with the observation of Mitchell (1986b) that atoll spinels are found exclusively in hypabyssal kimberlite within root zones, dykes and sills. However, it contradicts the occurrance of atoll spinels within volcaniclastic kimberlite at D/K1.

The presence of atoll spinels in volcaniclastic kimberlite can be explained by Roeder et al. (2001) who studied chromian spinel textures and compositions in basaltic magmas. They divided the growth into three stages. (1) Initial crystallisation of chromian spinel simultaneous with olivine. Variations in initial Cr/(Cr + Al) depend on localised variations in Cr content of the melt due to growth of chromian spinel, magma mixing and variations in the distribution of Cr between the melt and the growing crystal (Roeder et al., 2001). (2) Accelereated growth of olivine and spinel as magma is moving towards the Earth's surface producing zoned crystals. (3) Irregular textures grow during the final stage including veriform rims around spinel cores caused by a change over to celluar growth around

the smooth crystal interface as crystallisation of spinel becomes unstable and begins to breakdown. Roeder et al. (2001) believe this takes place close to or at the Earth's surface. If the growth of atoll spinel textures falls into the last category, it is feasible that some atolls are found in fragmented, volcaniclastic kimberlite.

The origin of spinels contained within the rims of ghost lapilli, or oxide necklaces (Mitchell, 1986b), are either primary growth features or they are remnants of glassy lapilli which have devitrified and subsequently altered. There was no compositional evidence to suggest ghost lapilli were droplets of magma from different magma batches. An alternative interpretation is offered by Vogt (1921; *cited in* Roeder et al. 2006) called the common interaction between spinel and olivine "synnuesis" which means swimming together (Roeder et al., 2006). Spinels have nucleated at the interface between olivine and melt because the activation enthalpy for crystallisation is lower at this location (Best, 2003). These spinels are predominantly poorly zoned and occasionally have thin 'atoll' rims, which are often replaced by titanite. The fragile nature of the spinels and their rims suggests they probably grew rapidly and out of equilibrium. This produced disequilibrium cruciform textures from their rapid growth and a large degree of undercooling.

4.10 Conclusion

Groundmass spinel compositions from the D/K1 kimberlite define a trend of decreasing Cr and Al with increasing Ti and Fe^{3+}. This is consistent with the 'Kimberlite Trend' of Barnes & Roeder (2001) and 'Magmatic Trend 1' of Mitchell (1986b). Early formed spinel compositions are marginally shifted along the Fe^{2+}/Fe^{2+}+Mg axis, suggesting melts of a slightly different starting composition. Parental melts may have different compositions if they derived from partial melts of a heterogeneous mantle mineralogy. Qualitative determination of fO_2 indicates that the prevailing conditions in the melt become more oxidising as spinel crystallisation proceeds. Spinel compositions reflect these conditions by becoming more ferrous. This trend is believed to be related to volatile exsolution and degassing as the magma ascends towards the surface (e.g. Shee 1985).

The aim of this study was to use spinel compositions as mineralogical fingerprints for the kimberlite lithofacies described in Chapter 3. Groundmass spinel

compositions from all D/K1 lithofacies are overlapping and therefore cannot be used to directly differentiate between individual lithofacies. However, more detailed examination of the dataset demonstrated that spinel compositions show lithofacies-specific behaviour which can be related to kimberlite emplacement. For example, the paucity of discrete groundmass spinels within the VK lithofacies indicates elutriation of the ash-sized fraction from the deposit which is supported by petrographic evidence in Section 3.5. This also correlates very well with the observations made in Chapter 6 where geochemistry also shows a deficiency in elements presumed to be related to kimberlite ash. In addition, an absence of the ulvöspinel-magnetite series in VK1 suggests the abrasion and/or resorbtion of more evolved spinel rims which is specific to this lithofacies.

Contrasting compositional trends within the same lithofacies were used to illustrate that SVK, PVK and DVK are comprised of more than one batch of magma. This evidence for multiple batches of magma aids the understanding of processes taking place during the formation of a kimberlite pipe. In particular, multiple magma batches preclude the hypothesis that a kimberlite pipe is formed from one phase of eruption from a single magma at Letlhakane (e.g. Scott Smith 1999).

Chapter 5

Groundmass Perovskite Mineral Chemistry

5.1 Introduction

The aim of this chapter was to use groundmass perovskite mineral chemistry to support division of the D/K1 pipe into the lithofacies described in Chapter 3, and add to the findings of the spinel mineral chemistry in Chapter 4. This was considered an important part of the thesis because of the high abundance of perovskite within the Letlhakane kimberlite. Perovskite compositions also vary in kimberlites and fingerprint evolution of the kimberlite magma (Chakhmouradian & Mitchell, 2000), although the effects are not as well documented as for spinel compositions. Perovskites are believed to have crystallised after spinels (Jones & Wyllie, 1985; Mitchell, 1986b)) and therefore perovskite compositions can further our understanding of the later stage processes taking place during kimberlite magma evolution. Oxygen fugacity conditions prevailing in the melt at the time of perovskite crystallisation are compared with the conditions derived from groundmass spinels.

An attempt was made at in situ dating of the perovskites from different lithofacies using U-Pb isotopes. This was not successful fundamentally because the majority of grains were too small ($\leq$50 μm) and the kimberlite is relatively young so the ratio of U/Pb was low producing a large error in the results. Despite this, perovskite dating was considered an important part of the study and it has therefore been included as Appendix D.

5.2 Previous Work

Perovskite is a common groundmass mineral in some kimberlite deposits worldwide (e.g. Armstrong et al. (2004); Chakhmouradian & Mitchell (2001, 2000); Jones & Wyllie (1984); Mitchell (1986b)). It is a major "sink" of incompatible elements in kimberlites such as Nb, Zr, Ba, Sr and light rare earth elements (LREE) (Jones & Wyllie, 1984). Perovskites have not been studied as extensively as groundmass spinels in kimberlites. Mitchell (1986b) characterised their major properties as follows: perovskites constitute around 10 volume% of the rock. They are typically euhedral to subhedral, often rounded grains with an average size between 1 μm and 0.5 mm (Chakhmouradian & Mitchell, 2000). Perovskite paragenesis can be divided into five types (Chakhmouradian & Mitchell, 2000); (i) discrete grains, (ii) as mantles around earlier-formed Ti-rich phases, mostly ilmenite, which have reacted with the later-stage kimberlite melt, (iii) as remnants of the original grain now in the form of a complex pseudomorphs, (iv) within upper mantle xenoliths, and (v) as inclusions in diamond. The latter two are extremely rare and not considered further here. Major element compositions of perovskite in kimberlites vary little when compared with the spinel solid solutions described in Chapter 4. Compositions remain close to ideal perovskite $CaTiO_3$ (Chakhmouradian & Mitchell, 2000; Mitchell, 1986b). Nb and REE are the primary substitutors of Ti, and Na typically replaces Ca to balance the charge (Boctor & Boyd, 1980). Incompatible element oxides including Nb_2O_5, Na_2O and the LREE can contribute up to about 7 wt% (Boctor & Boyd, 1980) and kimberlitic perovskites are enriched in LREE relative to heavy REE (Jones & Wyllie, 1984). There is minimal zoning in many grains; in "normally" zoned grains the LREE, Th and occasionally Nb and Na decrease from core to rim, occasionally with increasing Fe (Chakhmouradian & Mitchell, 2000). Complex zonation patterns occurred at the Benfontein Sills (Chakhmouradian & Mitchell, 2000). These grains had up to 24 oscillating zones between 0.2 - 3 μm thick.

There are negligible variations in perovskite compositions between separate kimberlite bodies (Jones & Wyllie, 1984; Mitchell, 1986b), with the exception of some Canadian kimberlite bodies including Lac de Gras and Kirkland Lake

(Chakhmouradian & Mitchell, 2001). There are only small compositional variations within the same kimberlite body. For example, perovskite compositions from the silicate-rich layers and the carbonate-oxide-rich layers of the Benfontein Sills in South Africa are overlapping (Boctor & Boyd, 1981). Similarly, there are no obvious differences in the compositions of discrete perovskites and those within a reaction mantle around ilmenite megacrysts (Agee et al., 1982; Chakhmouradian & Mitchell, 2000; Mitchell, 1986b).

Intimate associations between perovskites and other groundmass phases provide valuable insight into the crystallisation sequence of a kimberlite. Chakhmouradian & Mitchell (2000) carried out a review of perovskites from over forty worldwide kimberlite bodies and summarised their major textural relationships as (i) discrete groundmass phenocrysts, (ii) contained within pelletal lapilli, (iii) as mantles around ilmenite, magnesian-ulvöspinel-magnetites and (iv) rare occurrences with phlogopite and spinel as kelyphitic rims around garnet macrocrysts. Intergrowths between perovskite and atoll spinels demonstrate the co-crystallisation of perovskite and the spinel atoll rim (Chakhmouradian & Mitchell, 2000).

Mitchell (1986b) and Chakhmouradian & Mitchell (2000) both reported how susceptible perovskite is to alteration because it is unstable in CO_2-rich environments. Clarke & Mitchell (1975) proposed that late-stage, residual kimberlitic fluids are rich in CO_2, probably as a result of the separation of carbonate fluids from silicate fluids by liquid immiscibility (Boctor & Boyd, 1980). During this process calcium was leached from the perovskite leaving a TiO_2 phase (e.g. rutile or anatase) and a new calcite precipitate (Equation 5.1). Deposition of calcite with the TiO_2-phase often produces a spongy rim around the original perovskite grain (Chakhmouradian & Mitchell, 2000).

$$CaTiO_3 + CO_2 \Rightarrow TiO_2 + CaCO_3 \tag{5.1}$$

Bellis & Canil (2007) and Canil & Bellis (2007) calculated and applied an oxygen barometer from perovskites to determine the oxygen fugacity conditions as perovskites were crystallising. Canil & Bellis (2007) applied this barometer to kimberlitic perovskites and concluded that wide ranges in recorded oxygen fugacities were indicative of multiple episodes of crystallisation and/or crystallisation

from multiple batches of magma. This study also showed that oxygen fugacity of kimberlites can both increase and decrease, producing oxidising and reducing conditions respectively.

wt% oxide	1	2	3	4	5	6	7	8	9	10	11	12	13	14	15
Na_2O	0.79	0.73	0.64	0.70	0.63	0.71	1.43	1.40	0.93	0.73	0.05	0.38	0.27	0.48	0.39
MgO	0.34	0.21	0.90	0.34	0.38	0.31	nd	nd	nd	nd	nd	nd	nd	nd	nd
Al_2O_3	nd	nd	nd	nd	nd	nd	0.10	0.02	0.17	0.59	1.13	1.03	0.90	0.60	0.97
SiO_2	0.04	nd	nd	0.28	0.08	0.02	0.35	0.35	1.52	0.38	0.47	0.78	0.65	nd	0.52
CaO	36.54	36.93	35.59	36.11	36.50	36.51	36.36	37.27	37.44	34.56	34.95	35.64	36.58	34.57	35.84
TiO_2	54.28	54.67	54.63	54.62	54.38	54.52	58.26	58.01	54.00	50.24	47.93	47.14	48.46	49.21	48.77
Fe_2O_3	1.24	1.09	1.29	1.30	1.12	1.18	0.47	0.38	2.88	2.83	4.11	4.82	4.51	4.18	4.08
La_2O_3	0.67	0.52	0.58	0.78	0.66	0.65	nd	nd	nd	1.51	1.62	1.46	1.08	1.84	1.58
Ce_2O_3	2.41	2.37	2.66	2.45	2.29	2.38	0.68	0.54	0.52	4.40	4.80	3.84	4.50	4.84	5.09
Nd_2O_3	1.14	0.88	0.91	0.95	1.31	1.07	nd	nd	nd	1.29	1.34	1.35	1.1	0.99	1.12
Sm_2O_3	0.03	0.39	0.13	0.27	0.33	0.25	nd	nd	nd	nd	nd	nd	nd	nd	nd
SrO	nd	nd	nd	nd	nd	nd	1.96	2.20	1.44	0.14	0.47	0.36	0.33	0.26	0.48
Y_2O_3	nd	nd	nd	0.28	nd	0.13	nd	nd	nd	nd	nd	nd	nd	nd	nd
ZrO_2	nd	nd	nd	0.00	nd	0.00	nd	nd	nd	nd	nd	nd	nd	nd	nd
Nb_2O_5	0.79	0.71	0.93	0.60	0.87	0.74	nd	0.11	nd	2.26	2.09	1.78	2.16	1.67	1.98
BaO	nd	nd	nd	nd	nd	nd	nd	nd	nd	nd	nd	nd	nd	nd	nd
ThO_2	nd	nd	nd	nd	nd	nd	nd	nd	nd	0.66	0.66	0.5	0.87	0.46	0.05
Total	98.27	98.50	98.26	98.68	98.55	98.47	99.61	100.28	98.90	99.59	99.62	99.08	101.41	99.10	100.87

Table 5.1: Representative major element abundances of perovskites from other kimberlites. 1-6 Liqhobong, Lesotho (Boctor & Boyd, 1980); 7-15 Lac de Gras (Chakhmouradian & Mitchell, 2001). (nd - not determined)

wt% oxide	1	2	3	4	5	6	7	8	9	10	11	12	13	15	15	16
Na_2O	0.64	0.41	0.62	0.88	0.42	0.60	0.16	0.08	0.68	0.40	0.12	0.36	0.63	0.28	0.27	0.26
MgO	nd	nd	nd	nd	nd	nd	nd	nd	nd	nd	nd	nd	nd	0.13	0.15	0.15
Al_2O_3	0.67	0.94	0.74	nd	nd	nd	nd	nd	nd	0.36	0.29	nd	nd	0.44	0.46	0.49
SiO_2	0.59	0.43	0.57	nd	nd	nd	nd	nd	nd	nd	nd	nd	nd	0.15	0.13	0.05
CaO	32.33	32.94	29.64	36.00	39.02	38.72	40.19	34.79	35.68	37.73	38.90	39.42	39.20	37.70	37.80	38.00
TiO_2	45.16	45.18	43.33	53.82	55.28	57.28	57.59	52.97	52.80	54.80	55.55	57.46	57.46	51.70	51.60	51.90
Fe_2O_3	4.96	4.97	4.95	1.00	1.31	0.86	1.22	2.28	1.76	1.53	1.39	0.91	0.82	1.91	2.43	2.02
La_2O_3	1.84	2.24	3.44	0.95	0.38	0.02	nd	2.24	1.41	0.79	0.79	nd	0.19	1.12	1.11	1.13
Ce_2O_3	6.27	6.71	7.75	2.91	0.89	1.23	0.21	4.42	2.86	2.39	1.46	nd	0.93	2.68	2.59	2.52
Nd_2O_3	1.7	1.86	2.21	0.68	nd	0.13	nd	1.35	1.39	0.59	0.22	nd	nd	0.99	0.98	0.93
Sm_2O_3	nd	nd	nd	nd	nd	nd	nd	nd	nd	nd	nd	nd	nd	nd	nd	nd
SrO	0.23	0.33	0.45	0.33	0.34	0.27	0.31	0.24	0.46	0.27	0.37	0.27	nd	nd	nd	nd
Y_2O_3	nd	nd	nd	nd	nd	nd	nd	nd	nd	nd	nd	nd	nd	nd	nd	nd
ZrO_2	nd	nd	nd	nd	nd	nd	nd	nd	nd	nd	nd	nd		nd	nd	nd
Nb_2O_5	2.7	2.9	2.98	1.03	0.75	0.46	0.31	0.71	0.92	0.83	0.7	0.28	0.6	1.16	0.98	0.91
BaO	nd	nd	nd	nd	nd	nd	nd	nd	nd	nd	nd	nd	nd	nd	nd	nd
ThO_2	1.57	0.62	1.79	0.81	nd	0.36	nd	1.04	0.1	nd	nd	0.09	nd	nd	nd	nd
Total	98.66	99.53	98.47	98.41	98.39	99.93	99.99	100.12	98.06	99.69	99.79	98.79	99.83	98.26	98.50	98.36

Table 5.2: Representative minor and trace element abundances of perovskites from other kimberlites. 1-3 Lac de Gras (Chakhmouradian & Mitchell, 2001); 4-5 core and rim from Matsoko, Lesotho; 6-7 core and rim from Thaba Putsoa; 8 and 10 core and 9 and 11 rim compositions from Wesselton; 12 reaction mantle and 13 discrete matrix perovskite from Premier (4-13 Chakhmouradian & Mitchell 2000); 14-16 Igwisi Hills (Reid et al., 1975).(nd - not determined)

5.3 Groundmass Perovskites at D/K1

D/K1 has an unusually high abundance of groundmass perovskite; approximately 10 % of the groundmass. This gives a ratio of about 10:1 with groundmass spinels (Chapter 4), which is the inverse of a typical kimberlite as described by Mitchell (1986b). At D/K1 perovskites are predominantly rounded and 30-50 μm in diameter. They were classified into the following four parageneses; (a) discrete grains within the groundmass or matrix, (b) contained within ghost-lapilli or along grain boundaries of olivine macrocrysts and phenocrysts (Fig. 5.1), (c) intimate growths with groundmass spinel (Fig. 5.2), and (d) as a reaction mantle around ilmenite macrocrysts (Fig. 5.3). The first two types occurred as intergrowths with spinel (typically MUM) whereas the fourth type was always intergrown with spinel. There was therefore overlap between perovskite crystallisation and the crystallisation of magnesian-ulvöspinel-magnetites (Fig. 5.2).

5.4 Perovskite Analysis

149 perovskite analyses were collected from five kimberlite samples. Perovskite compositions were analysed using polished, carbon coated probe sections on a CAMECA SX50 wavelength dispersive spectrometer (WDS) at the Natural History Museum in London. Analyses were taken under conditions of 20 kV acceleration voltage and a beam current of 20 nA. The analytical instrument was calibrated using natural and synthetic standards. Counting time was 10 seconds for Na_2O, MgO, Al_2O_3, SiO_2, CaO, TiO_2, Cr_2O_3, MnO, Fe_2O_3, ThO_2, BaO, SrO and ZrO_2; 20 seconds for La_2O_3, Ce_2O_3, Y_2O_3 and Nb_2O_5; and 30 seconds for Nd_2O_3 and Sm_2O_3. Details of precision, accuracy and the variance within the collected dataset are given in Appendix B. Samples LDD10_02 and LDD16A_02 were analysed from VK1; samples LDD12_01 was analysed from PVK; sample LDD21_01 from SVK and sample LDD21_06 from CK. The number of samples analysed was limited in comparison with the study on groundmass spinels due to cost and time limitations on the WDS. The locations of the analysed samples are the same for samples analysed in Chapter 4 which are shown in Figure 4.7. Core

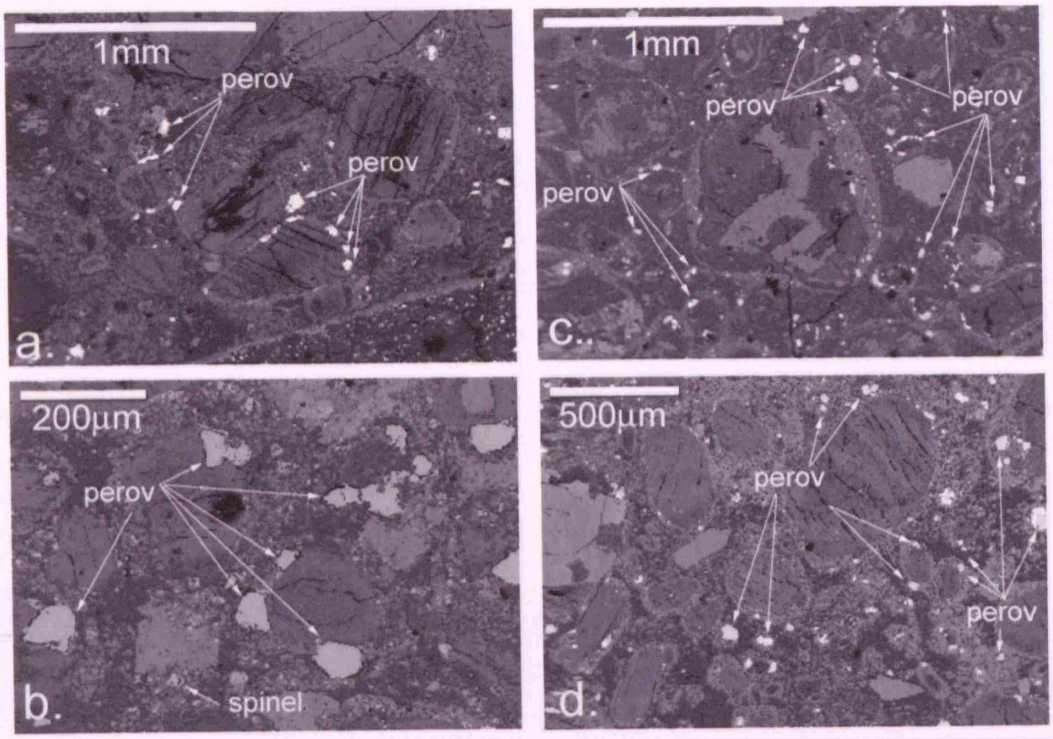

Figure 5.1: Back scattered electron images of the distribution of groundmass perovskites (bright albedos) within D/K1. (a) Discrete grains within the matrix and contained within the rim of ghost lapilli from the VK1 lithofacies. (b) Large, rounded perovskites contained within the rim of ghost lapilli and discrete within the matrix from DVK; spinel labelled for size comparison. (c) Clusters of perovskites contained within the rim of ghost lapilli from the PVK lithofacies. (d) Clusters of perovskites contained within the rim of ghost lapilli and discrete within the matrix enclosed by microlitic diopside; from the SVK lithofacies. (Perov - perovskite)

to rim analyses were collected where possible to record all compositions and any compositional zonations.

5.5 Perovskite Mineral Chemistry

Perovskite compositions from the Letlhakane D/K1 kimberlite contain detectable amounts of the following: Na_2O, MgO, Al_2O_3, SiO_2, CaO, TiO_2, Cr_2O_3, Fe_2O_3,

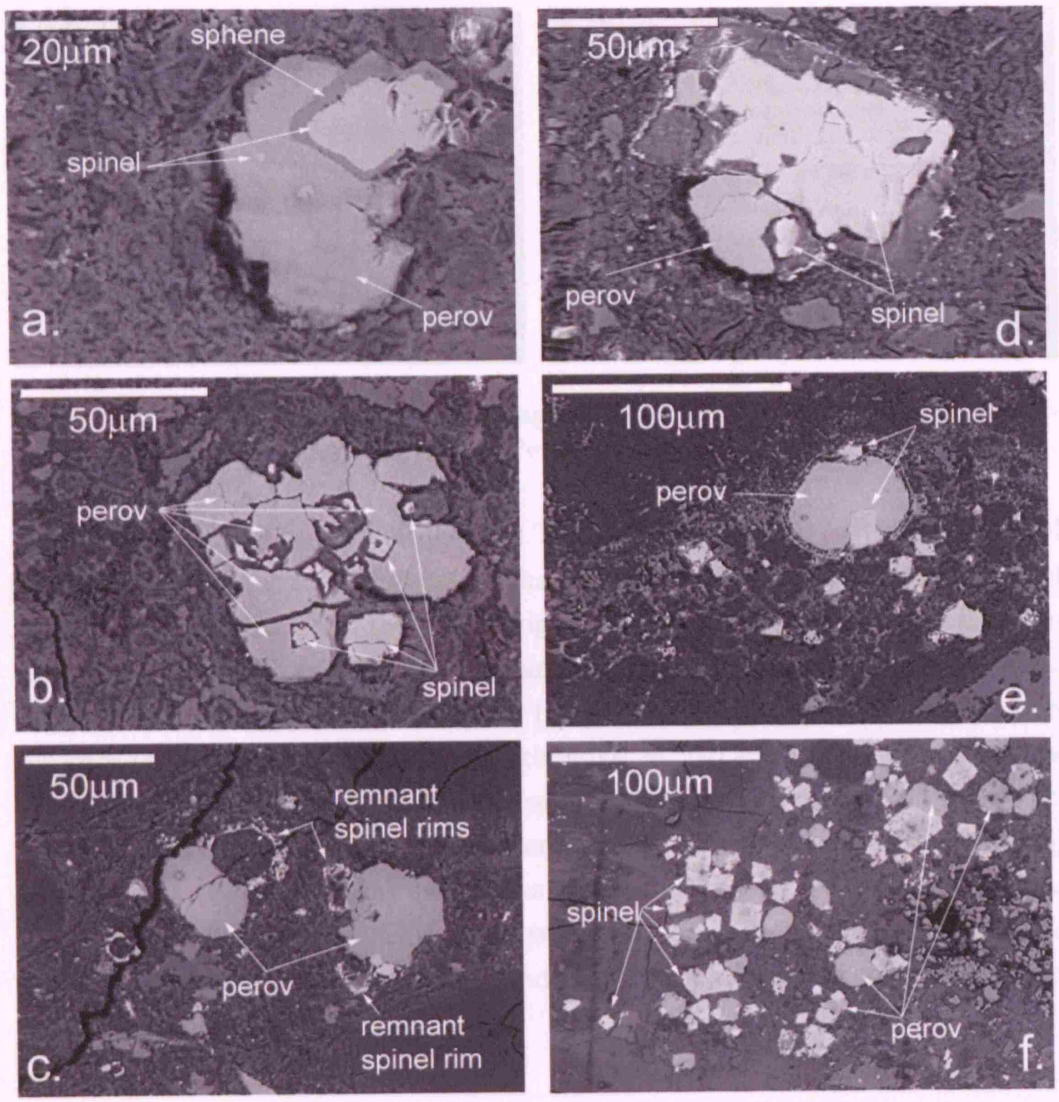

Figure 5.2: Back scattered electron images of perovskite intergrown with spinel. (a) Euhedral spinel with rounded, anhedral perovskite intergrowth with additional spinel inclusions. A band of sphene lies between spinel and perovskite (from VK1). (b) Complex glomerocryst of perovskite enclosing smaller euhedral spinels from the VK1 lithofacies. (c) Remnant atoll spinel rims attached to anhedral perovskites. (d) Spinel with an anhedral perovskite association. (e) Anhedral perovskite contained within the rim of a pelletal lapillus, with a spongy, TiO_2 rim and spinel intergrowths. (f) Cluster of spinel and perovskite intergrowths from the VK1 lithofacies. (N.B. spinels are paler grey to white compared with perovskite which is a medium grey colour phase. Perov - perovskite.)

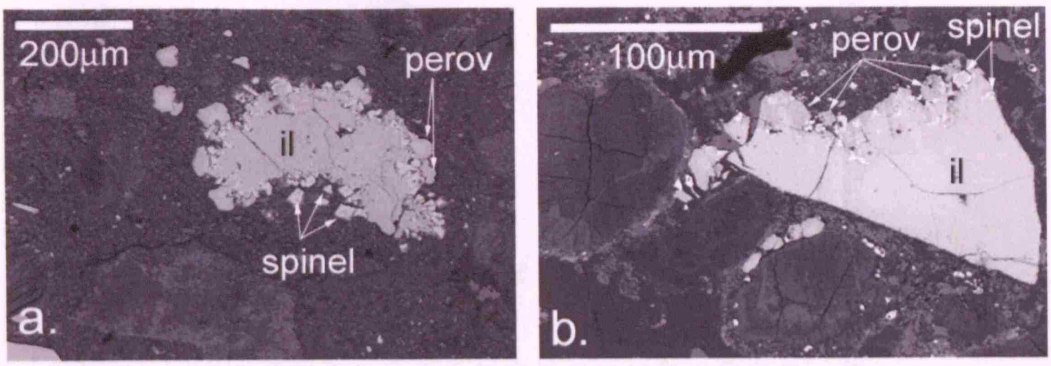

Figure 5.3: Back scattered electron images of ilmenite macroscrysts with a reaction mantle of spinel and perovskite (Perov - perovskite; il - ilmenite)

La_2O_3, Ce_2O_3, Nd_2O_3, SrO, Nb_2O_5 and ThO_2 (Table 5.5; Fig. 5.4). The analysed perovskites have the following major characteristics (Fig. 5.5): (i) an average of 95.7 mol.% pure $CaTiO_3$, the remaining composed of Na, Fe, Al and trace elements, notably REE and Nb; (ii) they are not unusually enriched in any element, unlike the Green Mountain kimberlite (Boctor & Meyer, 1979) or type III perovskites from Lac de Gras which are high in Na, Sr, Nb and LREE (Chakhmouradian & Mitchell, 2001); (iii) all compositions demonstrate a good negative correlation of Ca with Na and trace elements (REE, SrO, Nb_2O_5, BaO and ThO_2) from core to rim, with a few exceptions of reversely zoned grains; (iv) Fe^{3+} has a positive correlation with Al, a negative correlation with Na and trace elements (La, Ce,Nd, Sm, Sr, Y, Zr, Nb, Ba and Th) and it remains relatively constant with increasing Ca.

	All D/K1		VK1		PVK		SVK		CK	
	mean	std dev	mean	std dev	mean	std dev	mean	std dev	mean	std dev
Na_2O	0.47	0.13	0.50	0.17	0.50	0.11	0.44	0.10	0.42	0.11
MgO	0.07	0.07	0.10	0.09	0.07	0.06	0.06	0.04	0.05	0.04
Al_2O_3	0.20	0.04	0.19	0.04	0.18	0.03	0.23	0.03	0.21	0.03
SiO_2	0.09	0.13	0.12	0.20	0.10	0.12	0.07	0.06	0.06	0.04
CaO	38.01	0.91	37.84	1.12	37.82	0.79	38.06	0.71	38.70	0.68
TiO_2	55.72	0.59	55.88	0.66	55.56	0.55	55.79	0.59	55.70	0.44
Cr_2O_3	0.07	0.06	0.12	0.05	0.09	0.04	0.00	0.01	0.08	0.08
MnO	0.00	0.01	0.00	0.02	0.00	0.01	0.00	0.00	0.00	0.00
Fe_2O_3	1.12	0.16	1.11	0.18	1.02	0.10	1.23	0.11	1.17	0.14
La_2O_3	0.41	0.12	0.40	0.15	0.43	0.10	0.42	0.10	0.39	0.10
Ce_2O_3	1.03	0.43	0.97	0.54	1.11	0.37	1.04	0.35	0.92	0.41
Nd_2O_3	0.39	0.23	0.36	0.30	0.43	0.21	0.41	0.17	0.34	0.21
Sm_2O_3	0.04	0.04	0.04	0.04	0.04	0.04	0.06	0.03	0.01	0.03
SrO	0.19	0.05	0.19	0.06	0.18	0.04	0.19	0.05	0.21	0.04
Y_2O_3	0.03	0.03	0.03	0.03	0.03	0.03	0.04	0.04	0.02	0.02
ZrO_2	0.05	0.06	0.08	0.07	0.04	0.05	0.05	0.05	0.05	0.05
Nb_2O_5	0.52	0.09	0.59	0.09	0.50	0.08	0.50	0.07	0.50	0.07
BaO	0.01	0.02	0.01	0.02	0.01	0.02	0.02	0.03	0.00	0.02
ThO_2	0.13	0.14	0.12	0.17	0.15	0.13	0.11	0.11	0.14	0.13

Table 5.3: Mean and standard deviation of oxide wt% for all D/K1 perovskites analysed, and for each lithofacies (N=149).

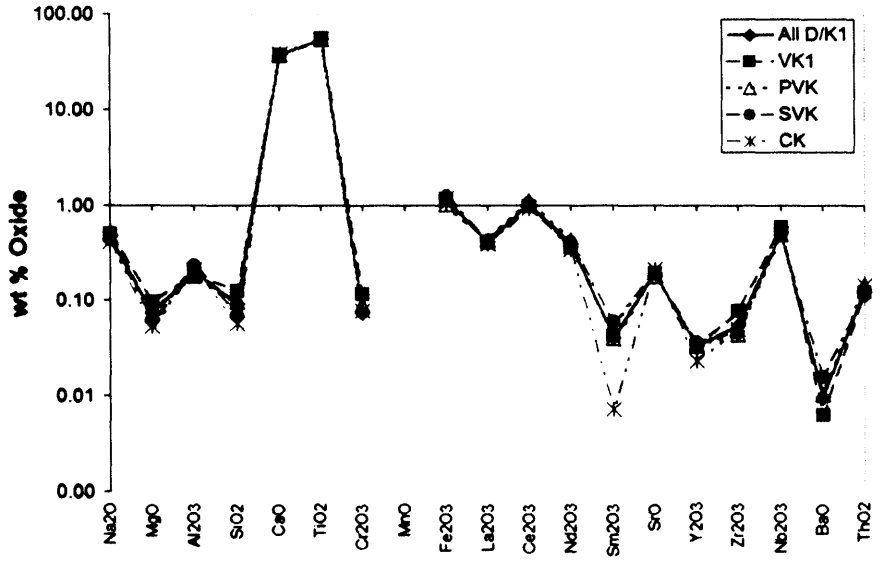

Figure 5.4: Averaged wt% oxides of groundmass perovskites analysed from each lithofacies and all D/K1 data.

5.5.1 Lithofacies

There was some correlation between perovskite composition and lithofacies, although the representation of these trends is not ideal as only one sample was analysed for CK, SVK and PVK. However, spinel analysis in the previous chapter demonstrated a clear divide between compositions from the PVK and SVK lithofacies, therefore the differences in perovskite compositions between the two samples LDD12_01 (PVK) and LDD21_01 (SVK) are considered to be indicative of the true trends. The strongest trend defined by D/K1 perovskite compositions is controlled by the Cr-content; SVK perovskites have the lowest Cr abundance (often below detection limit of 0.1 wt%) followed by PVK, and CK and VK1 have relatively higher Cr abundances (Fig. 5.5c). Al produces the opposite trend to that defined by Cr content; SVK perovskites have marginally higher Al contents to VK1 compositions (Fig. 5.5c). SVK also hosts Fe^{3+}-enriched perovskites relative to the other lithofacies (Fig. 5.5b). VK1 perovskites are enriched in Ti and host the highest Na and trace elements content (Fig. 5.5c). VK1 has the broadest range of compositions, although this is probably a function of the larger

number of grains analysed (Fig. 5.7). Na demonstrates a negative trend with Ca in D/K1 perovskites (0.01-0.03 cpu), although there is a subset of eight analyses relatively enriched with Na around 0.032-0.038 cpu.

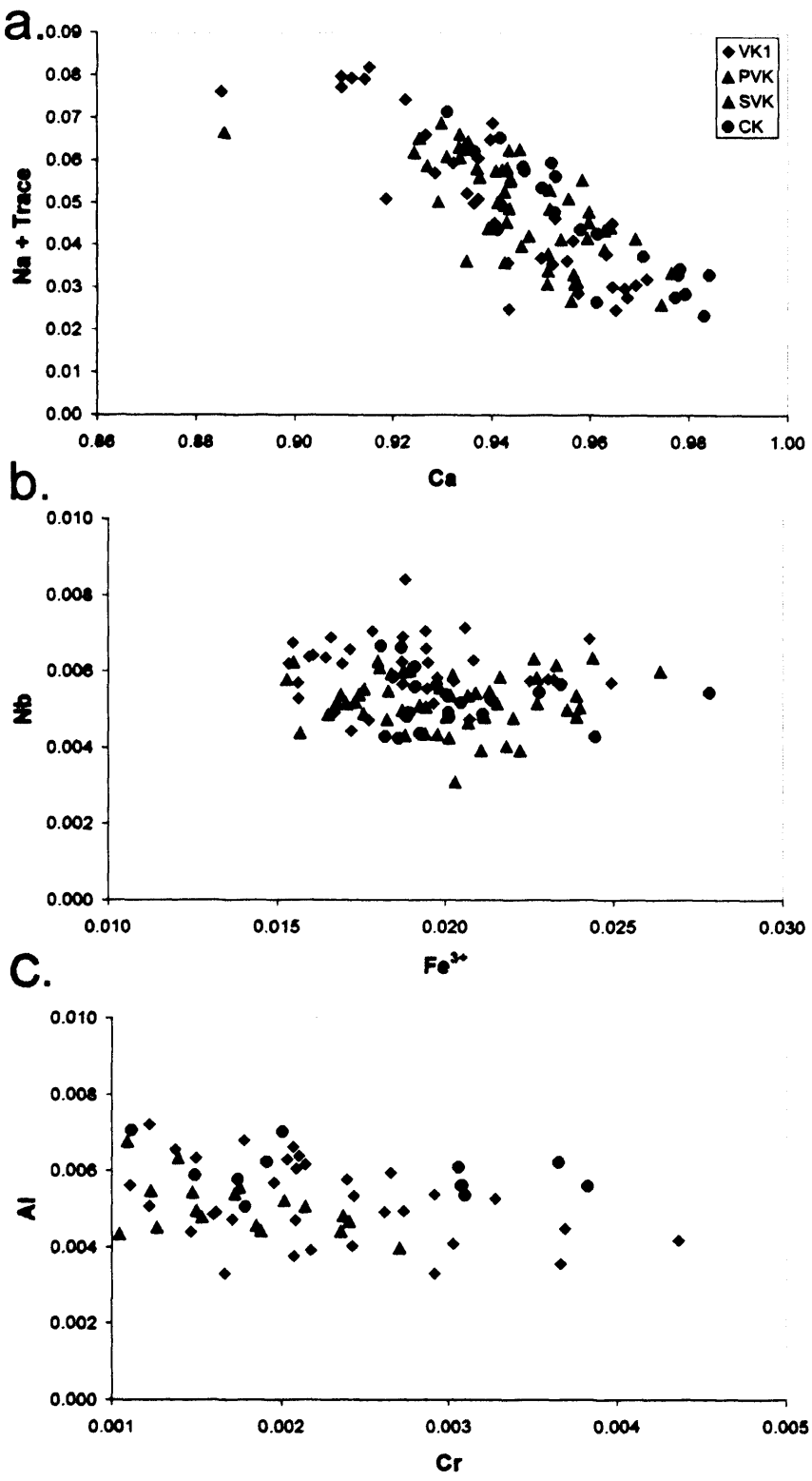

Figure 5.5: Bivariate plots of perovskite compositions divided by lithofacies: (a) Ca vs Na + trace elements; (b) Fe^{3+} vs. Nb; (c) Cr vs. Al

5.5.2 Paragenesis

Core to rim patterns follow the typical kimberlite trend of decreasing Ca, Na and trace elements with increasing Fe^{3+} and Al from core to rim, with the exception of a few grains (Figs. 5.6 and 5.7) which have reverse compositional zonation. Reversely zoned grains are typically contained within the rims of pelletal or juvenile lapilli (Fig. 5.7). These two parageneses also host grains with the least compositional zoning compared with perovskite located as discrete grains within the matrix. The core to rim relationships and paragenesis for each lithofacies analysed are shown in Figure 5.7 and demonstrate how perovskites in the matrix have slightly higher Ca, Na and trace element content than those contained within the rims of ghost lapilli. In general, however, compositions from different perovskite parageneses overlap.

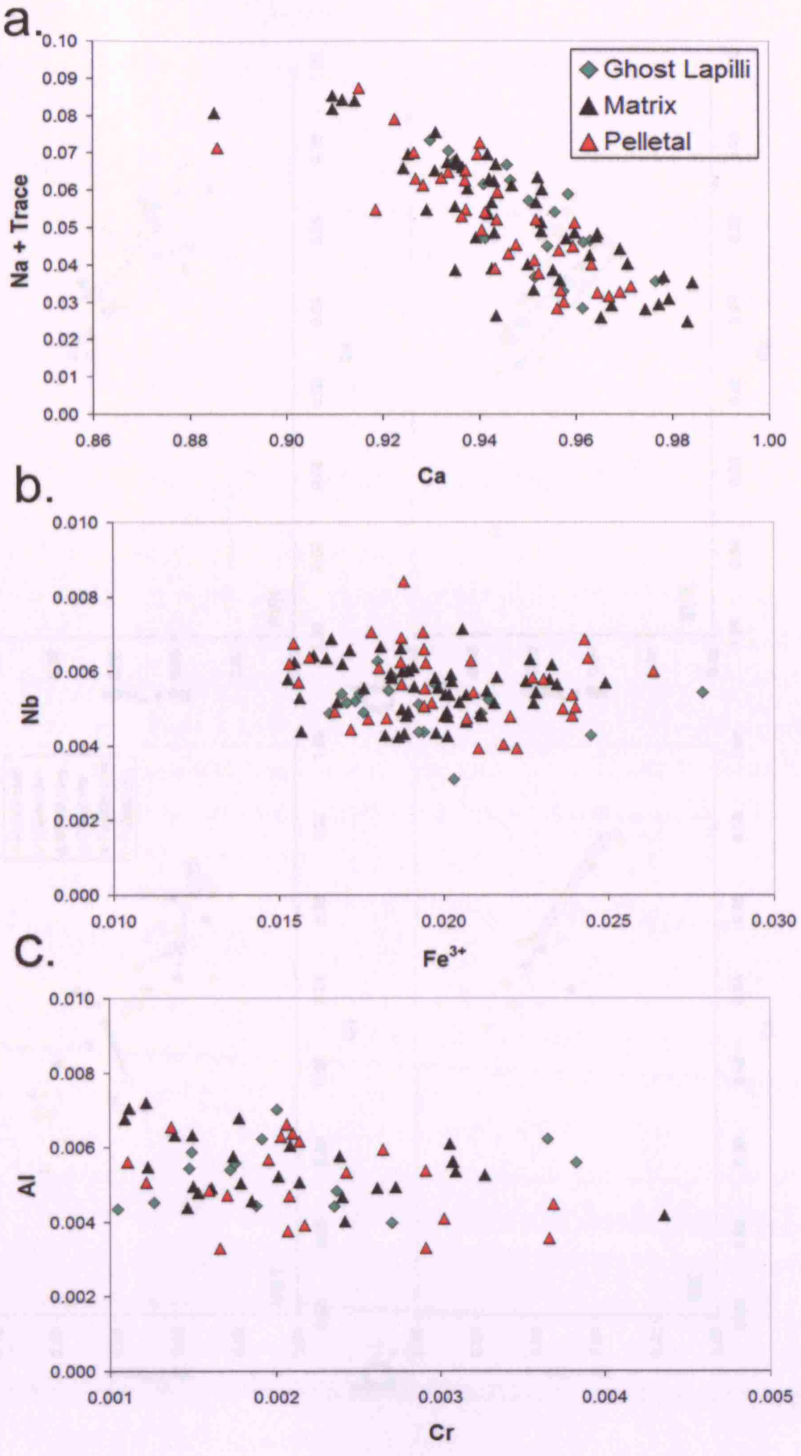

Figure 5.6: Bivariate plots of perovskite compositions divided by paragenesis: (a) Ca vs Na + trace elements; (b) Fe^{3+} vs. Nb; (c) Cr vs. Al (pelletal includes juvenile lapilli)

Figure 5.7: Variation diagrams of core to rim relationships for each lithofacies and paragenesis. (Closed symbols - core compositions; open symbols - rim compositions. Black arrows point in the direction of evolution from cores to rims.)

5.5.3 Rare Earth Elements

Figure 5.8 shows the typical REE distribution of perovskites from each lithofacies at Letlhakane overlap. The predominant trend is of LREE-enrichment relative to HREE. There is minimal influence by lithofacies except relatively lower Sm_2O_3 abundance from the perovskites from the CK lithofacies (Fig. 5.4). This trend corresponds well with published kimberlitic perovskite compositions (e.g. Chakhmouradian & Mitchell 2000). REE compositional variations from core to rim are shown in Figure 5.8. These are also similar to trends reported from other kimberlite bodies of decreasing REE from core to rim.

5.6 Interpretation and Discussion

The aim of analysing groundmass perovskite was to extend the understanding of how the D/K1 magma evolved as it approached the surface and to test if perovskite could also be used as a fingerprint of individual batches of kimberlite magma. Perovskite compositions do not vary significantly throughout the D/K1 pipe. The major variations are in Al and Cr abundance. Core to rim relationships illustrate a trend of increasing Ca with decreasing Na The discussion below looks at how groundmass perovskite compositions vary throughout the D/K1 pipe, and offers possible explanations why these variations have occurred.

5.6.1 Petrogenesis

Groundmass perovskites from Letlhakane have a small range of compositions which are not significantly influenced by paragenesis or lithofacies. It is possible that there was marginal compositional variation between kimberlite melts from which they crystallised, assuming they crystallised from more than one batch of magma. However, the variations which occurred in groundmass spinel compositions do not support this model. Alternatively, the conditions in the melt were the same for all magma batches when perovskite became a stable liquidus phase. This is plausible if perovskites crystallised over a narrow window of pressure and/or temperature and/or oxygen fugacity compared with the spinel stability field. There is very little variation in the Nb content of the analysed perovskites

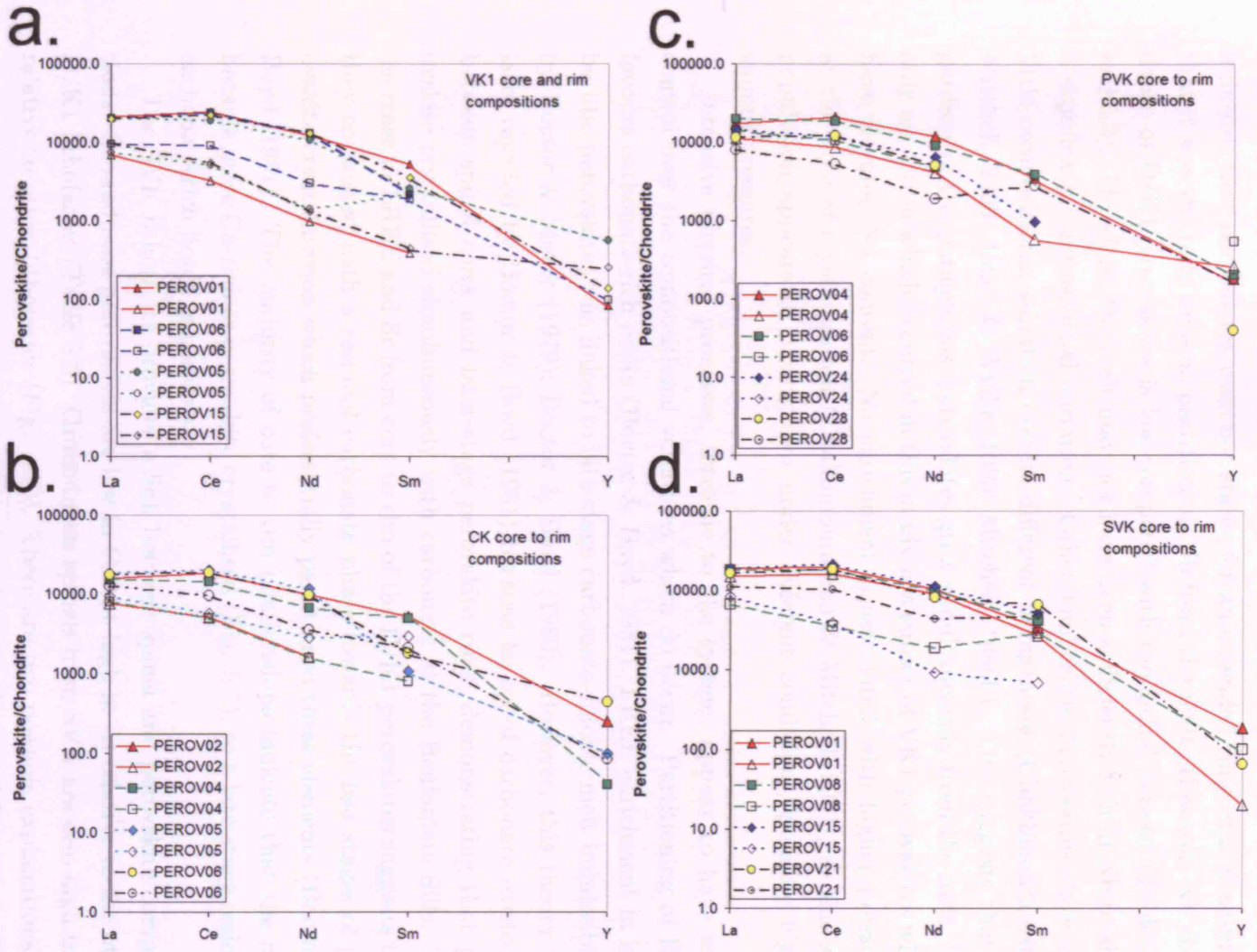

Figure 5.8: Chondrite normalised spiderdiagrams of REE showing the core to rim relationships for each lithofacies (values normalised to chondrite abundance using the data of Sun & McDonough 1989). (Closed symbols - core compositions; open symbols - rim compositions)

(0.52 ±0.09 wt%). Perovskite is a major sink of Nb in kimberlites. Constant Nb indicates that perovskites were not stable for an extended time, if it is assumed that it was the only mineral partitioning Nb from the melt. However, Nb abundance of D/K1 perovskites is low compared with the global dataset (Tables 5.2 and 5.5). Therefore, the melt may not have been sufficiently rich in Nb to show a significant compositional variation. Other kimberlitic perovskites show very little compositional variation despite different parageneses (Chakhmouradian & Mitchell, 2000; Jones & Wyllie, 1985; Mitchell, 1986b). This suggests that regardless of the paragenesis, perovskites grew simultaneously from the melt. The only exception which occurred in this study is a subset of VK1 perovskites which have elevated Na content. Na enrichment is associated with higher pressures at the time of crystallisation (Chakhmouradian & Mitchell, 2001), so this subpopulation appears to have grown under different conditions, possibly higher vapour pressures.

Intensive physical processes, intrinsic to the system, appear to have some control over the compositional variations which do occur. Partitioning of REE favours carbonate-rich melts (Boctor & Boyd, 1981). LREE enrichment in kimberlitic perovskites was linked to late-stage carbonate-silicate melt immiscibility by Boctor & Meyer (1979); Boctor & Boyd (1980). However, this theory was later rejected by Boctor & Boyd (1981) because layers of carbonate existed in between spinel cores and later-stage perovskite rims, demonstrating that perovskite crystallised simultaneously with carbonate at the Benfontein Sills. The decrease in LREE and Sr from core to rim of the D/K1 perovskites suggests that they co-existed with a residual carbonate phase towards the last stages of perovskite crystallisation which preferentially partitioned these elements (Boctor & Boyd, 1981). The majority of core to rim relationships indicate that the melt became more Ca-rich as perovskite crystallised (Fig. 5.7), so a late-stage residual carbonate-rich liquid is possible.

The SVK lithofacies provides a link between spinel and perovskite compositions. Groundmass perovskites are low in Cr but high in Al relative to the other D/K1 lithofacies (Table 5.5). Groundmass spinels from SVK are also high in Al relative to other lithofacies (Fig. 4.10). There are two possible explanations for Al-enrichment in this lithofacies; either the original melt was high in Al, or there

was an additional influence from a co-existing Al phase. Groundmass spinels defined a geochemical trend of increasing Al at very low Cr content (Fig. 4.16) implying that an Al-bearing mineral was resorbed. Release of Al cations into the melt towards the later stages of spinel crystallisation probably coincided with the onset of perovskite stability on the liquidus. The alternative explanation is that the melt from which the SVK lithofacies derived was pre-enriched in Al. (SVK has higher than average bulk rock Al, although this is not purely inherent of the parent melt composition; Chapter 6.)

5.6.2 Perovskite Growth

The relative abundance and larger size of perovskites, relative to spinels, suggests that they had different crystal growth dynamics. Chapter 4 discussed how spinel nucleation is high in kimberlite melts because of the contrasting atomic structures with the melts from which they crystallised (Best, 2003; Wada et al., 2004). The same is true of perovskite. Large nucleation densities produce many small crystals as the required elements for growth are quickly depleted from the melt (Best, 2003). However at D/K1 many larger (than spinels) crystals have grown. The melt must have been super-saturated in the elements required for perovskite growth, predominantly Ti and Ca, to sustain the growth of many crystals. Chapter 4 demonstrated that the melt was enriched in Ti towards the later crystallising spinel compositions (ulvöspinel-magnetite). A discussion of the crystallisation sequence in shallow level kimberlite is given in Section 7.3.

Groundmass perovskites from D/K1 have rounded habits, which either suggest a small degree of undercooling (but not sufficient to produce skeletal textures) or the grains have been abraded after crystallisation. Abrasion is difficult to substantiate because groundmass spinels have retained some very delicate and complex textures. Perovskites have preferentially grown by heterogeneous crystallisation at pre-existing grain boundaries of olivine, spinel and ilmenite where the activation enthalpy of crystallisation was lower (Best, 2003).

Oxygen Fugacity

The difficulties of accurately calculating oxygen fugacities for the D/K1 kimberlite using spinel-silicate pairs was discussed in Section 4.9.5. However, it would be very informative to constrain this parameter and understand how it varies through the crystallisation sequence of a kimberlite melt. Changes in oxygen fugacity would demonstrate changes in conditions from the shallow mantle through to eruption at the surface. Furthermore, to be able to fingerprint changes in fO_2 for separate eruptive phases would provide supporting evidence that the D/K1 kimberlite was produced by a very dynamic eruptive system.

Bellis & Canil (2007) experimentally derived an oxygen barometer based on ferric iron partitioning between perovskites and the kimberlite melt (Equation 5.2; where NNO is the nickel-nickel-oxide buffer). The barometer assumes that (i) all iron in natural perovskite is ferric (Chakhmouradian & Mitchell, 2000) and (ii) as fO_2 increases, Fe^{3+} in the melt will also increase and more Fe^{3+} will partition into the perovskite. This method is not suitable for compositions with greater than 1 wt% Nb_2O_5, but is applicable to the Letlhakane perovskites which have an average Nb_2O_5 of 0.52 wt% (Table 5.5). The results of fO_2 calculations for D/K1 perovskites are given in Table B.5 in Appendix B and shown in Figure 5.9.

$$wt\%Fe_2O_{3_{Pv}} = 0.25\ (\pm 0.04)\ \Delta NNO\ +\ 1.83\ (\pm 0.06) \qquad (5.2)$$

The range of oxygen fugacities calculated from D/K1 perovskites is ΔNNO -4 to ΔNNO -0.6. This is consistent with fO_2 of other kimberlites (Fig. 5.10). For example, Fedortchouk & Canil (2004) derived an fO_2 of ΔNNO -2.2 using spinel-olivine pairs from the Lac de Gras kimberlite. From Figure 5.10 it is clear that kimberlites have the largest range in fO_2 of all igneous rocks (Carmichael, 1991). Oxygen fugacities calculated from both groundmass perovskites and spinels from Letlhakane overlap. fO_2 from spinel inclusions in olivine lie towards the more reduced end of the scale (near the iron-wüstite buffer), as would be expected if they grew at greater depth in the upper mantle than perovskites. The range of oxygen fugacities determined by spinels is predicted to extend towards the fayalite-magnetite-quartz (FMQ) buffer if fO_2 could be calculated for later stage

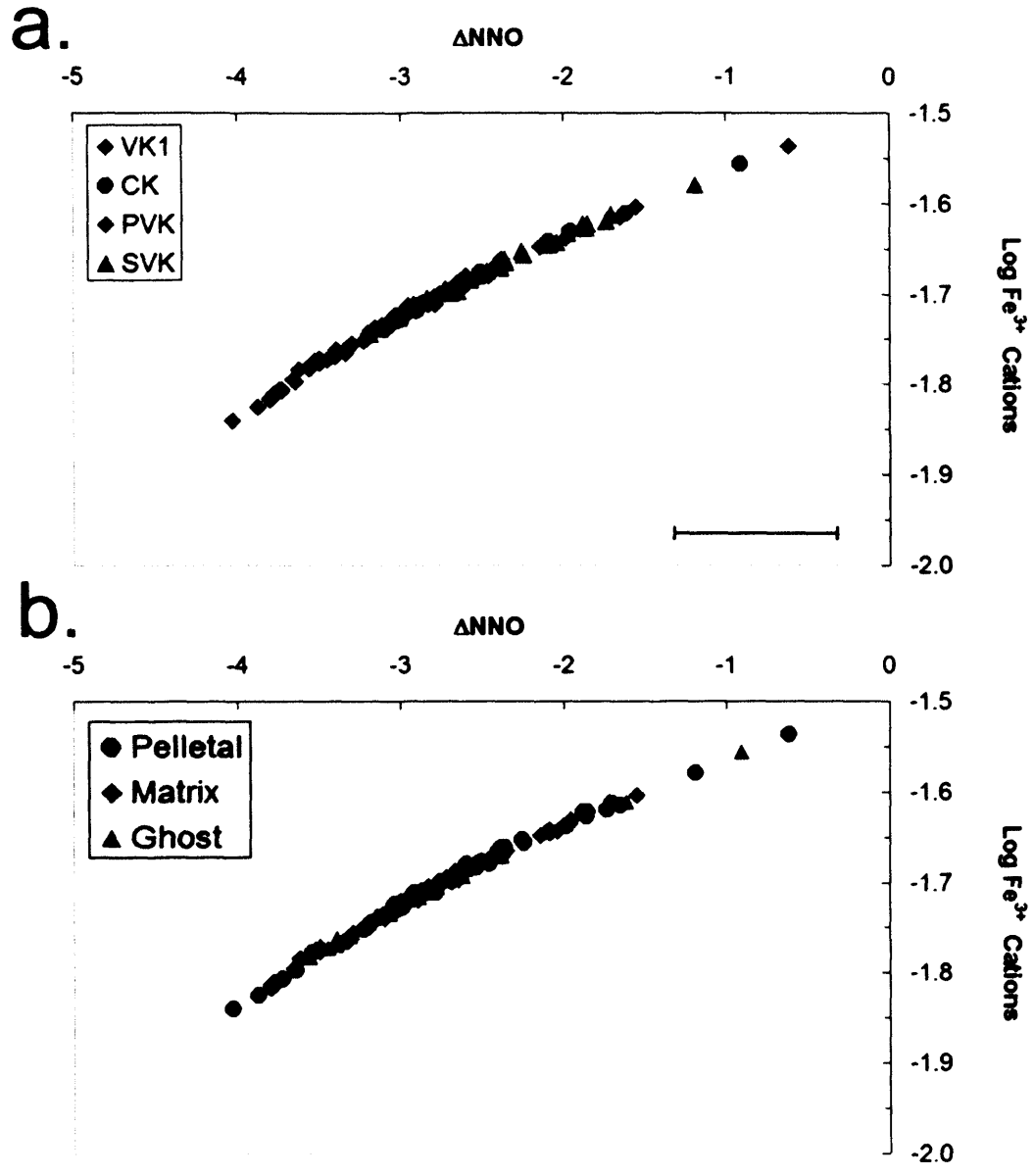

Figure 5.9: Results of oxygen fugacity calculations on groundmass perovskites on a plot of ΔNNO versus log Fe^{3+} cations. (a) plotted by lithofacies and (b) plotted by paragenesis. (Black scalebar in (a) indicates error of ± 1 log fO_2 (Bellis & Canil, 2007).)

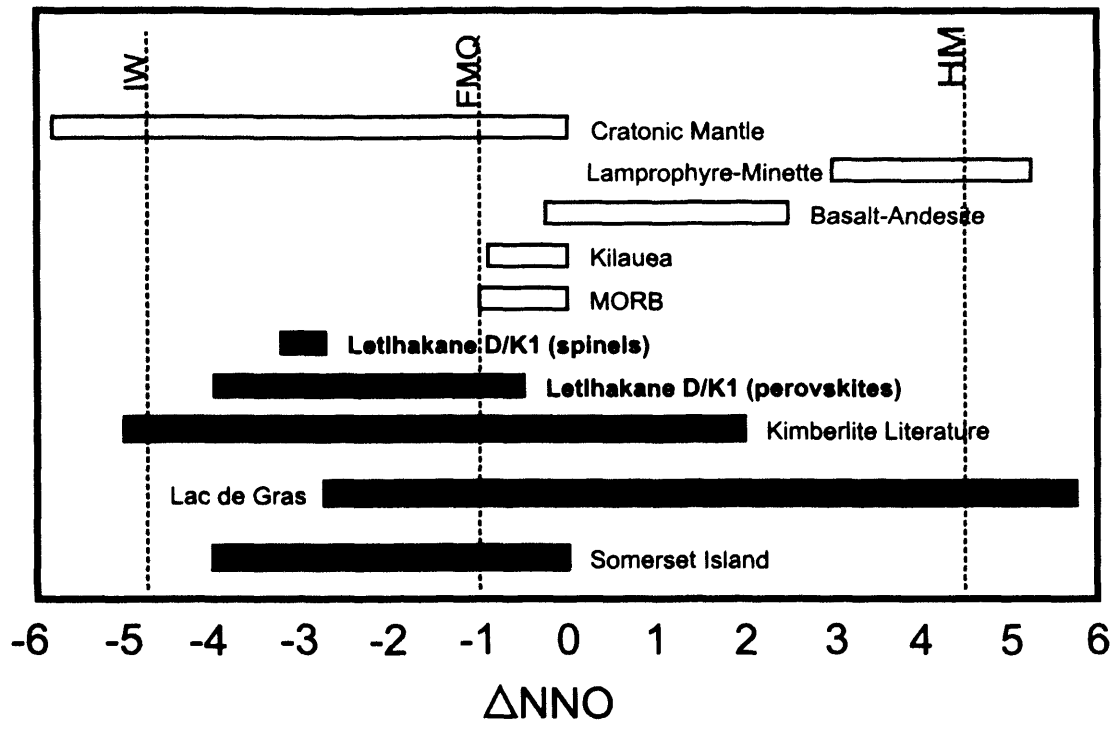

Figure 5.10: Oxygen fugacities (ΔNNO) of global kimberlite bodies and other mantle-derived magmas. Adapted from Figure 7 Canil & Bellis (2007) with the D/K1 dataset for comparison. (IW - iron-wustite; FMQ - fayalite-quartz-magnetite; HM - heamatite-magnetite.)

ulvöspinel and magnetite compositions. (These spinel endmember compositions are considered to have crystallised later in more oxidised environments than magnesian-chromites included in olivine phenocrysts; see Section 4.9.5.)

Figure 5.9 shows a positive correlation between the oxygen fugacity and Fe^{3+} of perovskites from this study. Bellis & Canil (2007) demonstrated that this relationship is a direct result of changing fO_2 in the system, and is not controlled by the bulk Fe in the magma. At Letlhakane there is a positive correlation between evolving perovskite compositions (i.e. increasing Ca from core to rim; Figure 5.7) and Fe^{3+} content supporting the hypothesis that perovskites were becoming more ferric as they crystallised. This trend was controlled by the fO_2 of the system. Bellis & Canil (2007) also demonstrated experimentally that temperature has a negligible effect on Fe^{3+} substitution into the perovskite. The principal

control is the fO_2 itself, which also seems to apply to the D/K1 kimberlite because the oxygen fugacities calculated from both spinel and perovskite overlap despite changing temperatures of crystallisation. This cannot be proved unequivocably until we have accurately constrained the phase relations of a shallow level kimberlite (Section 7.3).

There was variability in oxygen fugacity conditions between the lithofacies analysed in this study. Figure 5.11a shows the range of oxygen fugacity values separated by lithofacies. Although there is a degree of overlap, perovskites from the PVK lithofacies are relatively reduced. Figure 5.11b, c, d and e show some core to rim zonations of perovskites from each lithofacies. The predominant trend is of increasing fO_2 from core to rim. However, there are a few exceptions in most lithofacies where reverse zonation occurs. This is more common in the PVK lithofacies, in particular for perovskites contained within the rims of pelletal lapilli. The variation in characteristics between individual lapilli was discussed in Section 4.9.4. Variability in fO_2 between lapilli from PVK supports the hypothesis that magma pellets are potentially derived from separate eruptive phases and some from different parent melts. A similar conclusion was drawn by Canil & Bellis (2007) for the Nikos I, the Phoenix and Zulu pipes in Canada.

Variability in fO_2 in kimberlites can be caused by: entrainment of more oxidised crustal fragments; the titanium and magnesium content (Frost, 1991); the ferrous to ferric iron ratio in oxides (Frost, 1991); the hydrous nature of the melt (Canil & Bellis, 2007). Sudden degassing of volatiles from a kimberlite magma can trigger large amounts of crystallisation (Richard Brooker, *pers. comm.*), which can deplete the melt in ferrous iron thereby increasing ferric:ferrous iron ratio in the melt phase (Canil & Bellis, 2007).

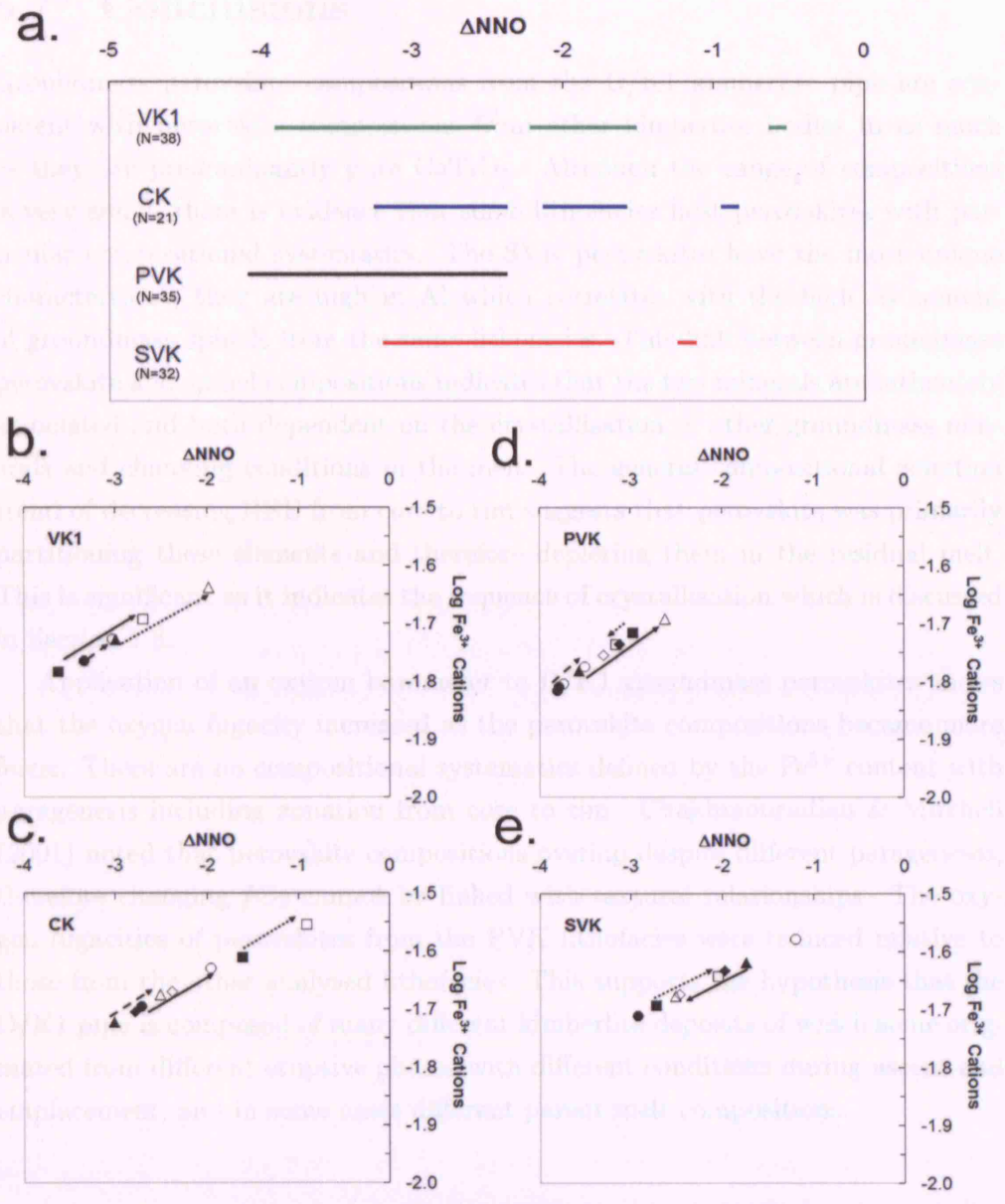

Figure 5.11: (a) The range of oxygen fugacity (ΔNNO) of each lithofacies within the D/K1 pipe. The number of perovskites analysed is given in brackets. (b) to (e) Black arrows indicate the direction of perovskite evolution defined by core to rim relationships. (Solid symbols - cores; open symbols - rims.)

5.7 Conclusions

Groundmass perovskite compositions from the D/K1 kimberlite pipe are consistent with perovskite compositions from other kimberlite bodies in as much as they are predominantly pure $CaTiO_3$. Although the range of compositions is very small, there is evidence that some lithofacies host perovskites with particular compositional systematics. The SVK perovskites have the most unique characteristics; they are high in Al which correlates with the high Al content of groundmass spinels from the same lithofacies. This link between groundmass perovskite and spinel compositions indicates that the two minerals are intimately associated and both dependent on the crystallisation of other groundmass minerals and changing conditions in the melt. The general compositional zonation trend of decreasing REE from core to rim suggests that perovskite was primarily partitioning these elements and therefore depleting them in the residual melt. This is significant as it indicates the sequence of crystallisation which is discussed in Section 7.3.

Application of an oxygen barometer to D/K1 groundmass perovskites shows that the oxygen fugacity increased as the perovskite compositions became more ferric. There are no compositional systematics defined by the Fe^{3+} content with paragenesis including zonation from core to rim. Chakhmouradian & Mitchell (2001) noted that perovskite compositions overlap despite different parageneses; therefore changing fO_2 cannot be linked with textural relationships. The oxygen fugacities of perovskites from the PVK lithofacies were reduced relative to those from the other analysed lithofacies. This supports the hypothesis that the D/K1 pipe is composed of many different kimberlite deposits of which some originated from different eruptive phases with different conditions during ascent and emplacement, and in some cases different parent melt compositions.

Chapter 6

Bulk Rock Geochemistry of the D/K1 Kimberlite

6.1 Introduction

This chapter presents the results of major and minor element compositions of bulk rock samples from the Letlhakane D/K1 kimberlite pipe. The aim was to test whether geochemistry could be used to validate the lithofacies subdivisions described in the previous chapters. This was achieved by processing the collected dataset using the multivariate statistical techniques of principal component analysis (PCA) and cluster analysis. The geochemical signatures of kimberlitic rocks are complex and cannot be assigned directly to magma compositions because they are modified by crustal and mantle fragments, the magma and post-emplacement hydrothermal alteration and weathering. The spatial distribution of the geochemical groups shows excellent consistency with the eleven lithofacies when plotted into the computer-simulated geological model of the D/K1 pipe discussed in Chapter 3. This result demonstrates that the D/K1 pipe is composed of multiple, chemically distinct, kimberlite lithofacies. There are currently no published data of the bulk rock geochemistry of the Letlhakane kimberlite, and therefore these results will add to the understanding of this one pipe in relation to other studied kimberlite bodies and related rocks.

Section 2.7 discussed the difficulties of analysing the bulk rock geochemistry of diatreme facies or volcaniclastic kimberlites (i.e. Clement & Skinner 1985 and

Shee 1985). This present study was undertaken to support the differences between individual kimberlite lithofacies, and to understand what processes have controlled these. The principal aim, therefore, was not to analyse and interpret the composition of the primary or uncontaminated kimberlite melt or to understand the details of melt petrogenesis.

6.2 Kimberlite Geochemistry

The bulk rock geochemistry of a kimberlite has characteristics that are inherent of the hybird nature of these rocks (Dawson, 1980; Mitchell, 1986b). Geochemical analysis of diatreme facies or volcaniclastic kimberlite for the purposes of understanding kimberlite petrogenesis has therefore been avoided. Clement (1982; *cited in* Shee 1985) derived a Contamination Index (C.I.) to quantify the extent of crustal contamination in a sample (Eq. 6.1). Unaltered aphanitic hypabyssal kimberlites have a C.I. of $\sim$1, whereas contaminated volcaniclastic kimberlites have a C.I. of $\geq$1.5. This is a useful way of assessing the relative amounts of crustal contamination in aphanitic and macrocrystal hypabyssal kimberlite, but it does not provide detailed information regarding the types of contamination of VKs. It is used below as an illustrative parameter to demonstrate the degree of contamination of the D/K1 kimberlite.

$$C.I. = \frac{SiO_2 + Al_2O_3 + Na_2O}{MgO + K_2O} \tag{6.1}$$

Table 6.2 presents compositions of other Group I and II kimberlites and related rock melilitite and lamprophyre.

	1	2	3	4	5	6	7	8	9	10
SiO_2	31.55	24.46	28.48	30.52	21.13	27.72	29.57	33.7	34.61	35.91
TiO_2	2	3.11	1.76	0.88	2.42	0.69	2.29	2.58	1.28	1.51
Al_2O_2	2.57	3.58	3.04	0.75	1.95	0.7	2.08	5.79	7.49	8.35
FeO_x	9.01	9.74	12.48	8.63	9.48	7.92	8.89	12.58	11.71	12.05
MnO	0.15	0.19	0.24	0.16	0.23	0.16	0.16	0.22	0.21	0.21
MgO	31.3	25.94	25.33	33.44	22.87	26.37	29.72	18.6	16.93	13.98
CaO	8.14	15.07	16.78	8.3	19.9	11.19	10.36	15.6	17.56	15.1
Na_2O	0.35	0.26	0.31	0.17	0.1	0.31	0.11	0.39	1.36	1.44
K_2O	1.29	0.68	0.77	0.16	0.14	0.26	1.08	2.26	0.44	1.36
P_2O_5	1	1.74	0.22	1.54	4.1	1.07	1.16	0.93	0.29	0.51
CO_2	4.26	6.92	nd	4.7	7.3	12.1	6.36	nd	nd	nd
H_2O^+	7.71	7.56	nd	9.93	9.27	8.93	7.85	nd	nd	nd
LOI	-	-	10.27	14.63	16.57	21.03	14.21	6.55	7.47	8.1
F	1784	2225	nd	nd	nd	nd	nd	nd	nd	nd
S	271	671	nd	nd	nd	nd	nd	nd	nd	nd
V	105	170	143	38	129	41	137	172	170	198
Cr	1291	2007	1228	633	1030	611	1323	809	520	564
Co	110	87	nd	97	65	85	90	nd	nd	nd
Ni	1233	729	1003	1414	657	1190	1213	503	592	412
Cu	60	105	140	36	79	28	73	125	196	147
Zn	88	111	100	64	81	62	72	89.8	99	121
Rb	78	60	25.4	7.2	8.9	14.1	78	238	18.9	47
Sr	905	1256	972	820	2261	1387	929	1167	1480	5165
Y	12	26	9.7	13.2	37	15.7	13.9	19.7	14	19
Zr	258	502	90	204	596	163	266	215	132	164
Nb	146	284	106	111	302	117	119	199	76	106
Ba	1198	1578	268	306	1428	930	980	3368	473	1038
Sc	nd	nd	19.8	18.3	17.5	17.3	16.8	24.5	13.7	18
Pb	nd	nd	6.5	0.69	12.1	8.46	5.5	8.05	12.1	5
Th	nd	nd	12.9	11.7	39	10.4	9.33	19.4	8.6	10

Table 6.1: Compositions of Group I and II kimberlites, melilitite and lamprophyre. 1. Wesselton macrocrystic kimberlite (MK) and 2. aphanitic kimberlite (AK) (Shee, 1985); 3. Kola monticellite kimberlite (MK) (Beard, 2000); 4. DuToitspan (AK - dyke) (Le Roex et al., 2003); 5. Bultfontein (AK - pipe and MK - dyke) (Le Roex et al., 2003); 6. Big Hole, Kimberly Mine (MK) (Le Roex et al., 2003); 7. Anatapur, Dharwar, India (Chalapathi Rao et al., 2004); 8. Kola melilitite (Beard, 2000); 9. Kandalaksha lamprophyre (Beard, 2000); 10. Swarttruggens Group II kimberlite (Mitchell, 1986b)

6.2.1 Previous Work

Nowicki (1993) demonstrated that bulk rock geochemistry was very effective in differentiating between lithofacies at Letlhakane. He identified three kimberlite lithofacies using bivariate plots and statistical processes. However, his work was limited because he only sampled three vertical drill cores; one in LM1, one in LM2W and one in LM2E (refer to the old model in Figure 3.2) which were collected at equidistant intervals of 100 m. Further geochemical investigation was needed to determine how bulk rock geochemistry varies laterally throughout the pipe, as well as to extend Nowicki's work to greater depths in the pipe. The aim was to widely sample the lithofacies identified in Section 3.5 and to evaluate the validity of the current model.

6.3 Methods

6.3.1 Analytical Methods

Every effort was made to collect unbiased samples wherever there was access to the mine outcrop. Samples were collected at 20 m intervals with additional samples collected at 10 m intervals where a boundary between lithofacies was predicted from the geological model (Chapter 3). This was to determine the nature of the contact, whether it is gradational or sharp. Samples from drill cores were taken at 20 m intervals. The samples were $\geq$2 kg[1] with the aim to avoid the effects of significant dilution and therefore contamination by any non-kimberlitic component, i.e. from the mantle or the crust. Samples with $\geq$50 vol% contamination, for example containing a large basalt fragment, were avoided. In this regard, the samples are not evenly distributed nor strictly unbiased. In total 66 samples were collected from the pit (Fig. 6.1) and 81 samples from drill cores.

X-ray fluorescence (XRF) was carried out at the Anglo American Research Laboratories (AARL), Johannesburg, South Africa, using a Philips PW1606 simultaneous XRF spectrometer on pressed powder pellets. Major elements were

[1]This is consistent with recommendations for sampling of coarse grained igneous rocks by The Australian Institute for Metallurgy's Field Geologist's Manual (2001).

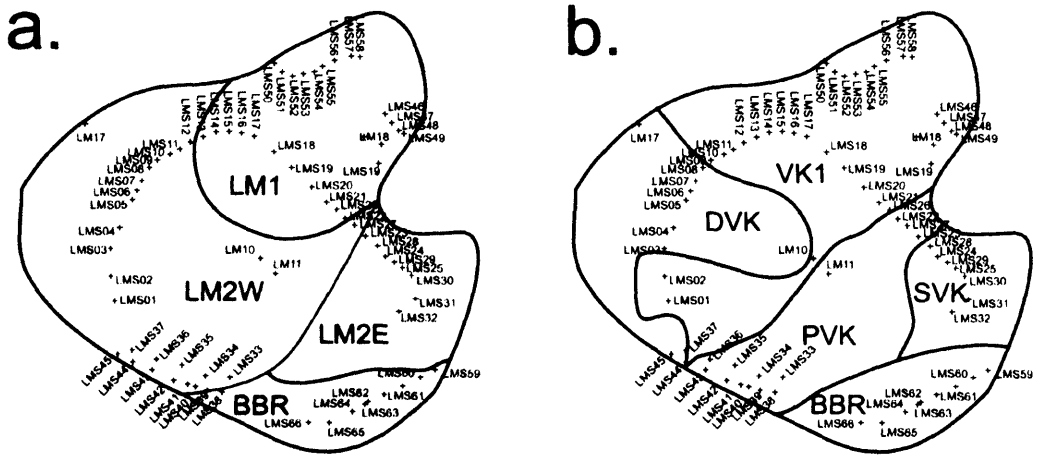

Figure 6.1: Schematic showing the location of geochemistry samples within the mine with outlines of lithofacies from (a) the old model and (b) the new, adjusted model.

analysed using an Oxford Link energy-dispersive X-ray analyser and trace elements were measured using wavelength-dispersive XRF utilizing instrumentation[1]. The major elements analysed were Al_2O_3, CaO, Cr_2O_3, Fe_2O_3, K_2O, MgO, MnO, Na_2O, NiO, P_2O_5, SiO_2, TiO_2, V_2O_5 and ZnO, and the trace elements analysed were Ce, Ba, Co, Cr, Cu, F, Nb, Nd, Ni, Rb, Sr, Th, U, V, Y, Zn, and Zr. Major elements were normalised to water-free compositions. A full table of all analyses and the standards used is given in Appendix B. This is a semi-quantitative technique chosen for speed of sample analysis.

Nine samples were crushed and milled at UCL/Birkbeck and analysed at the University of Edinburgh using a Panalytical PW2404 wavelength-dispersive sequential X-ray spectrometer. This is a quantitative technique used to calibrate the semi-quantitative process described above. Standards used are shown in Govindaroju (1994) and Figures B.2 and B.3 in Appendix B. A comparison between elemental abundances analysed by the two techniques shows good reproducibility between the two techniques. The only inconsistency was low Zn content from the AARL semi-quantitative analyses and a correction was applied to the AARL dataset.

[1]Taken from http://www.aarl.co.za/.

6.3.2 Multivariate Statistical Analysis

The results collected from geochemical analysis is a multivariate dataset comprised of 31 variables from 169 observations (or samples). The objective of identifying geochemical clusters in the dataset and observing which variables were controlling those clusters can only be achieved by visualising the data in all 31 dimensions, which is not possible (Swan et al., 1995). One and two dimensions are limiting as they do not explore all the variability in the dataset. The application of statistical analysis manipulates multivariate datasets and presents it in a way which either maximises or minimises the variance between samples. Two statistical techniques were applied to the D/K1 geochemical dataset; principal component analysis (PCA) and hierarchial cluster analysis. A summary of these methods is given below. For a more detailed explanation see Swan et al. (1995). An important consideration here is that this dataset is closed, in other words the variables are not independent of each other. For example, increasing SiO_2 will proportionally decrease minor elements through a dilution effect, not by a real geological process. This is also true for standard, Harker-style bivariate plots where oxide weight percent are normalised to 100%. The results from multivariate statistics are not directly representative of geological processes. However, for the purposes of identifying clusters within the data these techniques are very powerful, as shown in the following sections.

6.3.2.1 Principal Component Analysis

PCA maximises the variance in a multidimensional cloud of data by assigning new linear axes through the datapoints. These linear axes are called the principal components. The co-ordinates of a datapoint plotted on the new axes are called the scores and the weights, or eigenvectors, are calculated from the correlation matrix. The eigenvalues are the variance of the new, uncorrelated datapoints (Swan et al., 1995). A scree plot is produced which illustrates the cumulative variance versus the number of principal components and can be used to estimate how many components are needed to explain the variance. PCA was used as the first step to understand the variance in the D/K1 dataset and omit all outliers.

This was carried out by M. Field using Unscrambler software designed by K. H. Esbenson.

6.3.2.2 Hierarchical Cluster Analysis

Cluster analysis uses the spatial relationship between points in a multidimensional space, working on the basic assumption that two points with similar attributes will plot closer together than two points with very different attributes. Therefore, unlike PCA, cluster analysis will group the data based on dependence relationships between variables. There are a number of methods of clustering data. The linkage method, or hierarchical clustering, was chosen for this study as computational software (MiniTab) was readily available. The algorithm works through several stages; the first stage links the most similar (or dissimilar, depending on which method is used) datapoints, the second stage links the next most similar pair, and so on until all datapoints and subsequent clusters are linked together. The results were plotted on a dendrogram to visualise all the generated clusters. For this study, Wards method was used to calculate the linkage between points and clusters producing the most easily interpretable dendrogram. Wards method uses the least increase in the sum of squared deviations from cluster means (Swan et al., 1995). The resulting geochemical groups were plotted into the computer-generated geological model of the D/K1 pipe to determine if they were representative of the lithofacies identified from field study (Chapter 3).

6.4 Results

All D/K1 geochemical analyses of kimberlite and country rock samples are given in Appendix B in Tables B.7, B.8, B.9 and B.10. Average compositions and the range of all analysed elements of all D/K1 geochemistry samples are shown in Figures 6.2a and b. The geochemical subdivisions (Groups A, B, C and D) were derived using multivariate statistics which are described below. The results from D/K1 are first compared with compositions of other kimberlites and related rocks, the univariate statistics of the dataset are then presented. The results are then plotted using bivariate, Harker-style diagrams of major oxides and minor and trace elements versus SiO_2, except where stated otherwise in the text, which

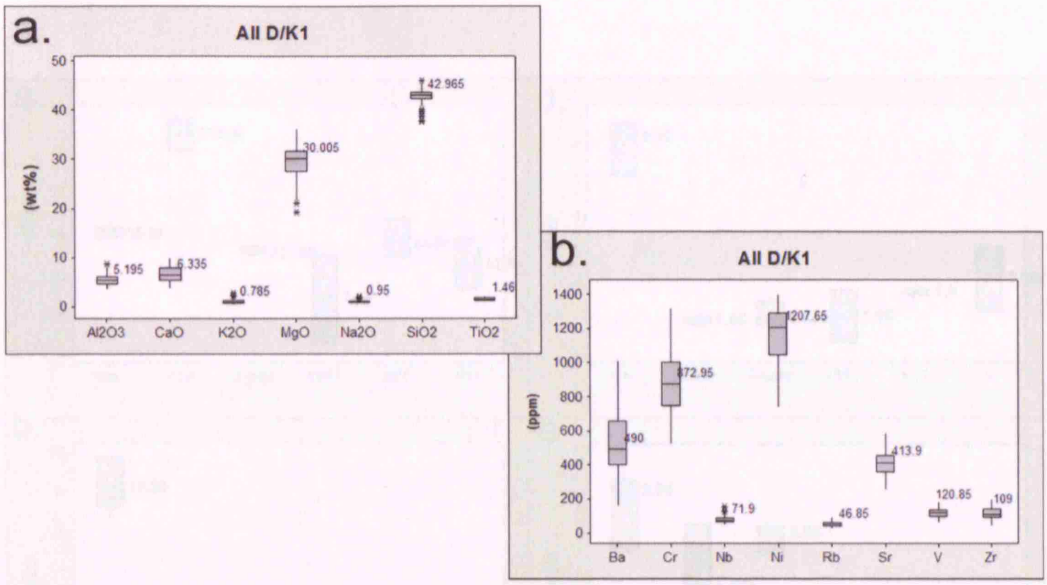

Figure 6.2: Boxplots illustrating the range and median compositions of all D/K1 geochemical samples. (a) Major elements and (b) minor elements. The solid line across the centre of the box is the median. The lower and upper divisions of the box represent the 25^{th} and 75^{th} percentiles respectively. The whiskers represent the range. Asterisks mark outliers from the dataset.

effectively shows the variation in the data. Analyses of country rock samples are also given to show how they have influenced the kimberlite geochemistry. The final sections look at the multivariate statistics and how the four geochemical groups were differentiated.

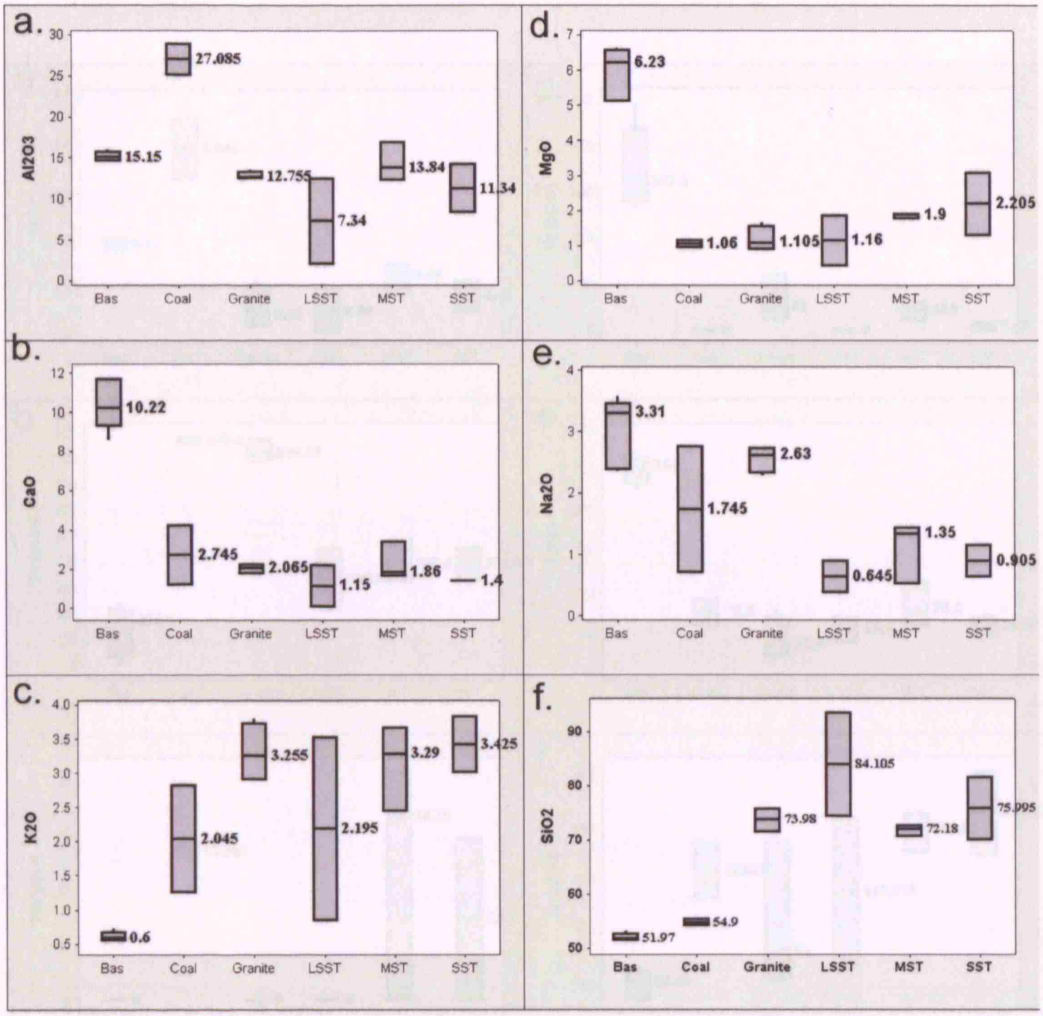

Figure 6.3: Boxplots illustrating the range and median of each D/K1 country rock type versus Al_2O_3, CaO, K_2O (wt%), MgO, Na_2O, and SiO_2. An explanation of boxplots and country rock abbreviations are given in Figure 6.2. (Bas - basalt; LSST - laminated sandstone; MST - mudstone; SST - sandstone.)

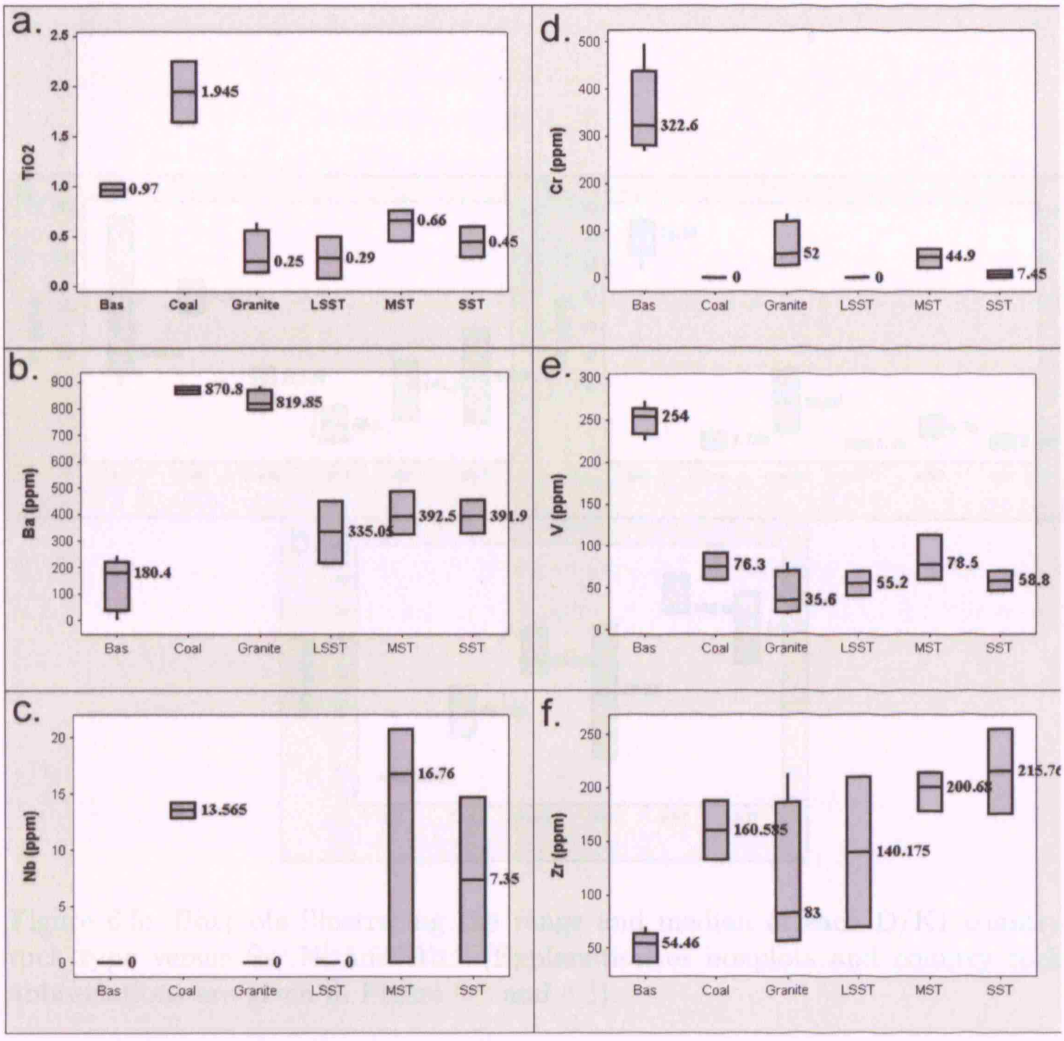

Figure 6.4: Boxplots illustrating the range and median of each D/K1 country rock type versus TiO_2, Ba, Nb, Cr, V, and Zr. (Explanation of boxplots and country rock abbreviations are given in Figure 6.2 and 6.3).

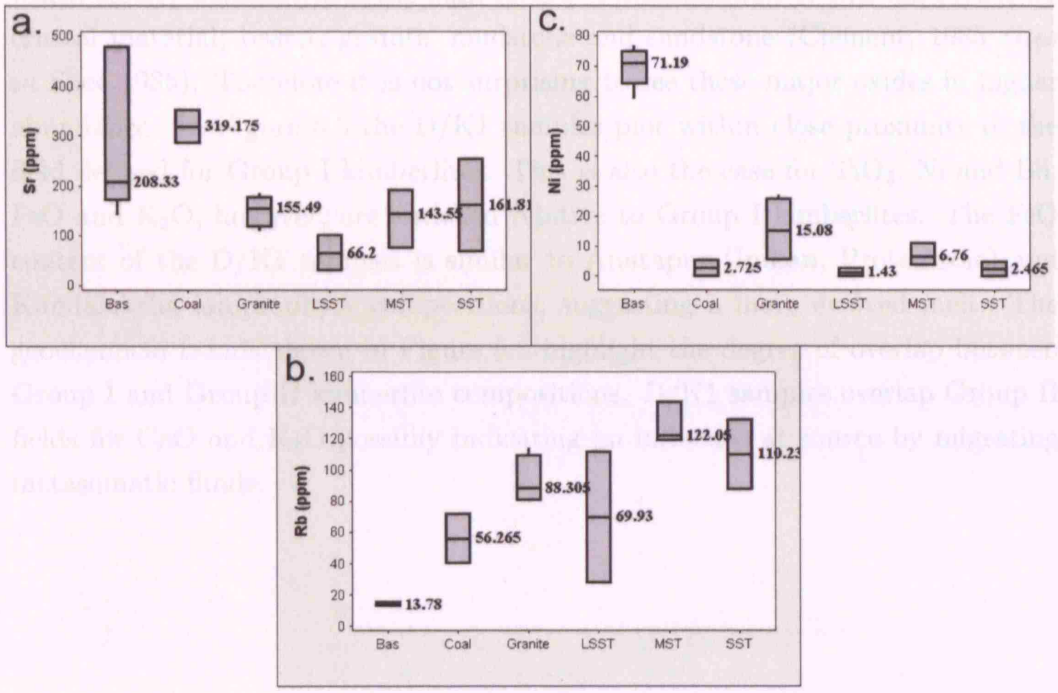

Figure 6.5: Boxplots illustrating the range and median of each D/K1 country rock type versus Sr, Ni and Rb. (Explanation of boxplots and country rock abbreviations are given in Figure 6.2 and 6.3).

6.4.1 Comparison with Other Kimberlites and Related Rocks

Figures 6.6a-f show the bulk rock geochemistry of a number of Group I and Group II kimberlites, and related rocks (lamprophyre and melilitite) and pristine[1] samples of D/K1 kimberlite. The D/K1 kimberlite samples are enriched in MgO and SiO_2. The contamination index (C.I.) of all averaged D/K1 samples is 1.63, which clearly demonstrates the high level of contamination of this kimberlite by crustal material; basalt, granite, mudstone and sandstone (Clement, 1985 *cited in* Shee 1985). Therefore it is not surprising to see these major oxides in higher abundance. In Figure 6.6 the D/K1 samples plot within close proximity of the field defined for Group I kimberlites. This is also the case for TiO_2, Ni and Ba. FeO and K_2O, however, are enriched relative to Group I kimberlites. The FeO content of the D/K1 samples is similar to Anatapur (Indian, Proterozoic) and Kandalaksha lamprophyre compositions, suggesting a more evolved melt. The geochemical trends shown in Figure 6.6 highlight the degree of overlap between Group I and Group II kimberlite compositions. D/K1 samples overlap Group II fields for CaO and K_2O possibly indicating an influence at source by migrating metasomatic fluids.

[1] An explanation of pristine samples is given below.

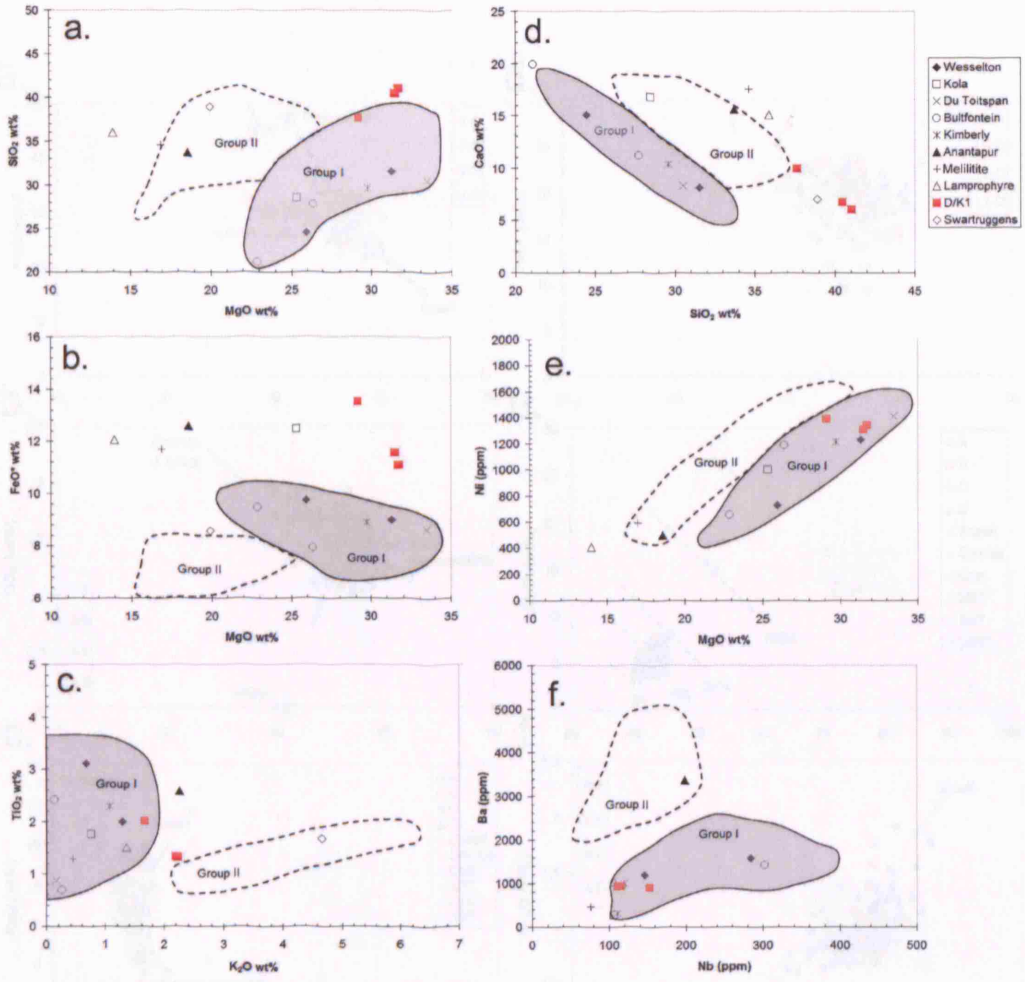

Figure 6.6: Bivariate plots of global Group I and Group II kimberlite and related rock melilitite and lamprophyre, and D/K1 kimberlite compositions. (a) SiO_2 vs. MgO; (b) FeO* vs. MgO; (c) TiO_2 vs. K_2O; (d) CaO vs. Si_2O; (e) Ni Vs. MgO; (f) Ba vs. Ni. Group I and Group II fields defined by Le Roex et al. (2003). (Wesselton macrocrystic kimberlite (MK) and aphanitic kimberlite (AK) (Shee, 1985); Kola monticellite kimberlite (MK) (Beard, 2000); DuToitspan (AK - dyke) (Le Roex et al., 2003); Bultfontein (AK - pipe and MK - dyke) (Le Roex et al., 2003); Big Hole, Kimberly Mine (MK) (Le Roex et al., 2003); Anatapur, Dharwar, India (Chalapathi Rao et al., 2004); Kola melilitite (Beard, 2000); Kandalaksha lamprophyre (Beard, 2000); Swarttruggens Group II kimberlite (Mitchell, 1986b))

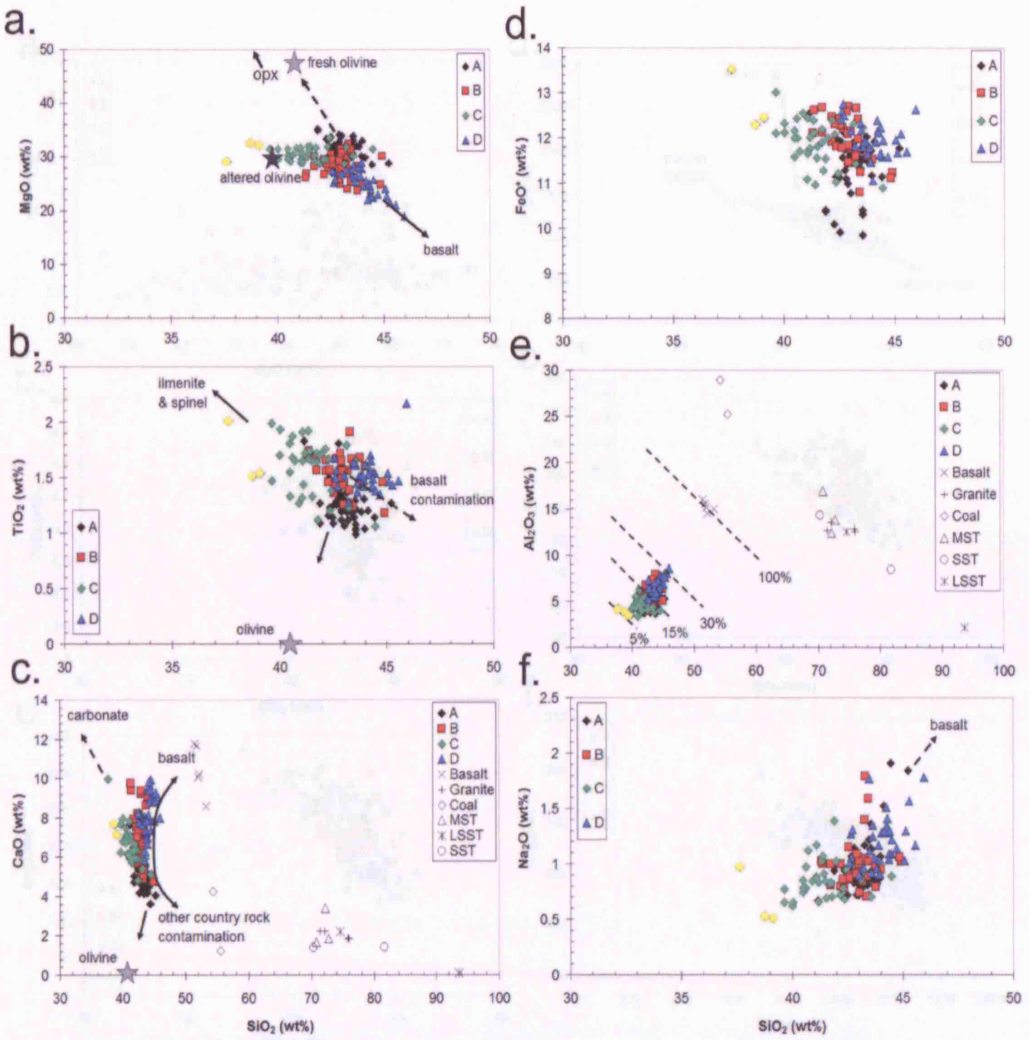

Figure 6.7: Bivariate plots of major elements (a) MgO, (b) TiO_2, (c) CaO, (d) FeO*, (e) Al_2O_3 (with country rock samples and estimated basalt contamination index) and (f) Na_2O versus SiO_2. (* - total Fe as analysed.) Yellow diamonds represent the pristine samples (see text).

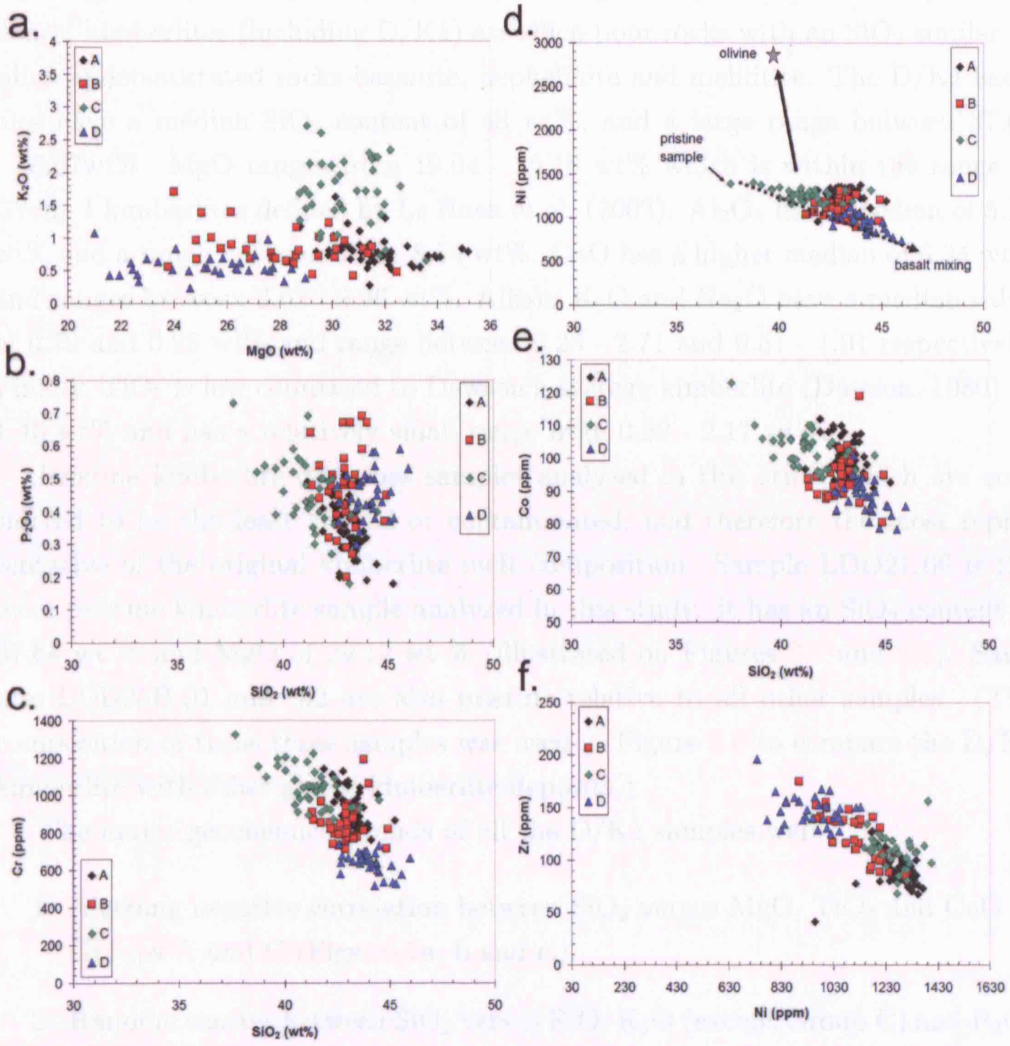

Figure 6.8: Bivariate plots of major and trace elements (a) K_2O vs. MgO, (b) P_2O_5, (c) Cr, (d) Ni and (e) Co vs. SiO_2 and (f) Zr vs. Ni. Yellow diamonds represent the pristine samples (see text).

6.4.2 Major Elements

Figure 6.2a presents the univariate statistics for major oxides Al_2O_3, CaO, Fe_2O_3, K_2O, MgO, Na_2O, SiO_2 and TiO_2. Despite SiO_2 having the highest average abundance, kimberlites (including D/K1) are silica-poor rocks with an SiO_2 similar to silica-undersaturated rocks basanite, nephelinite and melilitite. The D/K1 samples have a median SiO_2 content of 43 wt%, and a large range between 37.64 - 45.97wt%. MgO ranges from 19.04 - 35.16 wt% which is within the range of Group I kimberlites defined by Le Roex et al. (2003). Al_2O_3 has a median of 5.20 wt% and a range between 3.35 - 8.54 wt%. CaO has a higher median of 6.34 wt% and ranges between 3.63 - 9.96 wt%. Alkalis K_2O and Na_2O have a median value of 0.79 and 0.95 wt% and range between 0.23 - 2.71 and 0.51 - 1.91 respectively. Finally, TiO_2 is low compared to Dawson's average kimberlite (Dawson, 1980) at 1.46 wt% and has a relatively small range from 0.99 - 2.17 wt%.

Pristine kimberlite describes samples analysed in this study which are considered to be the least altered or contaminated, and therefore the most representative of the original kimberlite melt composition. Sample LDD21_06 is the most pristine kimberlite sample analyzed in this study. It has an SiO_2 content of 37.64 wt % and MgO of 29.12 wt % (illustrated on Figures 6.7 and 6.8). Samples LDD25B_01 and _02 are also pristine relative to all other samples. (The composition of these three samples was used in Figure 6.6 to compare the D/K1 kimberlite with other global kimberlite deposits.)

The major geochemical trends of all the D/K1 samples were:

1. A strong negative correlation between SiO_2 versus MgO, TiO_2 and CaO in Groups A and C (Figs. 6.7a, b and c.).

2. Random scatter between SiO_2 versus FeO, K_2O (except Group C) and P_2O_5 (Figs. 6.7d, 6.8a and b.).

3. A positive correlation between SiO_2 versus Al_2O_3, Na_2O and CaO geochemical Groups B and D (Figs. 6.7e, f and c.))

The major geochemical trends are described below according to the four geochemical Groups (A, B, C, and D) determined using cluster analysis, which is

presented below. Each group has an individual geochemical signature which are described below. SiO_2 and MgO negatively correlate along a mixing line between Group C to B, and Group B to D with increasing SiO_2 (37.64 - 45.97 wt %) and decreasing MgO (32.58 - 19.04 wt %) (Fig. 6.7 a). Group A samples are shifted towards higher SiO_2 and MgO. A similar continuum from Groups C to B, and B to D is observed between SiO_2 versus FeO and SiO_2 versus TiO_2. Group A samples are again the exception and are shifted towards lower values of FeO and TiO_2. SiO_2 versus CaO shows a negative correlation in Groups A and C, ranging from 9.96 - 3.63 wt % respectively, but a positive correlation in Groups B and D (Fig. 6.7c). SiO_2 versus K_2O displays little correlation except Group C samples where there is a clear negative trend. The same is seen with MgO versus K_2O where samples from Groups D, B and A form a near continuum from low to high MgO, but Group C clusters separately at higher K_2O content (Fig. 6.8a). Al_2O_3 and Na_2O positively correlate with SiO_2 and also forms a continuum from Group C with the lowest values (3.35 and 0.51 wt % respectively) and Group D the highest values of 8.54 and 1.78 wt % respectively (Fig. 6.7e and f). Group A and some Group B samples behave anomalously within Al_2O_3 space showing an almost negative correlation, although this is not a strong trend (Fig. 6.7e).

Country Rock Samples

Country rock compositions are presented in Figure 6.3.

6.4.3 Trace Elements

The behaviour of trace elements in igneous rocks is controlled by partition coefficients which define how an element is distributed between the crystal phase and the melt (Blundy & Wood, 2003). This distribution is described by Equation 6.2 (Best, 2003):

$$D = \frac{concentration\_in\_mineral}{concentration\_in\_liquid} \tag{6.2}$$

Elements with D $\geq$1 are called *compatible* trace elements and preferentially partition into the ordered crystal phase. Elements with D $\leq$1 are called *incompatible* trace elements and preferentially remain into the less ordered liquid phase. Some elements display both types of behaviour when conditions in the melt change (i.e. at a peritectic) and an element becomes compatible with respect to the new stable liquidus phase. The principal compatible trace elements in kimberlites are Ni and Co, which are compatible with olivine, and Cr which is compatible with spinel (chromite). The principal incompatible trace elements in kimberlites are K, Rb, Sr, Ba, Zr, Nb, Y and the rare earth elements (REE) (Shee, 1985). Kimberlites are enriched in these elements relative to other igneous rocks (e.g. Le Roex et al. 2003). This is shown by comparing incompatible trace element abundances of basalt and kimberlite in Figures 6.2 to 6.5. The behaviour of Ba, Rb and Sr is complicated further because they are mobile elements which are easily leached by secondary alteration processes (Dawson, 1980).

Figures 6.4 and 6.5 present the ranges of all trace elements from the analysed D/K1 samples. Incompatible trace elements Zr, Sr, REE and V show an overall scatter when plotted against SiO_2. Zr versus Ni however defines an excellent negative correlation from Group D (maximum Zr of 196 ppm) to Group B to C and finally Group A with the lowest Zr content of 40.9 ppm although this sample lies away from the general trend and is probably an anomaly (Fig. 6.8f). V versus TiO_2 defines a good positive trend where Group A and D form discrete clusters and Groups B and C spread across the trend. Group A contains the lowest V content of 83.4 ppm and sample LDD10_03 from Group D contains the highest of 181 ppm, although this sample is anomalous compared to the dominant trend (Fig. 6.9e). Sr content ranges between 300-500 ppm and all groups display general overlap except Group A which is shifted slightly towards lower abundances (Fig. 6.9d).

Ba, Rb and Nb display more correlation with SiO_2. Ba, Rb and Nb versus SiO_2 are all very similar plots (Figs. 6.9a, b and c). Group C has higher Ba, Rb and Nb abundances (approximately 600-1013 ppm, 65-92 ppm and 54-153 ppm respectively) than Groups A, B and D (Fig. 6.9a, b and c). Cu versus SiO_2 in Figure 6.9f shows a positive correlation for Groups B and D and a negative correlation for Groups A and C.

Country Rock Samples

The range of trace element abundances in the country rock samples are shown in Figures 6.4and 6.5.

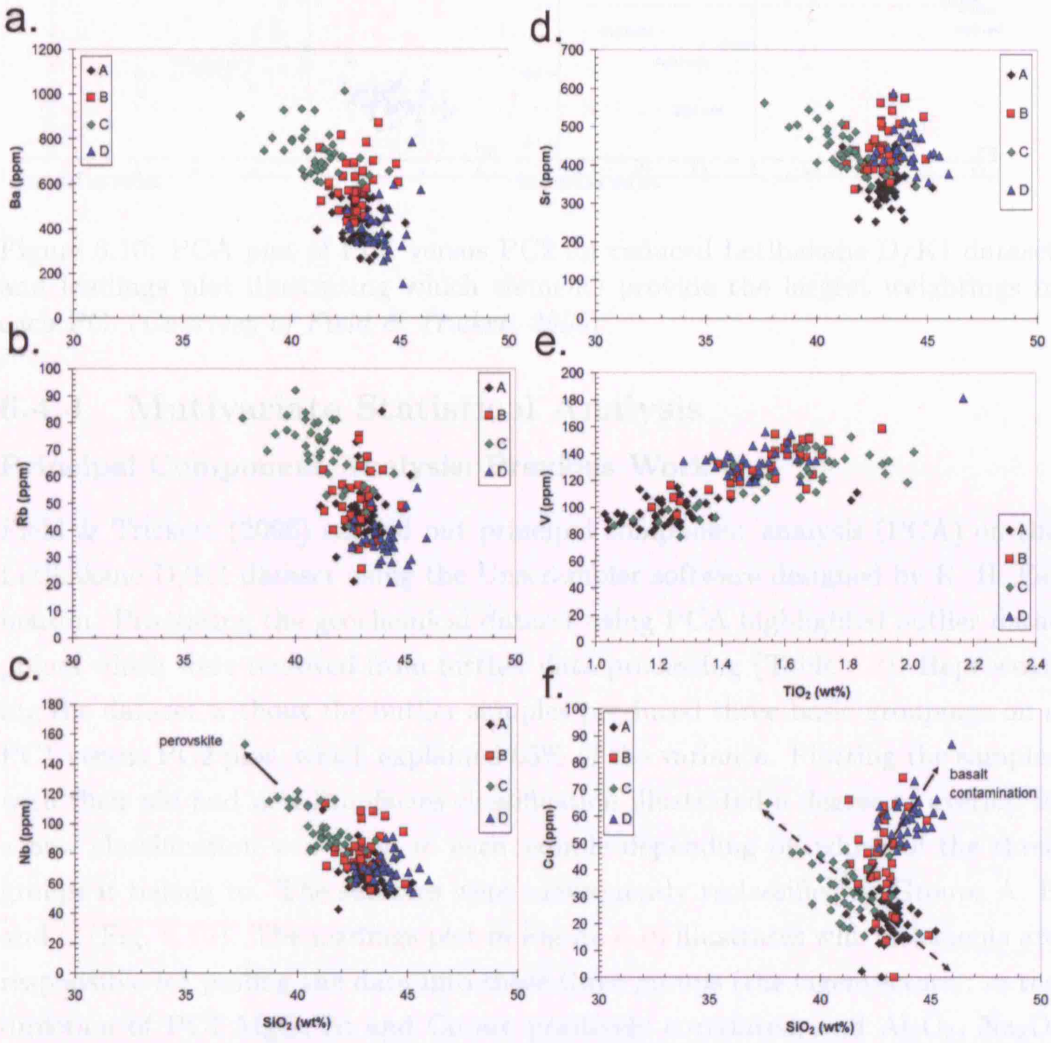

Figure 6.9: Bivariate plots of trace elements (a) Ba, (b) Rb, (c) Nb, (d) Sr, (e) V anf (f) Cu vs. SiO_2.

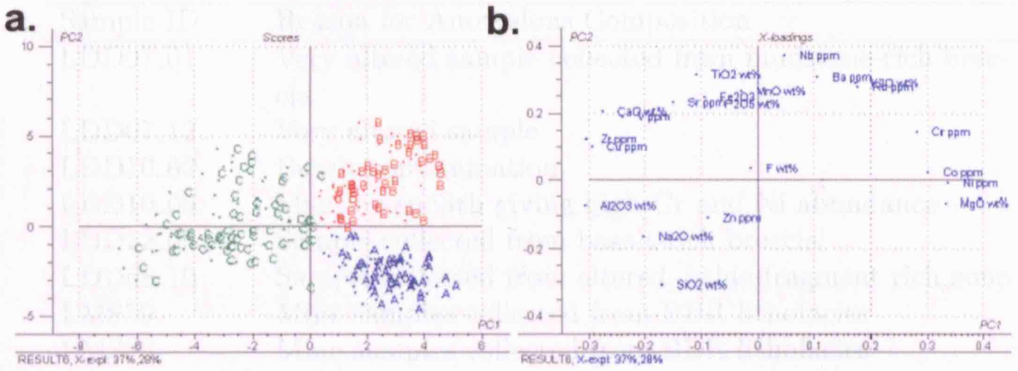

Figure 6.10: PCA plot of PC1 versus PC2 for reduced Letlhakane D/K1 dataset and loadings plot illustrating which elements provide the largest weightings in each PC. (*Courtesy of Field & Trickett 2006*)

6.4.4 Mutivariate Statistical Analysis

Principal Component Analysis; Previous Work

Field & Trickett (2006) carried out principal component analysis (PCA) on the Letlhakane D/K1 dataset using the Unscrambler software designed by K. H. Esbenson. Processing the geochemical dataset using PCA highlighted outlier datapoints which were removed from further data processing (Table 6.2). Reprocessing the dataset without the outlier samples produced three basic groupings on a PC1 versus PC2 plot, which explained 65% of the variance. Plotting the samples with their old and new lithofacies classification illustrated a degree of overlap so a new classification was given to each sample depending on which of the three groups it belong to. The samples were subsequently reclassified as Groups A, B and C (Fig. 6.10). The loadings plot in Figure 6.10 illustrates which elements are responsible for pulling the data into these three groups (the eigenvectors); in the direction of PC1 MgO, Ni and Co are positively correlated, and Al_2O_3, Na_2O, Zr and Cu are negatively correlated with the aforementioned; in the direction of PC2 Nb and TiO_2 are positively correlated and they are negatively correlated with SiO_2. If the reclassified samples highlighed inconsistencies in the delineation of lithofacies boundaries they were modified to include the new results, as shown in Figure 3.3.

Sample ID	Reason for Anomalous Composition
LDD07_01	Very altered sample collected from mudstone-rich breccia
LDD07_12	Very altered sample
LDD10_02	Basalt contamination
LDD10_09	Mantle xenolith giving high Cr and Ni abundance
LDD22_09	Sample collected from basalt-rich breccia
LDD68_10	Sample collected from altered, lithic fragment rich zone
LMS59	Mine samples collected from BBR lithofacies
LMS60	Mine samples collected from BBR lithofacies
LMS62-66	Mine samples collected from BBR lithofacies

Table 6.2: Table of outlier samples and reasons for their anomalous compositions.

Cluster Analysis

PCA divided the the D/K1 dataset into three geochemical groups which show reasonable correlation with the lithofacies divisions in the geological model. Hierarchial cluster analysis was performed as an alternative data analysis technique. The aim was to establish whether the same geochemical divisions could be reproduced by another multivariate statistical process. The processed dataset excluded the outliers identified by PCA. Geostatistical processing using cluster analysis produced five geochemical groups which are shown in the dendrogram in Figure 6.11a. The linkages between clusters are Euclidean distances which relate to the degree of similarity or variance between clusters and samples. The longer linkage distances represent weaker correlations (Junqueira-Brod et al., 2004). The small distances on the y-axis between geochemical clusters demonstrates how subtle the differences are between all samples. The small degree of variance between samples also illustrates how effective the cluster analysis technique was in subdividing this dataset.

Figure 6.11a shows five different coloured clusters. The blue and yellow clusters were linked together due to their small degreee of variance (high similarity). Four major geochemical groups were separated and interpreted; Groups A, B, C and D. Each cluster has been expanded in Figures 6.11b-f. The numbers on the x-axis relate to the position of each sample within the dataset. Each datapoint was given a new classification based on this position and assigned into one of the

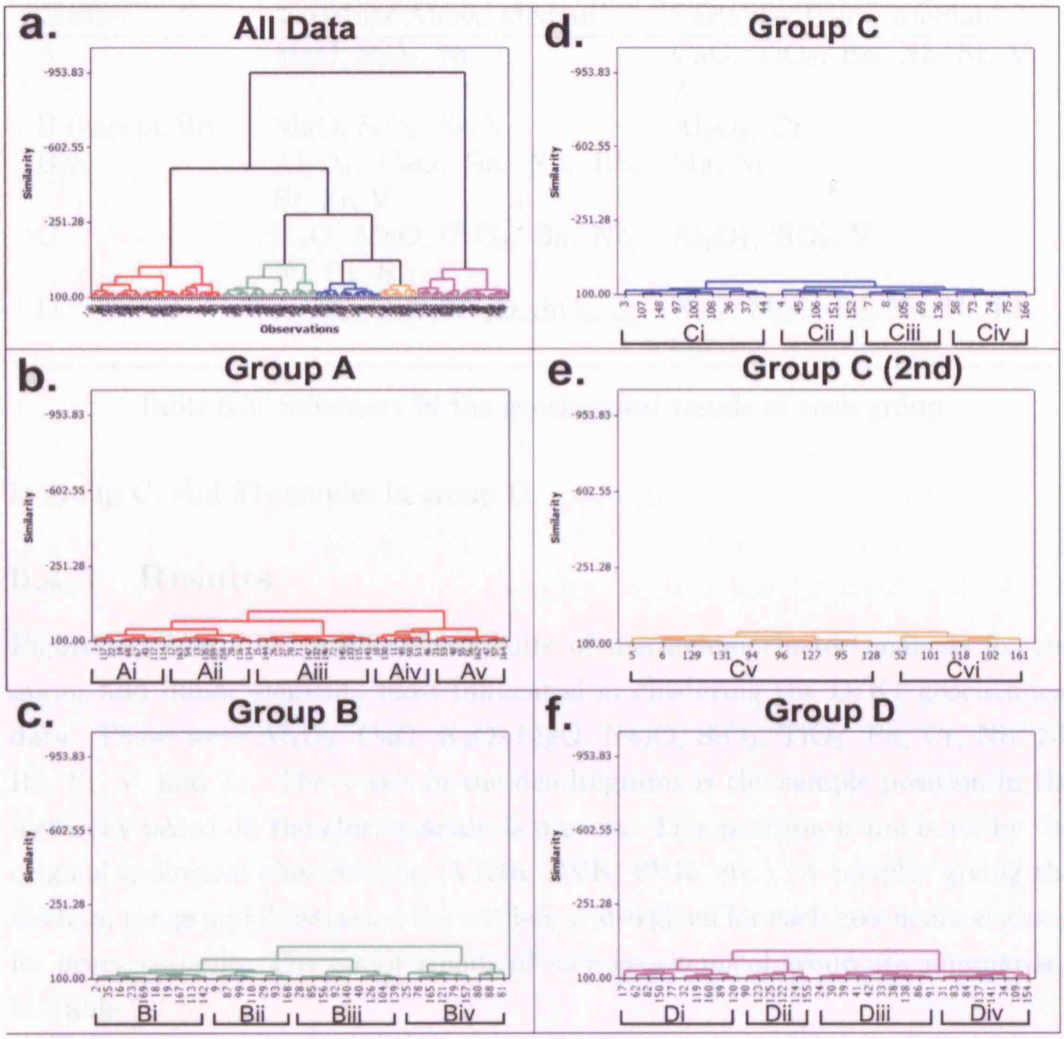

Figure 6.11: Dendrograms produced by hierarchial cluster analysis of all samples from the reduced Letlhakane D/K1 dataset. The x-axis is the hierarchial position of the sample within the processed dataset. (a) Full dataset. (b)-(f) dendrogram of each individual cluster from (a).

four groups. Each cluster was further subdivided as shown in Figures 6.11b-f. There is good correlation between field observations made in Chapter 3 and the division of each cluster. Groups A and B (except Biv) are consistent with VK1a, group C with DVK and VK1b, group D with PVK and sub-group Biv with SVK (Fig. 6.17). There are 49 samples in group A, 35 samples in group B, 38 samples

Cluster	Variables Above Median	Variables Below Median
A	MgO, SiO_2, Ni	CaO, TiO_2, Ba, Nb, Sr, V, Zr
B (except Biv)	MgO, SiO_2, Sr, V	Al_2O_3, Cr
Biv	Al_2O_3, CaO, Ba, Nb, Rb, Sr, Zr, V	Mg, Ni
C	K_2O, MgO, TiO_2, Ba, Nb, Ni, Cr, Rb	Al_2O_3, SiO_2, V
D	Al_2O_3, CaO, Na_2O, SiO_2, Zr	K_2O, MgO, Ba, Nb, Ni, Rb, Cr

Table 6.3: Summary of the geochemical trends of each group.

in group C, and 33 samples in group D.

6.4.5 Results

Figures 6.12 to 6.16 present the results of hierarchial cluster analysis for the major and minor elements most influential in clustering the D/K1 geochemical data. These were Al_2O_3, CaO, K_2O, MgO, Na_2O, SiO_2, TiO_2, Ba, Cr, Nb, Ni, Rb, Sr, V, and Zr. The x-axis in the dendrograms is the sample position in the hierarchy based on the cluster analysis process. This position is unbiased by the original geological classification (VK1a, DVK, SVK, etc.). A boxplot giving the median, range and illustrating the outliers is also given for each geochemical group for every variable. The major trends of each geochemical group are summarised in Table 6.4.5.

Cluster A

Cluster A is characterised by elevated MgO, SiO_2 and Ni and low CaO, TiO_2, Ba, Nb, Sr, V and Zr. From the dendrogram in Figure 6.11b there are 5 subsets within the cluster. All subsets have broadly similar compositions with the following exceptions: subset Aiv has elevated Ba, Cr, MgO and Sr, and depleted TiO_2 and Ni; subset Aiii is depleted in Ba; subset Av has elevated Cr (Fig. 6.15a). Spatially, cluster A correlates with the northern lobe of VK1 (Fig. 6.17).

Cluster B

Abundances of Cr, K_2O, Na_2O, Nb, SiO_2 and TiO_2 from Cluster B overlap with other Groups. There is broad geochemical scatter for the other variables. The group was divided into four sub-sets, as shown in Figure 6.11c. With the exception of subset Biv, group B demonstrates geochemical continuums with increasing abundances of Nb, TiO_2 and decreasing abundances of MgO and Ni from subset Bi to Biii. Ba content remains relatively constant; subsets Bi and Bii have very similar abundance and Biii is slightly depleted (Fig. 6.14b). Subset Biv is chemically distinct and is high in Al_2O_3, SiO_2, CaO, P_2O_5, Ba, Nb, Rb, Sr and Zr, and low in MgO, Cr and Ni. Subsets Bi to Biii display the most random spatial distribution in the pipe, predominantly located within the south-west part of VK1. Subset Biv is consistent with the location of SVK. Subset Biii cannot be correlated with a lithofacies as the samples are scattered throughout the D/K1 pipe (Fig. 6.17).

Cluster C

Cluster C has six sub-divisions (Fig. 6.11d and e). Cluster C is characterised by elevated Ba (especially in subset Cvi), Cr, K_2O, Nb (especially in subset Cv and Cvi), Ni, Rb and TiO_2 (except Cvi), and is low in Al_2O_3 and SiO_2. Subset Civ is relatively depleted in V and TiO_2. Subsets Cv and Cvi are quite distinct from the other sub-sets because of higher than average K_2O, Ba, Nb, Sr, Ni and Rb, and below D/K1 average in Na_2O and SiO_2. Within the geological model, subsets Ci, Cii and Ciii generally correlate well with the location of DVK. Subset Civ is confined exclusively to the northern tip of VK1, where VK1b is located (Section 3.5). Subset Cv is principally located $\leq$500 m elevation at the DVK-PVK contact. Subset Cvi is found $\leq$250 m elevation in the pipe, close to the wall rock (Fig. 6.17).

Cluster D

Cluster D has the most unique geochemical characteristics. It has four subsets and frequently shows bimodally distributed trends between subsets Di/Dii, and Diii/Dvi (Fig. 6.11f). In general, group D has high Al_2O_3, CaO, SiO_2, Na_2O and

Zr, and low K_2O, MgO, Ba, Nb, Ni, Rb and Cr. Subsets Di and Dii are rich in Al_2O_3, CaO, SiO_2 and depleted in Cr, MgO and Ni relative to subsets Diii and Div. Samples from Cluster D are predominantly located within the eastern side of the D/K1 pipe which is consistent with the location of the PVK lithofacies (Fig. 6.17).

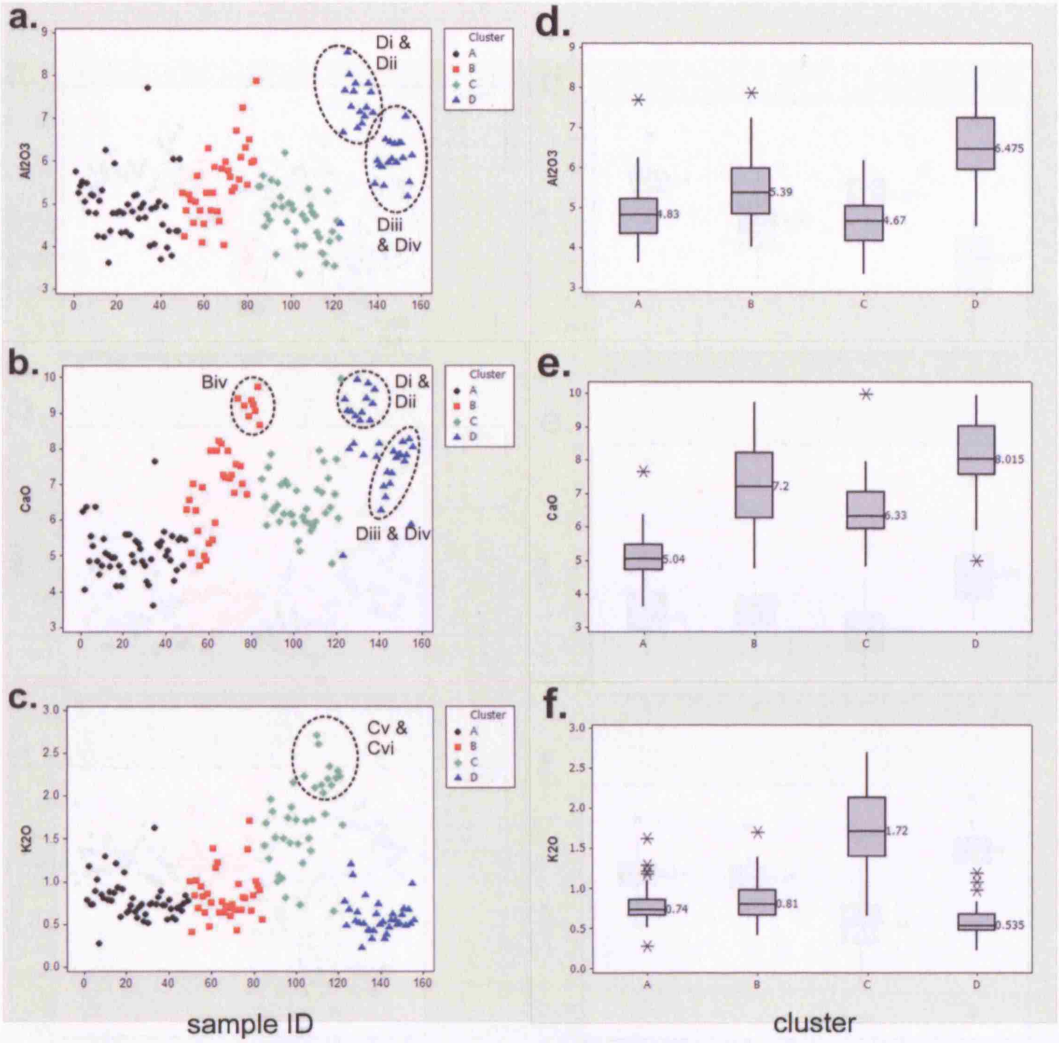

Figure 6.12: Scatterplots and boxplots illustrating the range and median of each cluster versus Al_2O_3, CaO and K_2O (wt%). The line through the centre of the box is the median, the upper and lower edges of the box are the 1st and 3rd quartiles respectively, and the whiskers represent the range. Asterisks mark outliers within the groups.

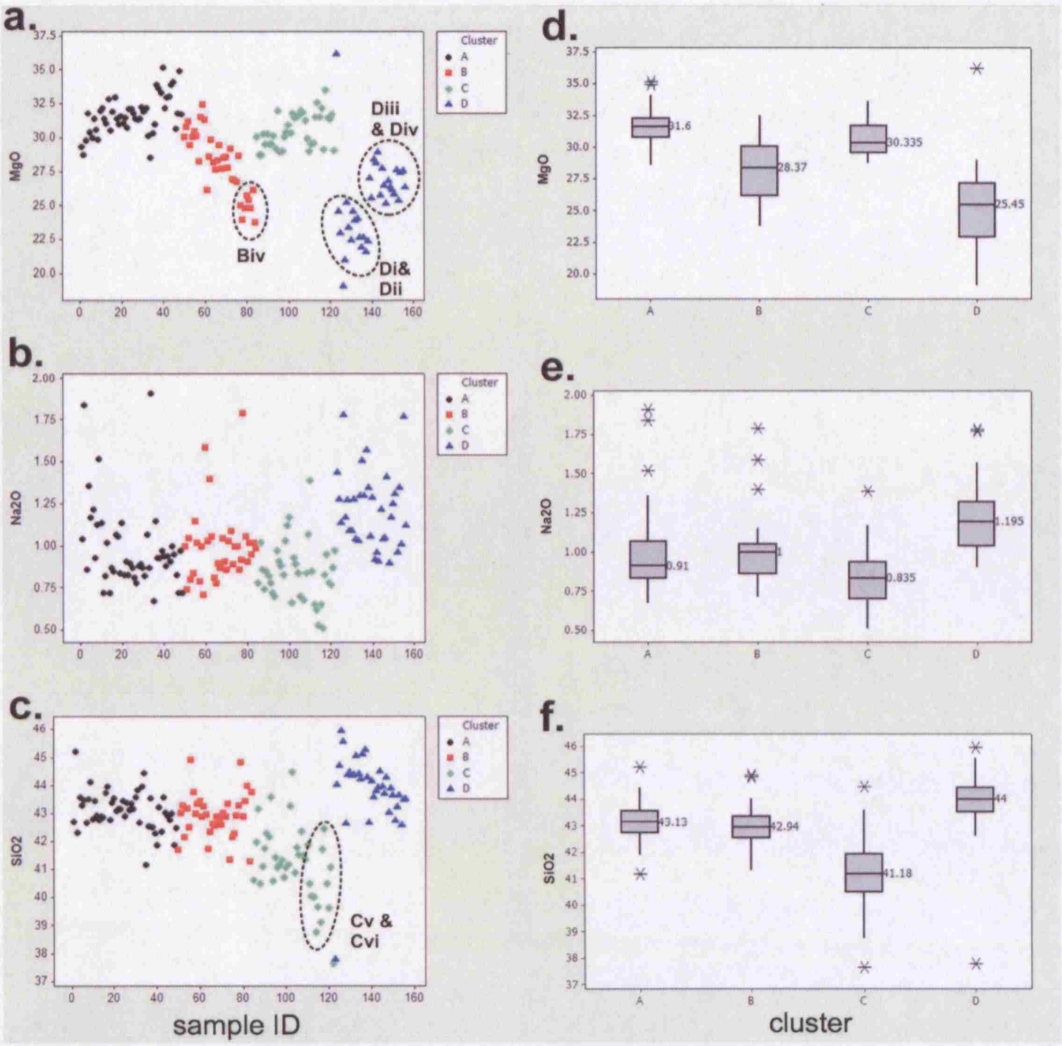

Figure 6.13: Scatterplots and boxplots illustrating the scatter, range and median of each cluster versus MgO, Na_2O and SiO_2 (wt%). Boxplots as in Figure 6.12.

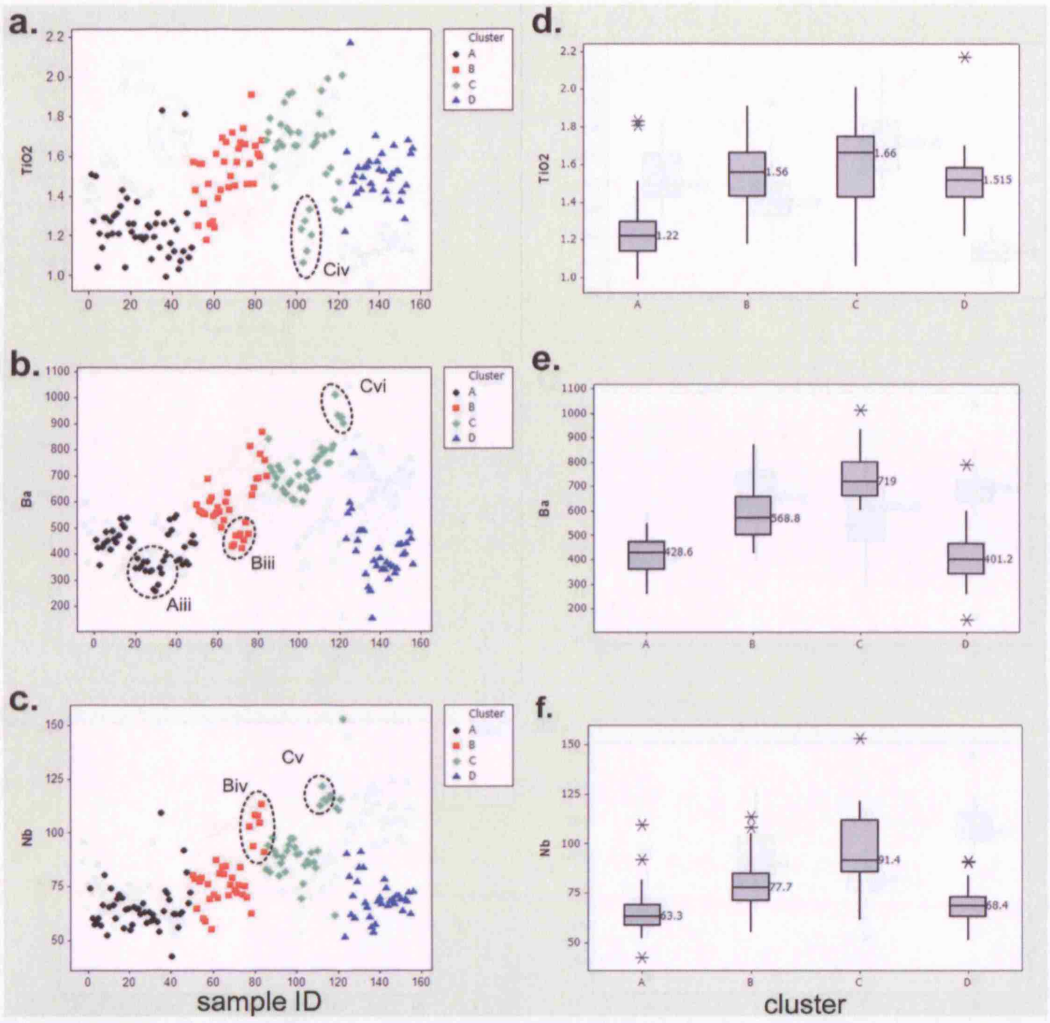

Figure 6.14: Scatterplots and boxplots illustrating the scatter, range and median of each cluster versus TiO_2, Ba and Nb (wt% and ppm). Boxplots as in Figure 6.12.

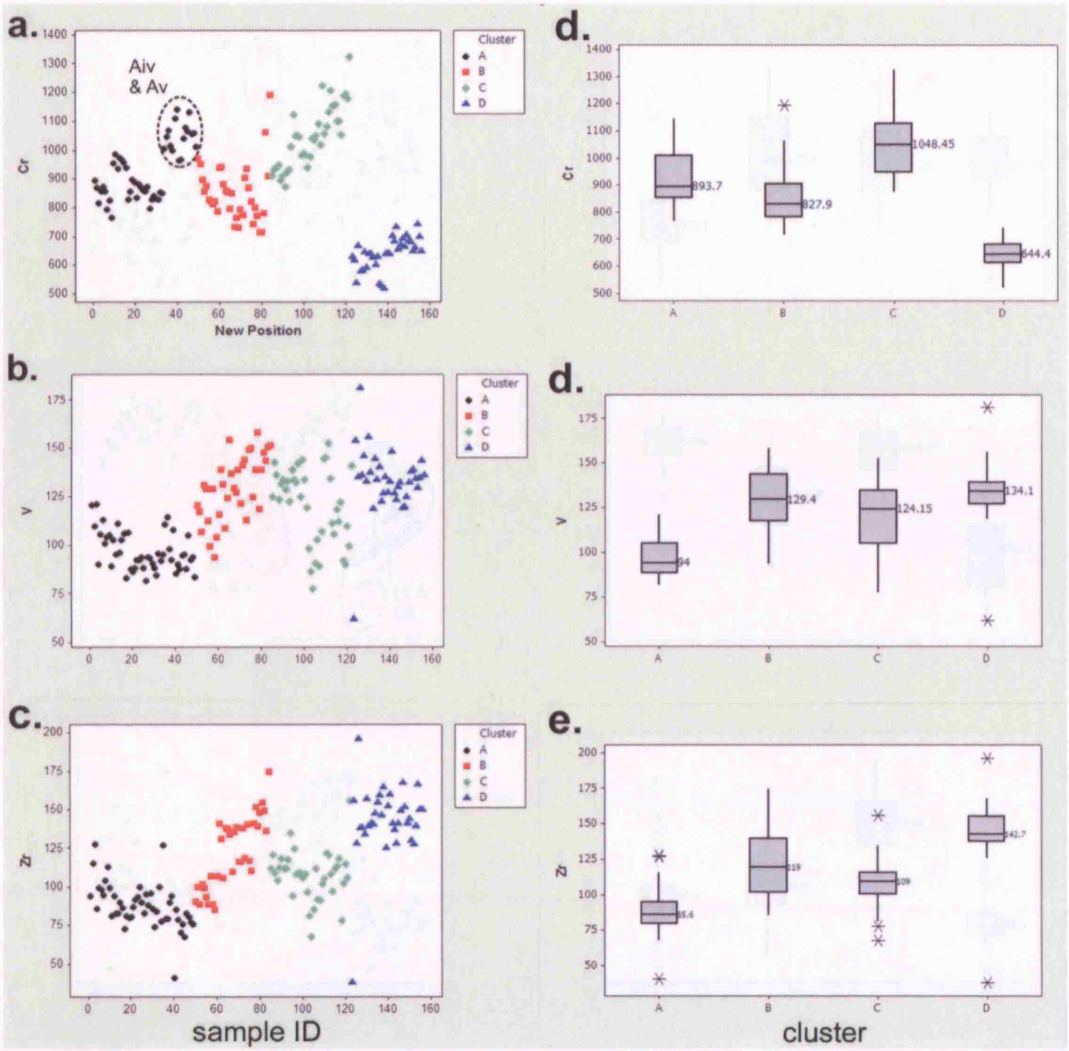

Figure 6.15: Scatterplots and boxplots illustrating the scatter, range and median of each cluster versus Cr, V and Zr (ppm). Boxplots as in Figure 6.12.

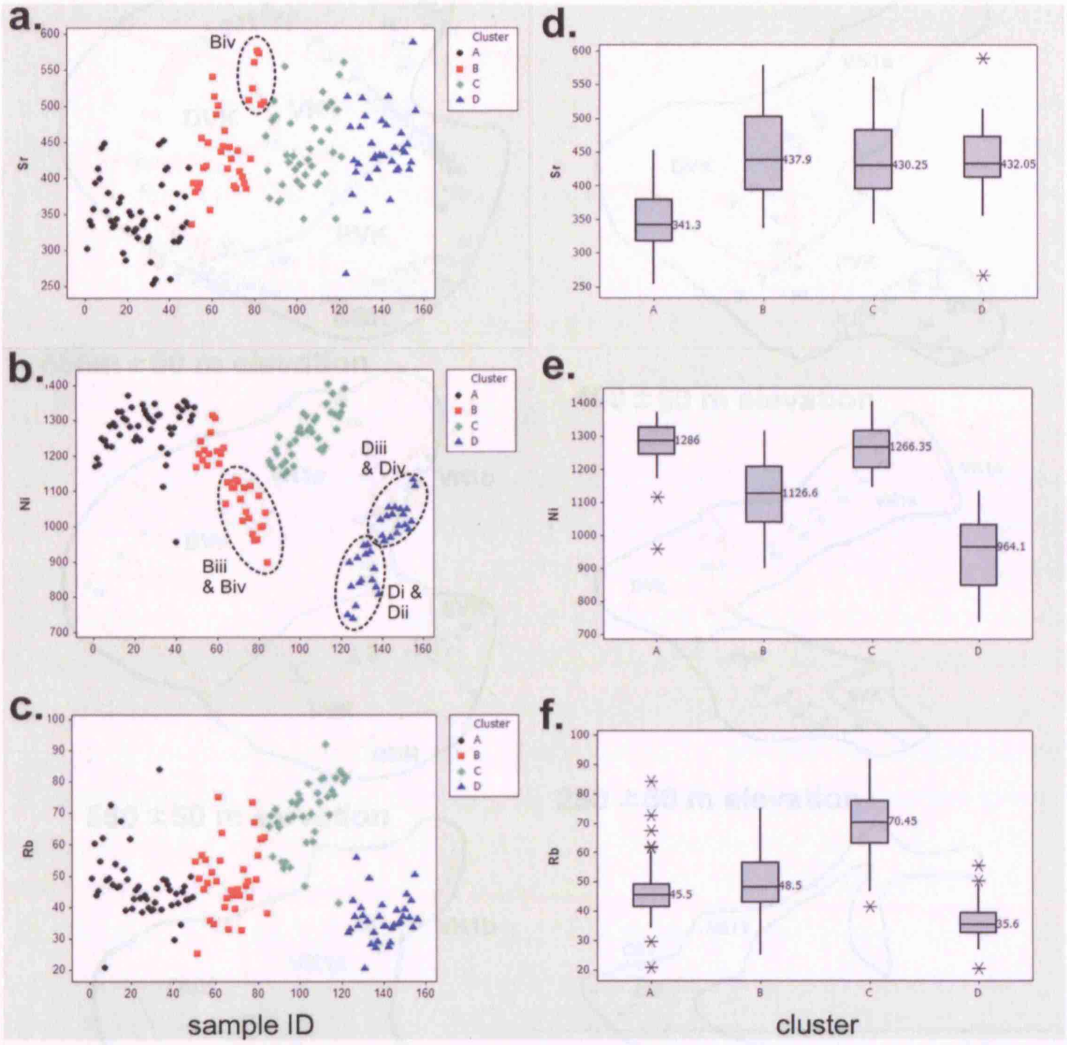

Figure 6.16: Scatterplots and boxplots illustrating the scatter, range and median of each cluster versus Sr, Ni and Rb (ppm). Boxplots as in Figure 6.12.

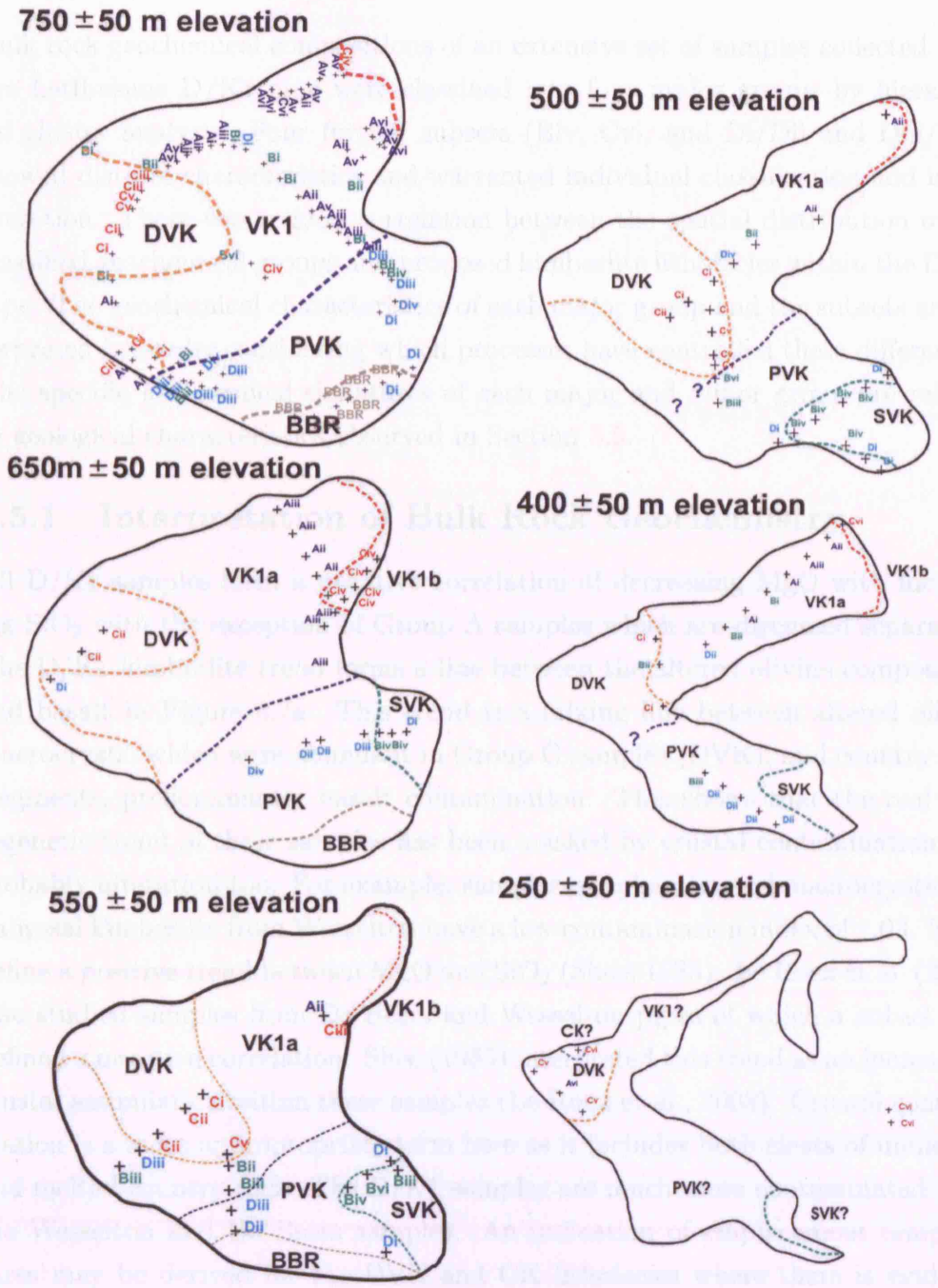

Figure 6.17: Plan sections of the D/K1 geological model with sample positions labelled by geochemical group, as defined in Figure 6.11. The boundaries have been drawn from the available drill core intersects, which diminish with depth. Consequently the boundaries become less reliable with depth.

6.5 Discussion

Bulk rock geochemical compositions of an extensive set of samples collected from the Letlhakane D/K1 pipe were classified into four major groups by hierarchical cluster analysis. Four further subsets (Biv, Cvi, and Di/Dii and Diii/Div) showed distinct characteristics and warranted individual classification and interpretation. There was a good correlation between the spatial distribution of the classified geochemical groups and proposed kimberlite lithofacies within the D/K1 pipe. The geochemical characteristics of each major group and the subsets are interpreted below by considering which processes have controlled these differences. The specific geochemical signatures of each major and minor group are related to geological characteristics observed in Section 3.5.

6.5.1 Interpretation of Bulk Rock Geochemistry

All D/K1 samples form a negative correlation of decreasing MgO with increasing SiO_2 with the exception of Group A samples which are discussed separately. The D/K1 kimberlite trend forms a line between the altered olivine composition and basalt in Figure 6.7a. This trend is a mixing line between altered olivine macrocrysts, which were abundant in Group C samples (DVK), and country rock fragments, predominantly basalt contamination. This shows that the real petrogenetic trend of these samples has been masked by crustal contamination and probably alteration too. For example, samples of aphanitic and macrocrystic hypabyssal kimberlite from Wesselton have a low contamination index of 1.03. They define a positive trend between MgO and SiO_2 (Shee, 1985). Le Roex et al. (2003) also studied samples from De Beers and Wesselton pipes of which a subset also defined a negative correlation. Shee (1985) interpreted this trend as an increase in crustal assimilation within these samples (Le Roex et al., 2003). Crustal contamination is a more appropropriate term here as it includes both clasts of unmelted and melted country rock. The D/K1 samples are much more contaminated than the Wesselton and De Beers samples. An indication of emplacement temperatures may be derived for the DVK and CK lithofacies where there is evidence of temperature driven reactions between the melt and exotic crustal inclusions. Other lithofacies did not display the same degree of reaction between melt and

host components. In fact, they are believed to have been emplaced at much lower temperatures to preserve material with a low melting threshold like coal. This issue requires a quantitative understanding of emplacement temperatures for the D/K1 kimberlite.

Mixing lines between "pristine" D/K1 kimberlite samples and contaminated samples were also observed in major oxides CaO, Al_2O_3 and to a lesser extent MgO (Fig. 6.7a,c and e). Figure 6.7e presents a basalt contamination index based on the basalt content of a number of samples on this figure. The linear geochemical trends in these plots is a signature defining the amount of contamination in the samples which is consistent with the data collected in Chapter 3. In this respect, and as previously mentioned, it is unlikely that these trends are representing the true petrogenetic behaviour of the kimberlite. However, the objective of this chapter was to differentiate the D/K1 kimberlite using bulk rock geochemistry and not to understand its petrogenesis.

In Figure 6.7c the D/K1 samples define two trends; Groups A and C define a neagtive correlation between SiO_2 and CaO, and Groups B and D which define a positive correlation. The petrographic descriptions given in Chapter 3 show that samples from Group C (the DVK and CK lithofacies) contain carbonate as a groundmass phase. Therefore geochemical Groups C represents the carbonate end-member of the D/K1 sample set. Group A samples contain comparatively rare patches of groundmass carbonate (Fig. 3.9f), but a sufficient amount to produce the same negative correlation between SiO_2 and CaO. Samples from Groups B and D typically contain more lithic fragments than A and C (Section 3.5). The positive trend in Figure 6.7c has been created by lithic fragment contamination. The basalt samples plotted in this figure show how they have influenced this trend.

SiO_2 versus K_2O shows no real correlation (Fig. 6.8a). K_2O remains approximately constant with increasing MgO. Group C however has the opposite trend; increasing K_2O and a small range in MgO content. A similar trend occurred in macrocrytal kimberlite samples from Wesselton (Shee, 1985). The anomalous enrichment in K_2O content within these samples was associated with elevated abundances of phlogopite-bearing peridotite xenoliths and phlogopite macrocrysts (Shee, 1985). By referring back to the drill core logs of these samples

from Group C the same association occurs; these samples have higher proportions of mantle xenoliths, for example the presence of glimmerite nodules in drill core LDD07. Group C contains samples LDD21_06. LDD25B_01 and _02 which belong to the CK lithofacies. CK contains phlogopite as a groundmass phase which will also contribute towards elevated K_2O content.

Group A samples show consistently different geochemical behaviour to the other groups. Samples are enriched in SiO_2 and MgO as well as trace elements Co, Ni and moderately enriched in Cr. These trace elements are compatible with olivine, except Cr which is associated with chromite. This result is consistent with the petrography of these samples (predominantly from VK1a) which have abundant altered olivine macrocrysts. Depletion in incompatible trace elements may be a side effect of dilution by olivine macrocrysts. The lithofacies which these samples belong to are depleted in groundmass components including spinel and perovskite (Chapters 3 and 4). This characteristic is discussed below in reference to the results from cluster analysis.

6.5.1.1 Interpretation of Results from Cluster Analysis

Figure 6.18 presents the results of cluster analysis performed on the major and minor elements (variables), which effectively grouped them into mantle and early phenocrysts (group iv), magma (group ii and iii) or crustal (group i) origins.

The elevated abundances of compatible elements Mg and Ni in group A indicates an accumulation of macrocrystic olivine and other mantle-derived material. This is also consistent with moderately high values of Cr, which relate to accumulation of chrome-spinel phenocrysts (Fig. 6.15d). Subsets Aiv and Av have higher Cr contents than subsets Ai to Aiii. Samples from Aiv and Av are predominantly mine samples collected from a concentrated zone within the northern tip of the pipe, close to location of samples from subset Cvi (Fig. 6.17). (Cvi has compositional similarities with subsets Aiv and Av.) Cluster A has low incompatible element abundances of Zr, Sr, Rb, Nb, TiO_2 and CaO, which suggest a low contribution from the kimberlite magma to the bulk rock geochemistry (Fig. 6.19). The abundance of Ba is comparatively low, especially in subset Aiii, relative to groups B and C. (Ba is problematic because of spectural interferences during analysis. However, there was good reproducibility in Ba content

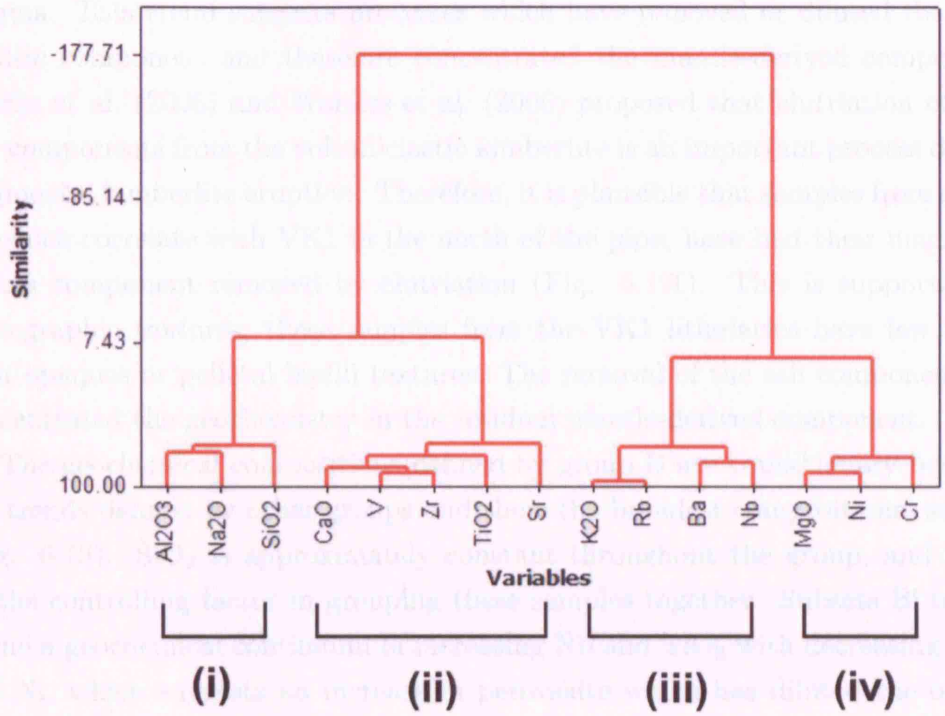

Figure 6.18: Dendrogram showing the results from hierarchial cluster analysis of selected variables (major and minor elements) illustrating four distinct groups.

between the Edinburgh and AARL datasets and therefore the given values are assumed to be reliable.) Ba was principally controlled by phlogopite crystallisation (Mitchell, 1986b), indicating that samples from group A have a low phlogopite content. Crustal derived elements Al_2O_3 and Na_2O are slightly below D/K1 average (Figs. 6.12, 6.13 and 6.2), indicating country rock contamination has not had a significant effect on the geochemical trends of group A. Figure 6.19a highlights this trend: it shows a continuum of increasing crustal contamination from group C to group D defined by increasing SiO_2 with declining MgO (c.f. Le Roex et al. 2003). However, group A is offset from this trend, showing an increase in both SiO_2 and MgO, which is consistent with the accumulation of olivine.

To summarise, group A is characterised by elevated abundances of compatible elements which are related to the accumulation of olivine and mantle-derived

material, and depletion in incompatible elements derived from the kimberlite magma. This trend suggests processes which have removed or diluted the kimberlitic component and therefore concentrated the mantle-derived component. Sparks et al. (2006) and Walters et al. (2006) proposed that elutriation of ash-size components from the volcaniclastic kimberlite is an important process during fragmental kimberlite eruption. Therefore, it is plausible that samples from group A, which correlate with VK1 in the north of the pipe, have had their magmatic or ash component removed by elutriation (Fig. 6.19f). This is supported by petrographic textures; these samples from the VK1 lithofacies have few interclast opaques or pelletal lapilli textures. The removal of the ash component has concentrated the geochemistry in the residual mantle-derived component.

The geochemical compositions defined by group B are transitionary between the trends defined by other groups and show the broadest compositional scatter (Fig. 6.19). SiO_2 is approximately constant throughout the group, and could be the controlling factor in grouping these samples together. Subsets Bi to Biii define a geochemical continuum of increasing Nb and TiO_2 with decreasing MgO and Ni, which suggests an increase in perovskite which has diluted the olivine component. Subset Bii is characterised by elevated Sr contents, which may also reflect a localised concentration in groundmass perovskite or carbonate (Mitchell, 1986b), or an increase in basalt or granite fragment content. Cluster B samples are predominantly distributed within the VK1 lithofacies (Fig. 6.17). The observed geochemical trends suggest group B (Bi to Biii) represents a volcaniclastic kimberlite with a similar paragenesis to group A, but which has had less of the kimberlitic magma component removed. These samples may be localised zones within the pipe where the rate of gas flow was lower and fewer particles were elutriated from the freshly erupted kimberlite deposit. Samples from subset Bi have very similar geochemical compositions to samples from group A, which are characterised by higher MgO and Ni and lower incompatible elements. Subset Bi samples are also located close to group A samples in the D/K1 model (Fig. 6.17). In summary, group B (Bi to Biii) represents volcaniclastic kimberlite samples with localised geochemical heterogeneities controlled by small-scale changes in their crustal and magmatic components, which have diluted the geochemical effects from mantle-derived material.

Subset Biv is geochemically distinct from Bi to Biii, and is characterised by high Al_2O_3, CaO, Ba, Sr and Zr. These variables suggest an increase in country rock fragment content, in particular granite, which has diluted the olivine macrocryst and other mantle-derived component (MgO, Cr and Ni). Na_2O and K_2O are not significantly high in subset Biv. These are highly mobile elements (Dawson, 1980) and may represent the effects of hydrothermal alteration. Samples from subset Biv spatially correlate with the location of the SVK lithofacies in the pipe, which is characterised by abundant, small altered granite lapilli. The geochemical signature of these samples is therefore substantiated by the geological characteristics.

Group C is enriched in incompatible elements and mantle-derived compatible trace elements Ni and Cr, and a relatively depleted in crustal-derived Na_2O. High Cr and Ni abundances correlate well with the high proportion of olivine macrocryst in the DVK lithofacies, from which many groups C samples were collected. Low Na_2O is consistent with the lower lithic content of these samples, especially in subset Cv which was logged with only 5 vol% lithic fragments. Subsets Cv and Cvi host samples with the lowest SiO_2 content of all D/K1 samples analysed. Cv is located at the contact between DVK and PVK, and Cvi is found below 250 m elevation consistent with the CK lithofacies, and as the satellite of kimberlite at the bottom of drill core LDD25B (Fig. 6.17). The samples from both subsets are characterised by dark, coherent kimberlite with abundant fresh olivine macrocrysts and low lithic contents, samples from subset Cv (lithofacies CK) also has a groundmass phlogopite phase. The Nb content of subsets Cv and Cvi is above group average, in particular one spurious datapoint (sample LDD21_06 from CK) with $\geq$150 ppm (D/K1 average is 71.9 ppm). This sample has the most coherent kimberlite texture seen during this study, that is characterised by abundant groundmass opaque minerals, predominantly perovskite which can explain the elevated Nb content. The high K_2O, Rb and Sr of these samples is consistent with more abundant groundmass phlogopite. Higher Ba contents, characteristic of subset Cvi, are consistent with the occurrence of groundmass carbonate (Mitchell, 1986b), which was analysed with up to 3 wt% BaO. Finally, there is a continuum from Ci, Ciii, Civ, Cv to Cvi defined by an increase in Cr content

(Fig. 6.15a), which may be proportional to increasing chromite abundance in the groundmass.

To summarise, group C displays compositional characteristics which correlate with a low lithic abundance and a high proportion of fresh olivine macrocrysts. Subsets Ci, Cii and Ciii are spatially consistent with the DVK lithofacies, which was described in Chapter 3 as an olivine-rich, competent kimberlite with moderately low lithic content and a fragmental texture. Subsets Cv and Cvi have high incompatible trace elements Nb and Cr content which correlate to the coherent nature of these kimberlite samples and groundmass phlogopite and carbonate phases. Therefore, Nb and Cr maybe used as a relative scale indicating the proportion of the primary magmatic fraction left in the deposit.

Group D has high abundance of crustal-derived elements Al_2O_3, Na_2O and SiO_2, and is significantly depleted in mantle-derived compatible elements MgO, Cr and Ni (average values 25.45, 644.4 and 964.1 respectively) relative to to D/K1 averages (30.01, 872.95 and 1207.65 respectively). As a first approximation, group D has abundant crustal contamination, predominantly basalt from the geochemical compositions, which has diluted the effects of mantle-derived components. A strong depletion in incompatible trace elements suggests the removal or dilution of the kimberlite magmatic component. Olivines are completely serpentinised in samples from this cluster, which has lowered the MgO content (Fig. 6.19d).

The geochemical trends of group D are divided between subsets Di/Dii and Diii/Div. Di/Dii are characterised by elevated Al_2O_3 and CaO, and lower MgO, Ni and Cr contents relative to Diii/Div (Figs. 6.12 and 6.13). Di is located at the edge of the PVK lithofacies adjacent to the wall rock (Fig. 6.17), suggesting a concentric zone of geochemically different kimberlite at the eastern edge of the pipe. The kimberlite samples from subset Di are characterised by abundant altered lapilli of mudstone and granite. These inclusion can explain the relative abundance of Rb and depletion of Cu relative to Dii. Samples from subset Dii were collected from the PVK lithofacies (Fig. 6.17) and are characterised by abundant juvenile lapilli (Section 3.5) and a high proportion of basalt lapilli. The kimberlite samples of geochemical subset Di also contain juvenile lapilli, which were described in Section 3.5 as mineralogically and texturally similar to the

volcaniclastic kimberlite from the SVK lithofacies. Di and Dii have very similar Al_2O_3, CaO, MgO and Zr contents to samples from subset Biv which were collected from the SVK lithofacies. This shows that exotic kimberlite inclusions have affected the bulk rock geochemical composition of their host. Subsets Diii and Div are geochemically more similar to groups A and B except for their significantly lower MgO, Cr and Ni contents, which were responsible for clustering them with Di and Dii.

Cluster D is geochemically distinct from groups A, B and C as it is low in MgO, Cr and Ni content and higher Al_2O_3, Na_2O and SiO_2. Abundances of incompatible trace elements are lower than the other groups, although this is probably a dilution effect caused by elevated Zr derived from lithic material. Group D is also interpreted as a volcaniclastic kimberlite which have been erupted by explosive fragmentation and lost its magmatic component. Subsets Di and Dii make an excellent correlation with geological observations from drill cores, and have clearly demonstrated how cluster analysis of geochemical compositions can identify geological variations in the kimberlite pipe.

6.6 Conclusion

This chapter has demonstrated how multivariate statistical analysis, in particular cluster analysis, is a powerful tool in delineating the geological variations within a single kimberlite pipe. Cluster analysis divided the analysed samples into 4 major groups with 19 subsets. Each subset has unique geochemical characterisics which correlated excellently with geological observations made from drill core logging and face mapping.

Investigating these geochemical trends reveals more significant observations regarding kimberlite emplacement, particularly from group C. Figures 6.19d and e show an elevated abundance of K_2O which is accompanied by elevated Rb but not Ba. These samples have phlogopite as a groundmass phase which was effectively absent from other lithofacies (except SVK). Furthermore, subset Cvi has a groundmass carbonate phase, and Ca-rich rims on olivine phenocrysts (Fig. 3.30d). It is therefore possible that a late-stage carbonate-rich phase (Clement, 1975) increased the partition coefficient of incompatible elements K_2O and Rb,

which crystallised as groundmass phlogopite and instead of degassing, the CO_2 dominated volatile phase crystallised as groundmass carbonate.

The separation of the dataset into groups and subsets can be explained by geochemical influences from (i) mantle-derived components, predominantly Ni and MgO consistent with olivine accumulation, and Cr from chrome-spinel accumulation (ii) magma-derived components, predominantly incompatible trace elements, CaO, K_2O and TiO_2 representing the last phases to crystallise from the magma, and (iii) crustal-derived Al_2O_3, Na_2O and to some extent SiO_2, which are consistent with observed lithic contents. This chapter has made a definitive connection between the bulk rock geochemistry and the geology and petrographic textures of the rocks. This has clearly illustrated how shallow-level processes, including those taking place during the eruption, have influenced the bulk rock geochemistry of kimberlite within the D/K1 pipe. Furthermore, this is potentially a quick and powerful tool in delineating volcaniclastic and coherent kimberlite lithofacies within a kimberlite pipe.

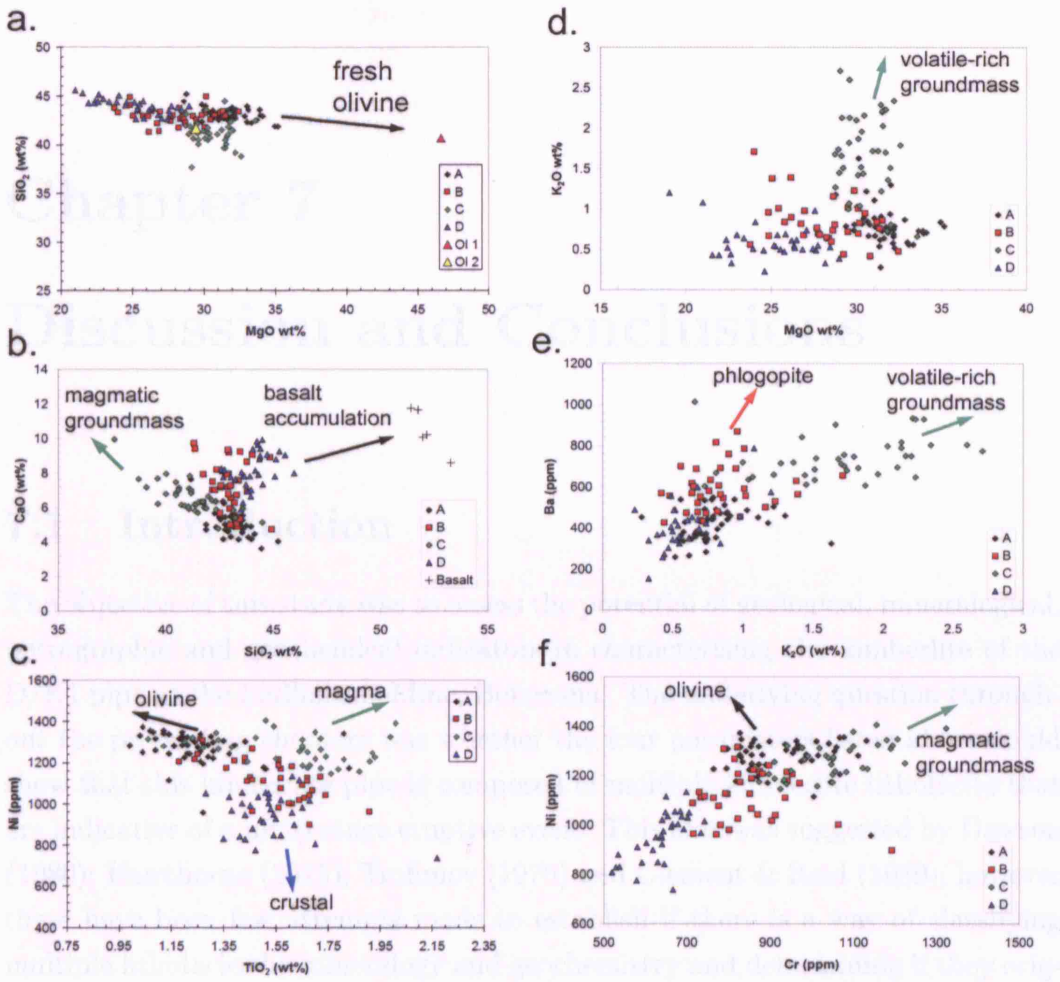

Figure 6.19: Bivariate plots presenting the results from bulk rock geochemistry illustrating trends controlled by the magma, mantle and crustal components. (a) MgO versus SiO_2 illustrating how olivine macrocrysts control the trends between geochemical groups. An example of a fresh olivine (Ol 1) and an altered (Ol 2) macrocryst are plotted for reference. (b) SiO_2 versus CaO demonstrates the effects of increased basalt lithic content and accumulation of incompatible magma-derived elements. Compositions of basalt wallrocks are plotted for reference. (c) TiO_2 versus Ni illustrating the effects of crustal-, olivine-, and magmatic-derived variables on separating the geochemical dataset. (d) MgO versus K_2O demonstrates the distinct trend of increasing K_2O in group C. (e) K_2O versus Ba shows the accumulation of volatile-rich groundmass phases in group C. (f) Cr versus Ni illustrates how the accumulation of olivine pulls group A towards higher Ni, but the magmatic-derived groundmass pulls group C to higher Cr contents

Chapter 7

Discussion and Conclusions

7.1 Introduction

The objective of this study was to assess the potential of geological, mineralogical, petrographic and geochemical indicators in characterising the kimberlite of the D/K1 pipe at the Letlhakane Mine, Botswana. The underlying question throughout the preceeding chapters was whether the four parameters listed above could show that this kimberlite pipe is composed of multiple kimberlite lithofacies that are indicative of a multi-stage eruptive event. This idea was suggested by Dawson (1980); Hawthorne (1975); Trofimov (1970) and Clement & Reid (1989), however there have been few attempts made to establish if there is a way of classifying multiple lithofacies by mineralogy and geochemistry and determining if they originate from one common batch of magma. This concept is particularly important at the Letlhakane D/K1 pipe because the kimberlite facies are very difficult to differentiate in the mine or in drill core samples. This study has presented an extensive look at the gross scale and small scale variation of the geology and petrography, the variation between lithofacies in groundmass oxide mineral compositions and bulk rock geochemistry. An attempt has been made to explain why the observed variations have occurred. This final chapter pulls together the major discussions and conclusions from the preceeding chapters into a crystallisation synthesis of the shallow level kimberlite and emplacement model.

7.2 Conclusions

The fundamental conclusions from this study were:

- The emplacement of the D/K1 kimberlite was a dynamic eruptive event which involved repeated episodes of activity that, in some cases, quarried out older deposits.
- Exotic fragments of crystallised kimberlite in younger deposits shows that mixing took place between lithofacies. The same conclusion was drawn from trends in groundmass spinel compositions.
- There was some indication of volume deficits in specific areas of the pipe from jigsaw-fragmented basalt blocks up to 600 m lower than their in situ stratigraphy. This suggests that at some stage parts of the pipe were empty.
- The current day D/K1 pipe does not conform to the classic southern African Class 1 kimberlite pipe of Hawthorne (1975) because it does not have a crater. Interpolating the rates of denudation of southern Africa by Gallagher & Brown (1999) and Brown et al. (2002) to Letlhakane, 2-3 km of post-emplacement erosion is estimated for Letlhakane, but this does not account for why a crater was preserved at Orapa A/K1, but not Letlhakane, or the many other pipes in this region. There is no reason why a crater should be present for all kimberlite pipes. However, an intraclast of bedded pyroclastic material from this study and accounts of crater-like kimberlite from previous work (Field, 1988a) indicate that the existence of a crater at the D/K1 pipe cannot be ruled out.
- Groundmass oxide compositions and compositional systematic (fO_2) are unique to some lithofacies, bridging the gap between geological/petrographic textures and groundmass mineral chemistry.
- Groundmass mineral chemistry shows that some lithofacies originated from separate parent magmas with different initial bulk melt compositions.

- Hierarchial cluster analysis of bulk rock geochemistry provided us with a quick way of delineating the D/K1 kimberlite body. Combining this with the textures of these samples demonstrated a strong correlation between grain size and geochemistry; removal of the groundmass component concentrated the remnant olivine and/or lithic fragment component. Volcaniclastic kimberlite should not be disregarded in terms of providing valuable information about the history of a kimberlite pipe.

7.3 Inferred Groundmass Crystallisation Sequence

The textures and compositions of groundmass spinel and perovskite (Chapters 4, 5) provide evidence of the sequence of crystallisation. For example, co-existence of ulvöspinel-magnetite and perovskite implies that later spinel compositions were co-crystallising with perovskite. It would be very informative to place these groundmass minerals on a phase diagram at near-surface conditions; $\leq$20 km deep corresponding to pressures of $\sim$7 kbars and magmatic temperatures between 500 – 1250 °C. Agee et al. (1982) constrain the onset of groundmass crystallisation to 965 – 1085 °C at pressures below 25-35 kbar. However, low pressure kimberlite phase diagrams have not been formed, but some have been proposed at high pressures and temperatures (e.g. Edgar et al. (1988); Edgar & Charbonneau (1993); Eggler et al. (1979); Girnis et al. (1995); Mitchell (2004); Ulmer & Sweeney (2002)). Figure 7.1 gives examples of experimentally derived phase relations in a kimberlite magma at pressures $\geq$10 kbar. Phase boundaries were extrapolated to lower pressure and temperature by comparison with experimental phase relations of an olivine melilitite at atmospheric pressure (Lloyd, 1985). Olivine melilitites provide a first order analogy to kimberlites. Therefore these boundaries only act as an approximate guide. Olivine melilitites are the result of slightly higher degrees of partial melt or a different source rock and have lower water contents than kimberlites (Brey & Green, 1977). Figure 7.1 shows the relationships between kimberlites and related rocks.

The solidus on Figure 7.1 was derived at approximately 1000 °C for calcic Group I kimberlites (Edgar et al., 1988; Edgar & Charbonneau, 1993), and at

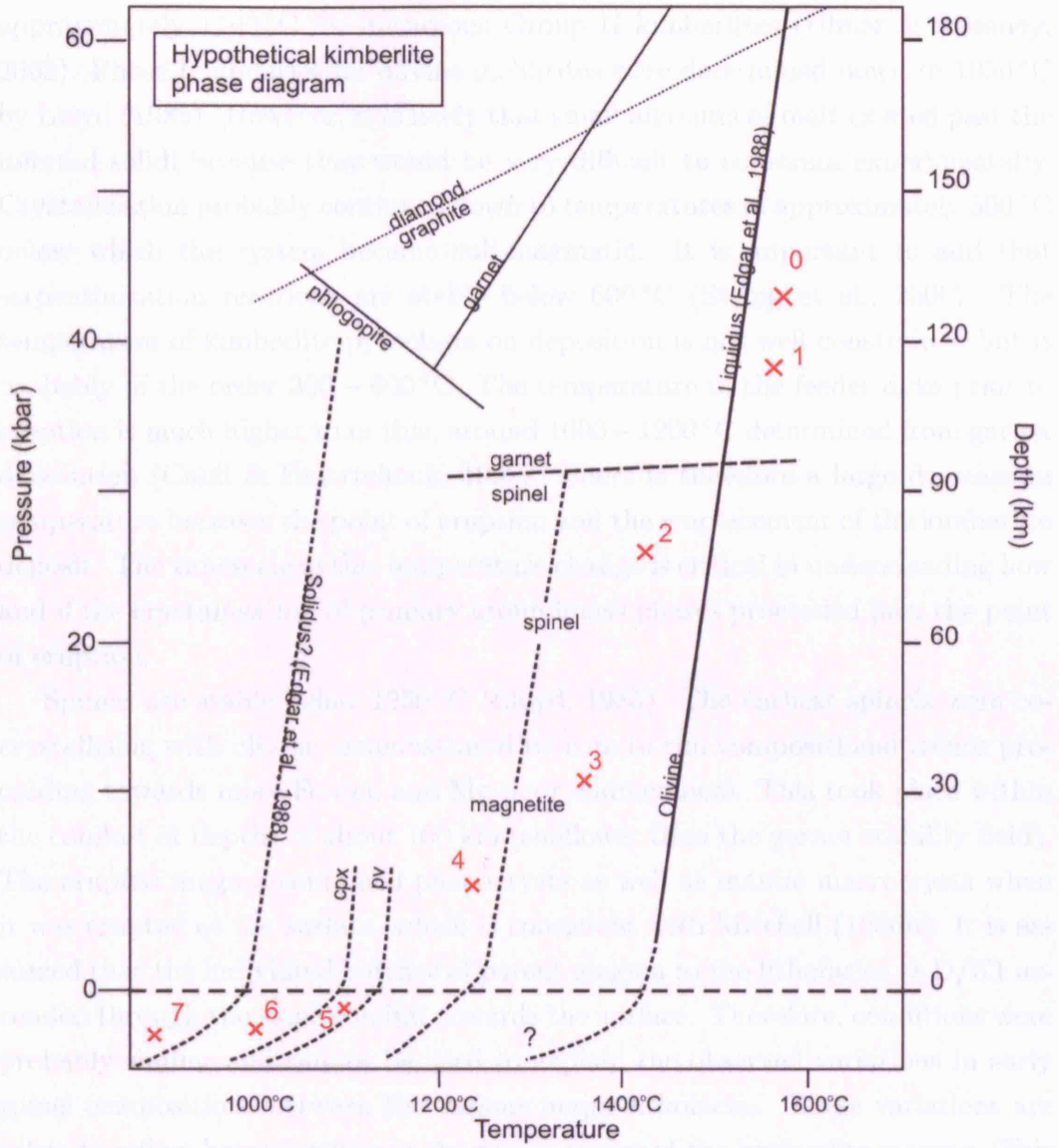

Figure 7.1: Hypothetical composite phase diagram of high and low pressure kimberlite. Adapted from phase diagrams in Ulmer & Sweeney (2002) for pressures ≥20 kbar, and Lloyd (1985) for olivine melilitite at 1 atm taken as an analogue for kimberlites at low pressure (≤10 kbars). Crystallisation sequence 1-7: L, ol + L, ol + L, ol + sp + L, ol + sp + pv + L, cpx + sp + pv + L, cpx + sp + pv + cc (where: L - liquid; ol - olivine; sp - spinel; pv - perovskite; cpx - clinopyroxene; cc - calcium carbonate.)

approximately 1100 °C for micaceous Group II kimberlites (Ulmer & Sweeney, 2002). Phase boundaries for olivine melilitites were determined down to 1050 °C by Lloyd (1985). However, it is likely that small amounts of melt existed past the inferred solidi because they would be very difficult to constrain experimentally. Crystallisation probably continued down to temperatures of approximately 500 °C below which the system became sub-magmatic. It is important to add that serpentinization reactions are stable below 600 °C (Stripp et al., 2006). The temperature of kimberlite pyroclasts on deposition is not well constrained but is probably of the order 300 – 600 °C. The temperature in the feeder dyke prior to eruption is much higher than this, around 1000 – 1200 °C determined from garnet dissolution (Canil & Fedortchouk, 1999). There is therefore a large decrease in temperature between the point of eruption and the emplacement of the kimberlite deposit. The timescale of this temperature change is critical in understanding how and if the crystallisation of primary groundmass phases proceeded past the point of eruption.

Spinels are stable below 1250 °C (Lloyd, 1985). The earliest spinels were co-crystallising with olivine, demonstrated by core to rim compositional trends proceeding towards more Fe-rich and Mg-poor endmembers. This took place within the conduit at depths of about 100 km (shallower than the garnet stability field). The erupted magma contained phenocrysts as well as mantle macrocrysts when it was erupted at the surface, which is consistent with Mitchell (1986b). It is assumed that the individual batches of parent magma to the lithofacies at D/K1 ascended through the same conduit towards the surface. Therefore, conditions were probably similar and cannot be used to explain the observed variations in early spinel compositions between the various major lithofacies. These variations are taken to reflect heterogenities in the source region of the kimberlite magma. This model is more consistent with the idea that kimberlites were produced by small degree partial melts of localized carbonated garnet lherzolite sources (Gudfinnsson & Presnall, 2003) which ascended in veins and coalesced, rather than more extensive melting of a region of metasomatised mantle (Mitchell, 2004). Compositional variation in later crystallising ulvöspinel-magnetite probably occurred during magma ascent but closer to the surface. If eruption temperatures are of the order 1000 – 1200 °C then it is feasible that spinels are still crystallising in

the feeder dyke during the eruption. There are many possible reasons why the later stage spinel compositions vary between lithofacies. Conditions in the melt would vary based on: (i) the proportion of co-crystallising phases, predominantly olivine and phlogopite contributing to the magma viscosity; (ii) differences in near-surface conditions, for example pressure and the depth at which magma began to fragment, oxygen fugacity, H_2O/CO_2 ratios; (iii) assuming crystallisation proceeded past the point of eruption then changes in eruption systematics including the amount of melt available if explosive fragmentation took place.

7.4 Emplacement Model of the D/K1 Eruption

This discussion draws together the geology, petrography and bulk rock geochemistry of the D/K1 kimberlite and relates them to the major models proposed for kimberlite emplacement outlined in Section 2.5. This interpretation is specific to the Letlhakane D/K1 pipe and is not intended to be a unilateral model for the emplacement of all kimberlite pipes worldwide. The three major kimberlite emplacement models presented in Section 2.5 are not mutually exclusive of each other; there is no clear reason why the formation of a kimberlite pipe cannot include phases of both phreatomagmatic and "dry" eruptions, as seen at other terrestrial volcanoes including Santorini. The proposed emplacement models cannot be used to explain all kimberlite eruptions and the formation of all pipes. There are clearly broad variations in the types of kimberlite pipes, (Field & Scott Smith, 1999) which are indicative of broad variations in the style of kimberlite eruptions.

Intrusive Fluidisation

Dawson (1971) developed a model whereby violent gas-expansion propelled the kimberlite explosively towards the surface from depths of 2-3 km and the diatreme was subsequently formed by intrusive fluidisation processes. There was no evidence of an explosion vent at the D/K1 pipe. However, neither mining or drilling

have reached a sufficient depth to exclude the possibility of this feature. Large-scale fluidisation would effectively mix material contained within the diatreme, but the features recognised at the D/K1 pipe are more heterogeneous, and clear packages or crude layers were presented in Chapter 3. Fluidisation processes can explain how large fragments of country rock have sunk through the pipe to great depths beneath their original location, and how an inferred block of pyroclastic kimberlite also sunk through the pipe. Rapid gas expansion in the ascending magma within 2-3 km of the surface provides a good propellent or trigger for a kimberlite eruption, which seems feasible for the Letlhakane D/K1 pipe.

Root Zone and Embryonic Pipes

Section 2.5 presented the arguments of Clement & Reid (1989) who proposed root zone and embyonic pipe formation. There is no obvious root zone at the D/K1 pipe. It is not clear whether a root zone was not intersected by drilling because it occurs at greater depth, or it does not exist at all. Clement & Reid (1989) suggested that the initiation of the diatreme took place at a depth of $\sim$ 500 m below the surface and fluidisation could extend to depths of 2 km. The depth exposed within the D/K1 pipe at Letlhakane, in addition to denudation at the surface (combined $\sim$3000 m) implies that some evidence of a root zone should have been exposed or intersected. This is also supported by the paucity of non-fragmental or hypabyssal kimberlite, with the exception of the CK, which is predominantly associated with the root zone (e.g. Clement & Skinner (1985)). The D/K1 pipe does have an irregular geometry which increases with depth. There is an inconsistency between the old and the new model regarding the pipe geometry at depth; the old model splits the pipe into three 'trouserlegs' whereas in the new model the pipe remains as one body which wraps around a large embayment of granite (see drill core LDD08 in Appendix A). There are not sufficient drill core intersects within this zone to constrain the geometry of the kimberlite body at depth. However, one drill core, LDD25B, intersects volcaniclastic kimberlite at $\sim$200 m elevation which is displaced from the modelled body. More information is needed about the nature of this 'satellite' kimberlite

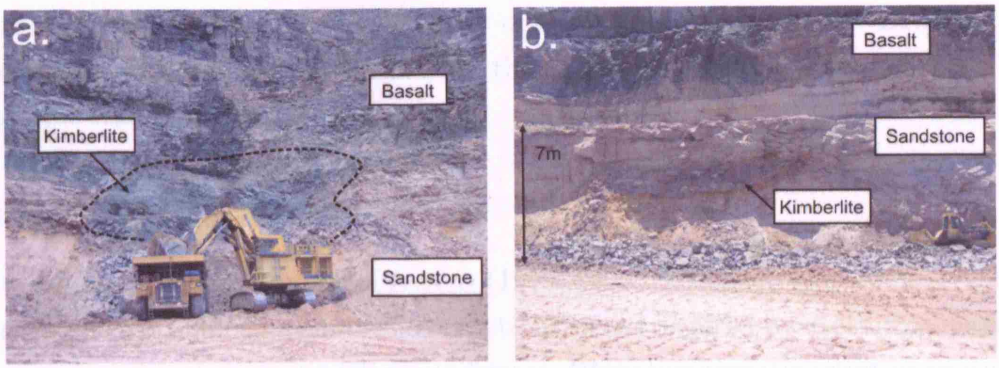

Figure 7.2: Photographs of kimberlite body located between the D/K1 and D/K2 pipes.

to establish if it fits with the 'discrete intrusions' of Clement & Reid (1989), and therefore indicating the presence of a root zone at the D/K1 pipe.

Some of the many textures that occur in the D/K1 kimberlite are consistent with Clement & Reid (1989) and their ideas which were further developed by Field & Scott Smith (1998). Gradational contacts between volcaniclastic "TKB"-type kimberlite with coherent "HK"-type kimberlite conform to preservation of a degassing front. However, the interclast textures were not indicative of the crystallisation of a degassing phase but rather a pore infill. There were no occurrences of preserved explosive subvolcanic breccias at D/K1, but there was a small kimberlite body located between the D/K1 and D/K2 pipes at the basalt to sandstone unconformity, and in the sandstone (Fig. 7.2). This strange body of kimberlite was not well constrained, but has been observed before and called LM3 (M. Field, *pers. com.*). The close proximity of the CMST-Br lithofacies (part of VK1) to the wall rock is consistent with an in situ contact breccia. However Clement & Reid (1989) described these deposits as monolithic that were formed by authigenic brecciation. This breccia at the D/K1 pipe is heterolithic and therefore not formed by authigenic brecciation, but more likely by the collapse and reworking of unstable wall rocks. The gas-solid fluidised system which established after explosive breakthrough of the surface aptly explains how large, relatively non-brecciated blocks of basalt are found in the kimberlite ~600 m below their original stratigraphy. Fluidisation processes can account for the bedded

pyroclastic intraclast (LVK) hosted by diatreme facies kimberlite. Deflation of the system would release pressure from the perimeter of the pipe and account for unstable wall rock collapses.

Phreatomagmatism

The phreatomagmatic model of Lorenz (1979, 1999); Lorenz & Kurszlaukis (2007) suggested that explosive kimberlite eruptions were triggered by ascending magma coming into direct contact with groundwater. Phreatomagmatic eruptive processes involve extreme fragmentation (up to 100%) and are typically associated with maars, tuff rings and tuff cones (Cas & Wright, 1988). Phreatomagmatic products include stratified and occasionally massive base surge deposits, finely laminated thin airfall deposits comprised of small juvenile fragments (ash and lapilli), accretionary lapilli and lithics including bombs which produce bomb sags where they impact the ground (Cas & Wright, 1988; Fisher & Schmincke, 1984). There were no examples of accretionary lapilli at Letlhakane, although they occur at other kimberlites (Arkhangelsk and Venetia) and the Argyle lamproite pipe (Kurszlaukis & Barnett, 2003; Lorenz & Kurszlaukis, 2007; Mahotkin et al., 2003). The remaining deposits cannot be excluded from explaining the D/K1 kimberlite. The finely laminated nature of the LVK lithofacies (intraclast of bedded pyroclastic) may have been produced during a phase of phreatic activity. Weinstein (2007) described phreatomagmatic deposits from the Golan Heights on the Arabian Peninsula which in some respects resemble the D/K1 kimberlite deposits. In particular, a coarse-grained lithic tuff breccia, which is composed of a poorly sorted deposit with massive layers up to 2 m thick, is texturally similar to the volcaniclastic lithofacies at Letlhakane. The major difference is the absence of preserved glass in the kimberlite, which returns to the debate regarding the primary or secondary nature of the interclast matrix of volcaniclastic kimberlites.

There was no solid evidence to argue against the involvement of water in the emplacement of the D/K1 volcaniclastic kimberlite deposits. The BBr2 lithofacies is the strongest example of kimberlite-water interaction. This breccia lithofacies was interpreted as a debris flow, and is similar to the viscous debris flows or lahars described by Lorenz (1999). This deposit may represent an earlier phase

of eruption where magma penetrated a source of groundwater, perhaps the locally known aquifer between the country rock sandstone and mudstone stratigraphies in the wall rocks at Letlhakane. Phreatomagmatic eruptions are believed to occur as a number of short-lived explosions (Cas & Wright, 1988), which could aptly explain the crude layering that characterises the D/K1 pipe infill.

7.4.1 Emplacement Model of the D/K1 Kimberlite Pipe

The observations and interpretations made in the sections above prefer the formation of the D/K1 kimberlite pipe through multiple phases of eruptions which took place over sufficient time to allow crystallisation of deposits from one phase before the eruption of another. This does not work very well with the short-lived, intrusive model proposed by Skinner & Marsh (2004). The presence of crude layering, infilled volume deficits, multiple phases of kimberlite deposits and associations with country rock breccias supports a dynamic, longer-lasting formation of the D/K1 pipe. Section 7.4 compared the characteristics of D/K1 with the interpretations of Clement & Reid (1989). There was not the exposure or drilling to sufficient depth to be certain that there is not a root zone or embryonic pipe system at D/K1. Therefore embryonic pipe formation cannot be ruled out.

The D/K1 kimberlite pipe was evidently formed by an energetic and dynamic volcanic system. The kimberlite deposits infilling the D/K1 pipe represent the waning stages of the D/K1 event. This is a common problem in interpreting volcanic bodies because we can only observe the later stages of eruptions and the exposed geology which we have access to. From careful study of the geological and petrographic features of the kimberlite it is possible to speculate and propose an emplacement model from the point at which magma began to ascend towards the Earth's surface. This synthesised model is summarised in Figure 7.3.

(i) Crystallisation of phenocrysts in the melt began in excess of 100 km within the mantle as the melt ascended towards the surface. Within 2-3 km gases in the volatile-rich melt suddenly exsolve and expand, and the magma began to fragment (Dawson, 1971). It is not clear whether the initial D/K1 eruption had a phreatomagmatic trigger. The magma was effectively propelled to the

surface where it broke through, probably via pre-existing structural weaknesses in the crust (Basson & Viola, 2004) (Fig. 7.3(i)). An initial vent was formed as material was energetically excavated which subsequently widened and deepened the vent. This was accompanied by wall rock collapses which also acted to widen and deepen the vent (Sparks et al., 2006). An eruption column was established by hot, buoyant ejected pyroclasts. The intensity of the eruption was sufficient to clear large blocks of lithic material from the vent.

(ii) The eruption column establised in Stage (i) collapsed as the pipe widened and eruption intensity diminished and the column became saturated with large, dense pyroclasts from Stage (i)[1]. At this stage the pipe began to infill (Sparks et al., 2006). VK1b is believed to be the oldest remnant kimberlite lithofacies at D/K1, and probably produced the protruding north lobe of the pipe.

(iii) VK1a erupted through VK1b, quarrying out most of this lithofacies except for a remnant at the northern wall rock contact. VK1a erupted at a diverted angle and expanded the pipe morphology to an oval shape. There were probably many phases of eruption of varying intensity as material collapsing from the wall rocks blocked the pipe and new pressure built up creating a new phase of explosivity. This accounts of the range in lithic shapes and crude layering. During the waning stages the gas flow diminished and the deposits became fluidised and acted as quasi-frictionless systems (Clement & Reid, 1989; Gernon et al., 2006; Woolsey et al., 1975).

(iv) A new pulse of eruptive activity pushed up through VK1a, producing pyroclastic material in the form of the DVK lithofacies. This phase was hotter than that of VK1, and juvenile pyroclasts agglutinated on deposition. BBr1 collapsed from the wall rocks simultaneously with the DVK eruptions as rock avalanches which incorporated VK1a and DVK deposits. During the waning phases gas fluidisation pipe(s) were formed.

[1]Comment made by R. Cas at the 2006 Kimberlite Emplacement Workshop, Canada.

(v) SVK erupted during this stage. SVK expanded the pipe geometry towards the east cutting across the VK1/DVK deposits and introduced a new generation of granite fragments into the lithic population. SVK probably erupted with concomitant wall rock collapses, however these are no longer seen in the pipe.

(vi) A second phase of activity in this region of the pipe quarried out part of the SVK and VK1 deposit, incorporating both lithofacies as porphyritic juvenile fragments. During phases of PVK activity a series of large wall rock collapses occurred on the south to south-eastern wall of the pipe, which were deposited as extensive blocky avalanche deposits and more localised debris flows (BBR), and debris flows towards the north of PVK close to the contact with VK1a (BBr2).

(vii) Explosive eruptions waned but the remaining gas flow fluidised localised zones in the pipe. Ash sized particles (~2 mm) were elutriated into the gas phase and expelled from the pipe, leaving a paucity in groundmass oxides within the interclast matrix phase. Wall rock collapses continued until the pipe walls became gravitationally stable.

(viii) The freshly deposited volcaniclastic kimberlite was permeable to meteoric waters which infiltrated the pipe and a complex hydrothermal, metamorphic environment established. Olivines were extensively serpentinised and mobile cations were leached and precipitated as serpentine and microlitic diopside interclast pore fill (c.f. Stripp et al. 2006).

The processes which produced kimberlite pipes are often deemed enigmatic because we do not know the composition of a kimberlite melt and therefore cannot accurately configure eruption dynamics, kimberlites are not well preserved in the geological record, and because we have not witnessed a kimberlite erupt. However, analogies between other volcanic rock types and kimberlites are sometimes overlooked. There are at least two other volcanic rock types which produce diatremes with similar features to kimberlites: carbonatite-melilitites and kamafugites (Junqueira-Brod et al., 2004; Stoppa, 1996; Stoppa & Principe, 1997).

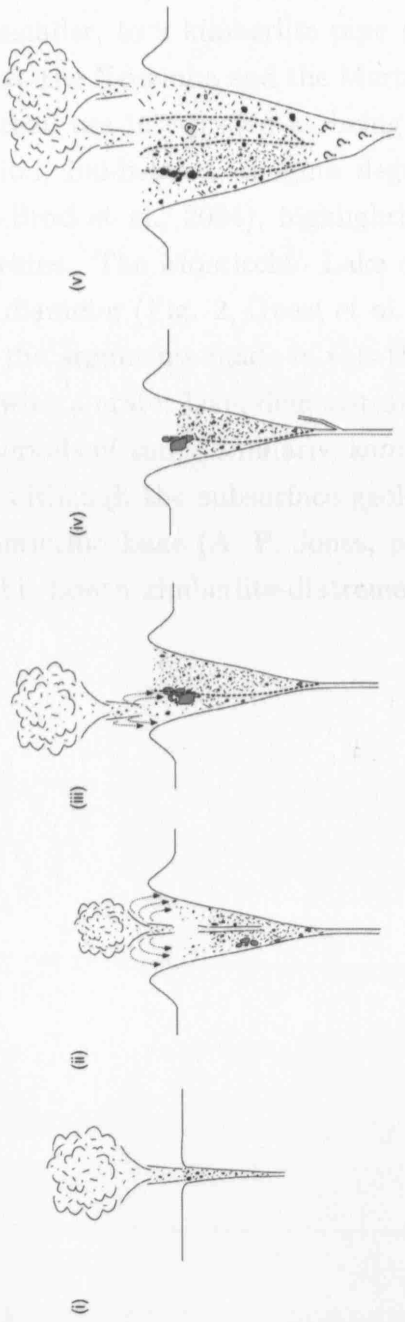

Figure 7.3: Model for possible eruption sequence for the formation of the D/K1 pipe.

Stoppa (1996) describes a "peculiar intrusive pyroclastic facies" which was produced by explosive fragmentation of a CO_2-rich carbonatite-melilitite at the San Venanzo maar in Italy. The two vents at this location are on a similar scale, if somewhat smaller, to a kimberlite pipe (Fig. 1 from Stoppa 1996). The Águas Emenadadas, the Neuzinha and the Marimbondo diatremes in the Goiás Alkaline Provine, Brazil are interpreted as being formed by processes including magma fragmentation, fluidisation, magma degassing and the formation of diatremes (Junqueira-Brod et al., 2004), highlighting a clear overlap between these rocks and kimberlites. The Monticchio Lake on Mount Vulture is a steep-sided vent ~500 m in diameter (Fig. 2, Guest et al. 1988). Monticchio Lake is fundamental to some of the arguments made in this thesis because it is infilled with sedimentary rocks with a crater lake, demonstrating that diatremes can remain open for extended periods of time. Similarly, kamafugite diatremes in Uganda are similar (Fig. 7.4), although the subsurface geology has not been explored in the same way as Monticchio Lake (A. P. Jones, *pers. comm.*). It is highly possible that they resemble how a kimberlite diatreme looked shortly after emplacement.

Figure 7.4: Photograph of kamafugite diatreme, Uganda (*taken by A. P. Jones*). Analogue to what a kimberlite pipe may look like today.

7.5 Outstanding Questions

This study has broadened our understanding of kimberlite bodies by evaluating how we can assess and quantify multiple kimberlite lithofacies within the D/K1 pipe at Letlhakane. Great potential for future study has stemmed from this research; as questions have been answered, more questions have arisen. The fundamental outstanding questions leading onto further study are:

1. Was there ever a crater above the currently exposed D/K1 pipe and how much material has been eroded?
2. What time elapsed between eruptive cycles and was there ever a point when the forming pipe (and crater) were empty? How long can a diatreme remain open for?
3. Where did crystallisation of the groundmass begin?
4. What is the temperature at eruption point of the kimberlite, and the temperature at deposition?
5. What is the interclast pore fill: primary products or secondary products of hydrothermal metamorphism?
6. How many groundmass oxides need to be analysed to be completely sure that all compositional variance has been accounted for?
7. Can other kimberlite pipes be delineated applying multivariate statistics to bulk rock geochemistry?

Bibliography

Agee, J. J., Garrison, J. R. J., & Taylor, L. A. (1982). Petrogenesis of oxide minerals in kimberlite, Elliot County, Kentucky. *American Mineralogist*, 67, 28–42. 4.9.3, 5.2, 7.3

Allan, J. F., Sack, R. O., & R., B. (1988). Cr-rich spinels as petrogenetic indicators: MORB-type lavas from the Lamont seamount chains, eastern Pacific. *American Mineralogist*, 73, 741–753. 4.2, 4.3

Armstrong, J. P., Wilson, M., Barnett, R. L., Nowicki, T., & Kjarsgaard, B. A. (2004). Mineralogy of primary carbonate-bearing hypabyssal kimberlite, Lac de Gras, Slave Province, Northwest Territories, Canada. *Lithos*, 76(1-4), 415–433. 5.2

Armstrong, K. A., Roeder, P. L., & Helmstaedt, H. H. (1997). Composition of spinels in the C14 Kimberlite, Kirkland Lake, Ontario. *Russian Geology and Geophysics*, 38 (2), 454–466. 4.3.1, 4.7, 4.9.2, 4.9.3, 4.9.4

Ballhaus, C., Berry, R. F., & Green, D. H. (1991). High pressure experimental calibration of the olivine-orthopyroxene-spinel oxygen geobarometer: implications for the oxidation state of the upper mantle. *Contributions to Mineralogy and Petrology*, 107, 27–40. (document), 4.3, 4.9.5, 4.23

Barnes, S. J. & Roeder, P. L. (2001). The range of spinel compositions in terrestrial mafic and ultramafic rocks. *Journal of Petrology*, 42(12), 2279–2302. 4.2, 4.6, 4.8, 4.9.2, 4.9.3, 4.9.4, 4.10

Barnett, W. (2004). Subsidence breccias in kimberlite pipes - an application of fractal analysis. *Lithos*, 76, 299–316. 4, 2.3.1.5

Basson, I. & Viola, G. (2004). Passive kimberlite fluid emplacement into dialating dyke-fracture systems in South Africa. *Lithos*, 76, 283 297. 2.5, 7.4.1

Beard, A. (2000). *Mineralogy and geochemistry of Devonian minor intrusions and their xenoliths from the Kola Peninsula and the Arkhangelsk region, Russia.* PhD thesis, Birkbeck College London. 6.1, 6.6

Beard, A. D., Downes, H., Hegner, E., & Sablukov, S. M. (2000). Geochemistry and mineralogy of kimberlites from the Arkhangelsk Region, NW Russia: evidence for transitional kimberlite magma types. *Lithos*, 51(1-2), 47 73. 1

Becker, M. & Le Roex, A. P. (2006). Geochemistry of South African On- and Off-craton, Group I and Group II Kimberlites: Petrogenesis and Source Region Evolution. *Journal of Petrology*, 47 (4), 673 703. 2.7

Bellis, A. & Canil, D. (2007). Ferric iron in CaTiO3 perovskite as an oxygen barometer for kimberlitic magmas: experimental calibration. *Journal of Petrology*, 48, 219 230. 5.2, 5.6.2, 5.9, 5.6.2, B.3.1

Berg, G. W. (1986). The significance of brucite in South African kimberlites. In *Kimberlites and Related Rocks*, volume 1 of *GSA Special Publication 14* (pp. 282–296).: Fourth International Kimberlite Conference Blackwell Scientific Publications. 2.6

Berryman, A., Scott Smith, B., & Jellicoe, B. (2003). Geology and diamond distribution of the 140/141 kimberlite, Fort a la Corne, Central Saskatchewan, Canada. *8th International Kimberlite Conference Long Abstract*, 1, 99 114. 2.4.2

Best, M. G. (2003). *Igneous and Metamorphic Petrology*, chapter 6: Chemical dynamic of melts and crystals, (pp. 122–148). Blackwell Publishing. 4.9.5, 5.6.2, 6.4.3

Blundy, J. & Wood, B. (2003). Partitioning of trace element between crystals and melts. *Earth and Planetary Science Letters*, 210, 383–397. 6.4.3

Boctor, N. A. & Meyer, H. O. A. (1979). Oxide and sulphide minerals in kimberlite from Green Mountain, Colorado. In *Proceedings of the Second International Kimberlite Conference. Kimberlites, Diatremes and Diamonds: Their Geology, Petrology and Geochemistry*, volume 1 (pp. 217–228). Washington D.C.: American Geophysical Union. 5.5, 5.6.1

Boctor, N. Z. & Boyd, F. (1980). Oxide minerals in the Liqhobong kimberlite, Lesotho. *American Mineralogist*, 65, 631–638. 5.2, 5.1, 5.6.1

Boctor, N. Z. & Boyd, F. R. (1981). Oxide minerals in a layered kimberlite-carbonate sill from Benfontein, South Africa. *Contributions to Mineralogy and Petrography*, 76, 253–259. 5.2, 5.6.1

Boyd, F. R. & Gurney, J. J. (1986). Diamonds in the African Lithosphere. *Science*, 232, 472–477. 2.1.1

Brey, G. & Green, D. H. (1977). Systematic study of liquidus phase relations in olivine melilitites + H2O + CO2 at high pressures and petrogenesis of an olivine melilitite magma. *Contributions to Mineralogy and Petrology*, 61, 141–162. 7.3

Brod, J. A., Gaspar, J. C., Diniz-Pinto, H. S., & Junqueira-Brod, T. C. (2005). Spinel chemistry and petrogenetic processes in the Tapira alkaline-carbonatite comples, Minas Gerais, Brazil. *Revista Brasileira de Geociencias*, 35, 23–32. 4.9.2

Brown, R. J., Tait, M., Field, M., & Sparks, R. S. J. (2006). Progressive enlargement and infill of a kimberlite pipe: K2 pipe, Venetia Kimberlite Field, Limpopo Province, South Africa. In *2006 Kimberlite Emplacement Workshop Long Abstracts* (pp. 1–5). 3.5.2, 3.6.1

Brown, R. W., Summerfield, M. A., & Gleadow, A. J. W. (2002). Denudational history along a transect across the Drakensberg Escarpment of southern Africa derived from apatite fission track thermochronology. *Journal of Geopysical Research*, 107, 1–18. 2.2.1, 7.2

Bulanova, G. P. (1995). The formation of diamond. *Journal of Geochemical Exploration*, 53(1-3), 1–23. 2.3.1.4

Canil, D. & Bellis, A. (2007). Ferric iron in CaTiO3 perovskite as an oxygen barometer for kimberlite magmas II: applications. *Journal of Petrology*, 48, 231–252. (document), 5.2, 5.10, 5.6.2

Canil, D. & Fedortchouk, Y. (1999). Garnet dissolution and the emplacement of kimberlites. *Earth and Planetary Science Letters*, 167(3-4), 227–237. 7.3

Capaccioni, B. & Cuccoli, F. (2005). Spatter and welded air fall deposits generated by fire-fountaining eruptions: Cooling of pyroclasts during transport and deposition. *Journal of Volcanology and Geothermal Research*, 145, 263–280. 2.4.5, 3.6.1

Carmichael, I. S. E. (1991). The redox state of basic and silicic magmas: a reflection of their source regions? *Contributions to Mineralogy and Petrology*, 106, 129–141. 5.6.2

Cas, R. A. F. & Wright, J. V. (1988). *Volcanic successions, modern and ancient : a geological approach to processes, products and successions.* Unwin Hyman. pp 544. 2.4.3, 2.4.4, 2.4.5, 2.5, 3.1, 3.4, 3.28, 3.6.1, 3.6.1, 3.6.1, 7.4

Chakhmouradian, A. & Mitchell, R. (2001). Three compositional varieties of perovskites from kimberlites of the Lac de Gras field (Northwest Territories, Canada). *Mineralogical Magazine*, 65(1), 133–148. 4.1, 5.2, 5.1, 5.2, 5.5, 5.6.1, 5.7

Chakhmouradian, A. R. & Mitchell, R. H. (2000). Occurrence, alteration petterns and compositional variation of perovskite in kimberlites. *The Canadian Mineralogist*, 38, 975–994. 4.9.4, 5.1, 5.2, 5.2, 5.5.3, 5.6.1, 5.6.2

Chalapathi Rao, N. V. C., Gibson, S. A., Pyle, D. M., & Dickin, A. P. (2004). Petrogenesis of proterozoic lamproites and kimberlites from the Cuddapah Basin and Dharwar Craton, southern India. *Journal of Petrology*, 45(5), 907–948. 2.1.1, 6.1, 6.6

Clarke, D. & Mitchell, R. H. (1975). Mineralogy and petrology of the kimberlite from Somerset Island, N.W.T., Canada. *Physics and Chemistry of the Earth*, 9, 123–135. 5.2

Clement, C. & Skinner, E. (1985). A textural-genetic classification of kimberlites. *Transactions of the Geological Society of South Africa*, 88, 403–409. 2.2, 2.3.1.2, 2.3.1.5, 2.3.3, 2.7, 2.4.4, 2.4.5, 3.3, 3.6.1, 3.6.2, 6.1, 7.4

Clement, C. R. (1975). The emplacement of some diatreme-facies kimberlites. *Physics and Chemistry of the Earth*, 9, 51–59. 2.3.1.5, 2.5, 2.6, 4.9.5, 6.6

Clement, C. R. & Reid, A. M. (1989). The origin of kimberlite pipes: An interpretation based on a synthesis of geological features displayed by southern African occurrences. In *Kimberlite and Related Rocks: Their Composition, Occurrence, Origin and Emplacement*, volume 1 of *GSA Special Publication* (pp. 634–646). Perth: Proceedings of the Fourth International Kimberlite Conference Blackwell Scientific Publications. 2.2, 2.3.1.5, 2.4.4, 2.4.5, 2.5, 2.5, 2.5, 2.6, 2.6, 3.6.1, 3.6.1, 3.6.1, 3.6.1, 7.1, 7.4, 7.4, 7.4.1

Clement, C. R. & Skinner, E. M. W. (1979). A textural classification of kimberlite rock. In *Kimberlite Symposium II* (pp. 129–139). Cambridge, England: De Beers Consolidated Mines Ltd. Extended Abstracts. 2.2, 2.3, 2.4.4, 2.4.5, 2.4.6

Clement, C. R., Skinner, E. M. W., & Scott Smith, B. H. (1984). Kimberlite redefined. *Journal of Geology*, 92, 223–228. 2.1, 2.3.1.3

Cox, K., Gurney, J., & Harte, B. (1973). *Xenoliths from the Matsoku Pipe*, (pp. 76–100). Cape and Transvaal Printers Ltd., Cape Town. 2.3.1.1

Cox, R. A. & Wilton, D. H. C. (2006). U-pb dating of perovskite by LA-ICP-MS: An example from the Oka carbonatitie, Quebec, Canada. *Chemical Geology*, 235, 21–32. D.1, D.3, D.4

Creaser, R. A., Herman, G., Carlson, J., & Crawford, B. (2004). Macrocrystal phlogopite RbSr dates for the Ekati property kimberlites, Slave Province, Canada: evidence for multiple intrusive episodes in the Paleocene and Eocene. *Lithos*, 76, 399–414. 8th International Kimberlite Conference. 2.1.1

Danchin, R. V., Ferguson, J., McIver, J. R., & Nixon, P. H. (1975). The composition of late-stage kimberlite liquids as revealed by nucleated autoliths. *Physics and Chemisty of the Earth*, 9, 235–245. 2.3.2

Dawson, J. (1972). Kimberlites and their relation to the mantle. *Philosophical transactions to the Royal Society London*, 271, 297–311. 2.1.1

Dawson, J. (1980). *Kimberlites and their Xenoliths*. Springer Verlag. 2.1, 2.2, 2.3, 2.3.1, 2.3.1.1, 2.3.1.5, 2.4.1, 2.4.2, 2.4.4, 2.5, 2.5, 2.6, 2.7, 4.9.5, 6.2, 6.4.2, 6.4.3, 6.5.1.1, 7.1

Dawson, J. B. (1971). Advances in kimberlite geology. *Earth Science Reviews*, 7, 187–214. 2.3.1.5, 2.4.1, 2.5, 2.5, 2.7, 4.9.5, 7.4, 7.4.1

Dawson, J. B. (1986). Geographic and time distribution of kimberlites and lamproites: relationships to tectonic processes. In J. Ferguson (Ed.), *Kimberlites and Related Rocks: Their Composition, Occurrence, Origin and Emplacement*, volume 1 of *GSA Special Publication* (pp. 323–342).: Proceedings of the Fourth International Kimberlite Conference Blackwell Scientific Publication. 2.1.1, 6

Dawson, J. B. (1987). The kimberlite clan: relationship with olivine and leucite lamproites, and inferences for upper-mantle metasomatism. *Geological Society Special Publication*, 30, 95–101. 2.7, 2.1

Dawson, J. B. (1994). Quaternary kimberlitic volcanism on the Tanzania Craton. *Contributions to Mineralogy and Petrology*, 116(4), 473–485. 2.4.1

Dawson, J. B. & Hawthorne, J. B. (1970). Intrusion features of some hybabyssal south African kimberlites. *Bulletin of Volcanology*, 34, 740–757. 2.3.1.5, 2.4.1

Deer, W. A., Howie, R. A., & Zussman, J. (1983). *An introduction to the rock forming minerals*. Longman. pp. 538. 2.6

Deines, P. & Harris, J. W. (2004). New insights into the occurrence of 13C-depleted carbon in the mantle from two closely associated kimberlites: Letlhakane and Orapa, Botswana. *Lithos*, 77, 125–142. 1.3, 2.3.1.4

Dominy, S., Noppe, M., & Annels, A. (2002). Errors and uncertainty in mineral resource and ore reserve estimation: The importance of getting it right. *Exploration Mining Geology*, 11, 77 98. 3.1.1

Dunbar, N. W., Jacobs, G. K., & Naney, M. T. (1995). Crystallisation processes in an artificial magma: variations in crystal shape, growth rate and composition with melt cooling history. *Contributions to Mineralogy and Petrology*, 120, 412 425. 4.9.5

Eccles, R. D., Heaman, L. M., Luth, R. W., & Creaser, R. A. (2004). Petrogenesis of the Late Cretaceous northern Alberta kimberlite province. *Lithos*, 76, 435 459. 2.3.2

Edgar, A. D., Arima, M., Baldwin, D. K., Bell, D. R., Shee, S. R., Skinner, W. M. W., & Walker, E. (1988). High-pressure-high temperature melting experiments on a SiO2-poor aphanitic kimberlite from the Wessleton mine, Kimberly, South Africa. *American Mineralogist*, 73, 524 533. 4.9.2, 7.3, 7.3

Edgar, A. D. & Charbonneau, H. E. (1993). Melting experiments on a SiO2-poor CaO-rich aphanitic kimberlite from 5-10 GPa and their bearing on sources of kimberlite magmas. *American Mineralogist*, 78, 132 142. (document), 4.9.2, 4.22, 4.9.5, 7.3, 7.3

Eggler, D. H., McCallum, M. E., & Smith, C. B. (1979). Megacryst assemblages in kimberlite from Northern Colorado and Southern Wyoming: Petrology, geochemetry-barometry, and areal distribution. In *Proceedings of the Second International Kimberlite Conference*, volume 2 (pp. 213 226). Washington D.C.: American Geophysical Union. 2.3.1.2, 7.3

Faure, F., Trolliard, G., Nicollet, C., & Montel, J.-M. (2003). A developmental model of olivine morphology as a function of the cooling rate and the degree of undercooling. *Contributions to Mineralogy and Petrology*, 145, 251263. 4.3.1

Fedortchouk, Y. & Canil, D. (2004). Intensive variables in kimberlite magmas, Lac de Gras, Canada and implications for diamond survival. *Journal of Petrology*, 45(9), 1725–1745. 5.6.2

Ferguson, J., Martin, H., Nicolaysen, L., & Danchin, D. (1975). Gross Brukkaros: A kimberlite-carbonatite volcano. *Physics and Chemistry of the Earth*, 9, 219–234. 2.4.1

Field, M. (1988a). *Notes on a visit to Orapa and Letlhakane Mines, Botswana.* Technical report, Anglo American Research Laboratories. 3.2, 3.2, 7.2

Field, M. (1988b). *The petrography of kimberlite specimens from Letlhakane D/K1 Mine, Botswana.* Technical report, Anglo American Research Laboratories. (document), 2.2.1, 3.1

Field, M. (1988c). *The petrography of rock specimens from the LM1 and LM2 TKBs, Letlhakane D/K1, Botswana.* Technical report, Anglo American Research Laboratories. 3.2

Field, M. (1991). *The petrography of samples from various levels in the Letlhakane D/K1 kimberlite, Botswana.* Technical report, Anglo American Research Laboratories. Kimberlite research and services laboratory. 3.2

Field, M., Gibson, J. G., Wilkes, T. A., Gababotse, J., & Khutjwe, P. (1997). The geology of the Orapa A/K1 kimberlite Botswana: Further insight into the emplacement of kimberlite pipes. *Geologiya I Geofizika*, 38(1), 25 41. 1.3, 2.2.1, 2.3.1.5, 2.4.3, 2.4.6, 3.6.1

Field, M. & Scott Smith, B. (1998). Textural and genetic classification schemes for kimberlite: A new perspective. *VIIth International Kimberlite Conference*, 1, 214–216. 1.3, 2.2, 2.4.5, 3.5.7, 7.4

Field, M. & Scott Smith, B. (1999). Contrasting geology and near-surface emplacement of kimberlite pipes in southern Africa and Canada. *VIIth International Kimberlite Conference*, 1, 217–237. 2.4, 2.3.2, 2.5, 3.6.1, 3.6.1, 7.4

Field, M. & Trickett, S. K. (2006). *Geochemistry of Samples from Letlhakane DK1: Constraints on the Geological Model.* Technical report, De Beers Consolidated Mines Ltd. (document), 6.10, 6.4.4

Fipke, C., Guerney, J., & Moore, R. (1995). *Diamond exploration techniques emphasising indicator mineral geochemistry and Canadian examples*, volume 423. Geological Survey of Canada. 2.1

Fisher, R. & Schmincke, H. (1984). *Pyroclastic Rocks*. Springer Verlag. pp. 472. 2.3.1.5, 2.3.2, 2.4.5, 3.1, 3.6.1, 3.6.1, 7.4

French, B. V. (1998). *Traces of Catastrophe: A Handbook of Shock Metamorphic Effects in Terrestrial Meteorite Impact Structures*. Lunar and Planetary Institute. 2.3.1.4

Frost, B. R. (1991). *Introduction to oxygen fugacity and its petrologic importance*, volume 25 of *Reviews in Mineralogy*, chapter 1, (pp. 1 8). Mineralogical Society of America. 5.6.2

Gallagher, K. & Brown, R. (1999). Denudation and uplift at passive marigins: the record on the Atlantic Margin of southern Africa. *Philosophical Transactions of the Royal Society of London*, 357, 835 859. 2.2.1, 7.2

Gernon, T. M., Sparks, R. J. S., Brown, R. J., & Field, M. (2006). Gas-segregation pipes in kimberlite: evidence for fluidisation at Orapa South Pipe, Botswana. In *2006 Kimberlite Emplacement Workshop Long Abstracts* (pp. 1 5). Saskatoon, Canada: 8th International Kimberlite Conference. 2.5, 3.6.1, 3.6.1, 7.4.1

Girnis, A. V., Brey, G. P., & Ryabchikov, I. D. (1995). Origin of Group 1a Kimberlites - fluid-saturated melting experiments at 45-55 Kbar. *Earth and Planetary Science Letters*, 134(3-4), 283 296. 4.9.2, 7.3

Govindaroju, K. (1994). Comilation of working values and sample descriptions for 383 geostandards. *Geostandards Newsletter*, 18, 1 158. 6.3.1, B.4

Gregoire, M., Rabinowicz, M., & Janse, J. A. (2006). Mantle mush compaction: a key to understand the mechanisms of concentration of kimberlite melts and initiation of swarms of kimberlite dykes. *Journal of Petrology*, 47, 631 646. 2.1.1, 2.5

Gregoire, M., Tinguelya, T., Belb, D., & le Roex, A. (2005). Spinel lherzolite xenoliths from the Premier kimberlite (Kaapvaal craton, South Africa): Nature and evolution of the shallow upper mantle beneath the Bushveld complex. *Lithos*, 84, 185 205. 5

Gudfinnsson, G. H. & Presnall, D. C. (2003). Continuous gradations among primary kimberlitic, carbonatitic, melilititic, and komatiitic melts in equilibrium with garnet lherzolite at 3-8GPa. In *8th International Kimberlite Conference Long Abstract* (pp. 1 5). 7.3

Gudmundsson, A. & Loetveit, I. F. (2005). Dyke emplacement in a layered and faulted rift zone. *Journal of Volcanology and Geothermal Research*, 144, 311 327. 2.5

Guest, J., Duncan, A., & Chester, D. (1988). Monte Vulture Vocano (Basilicata, Italy): an analysis of morphology and volcaniclastic facies. *Bulletin of Volcanology*, 50, 244 257. 7.4.1

Gurney, J. J. (1986). Diamonds. In *Kimberlites and Related Rocks: Their Mantle/Crust Setting, Diamonds and Diamond Exploration*, volume 2 of *GSA Special Publication* (pp. 935965).: Fourth International Kimberlite Conference Blackwell Scientific Publications. 2.3.1.4

Gurney, J. J., Jakob, W. R. O., & Dawson, J. B. (1979). Megacrysts from the Monastery Kimberlite Pipe, South Africa. In *Proceedings of the Second International Kimberlite Conference. The Mantle Sample: Inclusions in Kimberlites and Other Volcanic Rocks*, volume 2 (pp. 227 243). Washington D.C.: American Geophysical Union. 2.3.1.2, 4.3

Haggerty, S. (1991a). *Oxide Minerals: Petrologic and Magnetic Significance*, chapter 5: Oxide textures - a mini-atlas, (pp. 129 221). Mineralogical Society of America. 4.3.1

Haggerty, S. E. (1973). *Spinels of unique composition associated with ilmenite reactions in the Liqhobong kimberlite pipe, Lesotho*, (pp. 350). Lesotho National Development Corporation, Maseru. 4.2

Haggerty, S. E. (1975). The chemistry and genesis of opaque minerals in kimberlites. *Physics and Chemistry of the Earth*, 9, 295–307. 2.4.4, 4.1, 4.2, 4.3, 4.7, 4.8

Haggerty, S. E. (1991b). *Oxide Mineralogy of the Upper Mantle*, volume 25, chapter 10, (pp. 355–407). Mineralogical Society of America. 4.3, 4.6

Hansteen, T. H., Klugel, A., & Schmincke, H.-U. (1998). Multi-stage magma ascent beneath the Canary Islands: evidence from fluid inclusions. *Contributions to Mineralogy and Petrology*, 132, 48 64. 2.3.1.1

Harper, F. J. (1981). *Petrography of kimberlite, tuffisitc kimberlite breccia and basalt breccia derived from the Orapa and Letlhakane kimberlite fields.* Technical report, Anglo American Research Laboratories. 3.2

Harte, B. & Hawkesworth, C. (1986). Mantle domains and mantle xenoliths. In *Kimberlite and Related Rocks: Their Composition, Occurrence, Origin and Emplacement*, volume 2 of *GSA Special Publication* (pp. 649–687). Perth: Fourth International Kimberlite Conference Blackwell Scientific Publications. 2.3.1.2

Hawthorne, J. B. (1975). Model of a kimberlite pipe. *Physics and Chemistry of the Earth*, 9, 1–15. 2.2, 2.2.1, 2.3.1.5, 2.4.2, 2.4.3, 2.4.4, 2.5, 3.2, 7.1, 7.2

Head, J. W. & Wilson, L. (1989). Basaltic pyroclastic eruptions: Influence of gas-release patterns and volume fluxes on fountain structure, and the formation of cinder cones, spatter cones, rootless flows, lava ponds and lava flows. *Journal of Geothermal Research*, 37, 261–271. 3.6.1, 3.6.2

Heaman, L. M., Kjarsgaard, B. A., & Creaser, R. A. (2003). The timing of kimberlite magmatism in North America: implications for global kimberlite genesis and diamond exploration. *Lithos*, 71(2-4), 153–184. D.1

Helmstaedt, H. H. & Gurney, J. J. (1995). Geotectonic controls of primary diamond deposits: implications for area selection. *Journal of Geochemical Exploration*, 53, 125–144. 2.1.1

Hetman, C., Scott Smith, B., Paul, J., & Winter, F. (2004). Geology of the Gahcho Kue kimberlite pipes, NWT, Canada: root to diatreme magmatic transition zones. *Lithos*, 76, 29–50. 2.4.5, 3.6.1, 3.6.1

Higgins, M. D. (2000). Measurement of crystal size distributions. *American Mineralogist*, 85, 1105–1116. C.1.1

Higgins, M. D. (2002). Closure crystal size distributions (CSD), verification of CSD calculations, and the significance of CSD fans. *American Mineralogist*, 87, 171–175. C.1

Irvine, T. (1965). Chromian spinel as a petrogenetic indicator. part 1. *Canadian Journal of Earth Sciences*, 2, 648–672. 1.1, 4.1, 4.2, 4.3, 4.9.2

Irvine, T. (1967). Chromian spinel as a petrogenetic indicator. part 2. *Canadian Journal of Earth Sciences*, 4, 71–103. 1.1, 4.2, 4.9.2

James, D. E., Fouch, M. J., CanDecar, J., van der Lee, S., & Group, K. S. (2001). Tectospheric structure beneath southern Africa. *Geophysical Research Letters*, 28(13), 2485–2488. 1.3, 1.1

Janse, A. J. A. & Sheahan, P. A. (1995). Catalog of world wide diamond and kimberlite occurrences - a selective and annotative approach. *Journal of Geochemical Exploration*, 53, 73–111. 2.1.1, 2.1.1

Jeffries, T. E., Fernandez-Suarez, J., Corfu, F., & Alonso, G. G. (2003). Advances in U-Pb geochronology using a frequency quintupled Nd:YAG based laser ablation system (lambda = 213 nm) and quadrapole based ICP-MS. *Journal of Analytical Atomic Spectrometry*, 18, 847–855. D.2, D.3, D.5

Jelsma, H. A., de Wit, M. J., Thiart, C., Dirks, P. H. G. M., Viola, G., Basson, I. J., & Anckar, E. (2004). Preferential distribution along transcontinental corridors of kimberlites and related rocks of southern africa. *South African Journal of Geology*, 107, 301–324. 2.2

Jerram, D. A., Cheadle, M. J., Hunter, R. H., & Elliott, M. T. (1996). The spatial distribution of grains and crystals in rocks. *Contributions to Mineralogy and Petrology*, 125(1), 60–74. (document), C.1, C.2, C.1.1, C.4, C.5, C.1.2, C.1.3

Jones, A. P. & Wyllie, P. J. (1984). Minor elements in perovskite from kimberlites and distribution of the rare earth elements: an electron probe study. *Earth and Planetary Science Letters*, 69, 128–140. 5.2

Jones, A. P. & Wyllie, P. J. (1985). Paragenetic trends of oxide minerals in carbonate-rich kimberlites, with new analyses from the Benfontein Sill, South-Africa. *Journal of Petrology*, 26(1), 210–222. 2.6, 4.1, 5.1, 5.6.1

Junqueira-Brod, T. C., Brod, J. A., Gaspar, J. C., & Jost, H. (2004). Kamafugitic diatremes: facies characterisation and genesis - examples from the Goias Alkaline Province, Brazil. *Lithos*, 76, 261–282. 6.4.4, 7.4.1

Kamenetsky, V. S., Crawford, A. J., & Meffre, S. (2001). Factors controlling chemistry of magmatic spinel: an empiricial study of associated olivine, cr-spinel and melt inlusions from primitive rocks. *Journal of Petrology*, 42, 655–671. 4.3

Kano, K., Matsuura, H., & Yamauchi, S. (1997). Miocene rhyolitic welded tuff infilling a funnel-shaped eruption conduit Shiotani, southeast of Matsue, SW Japan. *Bulletin of Volcanology*, 59(2), 125–135. 2.4.5, 3.1

Kelley, S. P. & Wartho, J. A. (2000). Rapid kimberlite ascent and the significance of Ar-Ar ages in xenolith phlogopites. *Science*, 289, 609–611. D.1

Key, R. M. & Ayres, N. (2000). The 1998 edition of the national geological map of Botswana. *Journal of African Earth Sciences*, 30(3), 427–451. 1.1

Kurszlaukis, S. & Barnett, W. (2003). Volcanological and structural aspects of the Venetia Kimberlite Cluster - a case study of South African kimberlite maar-diatreme volcanoes. *South African Journal of Geology*, 106, 145–172. 7.4

Kurszlaukis, S., Bttner, R., Zimanowski, B., & Lorenz, V. (1998). On the first experimental phreatomagmatic explosion of a kimberlite melt. *Journal of Volcanology and Geothermal Research*, 80, 323–326. 2.5

Kurszlaukis, S. & Lorenz, V. (1997). Volcanological features of a low viscosity melt: the carbonatitic Gross Brukkaros volcanic field, Namibia. *Bulletin of Volcanology*, 58, 421–431. 3.1

Le Roex, A. P., Bell, D. R., & Davis, P. (2003). Petrogenesis of Group I kimberlites from Kimberley, South Africa: Evidence from bulk-rock geochemistry. *Journal of Petrology*, 44(12), 2261–2286. 1, 2.6, 2.7, 6.1, 6.6, 6.4.2, 6.4.3, 6.5.1, 6.5.1.1

Leahy, K. (1997). Discrimination of reworked pyroclastics from primary tephra-fall tuffs: a case study using kimberlites of Fort a la Come, Saskatchewan, Canada. *Bulletin of Volcanology*, 59(1), 65–71. 2.3.1.5

Lebani, A. & Khango, T. (2005). *Three dimensional geological modelling of the D/K1 and D/K1 kimberlite pipes and the surrounding country rock at Letlhakane Mine, Botswana.* Technical report, Debswana. pp 1-51. (document), 3.2, 3.3, 3.3

Lloyd, F. (1985). Experimental melting and crystallisation of glassy olivine melilitites. *Contributions to Mineralogy and Petrography*, 90, 236–243. 7.3, 7.1, 7.3

Lorenz, V. (1975). Formation of phreatomagmatic maar-diatreme volcanoes and its relevance to kimberlite diatremes. *Physics and Chemistry of the Earth*, 9, 17–27. 2.4.2, 2.4.3, 2.5, 2.5

Lorenz, V. (1979). Phreatomagmatic origin of the olivine melilitite diatremes of the Swabian Alb, Germany. In *Kimberlites, Diatremes and Diamonds: Their Geology, Petrology and Geochemistry*, volume 1 (pp. 354–363).: Proceedings of the Second International Kimberlite Conference American Geophysical Union. 2.4.2, 2.4.3, 2.5, 7.4

Lorenz, V. (1999). Discussion of the formation of kimberlite pipes: The phreatomagmatic model. *Comission on Explosive Volcanism Newsletter.* 2.5, 7.4

Lorenz, V. & Kurszlaukis, S. (2007). Root zone processes in the phreatomagmatic pipe emplacement model and consequences for the evolution of maar-diatreme volcanoes. *Journal of Volcanology and Geothermal Research*, 159, 4–32. 7.4

Mahotkin, I. L., Gibson, S. A., Thompson, R. N., Zhuravlev, D. Z., & Zherdev, P. (2000). Late devonian diamondiferous kimberlite and alkaline picrite (proto-kimberlite?) - magmatism in the Arkhangelsk Region, NW Russia. *Journal of Petrology*, 41(2), 201–227. 4.3

Mahotkin, I. L., Robey, J., Kurszlaukis, S., Valuev, E. P., & Pylaev, N. F. (2003). Pipe emplacement mode of the lomonosov diamond deposit, Arkhangelesk region, NW Russion. In *8th International Kimberlite Conference Abstracts* (pp.1̃). 7.4

Mainkara, D., Lehmannb, B., & Haggerty, S. E. (2004). The crater-facies kimberlite system of Tokapal, Bastar District, Chhattisgarh, India. *Lithos*, 76, 201–217. Proceedings of the 8th International Kimberlite Conference. 2.4.3

Mansun, K., Doyle, B., Ball, S., & Walker, S. (2004). The geology and mineralogy of the Anuri kimberlite, Nunavut, Canada. *Lithos*, 76, 75–97. 4.1

Markwick, A. J. W. & Downes, H. (2000). Lower crustal granulite xenoliths from the Arkhangelsk kimberlite pipes: petrological, geochemical and geophysical results. *Lithos*, 51(1-2), 135–151. 2.3.1.1

McCallum, M. E., Eggler, D. H., & Burns, L. K. (1975). Kimberlitic diatremes in Northern Colorado and Southern Wyoming. *Physics and Chemistry of the Earth*, 9, 149–161. 2.5, 3.6.1, 3.6.1

McClintock, M. K., Houghton, B. F., Skilling, I. P., & White, J. D. L. (2002). The volcaniclastic opening phase of karoo flood basalt volcanism: Drakensberg Formation, South Africa. In *EOS Transactions Vol 83*, number 47 (pp. V71B–1277).: AGU. 3.6.1

McFadden, P. (1977). A palaeomagnetic determination of emplacement temperatures of some southern African kimberlites. *Geophysical journal of the Royal Astronomical Society*, 50, 587–604. 2.3.1.5, 10

Mitchell, R. (1979). Mineralogy of the Tunraq Kimberlite, Somerset Island, N.W.T, Canada. In *Proceedings of the Second International Kimberlite Conference. Kimberlites, Diatremes and Diamonds: Their Geology, Petrology and Geochemistry*, volume 1 (pp. 161–172). 4.1, 4.2, 4.7, 4.8, 4.9.2, 4.9.3

Mitchell, R. (1986a). Aspects of the petrology of kimberlites and lamproites. In *Kimberlite and Related Rocks: Their Composition, Occurrence, Origin and Emplacement*, volume 1 of *GSA Special Publications 14* (pp. 7 45). Perth: Fourth International Kimberlite Conference Blackwall Scientific Publications. 2.1, 2.3.1.5, 4.3, 4.4

Mitchell, R. & Clarke, D. B. (1976). Oxide and sulphide mineralogy of the Peyuk Kimberlite, Somerset Island, N.W.T., Canada. *Contributions to Mineralogy and Petrology*, 56, 156–172. 4.1, 4.2, 4.3, 4.3.1, 4.1, 4.7, 4.8, 4.9.2, 4.9.3, 4.9.3, 4.9.4, 4.9.5, 4.9.5

Mitchell, R. H. (1986b). *Kimberlites: Mineralogy, Geochemistry and Petrology.* Plenum Press, New York. 1.2, 2.1, 2.2, 2.3, 2.3, 2.3.1.2, 2.3.1.3, 2.3.2, 2.4.1, 2.7, 2.4.4, 2.4.6, 2.6, 2.7, 3.6.1, 4.1, 4.3, 4.3.1, 4.1, 4.4, 4.7, 4.7.1, 4.7.3, 4.8, 4.9.3, 4.9.4, 4.9.5, 4.9.5, 4.9.5, 4.10, 5.1, 5.2, 5.3, 5.6.1, 6.2, 6.1, 6.6, 6.5.1.1, 7.3, D.5

Mitchell, R. H. (1995). *Kimberlites, Orangeites and Related Rocks.* Plenum. 2.1

Mitchell, R. H. (2004). Experimental studies at 5-12 GPa of the Ondermatjie hypabyssal kimberlite. *Lithos*, 76(1-4), 551 564. 4.9.2, 7.3, 7.3

Mock, A., Jerram, D., & Breitkreuz, C. (2003). Using quantitative textural analysis to understand the emplacement of shallow-level rhyolitic laccoliths - a case study from the Halle Volcanic Complex, Germany. *Journal of Petrology*, 44 (5), 833–849. C.1

Murck, B. W. & Campbell, I. H. (1986). The effects of temperature, oxygen fugacity and melt composition on the behavior of chromium in basic and ultrabasic melts. *Geochimica Et Cosmochimica Acta*, 50(9), 1871–1887. 4.9.2, 4.9.3

Naidoo, P., Stiefenhofer, J., Field, M., & Dobb, R. (2004). Recent advances in the geology of Koffiefontein Mine, Free State Province, South Africa. *Lithos*, 76, 161–182. 4.1, 4.2

Nixon, P., Ed. (1973). *Lesotho Kimberlites.* Cape and Transvaal Printers Ltd. 2.3.1.1, 2.3.1.2

Nixon, P. H. (1995). A review of mantle xenoliths and their role in diamond exploration. *Journal of Geodynamics*, 4, 305 329. 2.3.1.1

Nowell, G. M. & Pearson, D. G. (1998). Hf isotope constraints on the genesis of kimberlitic megacrysts: evidence for a deep mantle component in kimberlites. In *Extended Abstracts: 7th International Kimberlite Conference* Cape Town, South Africa: University of Cape Town. 4.3

Nowell, G. M., Pearson, D. G., Bell, D. R., Carlson, R. W., Smith, C. B., Kempton, P. D., & Noble, S. R. (2004). Hf isotope systematics of kimberlite and their megacrysts: New contraints on their source regions. *Journal of Petrology*, 45(8), 1583 1612. 2.3.1.2

Nowicki, T. (1993). *The HMA and geochemistry of boreholes LFD3, LFD5 and LFD6 , Letlhakane Mine, Botswana.* Technical Report R/93/075, Anglo American Research Laboratories. 1.2, 4.4, 6.2.1

O'Brien, H. E. & Tyni, M. (1999). Mineralogy and geochemistry of kimberlites and related rocks from Finland. *7th International Kimberlite Conference*, (pp. 625–636). 2.6

Pasteris, J. D. (1982). Representation of compositions in complex titanian spinels and application to the De Beers kimberlite. *American Mineralogist*, 67, 244 250. 4.5, 4.6, 4.8

Pasteris, J. D. (1983). Spinel zonation in the De Beers kimberlite, South Africa: possible role of phlogopite. *Canadian Mineralogist*, 21, 41–58. (document), 4.1, 4.2, 4.3.1, 4.9.2, 4.9.3, 4.9.3, 4.9.5, 4.9.5, 4.24

Pasteris, J. D., Boyd, F. R., & Nixon, P. H. (1979). The ilmenite association at the Frank Smith Mine, R.S.A. In *Proceedings of the Second International Kimberlite Conference. The Mantle Sample: Inclusions in Kimberlites and Other Volcanic Rocks*, volume 2 (pp. 265–278). Washington D.C.: American Geophysical Union. 2.3.1.2

Phillips, D., Machin, K. J., Kiviets, G. B., Fourie, L. F., Roberts, M. A., & Skinner, E. M. W. (1998). A petrographic and 40 Ar/ 39 Ar geochronological study of the Voorspoed Kimberlite, South Africa; implications for the origin of Group II kimberlite magmatism. *South Africa Journal of Geology*, 101(4), 299–306. 2

Plint, N. & Bocks, V. (2005). *Quality Summary*. Quality summary, Anglo American Research Laboratories, 8 Schonland Street, Theta, Johannesburg, South Africa. 2

Quane, S. & Russell, J. (2005). Ranking welding intensity in pyroclastic deposits. *Bulletin of Volcanology*, 67, 129–143. C.1.3

Reid, A. M., Donaldson, C. H., Dawson, J. B., Brown, R. W., & Ridley, W. I. (1975). The Igwisi Hills extrusive "kimberlite". *Physics and Chemistry of the Earth*, 9, 199–218. 2.4.1, 5.2

Reubi, O. & Hernandez, J. (2000). Volcanic debris avalanche deposits of the upper Marrone valley (Cantal Volcano, France): evidence for contrasted formation and transport mechanisms. *Journal of Volcanology and Geothermal Research*, 102, 271–286. 3.6.1

Reynolds, D. (1954). Fluidization as a geological process, and its bearing on the problem of intrusive granites. *American Journal of Science*, 252, 577–614. 2.4.4, 2.5

Richardson, S. H., B., S. S., & Harris, J. W. (2004). Episodic diamond genesis at Jwaneng, Botswana, and implications for Kaapvaal craton evolution. *Lithos*, 77, 143–154. 3

Roeder, P., Gofton, E., & Thornber, C. (2006). Cotectic proportions of olivine and spinel in olivine-tholeiitic basalt and evaluation of pre-eruptive processes. *Journal of Petrology*, 47 (5), 883–900. 4.9.5, 1

Roeder, P. & Reynolds, I. (1991). Crystallisation of chromite and chromium solubility in basaltic melts. *Journal of Petrology*, 32 (5), 909 934. 4.9.5

Roeder, P. L., Poustovetov, A., & Oskarsson, N. (2001). Growth forms and composition of chromian spinel in MORB magma: Diffusion-controlled crystallisation of chromian spinel. *Canadian Mineralogist*, 39, 397 416. 4.9.5

Sable, J. E., Houghton, B. F., Del Carlo, P., & Coltelli, M. (2006). Changing conditions of magma ascent and fragmentation during the Etna 122 BC basaltic Plinian eruption: Evidence from clast microtextures. *Journal of Volcanology and Geothermal Research*, 158, 333–354. 2.6

Sack, R. O. & Ghiorso, M. S. (1991a). Chromian spinels as petrogenetic indicators: Thermodynamic and petrological implications. *American Mineralogist*, 76, 827 847. 4.3

Sack, R. O. & Ghiorso, M. S. (1991b). *Oxide Minerals: Petrologic and Magnetic Significance*, chapter 9: Chromite as a petrogenetic indicator, (pp. 323 353). Mineralogical Society of America. 4.3

Scott Smith, B. (1999). Near-surface emplacement of kimberlites by magmatic processes. *Comission on Explosive Volcanism Newsletter*, (pp. 3–10). 4.10

Shane, P. (1998). Correlation of rhyolitic pyroclastic eruptive units from the Taupo volcanic zone by Fe-Ti oxide compositional data. *Bulletin of Volcanology*, 60(3), 224–238. 4.2

Shee, S. R. (1985). *The petrogenesis of the Wessleton Mine Kimberlite, Kimberly, Cape Province, R.S.A.* PhD thesis, University of Cape Town. 2.1, 2.5, 4.1, 4.4, 4.4, 4.9.2, 4.9.5, 4.9.5, 4.10, 6.1, 6.2, 6.1, 6.4.1, 6.6, 6.4.3, 6.5.1

Shee, S. R. & Gurney, J. J. (1979). The mineralogy of xenoliths from Orapa, Botswana. In *Proceedings of the Second International Kimberlite Conference. The Mantle Sample: Inclusions in Kimberlites and Other Volcanic Rocks*, volume 2 (pp. 37–49). Washington D.C.: American Geophysical Union. 1.3, 2.3.1.1, 2.3.1.2

Shirey, S. B., Richardson, S. H., & Harris, J. W. (2004). Integrated models of diamond formation and craton evolution. *Lithos*, 77, 923–944. 1.3

Skilling, I. (2006). Interpreting explosive eruption and primary depositional processes from kimberlite intra-crater deposits. In *2006 Kimberlite Emplacement Worshop Long Abstracts*: 8th International Kimberlite Conference. 3.6.1

Skinner, E. & Clement, C. R. (1979). Mineralogical classification of southern African kimberlites. In *Proceedings of the Second International Kimberlite Conference. Kimberlites, Diatremes and Diamonds: Their Geology, Petrology and Geochemistry*, volume 1 (pp. 129–139). Washington D.C.: American Geophysical Union. 2.3, 2.3.1.3, 2.3.3, 2.7, 2.4.6, 2.6

Skinner, E. M. W. (1986). Constrasting Group I and Group II kimberlite petrology: towards a genetic model for kimberlites. In *Kimberlite and Related Rocks: Their Composition, Occurrence, Origin and Emplacement*, volume 1 of *GSA Special Publication* (pp. 528–544).: Fourth International Kimberlite Conference Blackwell Scientific Publications. 2.6, 2.1

Skinner, E. M. W. & Clement, C. R. (1978). *Petrographic descriptions of kimberlite specimens collected by A. Davy.* Technical report, Anglo American Research Laboratories. 3.2

Skinner, E. M. W. & Marsh, J. S. (2004). Distinct kimberlite pipe classes with contrasting eruption processes. *Lithos*, 76(1-4), 183–200. 2.2, 2.4.1, 2.4.5, 2.4.6, 2.5, 2.5, 3.6.1, 7.4.1

Skinner, E. M. W. & Marsh, J. S. (2006). The emplacement of Class 1 kimberlites - Part 1, evidence of geological features. In *2006 Kimberlite Emplacement Workshop: Long Abstracts*: 8th INternational Kimberlite Conference. 2.5

Smith, C. B. (1983). Pb, Sr and Nd isotopic evidence for sources of southern African Cretaceous kimberlites. *Nature*, 304(5921), 51–54. 2.7, 2.1

Smith, R. (1984). The lithostratigraphy of the Karoo Supergroup in Botswana. *Geological Survey Department, Republic of Botswana*, 26. 1.3, 2.1

Sparks, R., Baker, L., Brown, R., Field, M., Schumacher, J., Stripp, G., & Walters, A. (2006). Dynamical constraints on kimberlite volcanism. *Journal of Volcanology and Geothermal Research*, 153. 2.3.1.5, 2.4.4, 2.4.5, 2.4.6, 2.5, 2.5, 2.5, 2.6, 2.7, 3.6.1, 3.6.1, 3.6.1, 4.9.5, 6.5.1.1, 7.4.1, C.1.3

Sparks, R. S. J., Tait, S. R., & Yanev, Y. (1999). Dense welding caused by volatile resorption. *Journal of the Geological Society*, 156, 217–225. 2.4.5, 3.6.2

SRK, C. (2001). *An investigation of the main failure planes at Letlhakane Mine, Botswana.* Technical report, SRK Consulting Engineers and Scientists, 28 Kennedy Drive, Greendale, Harare, Zimbabwe. 1.3

Sruoga, P., Rubinstein, N., & Hinterwimmer, G. (2004). Porosity and permeability in volcanic rocks: a case study on the Serie Tobifera, South Patagonia, Argentina. *Journal of Volcanology and Geothermal Research*, 132, 31–43. 3.6.1, 3.6.2

Stacey, J. S. & Kramers, J. D. (1975). Approximation of terrestrial lead isotope evolution by a two-stage model. *Earth and Planetary Science Letters*, 26, 227–247. D.1, D.3.1, D.2

Stiefenhofer, J. (1993). *The petrography, mineral chemistry and isotope geochemistry of a mantle xenoliths suite from the Letlhakane D/K1 and D/K2 kimberlite pipes, Botswana.* PhD thesis, Rhodes University. (document), 1, 2.3.1.1, 3.2, 3.2, 3.4, 4.7, 4.9.2, 4.19

Stiefenhofer, J. & Farrow, D. J. (2004). Geology of the Mwadui kimberlite, Shinyanga district, Tanzania. *Lithos*, 76(1-4), 139–160. 2.2.1, 2.4.3

Stiefenhofer, J., Field, M., Ekkerd, J., Colgan, E., Robey, J., Brown, R., Scott Smith, B., Kurszlaukis, S., & Kujawa, T. (2004). *Standards and procedures for measurement of the inclusion abundance in kimberlite, rock density determination, geological mapping and core logging techniques.* Technical report, De Beers Consolidated Mines Ltd. 3.3

Stiefenhofer, J., Viljoen, K., & Marsh, J. (1997). Petrology and geochemistry of peridotite xenoliths from the Letlhakane kimberlites, Botswana. *Contributions to Mineralogy and Petrology*, 127, 147–158. 1.3, 2.3.1.1, D.1

Stoppa, F. (1996). The San Venanzo maar and tuff ring, Umbria, Italy: eruptive behaviour of a carbontatite-melilitite volcano. *Bulletin of Volcanology*, 57, 563–577. 3.1, 7.4.1

Stoppa, F. & Principe, C. (1997). Eruption style and petrology of a new carbonatitic suite from the Mt. Vulture, Southern Italy: The Monticchio Lakes Formation. *Journal of Volcanology and Geothermal Research*, 78, 251–265. 7.4.1

Storey, C. S., Jeffries, T. E., & Smith, M. (2006). Common lead-corrected laser ablation ICP-MS U-Pb systematics and geochronology of titanite. *Chemical Geology*, 227, 37–52. D.1, D.2, D.3, D.2, D.3.1, D.3.1, D.3.1, D.4, D.5

Stripp, G., Field, M., Schumacher, C., Sparks, R., & Cressey, G. (2006). Post-emplacement serpentinization and related hydrothermal metamorphism in a kimberlite from Venetia, South Africa. *Journal of Metamorphic Geology*, 24, 515–534. 2.1, 2.3, 2.4.6, 2.6, 2.6, 2.6, 3.6.1, 3.6.1, 3.6.1, 3.6.2, 4.9.4, 7.3, 7.4.1

Sumner, J. M., Blake, S., Matela, R. J., & Wolff, J. A. (2005). Spatter. *Journal of Volcanology and Geothermal Research*, 142, 49–65. 3.6.1, 3.6.1

Sun, S. & McDonough, W. (1989). Chemical and isotopic systematics of oceanic basalts; implications for mantle composition and processes. In A. Saunders & M. Norry (Eds.), *Magmatism in the ocean basins.* (pp. 313–345). London: Geological Society of London. 5.8

Swan, A., Sandilands, M., & McCabe, P. (1995). *Introduction to Geological Data Analysis.* Blackwell Science. 6.3.2, 6.3.2.1, 6.3.2.2

Tait, M. A., Brown, R. J., & Mnyama, A. (2006). Internal architecture of the Venetia K1 kimberlite: A new geological model and implications for kimberlite emplacement processes. Venetia Mine, Limpopo, RSA. In *2006 Kimberlite Emplacement Workshop Long Abstracts* Saskatoon, Canada: 8th International Kimberlite Conference. 2.4.5

Takarada, S., Ui, T., & Yamamoto, Y. (1999). Depositional features and transportation mechanism of valley-filling Iwasegawa and Kaida debris avalanches, Japan. *Bulletin of Vocanclastic*, 60, 508–522. 3.6.1

Tomlinson, E., De Schrijer, I., De Corte, K., Jones, A. P., Moens, L., & Vanhaecke, F. (2005). Trace element compositions of submicroscopic inclusions in coated diamond: A tool for understanding diamond petrogenesis. *Geochimica et Cosmochimica Acta*, 69(19), 4719–4732. 2.3.1.4

Tompkins, L. A. & Haggerty, S. E. (1985). Groundmass oxide minerals in the Koidu kimberlite dikes, Sierra Leone, West Africa. *Contributions to Mineralogy and Petrology*, 91, 245–263. 4.1, 4.2, 4.4, 4.7, 4.8, 4.9.2

Trofimov, V. S. (1970). On the origin of diamantiferous diatremes. *Bulletin of Volcanology*, 34, 767–776. 2.1, 2.4.1, 2.5, 2.5, 2.5, 2.6, 2.6, 3.6.1, 7.1

Ulmer, P. & Sweeney, R. (2002). Generation an differentiation of Group II kimberlites: Constraints from a high-pressure experimental study to 10 GPa. *Geochimica et Cosmochimica Acta*, 66, 2139–2153. 4.9.2, 7.3, 7.1, 7.3

van Achterbergh, E., Griffin, W. L., & Stiefenhofer, J. (2001). Metasomatism in mantle xenoliths from the Letlhakane kimberlites: estimation of element fluxes. *Contributions to Mineralogy and Petrology*, 141, 397–414. 2.3.1.1

Wada, H., Harayama, S., & Yamaguchi, Y. (2004). Mafic enclaves densely concentrated in the upper part of a vertically zoned felsic magma chamber: The Kurobegawa granitic pluton, Hida Mountain Range, central Japan. *Geological Society Of America Bulletin*, 116 (7-8), 788–801. 4.9.5, 5.6.2

Wagner, P. A. (1914). *Diamond Fields of South Africa.* Johannesburg: The Transvaal Leader. 2.1, 2.1.1, 2.3.1.5, 2.7

Wagner, P. A. (1971). *The Diamond Fields of Southern Africa.* C. Struik (Pty) Ltd Cape Town. 2.1, 2.1.1, 2.3.1.5, 2.7

Walters, A. L., Phillips, J. C., Brown, R. J., Field, M., Gernon, T., Stripp, G., & Sparks, R. S. J. (2006). The role of fluidisation in the formation of volcaniclastic kimberlite: Grain size observations and experimental investigation. *Journal of Volcanology and Geothermal Research.* 2.4, 2.4.4, 2.5, 2.6, 3.6.2, 4.9.4, 4.9.5, 6.5.1.1

Watanabe, T., Koyaguchi, T., & Seno, T. (1999). Tectonic stress controls on ascent and emplacement of magmas. *Journal of Volcanology and Geothermal Research*, 91, 65–78. 2.5

Waychunas, G. A. (1991). *Crystal Chemistry of Oxides and Oxyhydroxides*, volume 25 of *Reviews in Mineralogy*, chapter 2, (pp. 11–61). Mineralogical Society of America. 4.3

Webb, K., ScottSmith, B., Paul, J., & Hetman, C. (2004). Geology of the Victor Kimberlite, Attawapiskat, Northern Ontario, Canada: cross-cutting and nested craters. *Lithos*, 76, 29–50. 3.6.1, 3.6.1

Wedepohl, K. H. & Muramatsu, Y. (1979). The chemical composition of kimberlites compared with the average composition of three basaltic magma types. In *Proceedings of the Second International Kimberlite Conference. The Mantle Sample: Inclusions in Kimberlites and Other Volcanic Rocks*, volume 2 (pp. 300–312).: American Geophysical Union. 2.7

Weinstein, Y. (2007). A transition from strombolian to phreatomagmatic activity induced by a lava flow damming water in a valley. *Journal of Volcanology and Geothermal Research*, 159, 267–284. 7.4

White, S. H., de Boorder, H., & Smith, C. B. (1995). Structural controls of kimberlite and lamproite emplacement. *Journal of Geodynamics*, 53, 245–264. 2.5

Wiedenback, M., Alle, P., Corfu, F., Griffin, W. L., Meier, M., Oberli, F., Von-quadt, A., Roddick, J. C., & Speigel, W. (1995). Natural zircon standards for U-Th-Pb, Lu-Hf, trace-elements and REE analyses. *Geochemical Newslatter*, 19, 1–23. D.2

Wolff, J. A. & Sumner, J. M. (2000). Lava fountains and their products. In H. Sigurdsson, B. Houghton, S. R. McNutt, H. Rymer, & J. Stix (Eds.), *Encyclopedia of Volcanoes* (pp. 321 329). Academic Press. (document), 2.4.5, 2.9, 3.6.1

Woolsey, T. S., McCallum, M. E., & Schumm, S. A. (1975). Modelling of diatreme emplacement by fluidization. *Physics and Chemistry of the Earth*, 9, 29 42. 2.5, 3.6.1, 7.4.1

Zadnik, M. G., Specht, S., & Begemann, F. (1989). Revised isotopic composition of terrestrial mercury. *International Journal of Mass Spectrometry and Ion Processes*, 89, 103–110. D.3.1

Zonneveld, J.-P., Kjarsgaard, B. A., Harvey, S. E., & D., M. (2006). Accomodation space and kimberlite edifice preservation: Implications for volcanilogical models of the Fort a la Corne kimberlites. In *2006 Kimberlite Emplacement Workshop Long Abstracts*: 2006 Kimberlite Emplacement Workshop Long Abstracts. 2.4.2

Zonneveld, J.-P., Kjarsgaard, B. A., Harvey, S. E., Heaman, L. M., McNeil, D. H., & Marcia, K. Y. (2004). Sedimentologic and stratigraphic constraints on emplacement of the Star Kimberlite, east-central Saskatchewan. *Lithos*, 1, 115–138. 2.4.2

Appendix A

Drill Core Logging

A.1 Drill Core Logging

Drill core logging templates were changed during the course of the study, as discussed in section 3.3. All drill core logs are given on the attached CD.

A.2 Face Mapping

Four face maps were collected, and are also given on the attached CD.

Appendix B

Analytical Methods

B.1 Electron Microprobe Analysis

B.1.1 Reproducibility and Standardisation

Major element analysis for spinel mineral compositions were collected using a Jeol 733 Superprobe at University College London. Analysis is explained in Section 4.5. Reproducibility was determined through multiple analysis of a single amphibole (Table B.1.1)[1] and spinel grain (Table B.1.1). The mineral standards used to standardise electron microprobe analysis are listed in Table B.1.1.

[1] analysis of MgO was omitted from these analyses due to error, however from (Beard et al., 2000) mean MgO is 10.69, and the standard deviation is 0.083

Amphibole										
wt% oxide	SiO_2	TiO_2	Al_2O_3	FeO	MnO	Cr_2O_3	CaO	Na_2O	K_2	Total
1	49.26	2.10	7.24	9.78	0.19	0.00	24.71	1.75	0.00	94.91
2	49.23	2.29	6.88	10.13	0.18	0.00	24.53	1.87	0.00	94.93
3	48.83	1.77	6.96	9.12	0.00	0.11	25.17	1.75	0.00	93.72
4	49.62	2.12	7.10	9.50	0.22	0.00	24.37	1.65	0.00	94.65
5	48.63	2.05	6.86	9.34	0.00	0.08	24.57	1.96	0.00	93.56
6	49.05	2.19	7.07	9.88	0.13	0.00	25.11	1.71	0.00	95.14
7	48.86	2.01	7.14	9.46	0.18	0.00	24.93	1.69	0.00	93.92
8	49.20	2.09	6.88	9.47	0.00	0.00	25.24	1.60	0.00	94.45
9	49.31	1.85	7.16	10.05	0.40	0.00	24.51	1.66	0.00	94.79
10	49.66	2.20	7.12	9.38	0.12	0.10	24.57	1.65	0.00	94.76
11	48.86	1.85	7.17	9.53	0.25	0.00	24.84	1.62	0.00	94.17
12	49.25	2.07	7.00	9.62	0.13	0.00	25.15	1.85	0.00	95.01
13	49.08	2.19	7.03	9.57	0.25	0.00	24.64	1.80	0.00	94.29
14	48.66	2.06	7.19	9.68	0.33	0.00	24.76	1.84	0.00	94.49
15	49.00	2.08	7.04	9.40	0.20	0.15	24.69	1.67	0.00	94.13
16	48.68	1.67	7.26	9.03	0.33	0.00	25.08	1.71	0.00	93.73
17	49.26	2.00	7.12	9.75	0.18	0.00	24.50	1.66	0.00	94.52
18	48.50	1.86	7.06	9.48	0.00	0.00	24.89	1.82	0.00	93.70
19	49.41	2.10	6.97	9.41	0.00	0.19	25.30	1.83	0.00	95.08
20	49.64	1.81	6.98	9.28	0.40	0.00	24.79	1.71	0.00	94.46
Mean	49.099	2.017	7.061	9.542	0.174	0.031	24.817	1.740	0.000	94.421
Std. Dev.	0.345	0.165	0.117	0.277	0.129	0.058	0.280	0.097	0.001	

Table B.1: Reproducibility of Jeol 733 Superprobe analysis on a single grain of amphibole.

Spinel (Sp04 from LDD10_04)

wt% oxide	SiO_2	TiO_2	Al_2O_3	FeO_x	MnO	Cr_2O_3	MgO	CaO	Total
1	0.28	6.14	5.64	29.00	3.99	44.70	10.19	0.10	100.04
2	0.17	5.96	5.70	28.21	3.85	44.89	10.30	0.12	99.20
3	0.19	6.11	5.85	28.80	4.01	44.82	10.30	0.12	100.20
4	0.15	5.98	5.78	28.38	3.96	44.53	10.24	0.10	99.12
5	0.20	6.01	5.77	28.53	3.93	44.78	10.18	0.03	99.43
6	0.26	6.04	5.79	28.53	4.09	44.49	10.18	0.06	99.44
7	0.18	5.97	5.90	28.55	3.86	44.56	10.26	0.11	99.39
8	0.14	6.08	5.86	28.25	4.02	44.87	10.13	0.19	99.54
9	0.13	6.20	6.07	28.34	3.72	44.58	10.27	0.09	99.40
10	0.12	6.15	5.91	28.44	4.13	44.37	10.20	0.14	99.46
11	0.29	5.92	6.11	28.10	3.88	44.08	10.25	0.07	98.70
12	0.32	6.13	5.93	28.16	3.70	44.34	10.25	0.07	98.90
13	0.17	5.93	6.01	28.35	3.76	44.30	10.40	0.07	98.99
14	0.26	6.21	6.19	28.38	3.91	44.00	10.22	0.16	99.33
15	0.12	6.01	6.04	28.14	3.58	43.99	10.14	0.10	98.12
16	0.28	6.21	6.21	28.17	3.60	43.95	10.31	0.07	98.80
17	0.24	6.05	6.09	28.12	3.96	43.58	10.29	0.07	98.40
18	0.22	6.08	6.02	28.22	3.66	44.10	10.16	0.14	98.60
19	0.17	6.08	6.05	27.89	3.66	44.06	10.08	0.11	98.10
20	0.31	6.25	6.29	28.29	3.68	43.79	10.32	0.12	99.05
Mean	0.210	6.076	5.961	28.343	3.848	44.339	10.234	0.102	99.111
Std Dev	0.066	0.099	0.177	0.254	0.167	0.382	0.077	0.038	

Table B.2: Reproducibility of Jeol 733 Superprobe analysis on a single grain of spinel.

	Standard Ref.	SiO_2	TiO_2	Al_2O_3	FeO	MnO	NiO	MgO	CaO	Na_2O	K_2O	P_2O_5	Total
Olivine	UCOL1	41.54	0	0	6.78	0	0.38	**51.03**	0	0	0	0	99.73
Olivine	UCOL2	35.04	0	0	**40.35**	0.48	0.18	23.7	0.07	0	0	0	99.82
Wollastonite	BKWOLL	**51.51**	0	0.02	0.42	0.12	0	0.1	**47.77**	0	0	0	99.94
Orthoclase	UCORTH	64.28	0	19.19	0.09	0	0	0.1	0.11	0.92	**15.3**	0	99.99
Jadeite	BKJAD	59.4	0	25.1	0.15	0	0	0.1	0.06	**15.1**	0	0	99.91
Apatite	UCAPA	0	0	0	0.22	0	0	0	56.35	0	0	**43.31**	99.88

Table B.3: Standards used to standardise major element compositions on Jeol 733 Superprobe. Oxide weight percents on **bold** type are the standards used for this study. For the remaining elements: pure natural corundum was used for Al_2O_3; pure natural rutile for TiO_2; pure Mn metal for Mn (99.999%); pure Cr metal for Cr (99.999%); pure Ni metal for Ni (99.999%); pure V metal for V (99.999%); pure NaCl for Cl; pyrite (FeS_2) for S; barite ($BaSO_4$) for Ba; pure Nb_2O_3 for $_2O_3$ (?).

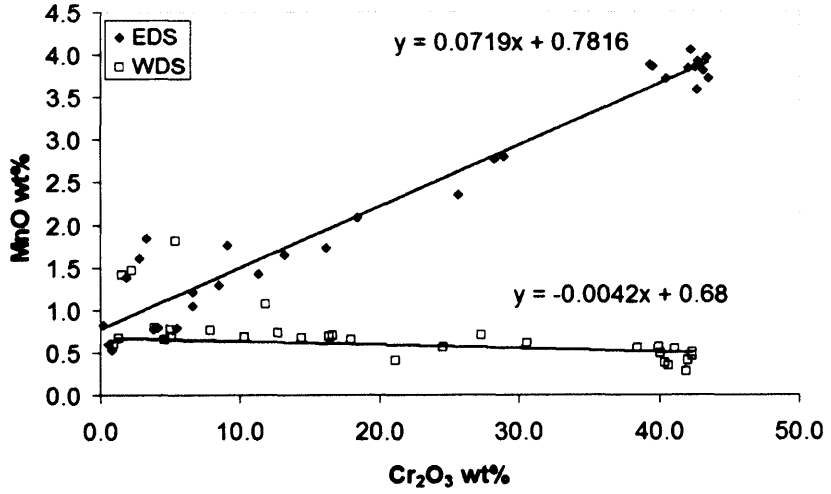

Figure B.1: Plot showing the difference in MnO analysis by electron dispersive spectroscopy (EDS) and wavelength dispersive spectroscopy (WDS). The gradient of each line is shown.

B.1.2 Interferring Peak Corrections

Correction was made for EDS analysis to account for the α-line of Mn interferring with the β-line of Cr. A correction coefficient (Equation B.1) was made by analysing Cr and Mn from the same spinels on EDS (at UCL) and WDS (at the Natural History Museum, see below). Figure B.1 demonstrates the excess Mn analysed by EDS, which is exponential with increasing Cr.

$$y = y' - (0.0761x) - 0.1016 \tag{B.1}$$

Where: y is WDS MnO
y' is EDS MnO
x is EDS Cr_2O_3

B.2 Wavelength Dispersive Spectroscopy

Analysis of groundmass perovskite and some spinel grains (Section B.1.2) were analysed using a Cameca SX50 wavelength dispersive electron microprobe (WDS) at the Natural History Museum, London. WDS has lower minimum detection limits and is therefore capable of analysing heavier elements including REE hence it was chosen to analyse perovskite compositions. Precision of analysis was determined by the variance of five analyses of a known spinel grain (Table B.2).

Sample SP1

wt% oxide	MgO	Al_2O_3	SiO_2	CaO	TiO_2	V_2O_5	Cr_2O_5	MnO	FeO	NiO	ZnO	Nb_2O_5	Total
1	15.014	9.749	0.032	0	0.105	0.105	60.502	0.139	13.415	0.23	0	0.054	99.347
2	15.057	9.749	0.047	0.013	0.117	0.116	60.806	0.167	13.216	0.241	0.093	0.036	99.657
3	15.218	9.407	0.075	0	0.105	0.114	61.05	0.22	13.257	0.169	0.06	0.009	99.683
4	15.286	9.827	0.088	0	0.095	0.123	61.036	0.163	13.233	0.145	0.116	0.009	100.12
5	14.939	9.634	0.034	0.022	0.112	0.086	61.182	0.217	13.185	0.193	0.057	0.007	99.67
mean	15.1028	9.6732	0.0552	0.007	0.1068	0.1088	60.9152	0.1812	13.2612	0.1956	0.0652	0.023	99.695
variance	0.001	0.002	0.009	0.012	0.001	0.001	0.001	0.006	0.000	0.007	0.024	0.016	

Table B.4: Precision (the variance) of the Cameca SX50 microprobe at the Natural History Museum.

B.3 Oxygen Fucacity Calculations

B.3.1 Perovskite

Calculations of oxygen fugacity using Fe^{3+} content in perovskites derived by Bellis & Canil (2007) in Equation B.2. The results are given in Table B.5 with an uncertainty of 2σ (Bellis & Canil, 2007).

$$wt\%Fe_2O_{3_{Pv}} = 0.25\ (\pm 0.04)\ \Delta NNO\ +\ 1.83\ (\pm 0.06) \tag{B.2}$$

Lithofacies	Sample-ID	Paragenesis	Fe^{3+}	Nb^{5+}	Fe_2O_3	log Fe^{3+} cations	ΔNNO	ΔNNO (max.)	ΔNNO (Min)
CK	LDD21_06	M	0.019	0.004	1.074	-1.730	-3.024	-2.814	-3.314
CK	LDD21_06	M	0.020	0.005	1.153	-1.696	-2.708	-2.541	-2.938
CK	LDD21_06	M	0.020	0.005	1.177	-1.689	-2.612	-2.459	-2.824
CK	LDD21_06	M	0.019	0.007	1.075	-1.728	-3.02	-2.810	-3.310
CK	LDD21_06	M	0.018	0.007	1.034	-1.743	-3.184	-2.952	-3.505
CK	LDD21_06	M	0.019	0.005	1.078	-1.723	-3.008	-2.800	-3.295
CK	LDD21_06	M	0.019	0.006	1.106	-1.719	-2.896	-2.703	-3.162
CK	LDD21_06	M	0.019	0.005	1.075	-1.725	-3.02	-2.810	-3.310
CK	LDD21_06	M	0.023	0.006	1.342	-1.630	-1.952	-1.890	-2.038
CK	LDD21_06	M	0.023	0.005	1.308	-1.642	-2.088	-2.007	-2.200
CK	LDD21_06	M	0.018	0.004	1.054	-1.740	-3.104	-2.883	-3.410
CK	LDD21_06	M	0.020	0.005	1.154	-1.698	-2.704	-2.538	-2.933
CK	LDD21_06	M	0.021	0.005	1.203	-1.676	-2.508	-2.369	-2.700
CK	LDD21_06	M	0.019	0.006	1.099	-1.719	-2.924	-2.728	-3.195
CK	LDD21_06	M	0.020	0.005	1.158	-1.697	-2.688	-2.524	-2.914
CK	LDD21_06	G	0.018	0.006	1.06	-1.734	-3.068	-2.852	-3.367
CK	LDD21_06	G	0.019	0.004	1.11	-1.716	-2.888	-2.697	-3.152
CK	LDD21_06	G	0.020	0.006	1.14	-1.705	-2.78	-2.603	-3.024
CK	LDD21_06	G	0.021	0.005	1.24	-1.671	-2.38	-2.259	-2.548
CK	LDD21_06	G	0.024	0.004	1.43	-1.612	-1.612	-1.597	-1.633
CK	LDD21_06	G	0.028	0.005	1.60	-1.556	-0.908	-0.990	-0.795
PVK	LDD12_01	P	0.015	0.005	0.86	-1.825	-3.876	-3.548	-4.329
PVK	LDD12_01	P	0.014	0.005	0.82	-1.840	-4.032	-3.683	-4.514
PVK	LDD12_01	P	0.019	0.005	1.10	-1.719	-2.908	-2.714	-3.176
PVK	LDD12_01	P	0.020	0.006	1.17	-1.689	-2.652	-2.493	-2.871
PVK	LDD12_01	P	0.020	0.005	1.12	-1.709	-2.86	-2.672	-3.119
PVK	LDD12_01	P	0.019	0.004	1.08	-1.721	-2.992	-2.786	-3.276
PVK	LDD12_01	P	0.022	0.003	1.23	-1.666	-2.404	-2.279	-2.576
PVK	LDD12_01	P	0.021	0.005	1.18	-1.679	-2.6	-2.448	-2.810
PVK	LDD12_01	P	0.017	0.004	0.94	-1.778	-3.544	-3.262	-3.933
PVK	LDD12_01	P	0.020	0.007	1.14	-1.699	-2.756	-2.583	-2.995
PVK	LDD12_01	P	0.019	0.005	1.07	-1.726	-3.04	-2.828	-3.333
PVK	LDD12_01	P	0.022	0.005	1.24	-1.662	-2.38	-2.259	-2.548

Lithofacies	Sample-ID	Paragenesis	Fe^{3+}	Nb^{5+}	Fe_2O_3	log Fe^{3+} cations	ΔNNO	ΔNNO (max.)	ΔNNO (Min)
PVK	LDD12_01	P	0.019	0.006	1.07	-1.730	-3.028	-2.817	-3.319
PVK	LDD12_01	P	0.019	0.005	1.07	-1.724	-3.04	-2.828	-3.333
PVK	LDD12_01	M	0.018	0.006	1.051	-1.735	-3.116	-2.893	-3.424
PVK	LDD12_01	M	0.019	0.006	1.081	-1.727	-2.996	-2.790	-3.281
PVK	LDD12_01	M	0.015	0.006	0.880	-1.816	-3.8	-3.483	-4.238
PVK	LDD12_01	M	0.015	0.006	0.885	-1.811	-3.78	-3.466	-4.214
PVK	LDD12_01	M	0.018	0.006	1.006	-1.755	-3.296	-3.048	-3.638
PVK	LDD12_01	M	0.019	0.005	1.073	-1.728	-3.028	-2.817	-3.319
PVK	LDD12_01	M	0.017	0.005	0.955	-1.776	-3.5	-3.224	-3.881
PVK	LDD12_01	M	0.016	0.004	0.898	-1.805	-3.728	-3.421	-4.152
PVK	LDD12_01	G	0.017	0.005	0.97	-1.772	-3.452	-3.183	-3.824
PVK	LDD12_01	G	0.017	0.005	0.98	-1.762	-3.392	-3.131	-3.752
PVK	LDD12_01	G	0.017	0.005	0.94	-1.782	-3.564	-3.279	-3.957
PVK	LDD12_01	G	0.020	0.003	1.18	-1.693	-2.62	-2.466	-2.833
PVK	LDD12_01	G	0.019	0.004	1.09	-1.713	-2.956	-2.755	-3.233
PVK	LDD12_01	G	0.018	0.005	1.01	-1.756	-3.3	-3.052	-3.643
PVK	LDD12_01	G	0.017	0.005	0.98	-1.769	-3.404	-3.141	-3.767
PVK	LDD12_01	G	0.018	0.006	1.03	-1.745	-3.2	-2.966	-3.524
PVK	LDD12_01	G	0.020	0.004	1.15	-1.698	-2.736	-2.566	-2.971
PVK	LDD12_01	G	0.017	0.005	1.00	-1.759	-3.316	-3.066	-3.662
PVK	LDD12_01	G	0.021	0.005	1.21	-1.676	-2.468	-2.334	-2.652
PVK	LDD12_01	G	0.019	0.005	1.09	-1.716	-2.968	-2.766	-3.248
PVK	LDD12_01	G	0.018	0.005	1.04	-1.738	-3.156	-2.928	-3.471
SVK	LDD12_01	P	0.021	0.005	1.20	-1.680	-2.528	-2.386	-2.724
SVK	LDD12_01	P	0.022	0.004	1.27	-1.653	-2.256	-2.152	-2.400
SVK	LDD12_01	P	0.024	0.005	1.37	-1.622	-1.848	-1.800	-1.914
SVK	LDD12_01	P	0.019	0.005	1.10	-1.712	-2.92	-2.724	-3.190
SVK	LDD12_01	P	0.026	0.006	1.53	-1.580	-1.188	-1.231	-1.129
SVK	LDD12_01	P	0.024	0.005	1.36	-1.622	-1.88	-1.828	-1.952
SVK	LDD12_01	P	0.023	0.006	1.31	-1.644	-2.088	-2.007	-2.200
SVK	LDD12_01	P	0.022	0.005	1.27	-1.657	-2.24	-2.138	-2.381
SVK	LDD12_01	P	0.022	0.004	1.24	-1.661	-2.36	-2.241	-2.524
SVK	LDD12_01	P	0.018	0.005	1.05	-1.738	-3.128	-2.903	-3.438

Lithofacies	Sample-ID	Paragenesis	Fe^{3+}	Nb^{5+}	Fe_2O_3	log Fe^{3+} cations	ΔNNO	ΔNNO (max.)	ΔNNO (Min)
SVK	LDD12_01	P	0.018	0.006	1.03	-1.744	-3.184	-2.952	-3.505
SVK	LDD12_01	P	0.024	0.005	1.40	-1.619	-1.732	-1.700	-1.776
SVK	LDD12_01	P	0.021	0.004	1.20	-1.677	-2.504	-2.366	-2.695
SVK	LDD12_01	P	0.024	0.006	1.40	-1.613	-1.704	-1.676	-1.743
SVK	LDD12_01	P	0.024	0.005	1.37	-1.627	-1.856	-1.807	-1.924
SVK	LDD12_01	M	0.020	0.005	1.148	-1.695	-2.728	-2.559	-2.962
SVK	LDD12_01	M	0.021	0.005	1.182	-1.685	-2.592	-2.441	-2.800
SVK	LDD12_01	M	0.019	0.006	1.079	-1.723	-3.004	-2.797	-3.290
SVK	LDD12_01	M	0.020	0.006	1.150	-1.694	-2.72	-2.552	-2.952
SVK	LDD12_01	M	0.020	0.005	1.157	-1.699	-2.692	-2.528	-2.919
SVK	LDD12_01	M	0.020	0.006	1.132	-1.703	-2.792	-2.614	-3.038
SVK	LDD12_01	M	0.023	0.006	1.337	-1.633	-1.972	-1.907	-2.062
SVK	LDD12_01	M	0.022	0.006	1.241	-1.665	-2.356	-2.238	-2.519
SVK	LDD12_01	M	0.021	0.005	1.234	-1.671	-2.384	-2.262	-2.552
SVK	LDD12_01	M	0.020	0.004	1.168	-1.696	-2.648	-2.490	-2.867
SVK	LDD12_01	M	0.023	0.005	1.320	-1.643	-2.04	-1.966	-2.143
SVK	LDD12_01	M	0.023	0.006	1.308	-1.645	-2.088	-2.007	-2.200
SVK	LDD12_01	M	0.020	0.004	1.122	-1.704	-2.832	-2.648	-3.086
SVK	LDD12_01	M	0.021	0.005	1.187	-1.684	-2.572	-2.424	-2.776
SVK	LDD12_01	M	0.019	0.004	1.077	-1.726	-3.012	-2.803	-3.300
SVK	LDD12_01	M	0.021	0.005	1.214	-1.675	-2.464	-2.331	-2.648
SVK	LDD12_01	M	0.022	0.005	1.229	-1.667	-2.404	-2.279	-2.576
VK1	LDD16A_02	P	0.021	0.006	1.22	-1.680	-2.456	-2.324	-2.638
VK1	LDD16A_02	P	0.017	0.004	1.00	-1.765	-3.336	-3.083	-3.686
VK1	LDD16A_02	P	0.019	0.006	1.07	-1.728	-3.024	-2.814	-3.314
VK1	LDD16A_02	P	0.016	0.006	0.92	-1.798	-3.644	-3.348	-4.052
VK1	LDD16A_02	P	0.021	0.006	1.20	-1.681	-2.528	-2.386	-2.724
VK1	LDD16A_02	P	0.017	0.005	0.94	-1.778	-3.548	-3.266	-3.938
VK1	LDD16A_02	P	0.019	0.006	1.07	-1.728	-3.028	-2.817	-3.319
VK1	LDD16A_02	P	0.016	0.006	0.90	-1.806	-3.728	-3.421	-4.152
VK1	LDD16A_02	P	0.018	0.007	1.03	-1.749	-3.204	-2.969	-3.529
VK1	LDD16A_02	P	0.019	0.007	1.08	-1.728	-2.992	-2.786	-3.276
VK1	LDD16A_02	P	0.023	0.006	1.34	-1.638	-1.98	-1.914	-2.071

Lithofacies	Sample-ID	Paragenesis	Fe^{3+}	Nb^{5+}	Fe_2O_3	log Fe^{3+} cations	ΔNNO	ΔNNO (max.)	ΔNNO (Min)
VK1	LDD16A_02	P	0.018	0.005	1.02	-1.752	-3.228	-2.990	-3.557
VK1	LDD16A_02	P	0.024	0.007	1.42	-1.615	-1.648	-1.628	-1.676
VK1	LDD16A_02	P	0.020	0.005	1.14	-1.707	-2.78	-2.603	-3.024
VK1	LDD16A_02	P	0.029	0.005	1.68	-1.537	-0.616	-0.738	-0.448
VK1	LDD16A_02	P	0.019	0.006	1.13	-1.712	-2.788	-2.610	-3.033
VK1	LDD16A_02	P	0.015	0.007	0.89	-1.811	-3.768	-3.455	-4.200
VK1	LDD16A_02	P	0.021	0.005	1.20	-1.684	-2.536	-2.393	-2.733
VK1	LDD10_02	P	0.019	0.008	1.07	-1.726	-3.048	-2.834	-3.343
VK1	LDD10_02	P	0.019	0.006	1.11	-1.711	-2.884	-2.693	-3.148
VK1	LDD10_02	P	0.019	0.007	1.12	-1.712	-2.828	-2.645	-3.081
VK1	LDD10_02	P	0.015	0.006	0.88	-1.815	-3.8	-3.483	-4.238
VK1	LDD10_02	P	0.019	0.007	1.10	-1.712	-2.908	-2.714	-3.176
VK1	LDD16A_02	M	0.021	0.007	1.173	-1.687	-2.628	-2.472	-2.843
VK1	LDD16A_02	M	0.025	0.006	1.442	-1.604	-1.552	-1.545	-1.562
VK1	LDD10_02	M	0.017	0.001	0.949	-1.774	-3.524	-3.245	-3.910
VK1	LDD10_02	M	0.017	0.007	0.940	-1.780	-3.56	-3.276	-3.952
VK1	LDD10_02	M	0.017	0.006	0.955	-1.772	-3.5	-3.224	-3.881
VK1	LDD10_02	M	0.023	0.006	1.339	-1.634	-1.964	-1.900	-2.052
VK1	LDD10_02	M	0.016	0.006	0.924	-1.784	-3.624	-3.331	-4.029
VK1	LDD16A_02	M	0.019	0.008	1.078	-1.729	-3.008	-2.800	-3.295
VK1	LDD16A_02	M	0.023	0.006	1.294	-1.648	-2.144	-2.055	-2.267
VK1	LDD16A_02	M	0.020	0.006	1.130	-1.705	-2.8	-2.621	-3.048
VK1	LDD16A_02	M	0.018	0.006	1.054	-1.735	-3.104	-2.883	-3.410
VK1	LDD10_02	M	0.016	0.005	0.895	-1.806	-3.74	-3.431	-4.167
VK1	LDD10_02	M	0.016	0.006	0.915	-1.794	-3.66	-3.362	-4.071
VK1	LDD10_02	M	0.017	0.007	0.984	-1.766	-3.384	-3.124	-3.743
VK1	LDD10_02	M	0.020	0.006	1.157	-1.694	-2.692	-2.528	-2.919

Table B.5: Oxygen fugacity results from calculations using perovskite compositions. Abbreviations: lith - lithofacies; samp = sample-ID; para = paragenesis.

B.4 Bulk Rock Geochemistry

XRF39

X-ray fluorescence was performed on all samples at the Anglo American Research Laboratories (AARL), Johannesburg, South Africa, using a Philips PW1606 simultaneous XRF spectrometer using pressed powder briquettes. Major elements were analysed using an Oxford Link energy-dispersive X-ray analyser and trace elements were measured using wavelength-dispersive XRF utilizing instrumentation [1]. Samples were halved at SGS Lakefield, Johannesburg (ISO/IEC 17025 compliant, by the South African National Accreditation System Accredited Laboratory); half for XRF analysis and half to keep as a record for the future. Samples were crushed and milled to 80-90% $\leq$70 μm using Labtechnik LM mills and chrome-free pulverising vessels. Quartz chips are milled at the start and end of a batch to check for contamination from mill pots. The vessels are cleaned manually between each sample[2]. The compositions of quality control reference materials S01, S7 and 100ppm are shown in Table B.4. This (XRF39) semi-quantitative technique was chosen for the rapid analytical turnaround time. Semi-quantitative data was considered suitable for carrying out multivariate statistics.

XRF at Edinburgh University

A subset of samples was crushed and milled at UCL/Birkbeck using steel jaw crusher and a tungsten carbide ring mill, and analysed at the University of Edinburgh using a Panalytical PW2404 wavelength-dispersive sequential X-ray spectrometer. This is a quantitative technique used to calibrate the XRF39 process described above. Standards used are given in Govindaroju (1994). The difference in elemental abundances between the two techniques are shown in Figures B.2 and B.3.

[1] Taken from http://www.aarl.co.za/.

[2] AARL information from Plint & Bocks (2005).

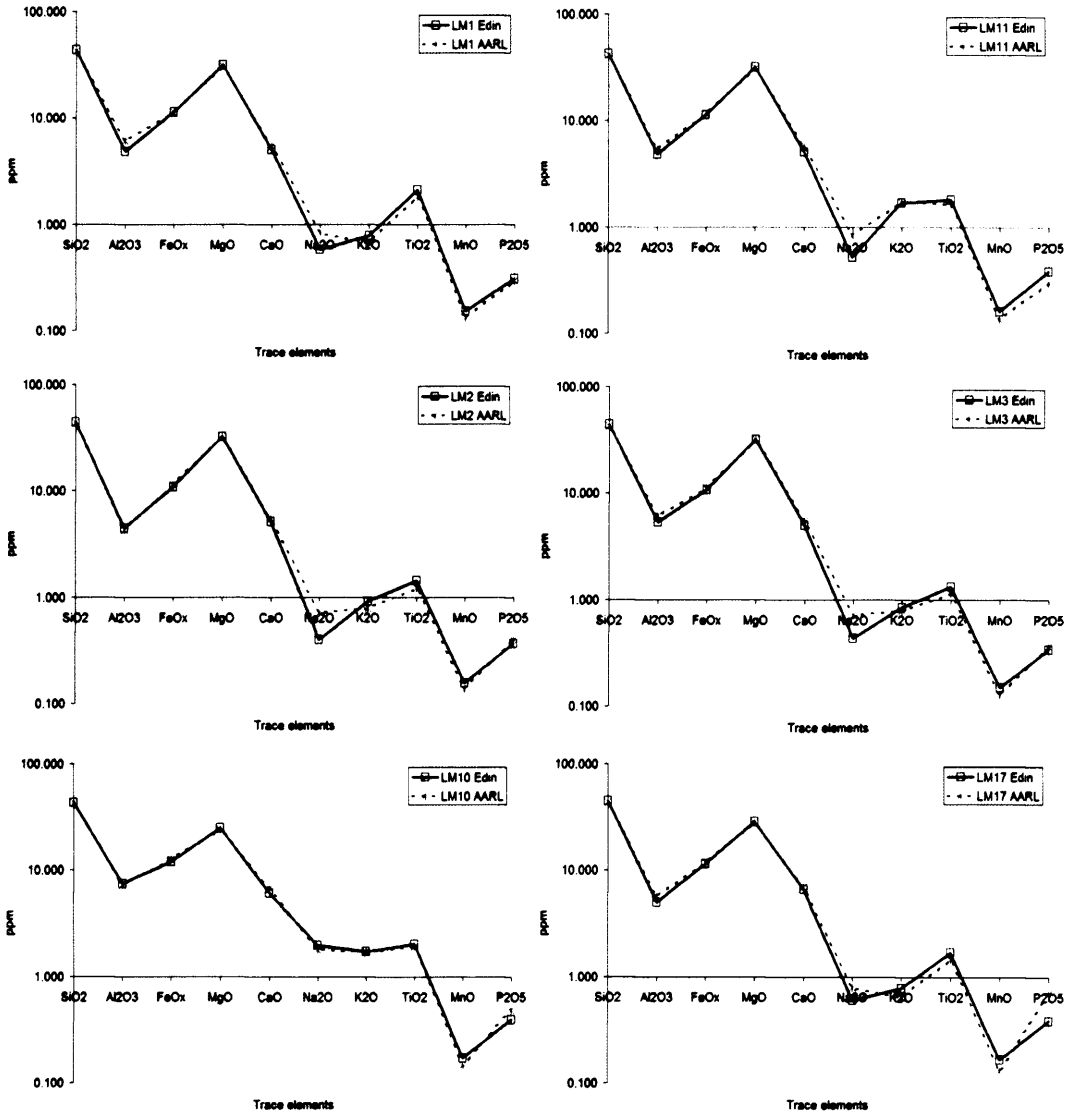

Figure B.2: Line graphs displaying the difference in major elements analysed by XRF at Edinburgh University and the AARL.

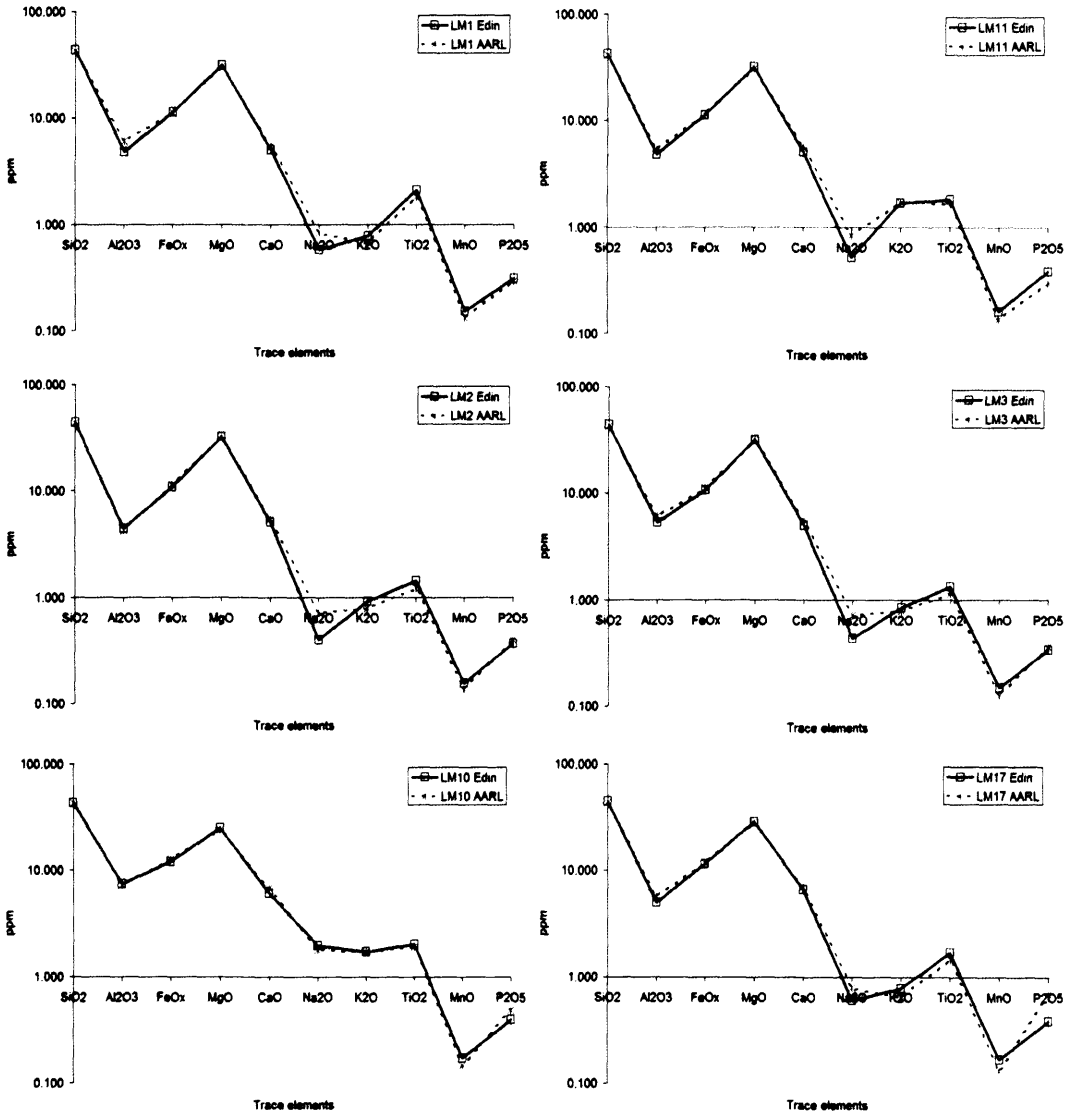

Figure B.2: Line graphs displaying the difference in major elements analysed by XRF at Edinburgh University and the AARL.

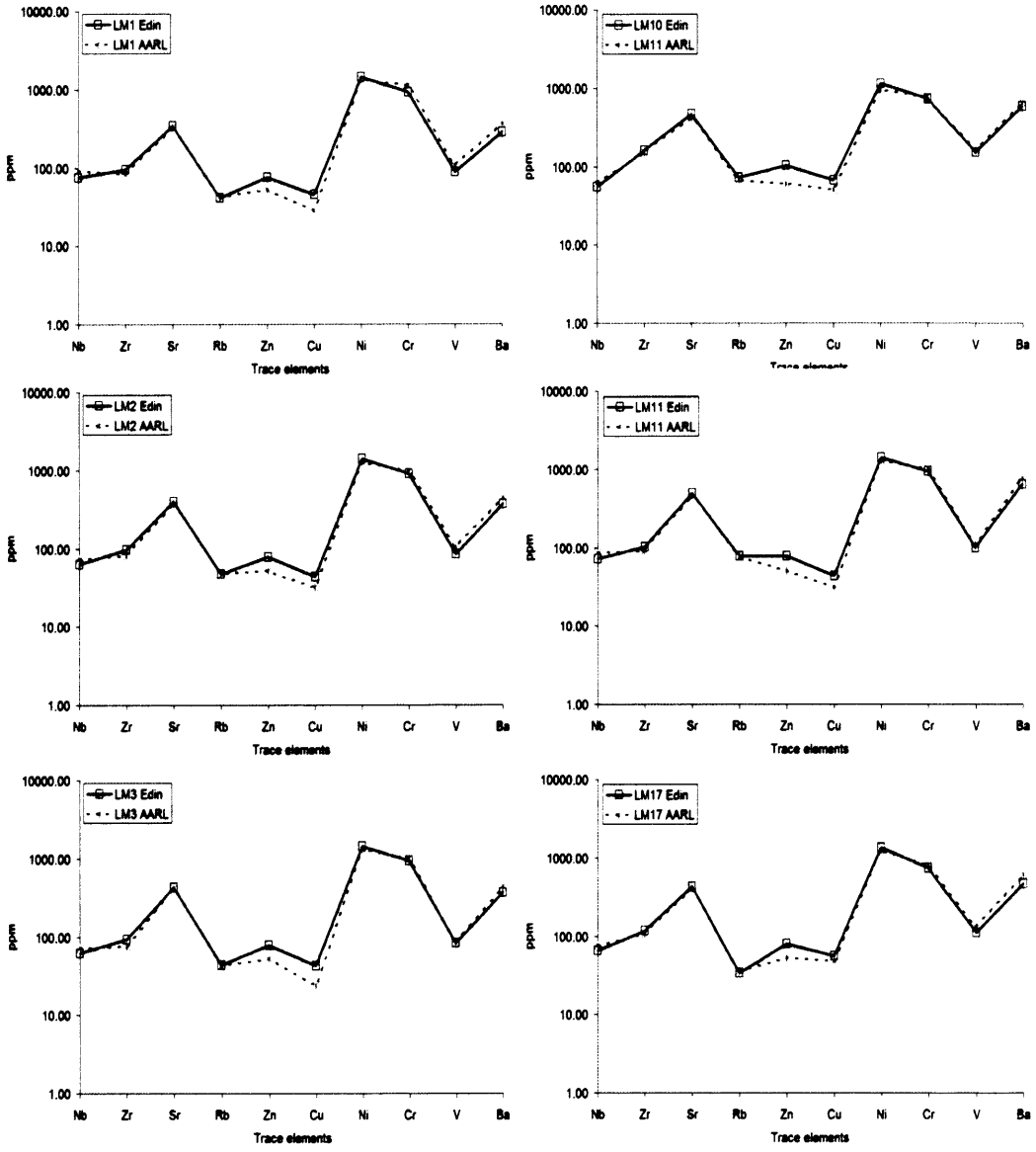

Figure B.3: Line graphs displaying the difference in trace elements analysed by XRF at Edinburgh University and the AARL.

Standard	S01			S7			100ppm		
Analyte	Lower	Average	Upper	Lower	Average	Upper	Lower	Average	Upper
Major elements (wt%)									
Total	92.65	95.71	98.77	93.84	96.21	98.57	94.32	98.24	102.16
F	0.06	0.07	0.08	0.05	0.07	0.08	0.04	0.06	0.08
Na_2O	0.94	1.01	1.09	0.74	0.81	0.88	0.16	0.26	0.36
MgO	2.69	2.74	2.8	27.39	28.15	28.91	0.21	0.25	0.28
Al_2O_3	13.5	14.52	15.54	3.96	4.63	5.31	$\leq$ 0.01	0.25	0.68
SiO_2	61.15	63.15	65.14	34.47	35.81	37.15	82.3	86.36	90.42
P_2O_5	0.2	0.43	0.65	1.25	1.49	1.73	0.06	0.28	0.49
SO_3	0.46	0.56	0.66	0.78	0.83	0.89	0.06	0.1	0.13
K_2O	2.87	3.02	3.16	1.01	1.1	1.18	$\leq$ 0.01	0.04	0.09
CaO	3.53	3.65	3.78	10.83	11.1	11.36	$\leq$ 0.01	0.05	0.09
TiO_2	0.61	0.68	0.74	1.32	1.39	1.47	0.01	0.06	0.11
V_2O_5	$\leq$ 0.01	$\leq$ 0.01	0.01	$\leq$ 0.01	$\leq$ 0.01	$\leq$ 0.01	$\leq$ 0.01	$\leq$ 0.01	0.01
Cr_2O_3	< 0.01	< 0.01	0.02	0.12	0.15	0.17	0.01	0.01	0.01
MnO	0.03	0.05	0.06	0.14	0.16	0.18	$\leq$ 0.01	0.01	0.02
Fe_2O_3	5.6	5.79	5.98	10.04	10.31	10.57	9.85	10.48	11.11
NiO	$\leq$ 0.01	0.01	0.02	0.16	0.18	0.2	$\leq$ 0.01	0.01	0.02
CuO	$\leq$ 0.01	0.01	0.03	0.01	0.02	0.03	0.01	0.02	0.03
ZnO	0.01	0.01	0.01	0.01	0.01	0.01	0.01	0.01	0.01
Trace Elements (ppm)									
Ni	19	20	22	1095	1102	1108	92	94	95
Cu	5	6	8	55	58	61	64	76	88
Zn	92	96	100	57	62	67	94	100	106
As	$\leq$ 10	3	10	$\leq$ 10	8	17	124	134	146
Se	$\leq$ 10	$\leq$ 10	1	$\leq$ 10	$\leq$ 10	1	4	5	6
Rb	109	110	111	54	55	56	99	100	102
Sr	164	165	167	1417	1421	1424	107	108	109
Y	20	20	21	12	12	13	106	107	109
Zr	165	166	168	274	277	280	122	123	125
Nb	12	13	13	129	130	131	130	131	132
Mo	$\leq$ 10	$\leq$ 10	$\leq$ 10	$\leq$ 10	$\leq$ 10	$\leq$ 10	89	96	102
Sn	$\leq$ 10	1	7	$\leq$ 10	$\leq$ 10	27	111	120	128
Sb	$\leq$ 10	$\leq$ 10	< 10	$\leq$ 10	< 10	< 10	113	117	121
Te	$\leq$ 10	$\leq$ 10	9	1	12	23	201	214	226
Ta	$\leq$ 10	$\leq$ 10	$\leq$ 10	$\leq$ 10	2	4	203	207	212
W	$\leq$ 10	$\leq$ 10	6	$\leq$ 10	$\leq$ 10	11	140	146	153
Pb	31	33	34	17	19	21	128	130	132
Bi	$\leq$ 10	$\leq$ 10	$\leq$ 10	$\leq$ 10	$\leq$ 10	$\leq$ 10	111	113	115
Th	6	9	12	12	15	18	131	139	146
U	$\leq$ 10	$\leq$ 10	$\leq$ 10	$\leq$ 10	$\leq$ 10	< 10	120	122	124
Cr	43	67	91	1291	1328	1365	87	101	116
V	116	143	170	90	116	143	106	126	146
Co	4	15	26	67	81	94	47	57	67
Ba	476	604	732	1591	1851	2111	73	136	200

Table B.6: Compositions of standards used for the semi-quantitative technique at AARL.

Lithology	Basalt					Coal		Granite				Lamintated-SST	
Major Elements (wt%)													
Al_2O_3	15.15	14.94	14.52	15.60	16.02	28.93	25.24	12.55	12.83	12.68	13.55	2.16	12.52
CaO	10.08	8.60	10.22	11.66	11.76	4.25	1.24	1.81	1.88	2.25	2.25	0.10	2.20
Cr_2O_3	0.02	0.02	0.02	0.02	0.02	0.02	nd	nd	nd	0.01	nd	nd	0.01
CuO	0.02	0.03	0.03	0.03	0.02	0.06	0.05	0.01	0.01	0.01	0.01	0.01	0.01
F	0.07	0.07	0.07	0.07	0.07	0.07	0.08	0.06	0.05	0.07	0.07	0.05	0.06
Fe_2O_3	10.98	11.11	11.13	11.40	11.06	5.89	8.94	2.60	2.36	4.63	4.34	2.11	3.42
K_2O	0.61	0.73	0.60	0.57	0.54	1.26	2.83	2.90	2.96	3.80	3.55	0.86	3.53
MgO	6.53	6.23	6.63	5.07	5.20	0.96	1.16	0.92	0.93	1.68	1.28	0.44	1.88
MnO	0.12	0.15	0.14	0.15	0.14	0.04	0.00	0.04	0.03	0.09	0.04	0.02	0.05
Na_2O	3.31	3.58	3.35	2.36	2.44	0.72	2.77	2.72	2.74	2.54	2.28	0.39	0.90
NiO	0.01	0.01	0.02	0.01	0.02	0.04	0.03	nd	nd	0.01	0.01	nd	nd
P_2O_5	0.17	0.24	0.17	0.24	0.31	1.07	0.38	0.33	0.17	0.18	0.16	0.13	0.32
SiO_2	51.97	53.27	52.16	51.76	51.42	54.30	55.50	75.89	75.87	71.40	72.09	93.64	74.57
SO_3	nd	nd	nd	nd	nd	0.13	0.11	nd	nd	nd	0.02	nd	nd
TiO_2	0.90	1.02	0.91	1.03	0.97	2.25	1.64	0.16	0.14	0.64	0.34	0.08	0.50
V_2O_5	0.03	0.01	0.02	0.02	0.01	nd	nd	nd	nd	nd	nd	nd	nd
ZnO	0.01	0.01	0.01	0.01	0.01	0.01	0.02	0.01	0.01	0.01	0.01	0.01	0.01
Trace Elements (ppm)													
As	nd	nd	nd	14.19	nd	nd	nd	nd	nd	nd	nd	nd	nd
Ce	nd	nd	nd	nd	72.30	47.70	39.00	nd	nd	nd	66.90	nd	nd
Bi	nd	nd	nd	nd	nd	nd	nd	nd	nd	nd	nd	nd	nd
Ba	75.30	246.10	nd	180.40	193.70	857.10	884.50	790.40	833.20	806.50	883.50	218.20	451.90
Co	45.00	42.10	43.10	47.00	54.10	14.70	14.90	nd	6.30	6.70	12.70	nd	8.50
Cr	292.90	322.60	268.40	381.50	495.70	nd	nd	25.60	34.00	135.70	70.00	nd	nd

Lithology	Basalt					Coal		Granite				Lamintated-SST	
Cu	57.01	67.87	57.55	118.10	53.73	nd	nd	nd	nd	nd	nd	nd	nd
La	nd	nd	nd	nd	nd	nd	nd	nd	nd	nd	nd	nd	nd
Nb	nd	nd	nd	nd	nd	14.26	12.87	nd	nd	nd	nd	nd	nd
Nd	nd	nd	nd	nd	nd	101.60	81.70	nd	nd	nd	nd	nd	nd
Ni	71.19	59.18	69.39	73.08	76.84	5.45	0.00	7.40	5.08	27.04	22.76	0.00	2.86
Pb	nd	nd	nd	nd	nd	56.83	20.91	77.99	77.39	33.70	30.90	nd	16.04
Rb	13.78	12.99	13.66	15.76	14.97	40.77	71.76	81.10	80.92	114.29	95.51	28.06	111.80
Sr	478.72	140.59	478.27	208.33	203.98	352.45	285.90	155.51	155.47	185.19	108.26	31.18	101.22
Th	10.60	nd	nd	nd	13.00	nd	22.80	20.70	23.30	nd	42.80	nd	19.40
U	nd	nd	nd	nd	11.30	nd	nd	nd	11.10	15.00	13.00	nd	11.80
V	271.90	225.30	254.00	254.20	242.20	92.30	60.30	18.90	28.70	79.90	42.50	41.10	69.30
Y	16.03	19.30	15.97	23.07	20.76	36.50	29.41	17.96	17.84	nd	nd	nd	27.08
Zn	54.63	58.45	53.91	57.84	57.71	46.11	111.76	30.08	30.39	62.10	48.32	17.80	44.33
Zr	36.82	54.46	36.79	69.51	58.69	188.15	133.02	56.78	58.65	213.26	107.35	69.82	210.53

Table B.7: Bulk rock geochemistry of country rock samples.

Lithology	Mudstone			Sandstone	
Major Elements (wt%)					
Al_2O_3	16.93	12.42	13.84	8.42	14.26
CaO	1.66	3.39	1.86	1.41	1.39
Cr_2O_3	0.01	nd	nd	nd	nd
CuO	0.01	0.01	0.01	0.01	0.01
F	0.06	0.07	0.06	0.06	0.07
Fe_2O_3	3.92	4.89	4.11	2.82	4.91
K_2O	2.45	3.67	3.29	3.02	3.83
MgO	1.80	1.90	1.91	1.32	3.09
MnO	0.02	0.08	0.01	0.03	0.02
Na_2O	1.45	0.53	1.35	0.65	1.16
NiO	nd	0.01	0.01	0.01	0.01
P_2O_5	0.09	0.37	0.12	0.22	0.37
SiO_2	70.77	72.18	72.73	81.72	70.27
SO_3	0.05	nd	0.04	nd	nd
TiO_2	0.76	0.46	0.66	0.30	0.60
V_2O_5	nd	nd	nd	nd	nd
ZnO	0.01	0.01	0.01	0.01	0.01
Trace Elements (ppm)					
As	nd	nd	nd	nd	nd
Ce	59.30	68.60	nd	46.40	nd
Bi	nd	nd	nd	nd	nd
Ba	326.80	392.50	489.40	454.90	328.90
Co	14.40	14.30	9.40	nd	8.30
Cr	62.10	44.90	21.50	nd	14.90

Lithology	Mudstone			Sandstone	
Cu	nd	nd	nd	nd	nd
La	nd	nd	nd	nd	nd
Nb	20.76	nd	16.76	nd	14.70
Nd	90.40	nd	nd	nd	nd
Ni	3.84	10.94	6.76	0.00	4.93
Pb	25.22	32.82	23.87	nd	17.66
Rb	119.41	122.05	143.55	87.80	132.67
Sr	143.55	77.34	192.75	69.89	253.73
Th	21.50	16.60	17.30	10.40	19.70
U	nd	nd	10.10	nd	nd
V	78.50	59.50	113.40	70.70	46.90
Y	31.39	29.14	23.72	nd	21.21
Zn	62.21	46.63	63.47	29.73	49.88
Zr	200.68	177.99	214.26	175.98	255.54

Table B.8: Bulk rock geochemistry of country rock samples.

SampleID	Geochem Grp	Al_2O_3	CaO	Cr_2O_3	CuO	Fe_2O_3	K_2O	MgO	MnO	Na_2O	NiO	P_2O_5	SiO_2	TiO_2	V_2O_5
LDD02A-01	Aiii	4.83	5.37	0.06	0.02	11.62	0.74	31.43	0.13	0.78	0.23	0.45	43.13	1.19	0.01
LDD02A-02	Aiii	4.91	4.30	0.06	0.02	11.46	0.74	31.95	0.12	0.82	0.24	0.34	43.83	1.19	0.01
LDD02A-03	Aii	5.94	4.16	0.08	0.02	11.55	1.11	31.04	0.12	0.84	0.24	0.25	43.38	1.26	nd
LDD02A-04	Aii	4.22	4.72	0.08	0.01	11.74	0.87	32.84	0.14	0.72	0.24	0.29	42.90	1.21	0.01
LDD02A-05	Ciii	4.01	5.14	0.07	0.01	10.90	1.22	31.45	0.12	0.89	0.24	0.40	44.48	1.06	nd
LDD07-02	Biii	5.39	9.41	0.06	0.02	12.63	0.68	26.89	0.15	1.00	0.20	0.48	41.36	1.74	0.01
LDD07-03	Ciii	4.87	6.84	0.07	0.02	12.02	1.44	30.38	0.14	0.66	0.22	0.41	41.18	1.72	0.01
LDD07-04	Cii	4.94	7.11	0.07	0.02	12.45	1.74	28.94	0.14	0.88	0.21	0.48	41.08	1.91	0.01
LDD07-05	Ci	5.40	6.65	0.07	0.01	12.00	1.68	28.74	0.15	1.02	0.20	0.38	41.98	1.72	0.01
LDD07-06	Ci	4.62	6.28	0.08	0.02	12.19	1.52	30.26	0.14	0.82	0.23	0.47	41.74	1.64	0.01
LDD07-07	Div	5.52	5.89	0.05	0.03	12.33	0.98	27.56	0.14	1.77	0.21	0.41	43.49	1.61	0.01
LDD07-08	Bii	4.84	5.94	0.06	0.02	11.80	1.23	29.86	0.14	1.06	0.23	0.40	42.98	1.43	0.02
LDD07-10	Ai	5.23	4.86	0.06	0.01	11.78	0.85	30.64	0.13	1.13	0.23	0.25	43.53	1.29	0.01
LDD07-11	Bi	4.85	5.01	0.07	0.01	11.76	0.86	31.51	0.14	1.00	0.24	0.29	43.00	1.26	nd
LDD07-12	Ai	5.21	4.48	0.06	0.02	11.93	0.81	29.86	0.13	1.52	0.23	0.42	44.12	1.20	nd
LDD07-13	Aiii	5.01	4.19	0.06	0.03	12.15	0.75	32.19	0.14	1.07	0.26	0.20	42.68	1.26	0.01
LDD07-14	Aii	4.79	4.73	0.06	0.01	12.10	0.91	31.44	0.15	1.06	0.24	0.34	42.77	1.39	0.01
LDD07-15	Ai	5.26	4.06	0.07	0.01	11.77	1.18	28.78	0.13	1.84	0.22	0.18	45.23	1.27	0.01
LDD07-16	Cvi	3.53	7.69	0.12	0.03	12.11	2.29	31.42	0.15	0.77	0.24	0.53	39.64	1.47	0.01
LDD10 01	Ci	5.65	5.85	0.00	0.00	12.31	1.27	28.76	0.17	0.86	nd	0.18	43.15	1.79	nd
LDD10 03	Di	8.54	7.99	0.00	0.00	12.64	1.20	19.04	0.14	1.78	nd	0.53	45.97	2.17	nd
LDD10 06	Cii	6.20	7.01	0.00	0.00	11.78	1.45	28.99	0.14	0.83	nd	0.69	41.18	1.72	nd
LDD10 07	Cii	4.58	6.18	0.00	0.00	12.40	1.87	30.10	0.15	1.03	nd	0.42	41.34	1.92	nd
LDD12 01	Div	6.14	8.04	0.00	0.00	12.18	0.55	26.34	0.17	1.12	nd	0.30	43.52	1.64	nd
LDD12 03	Dii	7.14	9.66	0.00	0.00	12.17	0.62	22.37	0.14	1.35	nd	0.58	44.27	1.70	nd
LDD12 04	Biii	4.03	7.94	0.00	0.00	12.60	0.60	28.53	0.15	0.91	nd	0.67	42.85	1.72	nd
LDD12 05	Biv	6.51	9.24	0.00	0.00	11.25	1.01	25.43	0.13	1.02	nd	0.35	43.45	1.61	nd
LDD13-01	Di	8.02	9.05	0.04	0.03	11.70	1.08	21.01	0.13	1.17	0.15	0.59	45.56	1.47	nd
LDD13-02	Biv	6.10	9.21	0.05	0.03	11.84	1.38	25.05	0.18	0.92	0.18	0.53	42.94	1.56	0.01
LDD13-03	Biv	5.46	9.36	0.06	0.03	12.10	0.84	25.78	0.13	0.91	0.20	0.56	42.90	1.65	0.01
LDD13-04	Biv	5.96	9.08	0.09	0.02	11.53	0.96	24.84	0.13	0.95	0.17	0.67	44.01	1.60	0.01
LDD13-05	Biv	7.88	8.66	0.10	0.02	11.69	0.56	23.77	0.14	0.99	0.15	0.59	43.76	1.68	nd
LDD13-06	Di	7.66	9.08	0.03	0.03	11.58	0.68	22.99	0.15	1.14	0.15	0.43	44.71	1.35	0.01

SampleID	Geochem Grp	Al_2O_3	CaO	Cr_2O_3	CuO	Fe_2O_3	K_2O	MgO	MnO	Na_2O	NiO	P_2O_5	SiO_2	TiO_2	V_2O_5
LDD16A 18	Aii	3.63	4.96	0.00	0.00	12.03	0.94	31.97	0.14	0.85	nd	0.31	43.74	1.43	nd
LDD16A 23	Aii	6.25	4.97	0.00	0.00	11.43	1.22	30.57	0.13	0.87	nd	0.33	42.88	1.35	nd
LDD21 01	Di	7.82	9.94	0.00	0.00	11.58	0.52	22.44	0.13	1.09	nd	0.45	44.48	1.54	nd
LDD21 06	Cvi	4.21	9.96	0.00	0.00	13.51	1.66	29.12	0.18	0.97	nd	0.73	37.64	2.01	nd
LDD22-01	Dii	6.88	7.82	0.04	0.02	11.97	0.84	24.07	0.15	1.03	0.18	0.37	45.07	1.54	0.01
LDD22-02	Diii	6.41	7.76	0.04	0.03	12.16	0.50	26.83	0.14	0.90	0.18	0.51	43.03	1.52	0.01
LDD22-03	Biii	5.99	7.19	0.05	0.02	11.79	0.74	28.61	0.14	0.86	0.20	0.36	42.60	1.45	nd
LDD22-04	Bii	5.87	8.22	0.07	0.02	11.81	0.77	27.67	0.13	0.78	0.19	0.51	42.37	1.57	0.01
LDD22-05	Cv	4.20	6.79	0.10	0.02	12.13	2.03	31.54	0.14	0.62	0.24	0.46	40.02	1.70	0.01
LDD22-06	Cv	3.60	7.18	0.10	0.02	12.44	2.34	32.20	0.16	0.51	0.24	0.54	39.12	1.54	0.01
LDD22-07	Cv	3.85	7.65	0.09	0.02	12.30	1.79	32.58	0.14	0.53	0.26	0.52	38.75	1.51	0.01
LDD22-08	Ci	4.47	7.48	0.09	0.02	12.16	1.96	30.29	0.15	0.74	0.23	0.39	40.48	1.55	nd
LDD22-10	Bii	6.31	5.45	0.05	0.02	11.60	1.16	28.63	0.13	1.40	0.20	0.38	43.26	1.39	0.01
LDD22-11	Ci	4.75	7.84	0.07	0.02	11.72	1.82	29.56	0.14	0.85	0.22	0.43	41.12	1.44	nd
LDD24-01	Di	7.63	8.92	0.04	0.03	11.63	0.64	23.40	0.15	1.09	0.16	0.54	44.37	1.41	nd
LDD24-02	Di	7.16	9.01	0.04	0.03	11.67	0.51	23.94	0.15	1.04	0.18	0.38	44.38	1.49	0.01
LDD24-03	Biv	6.32	8.92	0.05	0.03	11.11	0.67	24.86	0.12	1.06	0.18	0.37	44.84	1.46	0.01
LDD24-04	Dii	7.81	8.80	0.04	0.02	11.68	0.33	22.67	0.12	1.30	0.17	0.46	45.13	1.46	0.01
LDD24-05	Dii	7.05	9.42	0.04	0.03	12.23	0.44	22.63	0.13	1.30	0.19	0.58	44.40	1.55	0.01
LDD24-06	Dii	7.60	9.27	0.02	0.03	12.10	0.43	21.56	0.14	1.57	0.16	0.38	45.29	1.43	0.02
LDD24-07	Dii	7.25	9.85	0.03	0.03	12.39	0.43	21.95	0.14	1.51	0.17	0.43	44.23	1.57	0.01
LDD24-08	Biii	5.31	7.58	0.06	0.03	12.42	0.98	26.95	0.14	0.89	0.21	0.38	43.37	1.67	0.01
LDD24-09	Cv	3.83	6.22	0.11	0.02	13.01	2.20	31.51	0.16	0.65	0.26	0.39	39.65	1.99	0.01
LDD24-10	Cv	5.30	6.35	0.09	0.02	11.91	2.13	29.14	0.14	0.83	0.22	0.40	41.73	1.72	0.01
LDD24-11	Cv	4.72	6.86	0.08	0.01	12.01	2.60	29.58	0.15	0.85	0.22	0.59	40.49	1.81	0.02
LDD24-12	Aiv	4.01	7.65	0.08	0.03	12.54	0.82	30.32	0.15	0.67	0.23	0.49	41.17	1.83	0.01
LDD24-13	Cv	4.33	7.96	0.10	0.02	12.33	2.13	29.59	0.15	0.65	0.22	0.55	40.03	1.93	0.01
LDD25B-01	Cvi	4.34	6.73	0.11	0.03	11.58	2.21	31.50	0.14	0.78	0.24	0.52	40.48	1.33	nd
LDD25B-02	Cvi	4.60	6.07	0.11	0.01	11.09	2.23	31.72	0.15	0.87	0.22	0.54	41.06	1.32	nd
LDD67-01	Div	6.08	7.65	0.05	0.03	11.83	0.49	27.62	0.14	0.96	0.17	0.44	43.24	1.28	nd
LDD67-02	Diii	6.45	7.34	0.05	0.02	11.94	0.62	26.48	0.13	1.05	0.20	0.49	43.72	1.51	nd
LDD68-01	Ai	5.50	5.28	0.06	0.01	11.53	1.03	30.03	0.13	1.22	0.21	0.36	43.49	1.14	0.01
LDD68-02	Ai	5.05	5.55	0.07	0.01	11.65	0.89	30.41	0.15	1.17	0.23	0.32	43.28	1.21	0.01

SampleID	Geochem Grp	Al_2O_3	CaO	Cr_2O_3	CuO	Fe_2O_3	K_2O	MgO	MnO	Na_2O	NiO	P_2O_5	SiO_2	TiO_2	V_2O_5
LDD68-03	Ciii	4.34	5.42	0.07	0.02	11.42	0.73	31.81	0.13	0.93	0.23	0.39	43.25	1.23	0.01
LDD68-04	Aiii	4.35	5.05	0.07	0.02	11.48	0.66	32.17	0.13	0.90	0.24	0.28	43.45	1.19	0.01
LDD68-05	Aiii	4.99	4.85	0.08	0.02	11.49	0.58	32.14	0.13	0.87	0.24	0.51	42.91	1.19	0.01
LDD68-06	Aiii	5.22	4.87	0.07	0.02	11.76	0.62	31.38	0.12	0.89	0.25	0.38	43.16	1.24	0.01
LDD68-07	Civ	4.74	5.99	0.09	0.02	11.27	1.70	31.70	0.15	0.70	0.23	0.50	41.79	1.12	nd
LDD68-08	Civ	4.01	6.31	0.09	0.02	11.82	1.51	31.98	0.14	0.69	0.24	0.33	41.52	1.33	0.01
LDD68-09	Civ	4.62	5.91	0.10	0.02	11.04	1.36	31.85	0.14	0.68	0.22	0.50	42.35	1.20	0.01
LDD69-01	Biii	6.71	7.52	0.05	0.02	12.48	0.82	26.74	0.16	1.00	0.20	0.46	42.18	1.66	0.01
LDD74-01	Div	6.43	7.85	0.05	0.02	11.80	0.61	26.19	0.13	1.25	0.19	0.48	43.63	1.37	nd
LDD74-02	Div	6.43	8.20	0.05	0.03	12.51	0.69	25.84	0.15	1.31	0.20	0.43	42.73	1.42	0.01
LDD74-03	Biii	5.83	7.20	0.05	0.02	12.15	0.70	27.74	0.15	1.05	0.20	0.49	42.91	1.50	0.01
LDD74-04	Diii	6.06	7.93	0.04	0.03	12.12	0.55	25.16	0.14	1.41	0.19	0.41	44.30	1.65	0.02
LDD74-05	Bii	5.27	7.96	0.08	0.03	12.70	1.39	26.15	0.16	1.03	0.21	0.48	42.92	1.61	0.01
LDD74-06	Bvi	6.01	9.74	0.06	0.03	12.11	0.90	26.17	0.15	1.02	0.17	0.64	41.31	1.68	0.01
LDD74-07	Di	6.77	8.80	0.04	0.03	11.63	0.23	24.61	0.14	1.28	0.18	0.50	44.35	1.43	0.01
LDD76-01	Biii	5.79	7.27	0.06	0.02	12.16	0.68	27.84	0.14	1.03	0.20	0.20	43.02	1.57	0.01
LDD76-02	Div	7.04	7.82	0.05	0.02	11.92	0.68	25.36	0.14	1.35	0.17	0.34	43.65	1.45	0.01
LM01	Av	6.05	5.47	0.00	0.00	11.29	0.67	30.69	0.13	0.83	nd	0.29	42.77	1.81	nd
LM02	Aii	4.24	5.48	0.00	0.00	11.33	0.79	32.23	0.14	0.72	nd	0.40	43.46	1.21	nd
LM03	Av	6.05	5.45	0.00	0.00	11.13	0.78	31.73	0.13	0.72	nd	0.37	42.50	1.14	nd
LM10	Bvi	7.26	6.73	0.00	0.00	12.66	1.71	24.01	0.15	1.79	nd	0.48	43.29	1.91	nd
LM11	Civ	5.34	5.70	0.00	0.00	11.56	1.72	31.26	0.13	0.84	nd	0.30	41.49	1.65	nd
LM17	Bi	5.65	6.94	0.00	0.00	11.61	0.64	28.30	0.13	0.79	nd	0.69	43.78	1.46	nd
LM18	Bii	4.82	8.14	0.00	0.00	12.22	0.64	28.37	0.14	0.90	nd	0.45	42.65	1.67	nd
LM2W	Bi	5.10	6.28	0.00	0.00	11.45	0.70	30.09	0.12	0.84	nd	0.67	43.19	1.56	nd
LMC-2(1)	Bi	4.11	4.90	0.06	0.01	11.98	0.48	32.46	0.14	0.71	0.25	0.27	43.35	1.27	nd
LMC-2(2)	Aiii	4.68	4.92	0.07	0.02	11.72	1.63	30.12	0.14	0.87	0.23	0.32	43.96	1.31	0.01
LMC-2(3)	Aiii	4.82	5.62	0.06	0.02	11.88	0.67	31.08	0.14	0.83	0.23	0.29	43.10	1.26	0.01
LMC-2(4)	Aiii	4.66	4.75	0.07	0.02	11.52	0.52	32.24	0.13	0.87	0.25	0.32	43.57	1.08	nd
LMC-2(5)	Aiii	5.20	5.21	0.06	0.02	11.46	0.54	31.33	0.12	0.88	0.24	0.32	43.36	1.25	0.01
LMC-2(6)	Aiii	4.27	5.43	0.07	0.02	11.51	0.71	31.84	0.14	0.81	0.25	0.37	43.39	1.18	nd
LMS 12	Aii	4.78	4.75	0.07	0.01	11.10	1.30	32.01	0.14	1.14	0.22	0.39	42.81	1.27	nd
LMS 14	Ai	5.54	4.87	0.06	0.01	10.30	0.74	31.79	0.12	1.36	0.22	0.37	43.57	1.04	0.01

SampleID	Geochem Grp	Al_2O_3	CaO	Cr_2O_3	CuO	Fe_2O_3	K_2O	MgO	MnO	Na_2O	NiO	P_2O_5	SiO_2	TiO_2	V_2O_5
LMS 40	Biii	5.63	6.78	0.06	0.02	11.46	0.44	29.24	0.12	1.09	0.18	0.42	42.91	1.64	0.01
LMS 43	Ai	4.80	6.38	0.06	0.01	11.57	0.28	31.41	0.14	0.93	0.23	0.21	42.67	1.29	0.01
LMS 45	Cii	5.16	6.18	0.08	0.02	10.96	0.81	32.01	0.14	0.91	0.20	0.35	41.42	1.74	0.01
LMS 46	Aiv	3.71	5.02	0.11	0.01	10.37	0.79	35.16	0.12	0.94	0.20	0.41	41.88	1.27	nd
LMS 48	Av	3.97	5.56	0.07	0.01	10.40	0.56	33.08	0.12	0.91	0.23	0.49	43.57	1.03	0.01
LMS 49	Aiv	4.05	5.28	0.07	0.01	9.85	0.73	33.90	0.12	0.93	0.20	0.31	43.56	0.99	0.01
LMS 50	Aiv	4.93	5.41	0.08	0.02	9.91	0.73	33.65	0.11	0.93	0.20	0.41	42.52	1.09	0.01
LMS 51	Aiv	5.05	5.69	0.09	0.02	10.09	0.56	33.33	0.10	0.97	0.19	0.46	42.28	1.16	nd
LMS 52	Cvi	4.13	4.80	0.08	0.01	11.22	0.66	33.56	0.13	0.95	0.24	0.36	42.45	1.38	0.01
LMS 53	Av	4.96	4.88	0.08	0.01	11.14	0.58	33.02	0.13	0.94	0.24	0.42	42.35	1.23	0.01
LMS 55	Av	4.36	4.31	0.09	0.01	10.78	0.70	33.95	0.12	1.00	0.24	0.34	43.03	1.07	nd
LMS 56	Av	3.78	4.62	0.09	0.01	11.00	0.71	34.10	0.13	0.95	0.23	0.36	42.90	1.12	0.01
LMS 57	Av	4.36	4.73	0.10	0.02	10.40	0.84	34.94	0.13	0.97	0.21	0.34	41.88	1.09	0.01
LMS 58	Civ	3.35	6.11	0.11	0.02	12.56	2.23	31.63	0.17	0.84	0.28	0.55	40.89	1.27	0.01
LMS 6	Cv	4.81	5.96	0.09	0.02	11.54	2.71	29.04	0.13	1.39	0.21	0.50	41.89	1.70	0.01
LMS 61	Di	6.67	9.40	0.05	0.02	11.06	0.49	24.56	0.14	1.28	0.16	0.50	44.04	1.62	0.01
LMS 7	Ciii	5.01	6.16	0.07	0.01	11.71	2.16	30.44	0.14	1.12	0.22	0.56	40.73	1.65	0.01
LMS 8	Ciii	4.99	5.92	0.08	0.02	11.65	1.72	30.93	0.13	1.17	0.22	0.43	41.08	1.65	0.02
LMS 9	Bii	4.54	5.35	0.08	0.02	10.81	0.76	31.34	0.13	1.59	0.21	0.51	43.44	1.24	nd
LMS01	Ai	5.77	6.26	0.07	0.01	11.76	0.79	29.38	0.13	1.04	0.22	0.34	42.72	1.51	0.01
LMS02	Bi	5.26	6.32	0.08	0.01	12.13	1.01	30.08	0.14	1.00	0.22	0.44	41.73	1.57	nd
LMS03	Ci	5.40	7.15	0.08	0.02	12.00	1.42	30.07	0.13	0.78	0.22	0.41	40.62	1.68	0.01
LMS04	Cii	5.50	7.01	0.08	0.03	12.43	1.51	29.22	0.14	0.97	0.21	0.41	40.60	1.87	nd
LMS05	Cv	4.96	5.82	0.12	0.01	12.11	2.10	29.98	0.13	1.07	0.22	0.44	41.36	1.67	0.01
LMS10	Aiv	7.71	3.63	0.10	0.01	11.14	0.74	28.59	0.13	1.91	0.21	0.24	44.44	1.14	0.01
LMS11	Aiv	4.89	5.33	0.12	0.02	11.94	0.89	31.03	0.14	1.15	0.23	0.42	42.56	1.26	0.01
LMS13	Aii	5.33	5.04	0.09	0.02	11.76	0.78	31.10	0.12	1.02	0.24	0.42	42.76	1.31	0.01
LMS15	Aiii	4.79	4.56	0.07	0.02	11.73	0.64	31.60	0.14	1.14	0.24	0.30	43.55	1.22	nd
LMS16	Bi	4.85	5.10	0.08	0.02	11.70	0.84	31.18	0.14	1.05	0.23	0.27	43.30	1.25	nd
LMS18	Bi	4.55	5.71	0.06	0.02	12.43	0.95	30.48	0.14	1.15	0.24	0.39	42.53	1.36	nd
LMS19	Bi	5.05	4.75	0.06	0.02	11.23	0.83	30.16	0.11	1.02	0.22	0.45	44.92	1.18	nd
LMS20	Aii	4.37	4.18	0.06	0.01	11.17	0.59	32.99	0.12	1.07	0.24	0.19	43.98	1.04	nd
LMS21	Av	4.51	5.16	0.07	0.02	11.46	0.69	32.18	0.12	0.88	0.24	0.30	43.23	1.12	0.01

SampleID	Geochem Grp	Al_2O_3	CaO	Cr_2O_3	CuO	Fe_2O_3	K_2O	MgO	MnO	Na_2O	NiO	P_2O_5	SiO_2	TiO_2	V_2O_5
LMS22	Ai	5.43	6.38	0.06	0.02	12.01	0.74	29.84	0.14	0.86	0.21	0.45	42.34	1.50	0.01
LMS23	Bi	5.22	7.03	0.08	0.03	11.93	1.02	29.49	0.13	0.80	0.22	0.32	42.17	1.56	nd
LMS24	Diii	5.48	7.78	0.06	0.02	12.76	0.74	27.06	0.14	1.06	0.20	0.43	42.68	1.57	0.01
LMS25	Bvi	5.58	7.03	0.06	0.02	12.32	0.81	28.72	0.14	0.86	0.23	0.48	42.29	1.46	0.01
LMS26	Aiii	4.32	5.61	0.08	0.02	11.69	0.73	31.50	0.13	0.91	0.24	0.39	43.17	1.19	0.01
LMS27	Aiii	4.78	5.60	0.08	0.02	11.90	0.81	30.76	0.13	0.83	0.25	0.32	43.16	1.37	nd
LMS28	Biii	4.60	7.29	0.06	0.02	12.29	0.72	29.48	0.13	0.87	0.23	0.31	42.57	1.44	nd
LMS29	Bii	5.26	7.94	0.06	0.02	12.68	0.65	28.25	0.14	0.81	0.20	0.54	41.74	1.69	0.01
LMS30	Diii	6.02	8.16	0.04	0.02	11.91	0.50	25.54	0.14	1.29	0.18	0.50	44.15	1.53	0.01
LMS31	Div	5.96	7.83	0.05	0.03	11.79	0.52	26.38	0.13	1.17	0.18	0.51	43.90	1.52	0.01
LMS32	Di	7.27	8.15	0.04	0.02	12.61	0.54	25.25	0.14	1.27	0.18	0.37	42.64	1.50	0.01
LMS33	Diii	6.50	7.35	0.05	0.03	11.95	0.47	25.76	0.14	1.22	0.17	0.47	44.50	1.38	0.01
LMS34	Div	5.19	8.27	0.05	0.03	12.42	0.51	27.43	0.15	1.01	0.18	0.48	42.59	1.68	0.01
LMS35	Bi	4.24	6.57	0.07	0.02	11.84	0.42	30.78	0.14	0.74	0.22	0.49	43.03	1.43	0.01
LMS36	Ci	5.55	6.37	0.06	0.02	12.09	1.00	29.52	0.14	0.78	0.21	0.27	42.31	1.67	0.01
LMS37	Ci	4.95	6.42	0.08	0.02	12.39	1.07	29.56	0.15	0.72	0.22	0.49	42.16	1.76	0.01
LMS38	Diii	5.96	7.03	0.04	0.02	11.47	0.55	27.73	0.11	1.04	0.19	0.42	43.96	1.48	nd
LMS39	Diii	5.91	6.28	0.04	0.03	11.90	0.53	28.45	0.13	0.92	0.19	0.43	43.58	1.61	0.01
LMS41	Diii	5.86	6.95	0.05	0.03	11.65	0.33	28.16	0.10	0.96	0.19	0.37	43.81	1.52	0.01
LMS42	Diii	5.43	6.66	0.05	0.02	11.46	0.39	28.98	0.11	0.91	0.19	0.42	43.94	1.42	0.01
LMS44	Ci	3.80	5.95	0.08	0.03	12.23	1.04	30.18	0.14	0.70	0.21	0.41	43.57	1.65	0.01
LMS47	Av	4.36	5.51	0.09	0.02	11.61	0.75	31.81	0.14	0.72	0.24	0.42	43.01	1.31	0.01
LMS54	Aii	5.08	5.08	0.09	0.02	11.53	0.88	31.43	0.13	0.82	0.24	0.43	42.95	1.30	0.01

Table B.9: Bulk rock major element geochemistry (wt%) of D/K1 kimberlite samples.

SampleID	Geochem Grp	Ce	Ba	Co	Cr	Cu	F	Nb	Nd	Ni	Rb	Sr	Th	U	V	Y	Zn	Zr
LDD02A-01	Aiii	nd	332.1	96.4	797.8	31.4	0.1	63	nd	1309.4	42.8	335.8	nd	nd	93.8	nd	53.4	95
LDD02A-02	Aiii	45.5	283.9	107.6	829	14.3	0.1	62	nd	1316.5	41.6	283.5	nd	nd	84.7	nd	52.6	74.2
LDD02A-03	Aii	nd	451.8	100.1	898.3	16.3	0.1	64.7	nd	1338.8	61.8	286.2	9.9	nd	88.1	nd	54	80.2
LDD02A-04	Aii	nd	511.9	99.6	966.5	11.8	0.1	69.1	nd	1325.7	46.8	335.5	11.3	nd	96.5	nd	53.2	83.1
LDD02A-05	Ciii	48.1	659.1	100.9	976.7	16.2	0.1	76.1	nd	1312.8	60.8	343.8	14.2	nd	86.5	nd	51.8	80.8
LDD07-02	Biii	nd	522.5	91.4	870.3	42.1	0.1	71.2	nd	1042.8	47	402.7	12.5	nd	149.2	13.8	58.8	140.7
LDD07-03	Ciii	47.7	656.8	105.1	983.1	35.4	0.1	90.2	nd	1265.7	69	420.6	11	nd	119.2	nd	54.3	108.1
LDD07-04	Cii	63.5	680.1	105.5	1049.9	27.7	0.1	94.4	nd	1205	73.5	422.4	9.2	nd	132.2	10.3	55.1	124.5
LDD07-05	Ci	nd	735.4	94.2	932.3	15.3	0.1	94	nd	1175.8	69.3	411.2	14.9	nd	142.5	nd	56.7	120.4
LDD07-06	Ci	nd	738.5	96	910.1	31.7	0.1	89.7	nd	1255.8	65.7	485.9	10.9	11.7	133.6	nd	56.9	118.3
LDD07-07	Div	nd	458	95.2	699	47.1	0.1	62.1	nd	1134.1	50.5	588.9	20.6	15.7	143.7	13.1	61	150.3
LDD07-08	Bii	nd	529.6	94.7	859.5	30.1	0.1	81.3	nd	1224.2	63.9	500.9	12.7	nd	109.1	nd	55.2	106
LDD07-10	Ai	38.4	417.7	101.6	827	25.8	0.1	80.3	nd	1284.9	48.7	443.2	14.6	13.1	104.4	nd	56.3	103.8
LDD07-11	Bi	nd	545.7	99.1	821	13.5	0.1	69.3	nd	1316	51.4	450.4	16.6	12.6	93.8	nd	54.1	88.9
LDD07-12	Ai	nd	491	98.1	764.2	25.8	0.1	52.3	nd	1227.8	49.4	449	10.6	nd	105.4	nd	105.2	113
LDD07-13	Aiii	nd	346.4	103.7	853.7	12.5	0.1	59.4	nd	1317.9	46.2	253.8	11.5	nd	96	nd	53.3	84.3
LDD07-14	Aii	nd	460.2	99.9	855.7	0	0.1	64.2	nd	1284.4	49.1	296.3	12.7	nd	106.6	nd	53.3	81.2
LDD07-15	Ai	38.8	425	92.7	869.8	17.4	0.1	60.3	nd	1196.1	60.5	341.2	10.5	nd	109.7	nd	56.2	115.5
LDD07-16	Cvi	40.7	928.7	105.3	1194.2	42.2	0.1	110.4	nd	1322.9	82.6	544.1	17.2	nd	110.1	nd	50.9	114.6
LDD10 01	Ci	nd	715	101	939	45.1	0.1	81.6	nd	1167	56.3	373	nd	nd	136	nd	55.2	109
LDD10 03	Di	nd	575	85.5	667	86.7	0.1	62	nd	739	37	377	nd	nd	181	nd	64.6	196
LDD10 06	Cii	nd	611	107	1050	41.8	0.1	97.4	nd	1173	69	476	nd	nd	142	nd	52.7	108
LDD10 07	Cii	nd	607	110	1047	18.2	0.1	97.2	nd	1246	73	431	nd	nd	125	nd	54	109
LDD12 01	Div	nd	362	101	650	63.7	0.1	72.4	nd	1116	36.2	494	nd	nd	136	nd	55.2	150
LDD12 03	Dii	nd	354	84.9	520	73	0.1	57.3	nd	809	37.2	413	nd	nd	135	nd	55.7	165
LDD12 04	Biii	nd	474	103	730	59.6	0.1	79.1	nd	1134	39.8	427	nd	nd	139	nd	56.1	139
LDD12 05	Biv	nd	786	94.6	781	64.2	0.1	108	nd	1001	61.9	578	nd	nd	148	nd	51.1	155
LDD13-01	Di	nd	788.4	78.4	579	60.5	0.1	70.4	nd	776	55.8	425.4	23.2	18.2	136.3	15.2	54.5	138.2
LDD13-02	Biv	nd	629.9	92.2	801.4	58.5	0.1	103	nd	980.8	73.6	509	20.5	13.9	139.1	13.2	52.5	141.3
LDD13-03	Biv	nd	692	89.6	714.2	63.7	0.1	108.3	nd	1089.7	56.7	562	15.5	nd	139.1	13.4	56.4	148.1
LDD13-04	Biv	nd	870.1	94.5	1063.6	63.4	0.1	104.9	nd	1002.3	62.2	573.6	20.6	15.8	143.8	14.1	54.5	149.4
LDD13-05	Biv	nd	700.5	86.5	1192.6	74.2	0.1	91.1	nd	898.9	38.2	505.8	22.5	12.8	151.4	16.8	59.4	174.6
LDD13-06	Di	nd	598.6	78.8	537.9	55.6	0.1	79.7	nd	830.7	42.3	471.1	17.2	14.5	135.1	14.3	52.8	128.5

SampleID	Geochem Grp	Ce	Ba	Co	Cr	Cu	F	Nb	Nd	Ni	Rb	Sr	Th	U	V	Y	Zn	Zr
LDD16A 18	Aii	nd	539	105	938	15.2	0.1	69.6	nd	1304	52.3	366	nd	nd	106	nd	54.1	86.2
LDD16A 23	Aii	nd	504	107	959	22	0.1	71.3	nd	1308	67.5	344	nd	nd	103	nd	54.1	90.2
LDD21 01	Di	nd	489	93.5	592	65.1	0.1	83.9	nd	849	37.3	472	nd	nd	156	nd	53.2	157
LDD21 06	Cvi	nd	903	123	1324	64.8	0.1	153	nd	1392	81.6	561	nd	nd	141	nd	52.2	156
LDD22-01	Dii	nd	324.5	85.8	625.3	55.7	0.1	67.2	nd	950.7	49.2	355.1	12.5	nd	144.8	12.8	55	140.6
LDD22-02	Diii	nd	343.4	91.2	665.4	60.4	0.1	70.7	nd	1003.1	35.5	413.8	15.3	11	124.8	14.2	58.9	151.9
LDD22-03	Biii	nd	472.4	97.5	792.4	46.2	0.1	73.5	nd	1128.1	45.8	390.4	10.9	nd	121.6	10.1	55.4	116.3
LDD22-04	Bii	nd	633.9	95.6	797.1	42.3	0.1	81	nd	1126.6	43.2	445.2	16.8	nd	154.2	12.2	58.2	137.9
LDD22-05	Cv	nd	797.9	106.8	1206.4	36.6	0.1	115.5	nd	1348.3	75.2	406.4	15.6	10.5	111.2	nd	51	108
LDD22-06	Cv	nd	803.4	106	1099.4	46.2	0.1	117.4	nd	1377.9	75.7	505.5	23.3	16.8	112.4	nd	52.7	113.4
LDD22-07	Cv	44.6	747.1	110	1155.4	46.4	0.1	114.8	nd	1405.2	69.5	499.2	19.1	13.8	105.9	nd	50.7	97.2
LDD22-08	Ci	40.2	662.3	99.8	949.9	34.5	0.1	97.7	nd	1220.5	71.2	480.3	12	nd	123.3	nd	51.3	104.3
LDD22-10	Bii	nd	501.5	101.1	881.7	42.2	0.1	69.7	nd	1208.1	54.9	488.9	nd	nd	131.5	11.2	60.3	131.1
LDD22-11	Ci	41.5	692.4	102.8	896.5	47.4	0.1	91.4	nd	1206.7	67.1	508.2	14.8	10.8	131.4	0	52.5	112.3
LDD24-01	Di	nd	453.2	84	645.6	55.7	0.1	77.2	nd	842	40	419.5	15.1	11	133	14.6	53.2	134.3
LDD24-02	Di	nd	488.3	86.6	640.1	53.3	0.1	83.8	nd	922.3	35.7	486.9	14.9	nd	118.6	13.9	53.3	141.4
LDD24-03	Biv	nd	688.1	80.6	715.9	58.2	0.1	94.2	nd	964.9	49.1	525.7	15.8	11.9	118.7	12.7	51.2	139.4
LDD24-04	Dii	nd	154.2	85.4	534.7	61.4	0.1	56.2	nd	880.4	27	427.5	nd	nd	122.6	15	58.3	159.7
LDD24-05	Dii	nd	273	86.3	602.5	56	0.1	65.2	nd	928.5	28.2	399.8	18.3	10.6	133.8	13.8	55.6	147.8
LDD24-06	Dii	43.5	374.1	82.7	528.8	66.3	0.1	53.6	nd	828.6	29.1	431.9	13.1	nd	126.6	15	57	146.8
LDD24-07	Dii	nd	257.5	80.7	629.8	68.1	0.1	60.7	nd	849.6	32.1	448.7	14.8	nd	140.3	15.2	56.7	155
LDD24-08	Biii	nd	454.9	92.6	935.5	49.1	0.1	84	nd	1110.9	52.3	410.5	22.1	15.2	113.1	10.2	54	119
LDD24-09	Cv	40.1	749.4	100.2	1158.6	27.2	0.1	116.1	nd	1324.8	77.1	468.2	13.6	10.7	118.4	nd	50.1	111.8
LDD24-10	Cv	nd	817.1	100.5	1099.5	31.5	0.1	115.7	nd	1319	81.1	435.8	21.6	12.3	122.1	nd	55.6	118
LDD24-11	Cv	51.1	804.8	105.9	1082.6	25	0.1	112.5	nd	1214.9	81.1	451.3	16.9	nd	152.5	nd	53.1	121.5
LDD24-12	Aiv	48.4	394.9	96.7	1046	23.7	0.1	109.4	nd	1175	49.1	447.9	11.1	nd	110.8	nd	53.2	127
LDD24-13	Cv	41.5	790.1	104.7	1133.3	45.4	0.1	121.5	nd	1227.9	91.9	520.6	15.4	nd	134.2	nd	51.6	120.6
LDD25B-01	Cvi	41.6	934.2	105.5	1190	29	0.1	111.3	nd	1310	83.6	494.6	22.7	14.3	90.4	nd	51.3	102.3
LDD25B-02	Cvi	nd	928.5	104.4	1180.1	18.7	0.1	115.4	nd	1344	80.1	429.5	19.6	11	99.8	nd	49.6	106.1
LDD67-01	Div	nd	404.6	87	648.4	53.2	0.1	68.9	nd	1051.8	36.8	447.5	nd	nd	134.4	12.2	58.8	127.6
LDD67-02	Diii	nd	348.9	93.8	671.4	57.9	0.1	69	nd	1055.5	39	442.5	14.2	nd	119.3	12.8	59.1	149.6
LDD68-01	Ai	nd	487.2	97.6	855.7	21.6	0.1	56.9	nd	1245.4	62.1	414	nd	nd	113.3	nd	56.1	98.4
LDD68-02	Ai	nd	442.2	97.6	873.6	21.9	0.1	60.1	nd	1246.1	54.8	394.2	14.4	10.7	105.7	nd	56.5	99.5

SampleID	Geochem Grp	Ce	Ba	Co	Cr	Cu	F	Nb	Nd	Ni	Rb	Sr	Th	U	V	Y	Zn	Zr
LDD68-03	Ciii	nd	603.1	102.5	940.7	30.1	0.1	69.1	nd	1321.3	46.8	390.5	nd	nd	98	nd	54.7	96.7
LDD68-04	Aiii	nd	370.1	102.1	861.6	25.7	0.1	64.7	nd	1347.4	43	329.9	22.1	14.3	93.9	nd	55.1	100
LDD68-05	Aiii	nd	337.5	102.2	856.3	28.5	0.1	62.3	nd	1331.7	38.6	317.7	10.2	nd	88.2	nd	54.4	89.8
LDD68-06	Aiii	nd	266.8	99.3	842	35.1	0.1	63	nd	1298.8	39	311.9	11.3	nd	90.6	nd	55.1	95.9
LDD68-07	Civ	nd	711.1	95.2	1034.2	25.2	0.1	87.1	nd	1281	69.7	426.9	16.4	nd	90.7	nd	51.2	85.3
LDD68-08	Civ	nd	684.7	104.8	1050.5	37.2	0.1	85.9	nd	1268.2	60.9	441.2	18.8	11.5	103.1	nd	51.9	112
LDD68-09	Civ	nd	718.7	104.1	1090.4	29.3	0.1	90.8	nd	1301.8	64.2	418.1	11.9	nd	89.1	nd	52.6	91.6
LDD69-01	Biii	nd	481	87.7	822.3	46.1	0.1	75.4	nd	1026.3	48.5	393.6	14.4	12.3	150.2	11.6	57.2	116.8
LDD74-01	Div	nd	439.1	91.3	687.9	53.2	0.1	68.7	nd	1034.5	39.5	439.8	18.9	nd	137.9	13	57	144
LDD74-02	Div	nd	397.8	89.5	678.7	63.6	0.1	63.7	nd	1004.7	44.3	436.6	11.5	nd	138.9	12.9	59.6	130.3
LDD74-03	Biii	nd	438.7	95.2	763.9	53.8	0.1	75.7	nd	1110.6	43.8	444.3	11.2	nd	127.3	11.9	58	136
LDD74-04	Diii	nd	326	88.4	692.9	62.8	0.1	67	nd	983.5	34.9	411.3	16.3	13.4	119.7	14.1	57.7	167.5
LDD74-05	Bii	nd	564.5	98.7	941	60.4	0.1	87.4	nd	1180.3	75.1	514.2	15.8	12.4	139	11	58	141.2
LDD74-06	Bvi	nd	760.5	93.9	912.3	65.8	0.1	113.4	nd	1040.4	62.3	502.6	23.4	15.1	150.5	12.5	53.5	136.4
LDD74-07	Di	nd	488.8	86.7	639.7	61.1	0.1	91.1	nd	948.2	20.6	510.9	18.4	0	137.7	14.2	53.5	139.5
LDD76-01	Biii	nd	477.8	89.2	776.5	38.8	0.1	72.1	nd	1077.9	43.9	386.9	12.2	11.9	141.5	10.6	54.6	116.2
LDD76-02	Div	39.5	442	89.6	662.3	50.5	0.1	68	nd	992.9	42.3	412.5	nd	nd	129.5	12.4	55.1	139.5
LM01	Av	nd	361	104	1131	28.6	0.1	91.9	nd	1342	42.5	332	nd	nd	105	nd	52.8	82.9
LM02	Aii	nd	445	105	986	32.1	0.1	74.2	nd	1286	47.3	380	nd	nd	103	nd	52.7	81
LM03	Av	nd	443	109	1011	23.9	0.1	72.1	nd	1339	43.3	415	nd	nd	83.6	nd	53.6	75.7
LM10	Bvi	nd	656	91.8	771	49.8	0.1	62.6	nd	963	67.2	428	nd	nd	158	nd	61.5	152
LM11	Civ	nd	756	109	1018	31.3	0.1	86.1	nd	1311	76.3	470	nd	nd	107	nd	51.7	91.1
LM17	Bi	nd	618	119	814	48.6	0.1	76.3	nd	1268	36	417	nd	nd	129	nd	53.5	107
LM18	Bii	nd	570	97.7	851	49.7	0.1	84.7	nd	1127	33.2	467	nd	nd	137	nd	54.1	134
LM2W	Bi	nd	553	104	875	37.2	0.1	79.1	nd	1217	45.9	394	nd	nd	129	nd	51.7	99.4
LMC-2(1)	Bi	nd	556	99.1	788.7	nd	0.1	55.2	nd	1308.8	34.8	356.2	10.8	nd	104.2	nd	54.4	85
LMC-2(2)	Aiii	nd	325	95.7	849.8	19.6	0.1	58.7	nd	1224.9	84.2	259.5	17.5	16.4	91.9	nd	58.4	99.9
LMC-2(3)	Aiii	38.7	383.2	95.9	833.8	19.4	0.1	57.2	nd	1256.3	42.9	353.2	13.4	nd	88.2	nd	62.3	87.2
LMC-2(4)	Aiii	nd	259.3	99.5	830.6	23.7	0.1	59.1	nd	1347.9	39.5	318.6	18.1	14.1	88.4	nd	57.7	85.6
LMC-2(5)	Aiii	nd	336.7	99.1	829.8	26.3	0.1	58.2	nd	1275.6	39.9	341.3	18.7	17.3	93.3	nd	58.7	88.2
LMC-2(6)	Aiii	nd	371.5	96.5	872.4	25.6	0.1	67.2	nd	1318.5	43.9	353.3	nd	nd	81.8	nd	62.4	82.8
LMS 12	Aii	nd	460	98.3	954	23.4	0.1	65.4	nd	1293	72.8	355	10.5	13.5	89.2	10.1	57.1	99.4
LMS 14	Ai	nd	429	101	856	20.9	0.1	58.6	nd	1250	45.4	357	18.2	17.6	90.3	nd	54.3	85.6

SampleID	Geochem Grp	Ce	Ba	Co	Cr	Cu	F	Nb	Nd	Ni	Rb	Sr	Th	U	V	Y	Zn	Zr
LMS 40	Biii	56.4	426	97.4	904	59.2	0.1	76	nd	1018	32.9	439	12.9	14.2	144	14.9	58.8	138
LMS 43	Ai	56.4	453	99.3	795	32.7	0.1	66.3	nd	1230	20.9	400	13.8	12.3	101	10.8	53.7	94.8
LMS 45	Cii	60.2	668	110	1122	38.5	0.1	91.6	nd	1232	52.7	433	9.6	nd	134	10.1	55.1	94.3
LMS 46	Aiv	nd	549	112	1142	2.3	0.1	42.5	nd	958	29.8	260	16.8	21.8	85.5	nd	41.4	40.9
LMS 48	Av	41.1	361	107	1041	21.5	0.1	56.1	nd	1331	34.4	379	nd	nd	94.9	nd	53.1	70.3
LMS 49	Aiv	nd	535	105	1015	27.4	0.1	73	nd	1282	47.4	453	13.3	nd	98.4	nd	51.9	79.5
LMS 50	Aiv	61.9	492	110	1000	37.7	0.1	71.7	nd	1262	45.5	412	16.8	17.4	92.6	nd	53	89.7
LMS 51	Aiv	52.3	539	108	1111	36.9	0.1	69	nd	1282	40.9	415	18.4	16.7	108	nd	54.4	93.8
LMS 52	Cvi	53.1	1013	105	1052	24.7	0.1	61.4	nd	1275	41.5	344	9	nd	92.3	nd	54.7	77.9
LMS 53	Av	51.4	381	104	967	17.6	0.1	62.3	nd	1311	41.4	313	17.2	21.3	88	nd	54	78.8
LMS 55	Av	44.9	430	108	1077	14.2	0.1	62.3	nd	1356	45.1	312	17.2	18.7	95.2	nd	52.5	75.6
LMS 56	Av	45.6	372	110	1067	13.8	0.1	63.3	nd	1355	46.9	318	nd	10.9	88	nd	53.4	67.5
LMS 57	Av	nd	472	108	1059	22.2	0.1	67.4	nd	1316	49.9	339	nd	nd	94	nd	54.4	77.2
LMS 58	Civ	43.7	647	97.3	1040	19.9	0.1	84.9	nd	1273	79.6	405	13	nd	77.7	nd	50.9	67.8
LMS 6	Cv	nd	774	95.6	1056	29.3	0.1	91.4	nd	1219	80.9	394	13.6	12.2	145	10.2	70.6	105
LMS 61	Di	nd	556	84.3	618	60.1	0.1	90.4	nd	899	33.1	514	21	14.4	154	16.8	160	156
LMS 7	Ciii	40.2	751	99.7	982	29.4	0.1	93.1	nd	1267	76.1	413	14.9	17.9	144	10.5	64.9	109
LMS 8	Ciii	56.6	702	105	991	31.2	0.1	89.8	nd	1280	74.5	396	11.3	nd	134	10.9	62	106
LMS 9	Bii	50.1	581	102	940	22.1	0.1	71.4	nd	1216	48.6	541	16.2	17.6	116	11.4	56.9	107
LMS01	Ai	nd	457	96.6	893.7	32.9	0.1	74.4	nd	1171.4	49.2	303.1	nd	nd	120.8	nd	53.2	94.3
LMS02	Bi	nd	591.2	94.4	970.5	34.7	0.1	80.6	nd	1170.8	54.7	336.7	11.3	nd	120.9	nd	51	90.7
LMS03	Ci	40.8	842.3	97.7	910.8	34.3	0.1	83	nd	1187.9	65.9	459.3	9.5	nd	125	nd	54.6	111.5
LMS04	Cii	nd	633.3	99.9	1012.8	43	0.1	81.6	nd	1157	68.2	555.3	15.6	10.5	138.9	10.5	54.9	134.5
LMS05	Cv	45.6	695.7	103.2	1224.1	26.4	0.1	83.9	nd	1251	73.6	391.3	10.3	nd	144.4	nd	51.2	101.8
LMS10	Aiv	nd	373.1	91	1004.5	23.9	0.1	54.2	nd	1115.2	39.5	345.9	nd	nd	95.3	nd	45.8	77.8
LMS11	Aiv	nd	476.4	93.5	1067.4	23	0.1	63.7	nd	1206.8	48.7	391.2	17.4	11.3	114.4	nd	48.9	79.6
LMS13	Aii	42.7	538.5	100.9	974	17.3	0.1	60.3	nd	1259.5	46.6	333.1	11.9	nd	111.2	nd	52.6	82.8
LMS15	Aiii	nd	347.5	97	889.4	13.8	0.1	54.8	nd	1244.4	39.7	330.5	nd	nd	86.3	nd	50.7	80.4
LMS16	Bi	nd	563.8	96.2	896.9	22.7	0.1	64.6	nd	1242	49.2	381.8	10.7	nd	107.1	nd	50.2	89
LMS18	Bi	nd	689.8	91.6	827.9	19.7	0.1	60.3	nd	1174.4	55.4	456.7	nd	nd	112.7	nd	51.6	93.7
LMS19	Bi	nd	606.3	94.9	822.5	15.5	0.1	58.9	nd	1207.2	48	415.3	10.9	nd	99.6	nd	53.3	88.5
LMS20	Aii	nd	428.6	100.6	827.5	14.7	0.1	55.5	nd	1373	39.1	373.4	nd	nd	83.4	nd	52.2	72.8
LMS21	Av	nd	378.5	101.1	963.2	18.2	0.1	62.4	nd	1341	44.5	358.3	nd	nd	90.3	nd	52.7	85.2

SampleID	Geochem Grp	Ce	Ba	Co	Cr	Cu	F	Nb	Nd	Ni	Rb	Sr	Th	U	V	Y	Zn	Zr
LMS22	Ai	60	357.3	97.3	817.2	30.9	0.1	57.3	nd	1178	43.8	335.4	11.1	nd	121.2	10.4	56.6	127.6
LMS23	Bi	nd	557.3	89.1	855.5	40	0.1	77.7	nd	1189.3	56.8	388	13	10.8	130.8	nd	51.5	101.5
LMS24	Diii	nd	422.8	84.5	640.5	48.4	0.1	68	nd	1021	40.9	432.2	14	nd	127.1	10.9	52.6	125.5
LMS25	Bvi	nd	816.3	88.4	742.8	37.2	0.1	70.3	nd	1116.5	43.5	386.2	16.4	13.8	125.1	nd	50	110.3
LMS26	Aiii	nd	345.5	94.3	880.9	17.9	0.1	65.6	nd	1284.8	45.7	349.4	11.2	nd	92.6	nd	51.2	91.9
LMS27	Aiii	nd	353.3	95.6	871.8	27.1	0.1	64.7	nd	1245.5	46.7	326.8	13.3	nd	92.6	nd	51.2	93.5
LMS28	Biii	nd	432.5	88.7	734.6	37.7	0.1	71.1	nd	1112.2	45.5	414.4	10.2	nd	129.4	nd	51.3	110.2
LMS29	Bii	42.1	602.9	89	854.9	50.9	0.1	84.2	nd	1066.6	40.1	437.9	12.5	nd	124.2	10.9	51.9	138
LMS30	Diii	nd	383.6	88.4	643.2	59.2	0.1	69.5	nd	975.1	34.1	480.5	17.6	13.9	132.7	11.7	52.3	152.5
LMS31	Div	nd	435.5	91.6	705.7	58.7	0.1	70.6	nd	1051.1	37	462.5	14.1	11.2	132.5	12.6	54.2	141.2
LMS32	Di	nd	412.2	84.1	581	59	0.1	60.4	nd	911.2	34.2	409	10.9	nd	145.8	12.4	56.5	138
LMS33	Diii	nd	303.4	89.9	733.9	61.5	0.1	65.8	nd	969.1	33.5	369.5	11.2	nd	130.1	12.5	54.5	128.4
LMS34	Div	54.8	486.4	90.1	742.4	56.4	0.1	72.1	nd	1015.8	33.8	423	16.8	nd	134.6	13.2	54.4	166.3
LMS35	Bi	54.3	568.8	99.4	952.8	34.6	0.1	78.9	nd	1207.1	25.3	393.5	16.7	10.6	117.6	nd	48.7	99.7
LMS36	Ci	43.8	719.3	96.8	873.5	40.4	0.1	80.2	nd	1175.3	54.6	367.1	11.1	nd	128.5	nd	51.7	111.8
LMS37	Ci	nd	647.8	96.5	924.5	40.6	0.1	85.9	nd	1146.1	52.5	369.9	12.3	nd	132.7	nd	51	111.6
LMS38	Diii	nd	356.8	89.3	653.6	54.2	0.1	68.1	nd	1036.4	34.4	423.3	nd	nd	132.4	12.5	53.2	141.1
LMS39	Diii	nd	340.8	90.5	638.3	65.3	0.1	66.8	nd	959.1	33.9	431.8	18.4	12	148.4	13.8	57.2	160
LMS41	Diii	43.6	339.6	92.6	702.4	60.4	0.1	78.3	nd	1030.4	27.4	473.9	14.6	nd	127	11.6	52	141.1
LMS42	Diii	nd	367.5	94.2	684.5	49.7	0.1	74.1	nd	1056.7	28.8	513.6	16.1	13.4	123.5	11.8	52	137
LMS44	Ci	nd	635.6	96.3	933.5	48.3	0.1	88.5	nd	1184.2	54.6	391.4	11.2	nd	122.6	nd	51.2	117.6
LMS47	Av	nd	444.2	99.8	1054.7	29.9	0.1	81.8	nd	1299.8	42.8	375.3	nd	nd	92.5	nd	48.7	80.7
LMS54	Aii	nd	472.9	100	935.7	21.5	0.1	66.3	nd	1327.2	53.8	340.9	15.2	13.5	95.6	nd	49.1	94.1

Table B.10: Bulk rock trace element geochemistry (ppm) of D/K1 kimberlite samples .

Appendix C

Image Analysis

C.1 Quantitative Image Analysis

Chapter 3 qualitatively describes the major petrographic differences between each lithofacies at D/K1. Quantifying the petrography is ideal, however conventional point counting techniques were considered to be too labour intensive for this thesis as widespread small scale heterogeneities in these rocks would require large volumes of kimberlite to be quantified. The aim of this section was to quantify the different emplacement mechanisms between lithofacies, rather than different mineralogies. A method of quantifying D/K1 kimberlite textures by image analysis was investigated. This technique of using statistical methods of quantifying spatial distribution patterns (SDPs) within grain populations (Jerram et al., 1996) is a popular tool in interpreting textures in volcanic rocks and their relationships to emplacement and lithification processes (Higgins, 2002; Mock et al., 2003).

C.1.1 Crystal Size Distribution

This was a pilot study investigating how well image analysis could be applied to textures in kimberlites. Ongoing work by M. Field is investigating the same technique at hand specimen scale, using polished slabs of kimberlite (Field, *pers.*

comm). For this study seven samples were analysed: LDD10_02 and LDD16A_02 from VK1; LDD10_04 from BBr1; LDD10_07 from DVK; LDD12_01 from PVK; LDD21_01 from SVK; LDD21_06 from CK (as described in Section 3.5). Outlines of the chosen components were digitised by hand on photomicrographs using the ImageJ software[1]. Three different textural criteria were explored: (i) olivine phenocrysts; (ii) olivine pheno- and macrocrysts; (iii) all non-groundmass components. The following criteria were developed to ensure systematic selection of olivine grains:

1. Olivine phenocrysts must have two euhedral crystal faces.
2. Olivine macrocrysts including any olivines with subhedral/anhedral habit.
3. Selection of the grain boundary; any oxide necklace or alteration rim was considered either of the groundmass or secondary alteration (Fig. C.1).
4. All non-groundmass components included all olivines, country rock fragments, mantle xenoliths and xenocrysts and excluded groundmass oxides, phlogopite, calcite segregations, alteration haloes around other grains and rims of juvenile and pelletal lapilli.

[1]Shareware software created and made public by the US National Institutes of Health by W. Rasband (Roeder et al., 2006)

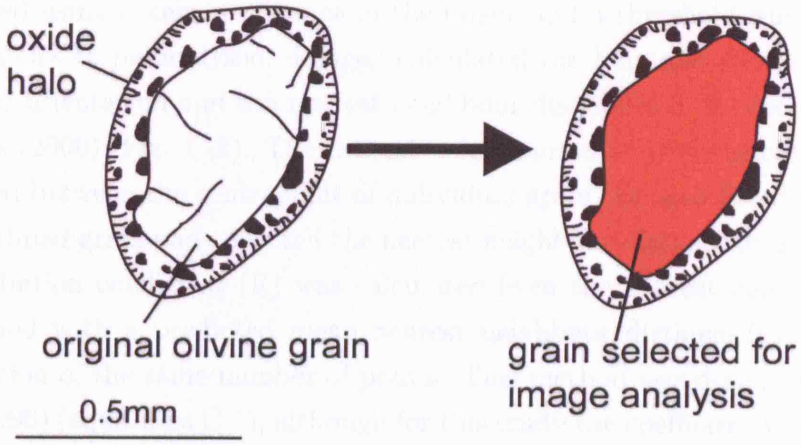

Figure C.1: Schematic illustrating grain boundary selection of an olivine grain with an oxide halo.

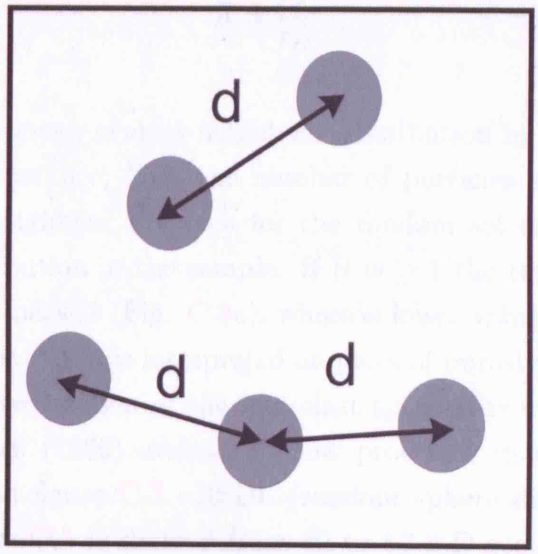

Figure C.2: Schematic showing how the nearest neighbour distance is taken. d - distance between neighbouring grains. (Fig.2 from Jerram et al. (1996).)

Once the image had been digitised and grains selected (Fig. C.3), a scale was calibrated using a known distance in the image and a threshold was selected for the particles to be analysed. ImageJ calculated the long and short axis of each grain, its orientation and the nearest neighbour distribution or centroid location (Higgins (2000); Fig. C.2). The nearest neighbour value is the shortest distance measured between the centrepoint of individual grain. ImageJ fitted ellipsoids to each outlined grain and collected the nearest neighbour distance as a co-ordinate. A distribution coefficient (R) was calculated from the nearest neighbour values normalised with a predicted mean nearest neighbour distance from a random distribution of the same number of points. This method was designed by Jerram et al. (1996) (equations C.1), although for this study the coefficient was calculated using a programme called BigR, created by Michael Higgins.

$$r_A = \frac{\Sigma r}{N}$$
$$r_E = \frac{1}{2\sqrt{\rho}}$$
$$R = \frac{r_A}{r_E}$$

Where r_A is the mean nearest neighbour distribution in the sample; r is the nearest neighbour distance; N is the number of particles measured; r_E is the predicted nearest neighbour distance for the random set of particles; ρ is the density of the distribution in the sample. If R is ≥ 1 the texture is ordered, for example cubic-close packed (Fig. C.4a), whereas lower values and the texture is clustered (Fig. C.4b). Data is interpreted on plots of porosity versus R. Porosity was taken as the area fraction of the interclast space (the white area on Figure C.3c). Jerram et al. (1996) evalutated how processes in natural rocks affect R, as summarised in figure C.5. RSDL (random sphere distribution reference line) shown in figure C.5 is derived from 40 to 50 2-D sections through a 3-D model simulation of a random distribution of spheres (Jerram et al., 1996). An R value above the curve represents an ordered texture, whereas a value below is clustered. Figure C.5 illustrates how natural rock-forming processes affect the spatial distribution of grains and their R values.

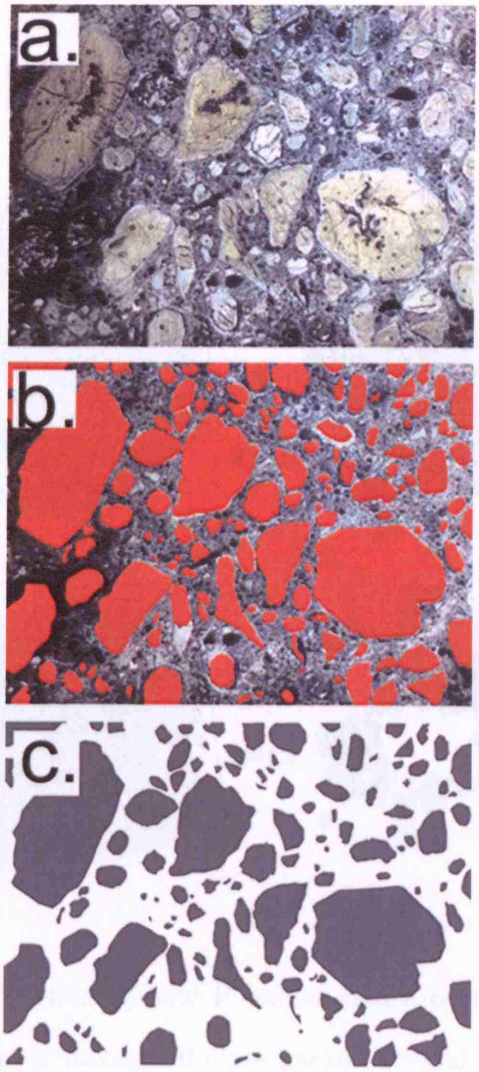

Figure C.3: Example of grain selection for image analysis from sample LDD10_02. a. Initial photomicrograph. b. Grain outlines superimposed over photomicrograph. c. Selected grain outlines. (FOV = 8mm)

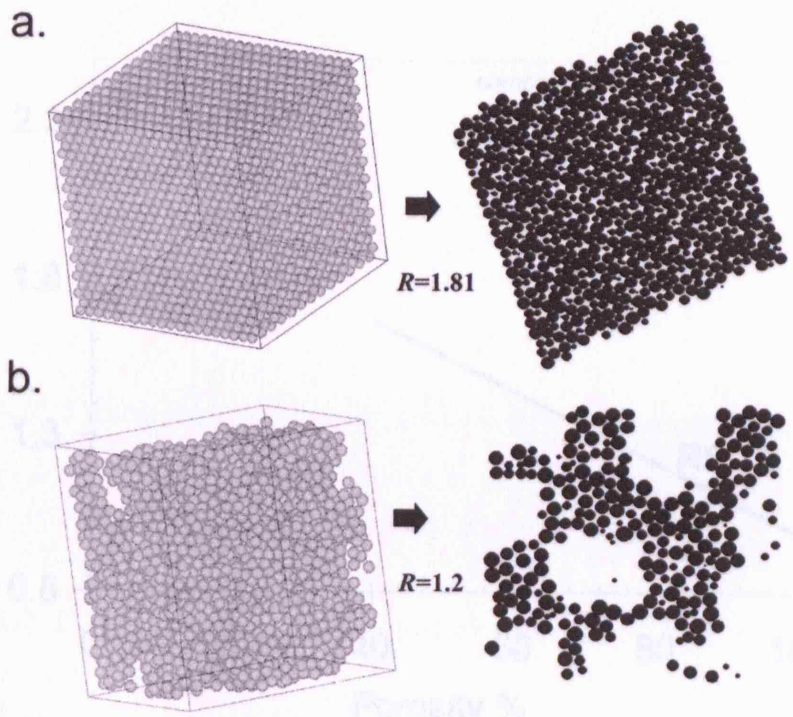

Figure C.4: Schematic showing how R values relate to textures (from Jerram et al. (1996)). a. Cubic or hexagonal close packed crystal structure will produce R values $\geq$1. b. Clustered textures produce lower R values.

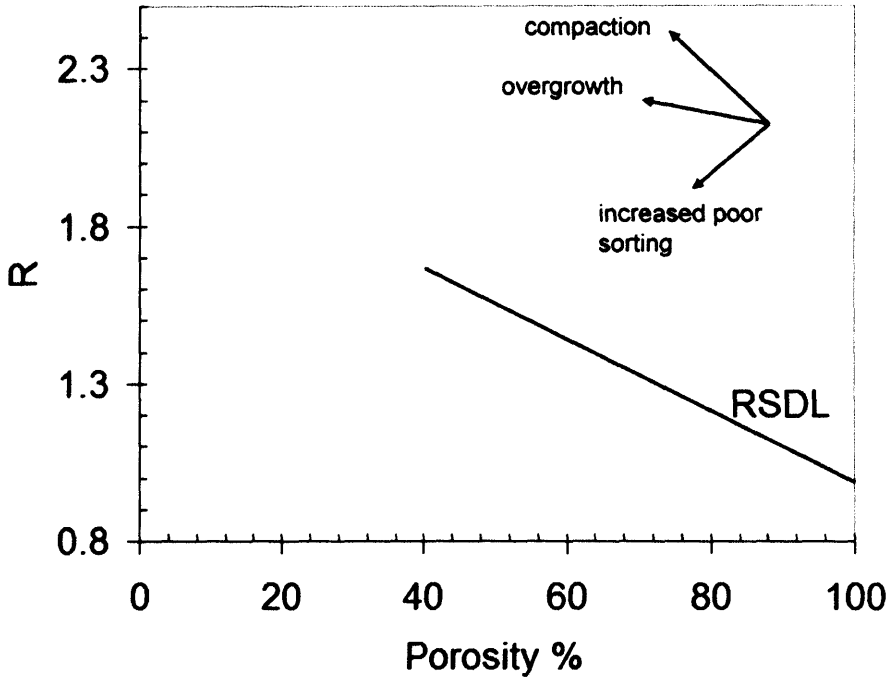

Figure C.5: Plot of porosity versus R from Jerram et al. (1996). RSDL is the random sphere distribution reference line (see text). The effects of compaction, sorting and overgrowth are illustrated.

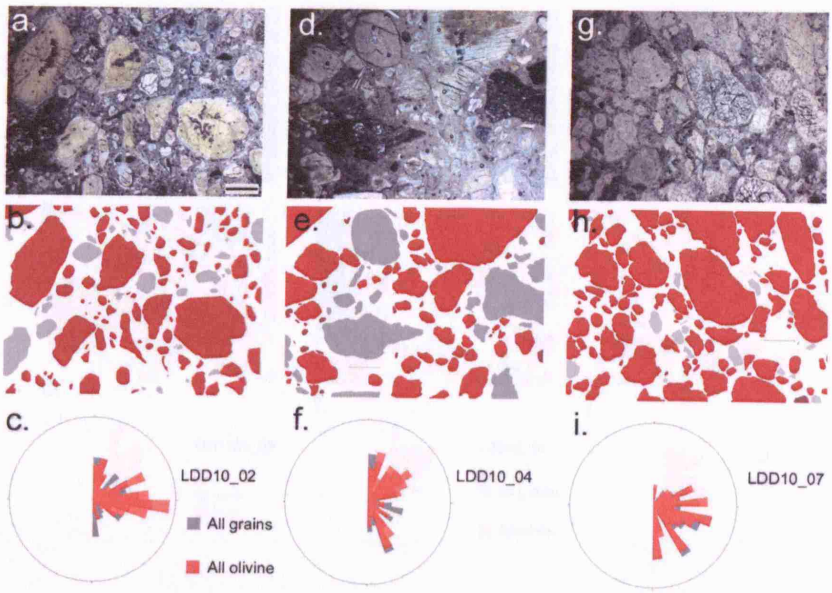

Figure C.6: Photomicrographs, grain outlines and rose diagrams of grain alignment for samples LDD10_02, LDD10_04 and LDD10_07

Grain Alignment

The angle of grain alignment was measured by ImageJ and used to determine any fabric in the textures.

C.1.2 Results

The sample area used for this thesis and values of N give the predicted error of R values between ± 0.1 to 0.2 from Figure 4 in Jerram et al. (1996). This is large and could move R values for phenocrysts above or below the RSDL (between clustered and ordered domains). However, for the purposes of this "pilot" study they are included for illustration of the technique, although limitation of the results must be considered.

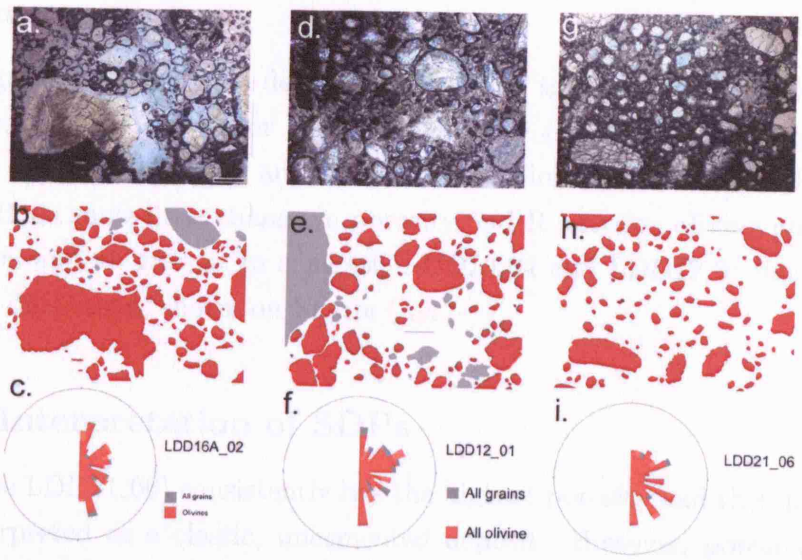

Figure C.7: Photomicrographs, grain outlines and rose diagrams of grain alignment for samples LDD16A_02, LDD12_01 and LDD21_06

Olivine Phenocrysts

N is small for olivine phenocrysts at D/K1; between 5 and 105. This is represented by the high porosity in Figure C.8a. Of the seven samples analysed, three have ordered textures: LDD10_07 (DVK); LDD10_04 (BBR); LDD21_06 (HK?). LDD10_02 (VK1) has the lowest R value of 0.84 at an area fraction of 5.57%, and lies within clustered the clustered domain.

Olivine Phenocrysts and Macrocrysts

The addition of olivine macrocrysts to the analysis decreases the porosity (Fig. C.8b). Whereas olivine phenocrysts were controlled by the olivine pheno- and macrocrysts distributions are influenced by porosity with minimal control by R. CK remains within the ordered domain, and the other six (VK) samples now have clustered distributions. Sample LDD10_07 has the lowest porosity of 48.66% and all other samples are $\geq$60%.

All Grains

All (non-groundmass) grains demonstrate similar trends to olivine pheno- and macrocrysts in that the major control in porosity (Fig. C.8c). Again, CK remains the only sample with an ordered distribution. LDD10_07, LDD16A_02 and LDD21_06 show little change in porosity and R between olivine pheno- and macrocrysts and all grains. In contrast, LDD10_04 and LDD12_01 demonstrate significant differences, shown on Figure C.9.

C.1.3 Interpretation of SDPs

CK (sample LDD21_06) consistently has the highest porosity and therefore could be misinterpreted as a clastic, uncemented deposit. However, porosity here is taken as the proportion of interclast material or matrix[1]. Therefore, CK has the highest proportion of matrix relative to the other analysed samples. Figure C.9 illustrates the small difference between proportion of olivine phenocrysts and macrocrysts, and all grains. Negligible influence from all grains means minimal accidental fragments have been entrained into this deposit, supporting the idea that CK has undergone relatively little explosive fragmentation as seen in other lithofacies.

VK1 samples (LDD10_02 and LDD16A_02) have similar proportions of all three analysed components. If the amount of entrained accidental material is indicative of the explosivity of an eruption, then these two samples have been erupted by similar intensity processes. Sample LDD10_04, collected from BBr1 (Fig. 3.4) has very few olivine phenocrysts. It is unlikely the ordered nature proposed in Figure C.8a) is truly representative as errors are ± 0.2. BBr1 has entrained almost 20% accidental material (excluding olivine macrocrysts), showing the dynamic, fragmenting processes of its emplacement. Samples LDD12_01 and LDD21_01 from PVK and SVK respectively also have similar proportions of the analysed components relative to each other; the PVK sample has a slightly higher (6%) accidental fragment content. This similarity also indicates similar

[1] matrix is the interclast phase in a coherent kimberlite

emplacement mechanisms that are subtley different from VK1 which has a higher capacity to entrain accidental material including olivine macrocrysts (Fig. C.9).

DVK (sample LDD10_07) demonstrates different SDP characteristics to the other VK lithofacies: (i) there is a significant difference in proportion between olivine phenocrysts and olivine macrocrysts; (ii) it has the lowest porosity (and therefore smallest groundmass fraction); (iii) there is only a small amount of entrained accidental material. DVK is a well packed, crystal-rich rock and is dark grey and competent in hand specimen. In thin section olivine macrocrysts have fresh cores. Unlike CK, DVK does not have a coherent matrix phase and therefore appears to have been subjected to fragmental emplacement mechanisms (Section 3.5). This sample also demonstrates stronger grain alignment compared with other lithofacies. Compaction is a plausible interpretation of these characteristics. The increased porosity is influenced by olivine macrocrysts and therefore cannot be a consequnce of primary growth. Grain alignment may have been secondary if a uniaxial stress was imposed on the deposits. Extrusive tuffs and intrusive igneous rocks can be welded, and a discussion of welding is given in Section 3.5. Welding reduces the porosity of a clastic deposit (Quane & Russell, 2005) and in terms of SDP will increase R as clustered textures are forced into more ordered frameworks (Jerram et al., 1996). Sparks et al. (2006) proposed the interpretation of dark, dense, "magmatic" kimberlites as welded deposits. DVK may have been erupted at a higher temperature than other VKs at D/K1 as it has a lower proportion of entrained accidental, in particular country rock, fragments capable of dissipating some heat. Decreased porosity or reduced pore space would inhibit movement of hydrothermal fluids through the rock post-eruption, and therefore olivines are relatively unaltered.

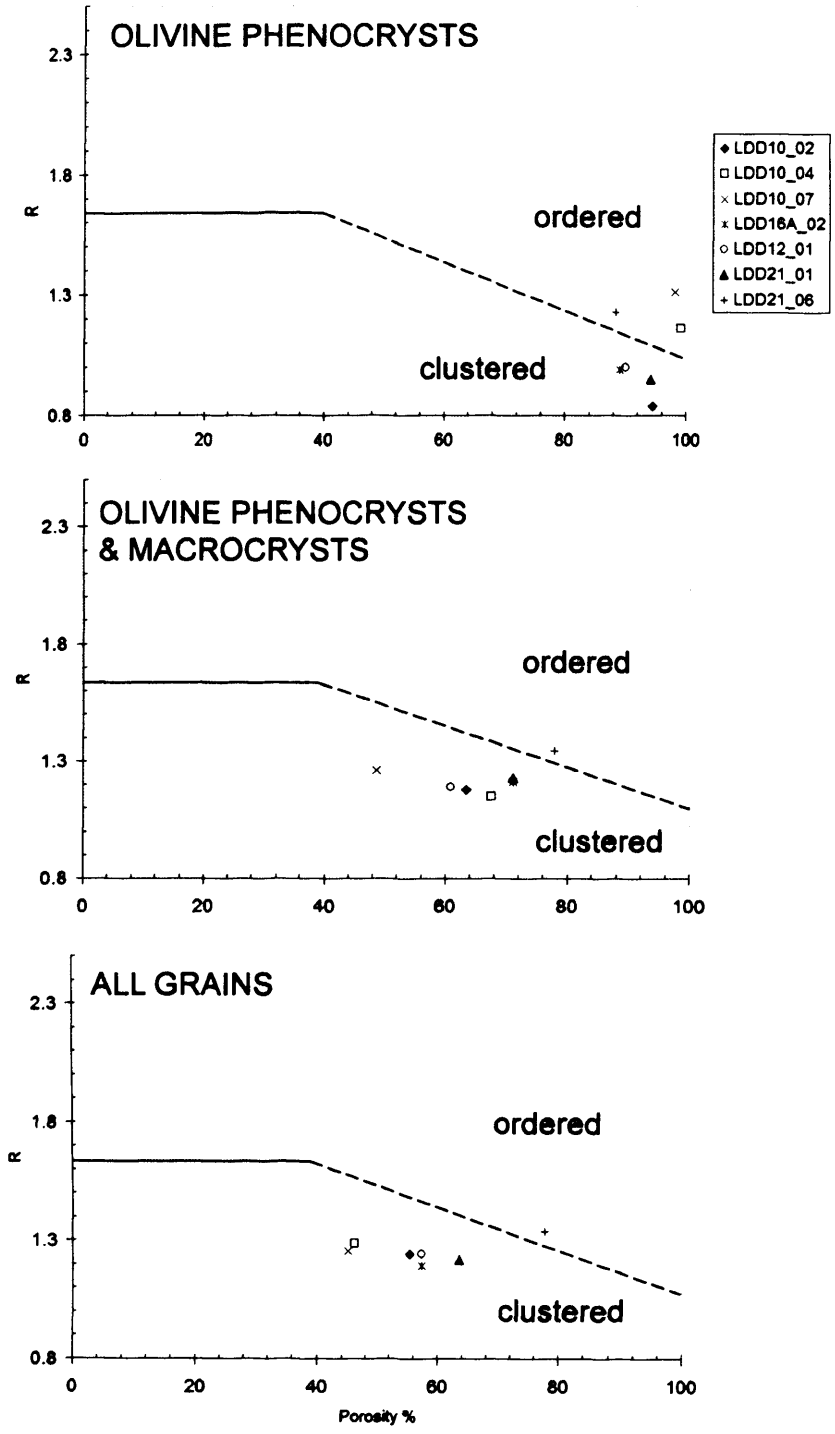

Figure C.8: Porosity versus R for (i) olivine phenocrysts, (ii) olivine phenocrysts and macrocrysts and (iii) all grains except groundmass. (Dashed line - RSDL.)

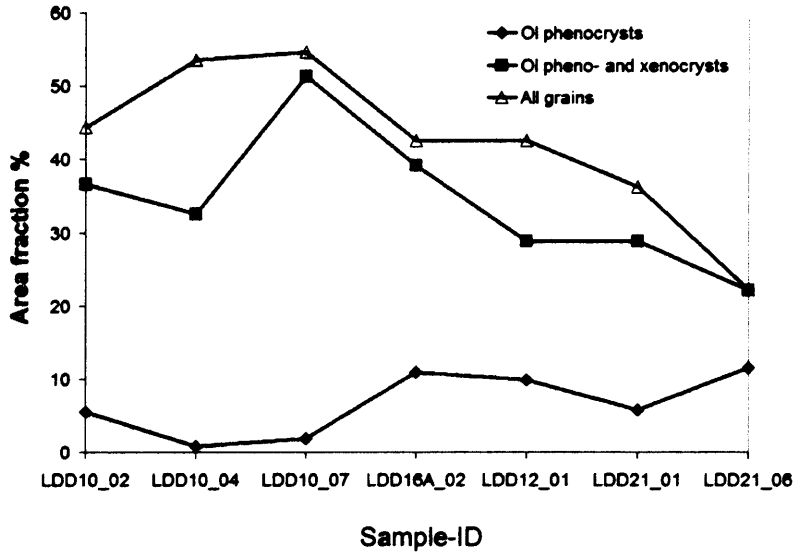

Figure C.9: Spiderplot showing area fraction for each component analysed in each sample.

Appendix D

U-Pb Dating Perovskite in Kimberlite

D.1 Introduction

A well constrained age of the Letlhakane Kimberlite has not been published, although we can consider that it lies around 93 Ma, which is the age of the Orapa kimberlite that is believed to have approximately the same age (Stiefenhofer et al., 1997). Unpublished age data from E. Barton dates Letlhakane between 79 ± 5 Ma and 92 ± 1 Ma (Table D.1). U-Pb LA-ICP-MS in situ dating of groundmass perovskites from Letlhakane aimed to accurately constrain the age of the kimberlite body, and determine individual ages for each kimberlite lithofacies. This was not sucessfully achieved due to numerous complexities discussed in this appendix. However, this study did highlight many interesting, philosophical issues and considerations which must be addressed to develop this as a useful technique of inexpensively dating kimberlites in the future.

Constraining kimberlites ages is complicated by their hybrid make-up and history of extensive alteration and hydrothermal metamorphism (Chapter 1). There is still wide scope to investigate and understand crystallisation paths in kimberlites and recognising phases which are directly inherited from the primary magma.

Report No.	Dating Technique	Age (Ma)
Star 15323	Fission track	84
Star 44824	Rb/Sr (phlogopite)	92 ± 1
	Perovskite U-Pb	79 ± 5

Table D.1: Ages determined for the Letlhakane kimberlite by Erika Barton at the GSC, Johannesburg.

Misinterpretation of 'emplacement' dates from certain minerals is highly probable, for example Kelley & Wartho (2000) measured Ar-Ar ages from phlogopite in a xenolith which gave the timing of a mantle metasomatism event rather than the actual kimberlite emplacement. Matrix zircons and perovskites are considered to have crystallised as primary phases from a kimberlite melt and are therefore good minerals for dating kimberlites (Cox & Wilton, 2006), as demonstrated by Heaman et al. (2003). U-Pb dating of perovskites in hindered because, as such, there is no external reference perovskite standard to calculate U/Pb ratios. Cox & Wilton (2006) analysed a known and an unknown zircon from the Oka carbonatite to support perovskite U-Pb ages. Storey et al. (2006) has demonstrated how zircon is an appropriate external standard for titanite, and the same assumption was applied here.

D.2 Data Analysis

Radiometric U-Pb dating of perovskite grains was carried out by laser ablation inductively coupled mass spectrometry (LA-ICP-MS) at the Natural History Museum (NHM) in London, under the supervision of Drs. Craig Storey and Teresa Jeffries. The method follows that of Jeffries et al. (2003) which was developed as an inexpensive technique for U-Pb dating of *in situ* zircons grains, relative to more expensive analysis using high mass resolution-secondary ionisation mass spectrometry (HR-SIMS) (Storey et al., 2006). Twenty-four perovskite grains were selected from sample LDD16A_02 as they were the largest, had no inclu-

sions and did not appear to have been affected by alteration or hydrothermal metamorphism. Measurements were collected from individual grains *in situ* on c.150 μm thick polished sections, cleaned prior to analysis with weak nitric acid and isopropanol. Grains were selected for dating during preliminary electron backscatter imaging at the NHM using a Jeol 5900LV energy dispersive electron microprobe. U-Pb analysis was carried out using an enhanced sensitivity option New Wave UP213 aperture imaged frequency quintupled Nd:YAG solid state laser source with an operating wavelength of 213 nm, coupled to a Thermo Elemental PlasmaQuad 3 quadrapole-based ICP-MS (Storey et al., 2006). Analytical conditions were reviewed by Storey et al. (2006) and given in Table D.2. Gold traps are attached to Ar and He gas lines which reduce atmospheric Hg ions which has an isobaric interference on ^{204}Pb and therefore complicates correction. Laser spot size was chosen according to the size of each grain and analyses were collected using a one line-scan raster, which repeatedly moved up and down along the line. The first few seconds of analysis were not used in U-Pb age calculations to avoid any surface contamination (Storey et al., 2006). Four zircon standard 91500 (1065 Ma Wiedenback et al. 1995) measurements were taken at the beginning and end of each batch (12 grains) as an external normaliser for U/Pb ratio calculation.

D.3 Data Reduction

Data reduction and ^{206}Pb/^{238}U and ^{207}Pb/^{235}U ratios were determined using LAMTRACE, an off-line macro-based spreadsheet designed in Lotus 1-2-3 by Simon Jackson of Macquarie University, Australia (Storey et al., 2006) by the same processes described by Jeffries et al. (2003). Concordia, Tera-Wasserburg and weighted mean figures were made by C. Storey using Isoplot, an Excel plug-in designed by Ludwig (see Cox & Wilton (2006); Storey et al. (2006)).

D.3.1 Common-Pb Correction

U-Pb dating of perovskites presented a challenge because they contain approximately 50% common-Pb (Table D.3), which isobarically interferes with radiogenic

Laser parameters	
Laser	New Wave Research UP213 with apeture imaging
Wavelength	213 nm
Pulse width	3 ns
Pulse energy	0.01-0.1 mJ per pulse
Energy density	4 J cm^{-2}
Energy distribution	Homogenised, flat beam, aperture imaged
Focus	Fixed at surface
Repetition rate	20Hz (au22a05), 10 Hz (Jn14005)
Raster scan speed	10 μm s^{-1}
Nominal spot size diameter	15-30 μm (unknowns), 50 μm (standard)
ICP-MS parameters	
ICP-MS	Thermo Elemental PlasmaQuad 3 with 's-option'
Forward power	1350 W
Gas flows:	
Coolant (plasma)	Ar: 13 l min^{-1}
Auxiliary	Ar: 0.8 l min^{-1}
Sample transport	He: c. 1.1 l min^{-1}
Ar: c. 0.9 l min^{-1}	
Analysis protocol	
Scanning mode	Peak hopping, 1 point per peak
Acquisition mode	Time resolved analysis
Analysis duration	150 s (c.40 s backgroud, 120 s ablation)
Dwell times:	
^{201}Hg,^{202}Hg, $^{204}Hg/Pb$, ^{206}Pb,	10 ms
^{208}Pb, ^{232}Th, ^{238}U	
^{207}Pb, ^{235}U	30 ms

Table D.2: Analytical conditions of laser and ICP-MS used during this study and analytical protocol for measurements (modified from Storey et al. (2006))

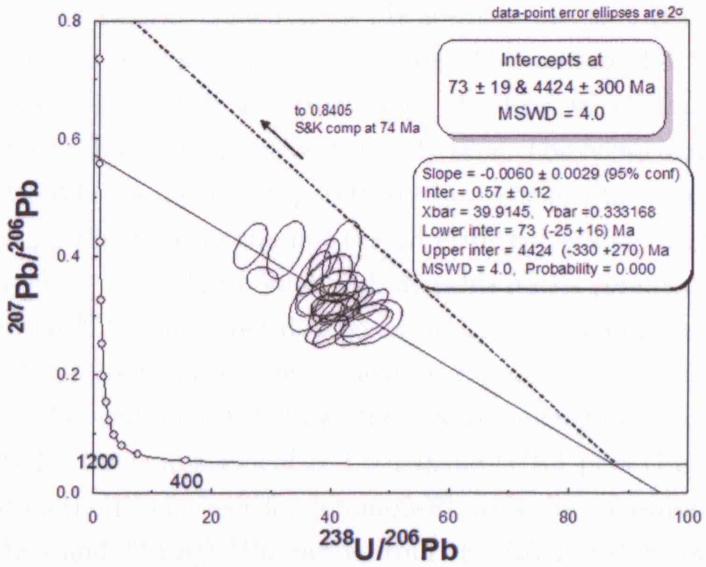

Figure D.1: Tera-Wasserburg plot showing regression (solid line) through uncorrected U-Pb data for Letlhakane perovskites. The y-axis intercept is displayed and used as the initial common-$^{207}Pb/^{206}Pb$ ratio. The lower intercept gives the average age of the perovskites. The dashed line represents the regression if the initial common-$^{207}Pb/^{206}Pb$ correlated with Stacey & Kramers (1975) modelled ratio of 0.87. (Figure courtesy of C. Storey)

Pb. Interference is particularly prevalent in younger deposits, such as these Letlhakane samples. There are two methods to correct for common-Pb, which are explained below and in depth by Storey et al. (2006).

The first method plots a regression through the data displayed on a Tera-Wasserburg diagram from which the initial common-$^{207}Pb/^{206}Pb$ at the time of crystallisation is taken as the y-axis intercept. The line of regression is effectively a mixing line between pure common-Pb and pure radiogenic-Pb. This technique assumes the data are concordant, in other words no Pb has been lost from the system since crystallisation. Initial common-$^{207}Pb/^{206}Pb$ is 0.57 ± 0.12 for the

Letlhakane perovskites, which when compared to modelled value predicted by Stacey & Kramers (1975) of 0.8405 at 74 Ma seems unrealistic (Fig. D.1), especially considering the present day ratio is ~0.69. This method has an additional issue that the data cluster into a narrow range of ratios, which could elevate errors in performing a reliable regression through data. The mean square weighted distribution (MSWD) of 4.0 is comparatively low, suggesting a good fit of the regression through the data points, but the 2σ error ellipses are large and therefore the regression is probably unreliable. Using this initial common-$^{207}Pb/^{206}Pb$ ratio produces the ^{207}Pb-corrected data given in Table D.3 and a calculated age of 74.1 ± 7.9 Ma plotted as a weighted mean in Figure D.2(b). Using the initial common-$^{207}Pb/^{206}Pb$ ratio modelled by Stacey & Kramers (1975) gives an age of 101.5 ± 4.0 Ma for the emplacement of Letlhakane D/K1 pipe (Fig. D.2(c)).

The second method to correct for common-Pb uses the measured initial common $^{206}Pb/^{204}Pb$ and $^{206}Pb/^{204}Pb$ ratios from the LA-ICP-MS data. Isobaric interference from Hg complicates this data and a correction for ^{204}Hg must first be applied to the 204 amu signal. This was done by calculating $^{201}Hg/^{204}Hg$ ratio from the background signal, and to ensure there was no measurement of ^{204}Pb, this ratio was compared with the natural $^{201}Hg/^{204}Hg$ of 0.521 determined by Zadnik et al. (1989) (c.f. Storey et al. (2006)). The use of gold traps (Section D.2) elevated reproducibility of these corrections. The common-Pb correction was carried out via equations D.1 and D.2. This method, unlike the first, does not force the data to be concordant allowing interpretation regarding the closed or unclosed nature of the perovskite system. The data for this correction is presented in Table D.3, however in 4 grains for $^{206}Pb/^{204}Pb$ and seven grains for $^{207}Pb/^{204}Pb$ too much ^{204}Hg was stripped from the 204 amu signal yielding a negative corrected value. These grains were discarded from age calculations. Figure D.2(a) illustrates how the corrected values push the data towards concordia and also how common-Pb has a greater effect on radiogenic ^{207}Pb than ^{206}Pb. This latter point relates to greater initial ^{238}U abundances of ~99% compared to ~0.7% ^{235}U despite the longer half-life of ^{238}U, and the young age of these perovskites. The age from the corrected data is 96.4 ± 7.8 Ma (Fig. D.2(b)).

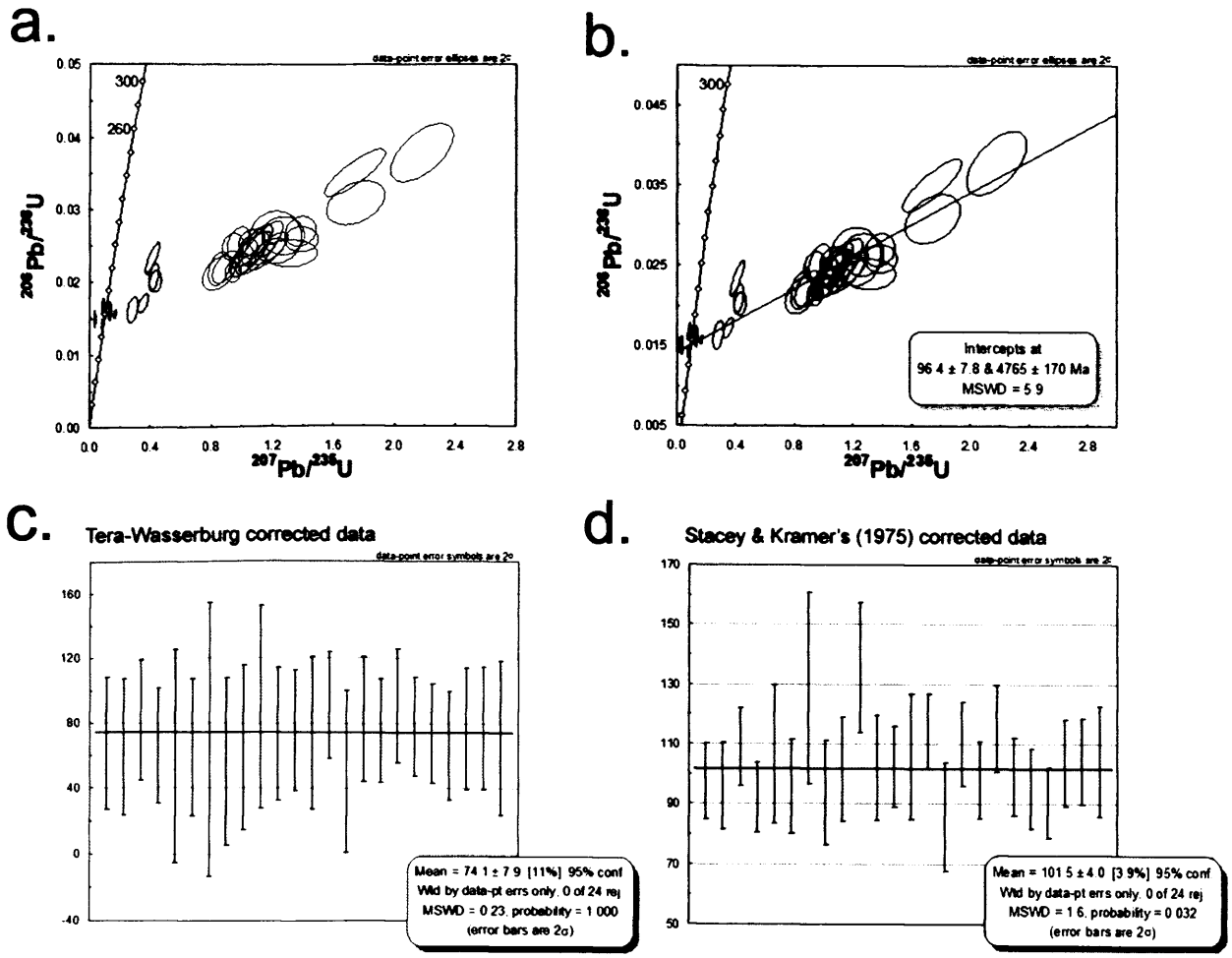

Figure D.2: Figures of Letlhakane perovskite LA-ICP-MS U-Pb age data. (a) ^{207}Pb-corrected (black ellipses) and uncorrected (red ellipses) data on traditional concordia diagram. (b) All corrected and uncorrected data plotted in a traditional concordia diagram illustrating U-Pb age using ^{206}Pb/^{204}Pb and ^{207}Pb/^{204}Pb ratios Stacey & Kramers (1975) modelled for 74.1 Ma. (c) ^{206}Pb/^{238}U ages from ^{207}Pb-corrected data according to the y-axis intercept on Tera-Wasserburg diagram (Fig. D.1) plotted as weighted average. (d) Weighted mean age based on initial common-^{207}Pb/^{206}Pb ratio as modelled by Stacey & Kramers (1975) for 74.1 Ma. (Figures courtesy of C. Storey)

$$\frac{\left(\frac{^{206}Pb}{^{204}Pb}\right)_{tot} - \left(\frac{^{206}Pb}{^{204}Pb}\right)_{i}}{\left(\frac{^{238}U}{^{204}Pb}\right)} = \frac{^{206}Pb}{^{238}U_{cor}} \tag{D.1}$$

$$\frac{\left(\frac{^{207}Pb}{^{204}Pb}\right)_{tot} - \left(\frac{^{207}Pb}{^{204}Pb}\right)_{i}}{\left(\frac{^{235}U}{^{204}Pb}\right)} = \frac{^{207}Pb}{^{235}U_{cor}} \tag{D.2}$$

Storey et al. (2006) recommended plotting the $^{206}Pb/^{207}Pb$ (^{204}Pb corrected) ratio against the ^{206}Pb intensity to asses the efficiency of the common-Pb correction. However, the 206 signal intensity is relatively very low for the Letlhakane perovskites, ranging from below 1000 up to 5000 counts per second (cps) compared with $\geq$10000 cps from titanites in Storey et al. (2006). Low intensity is partly correlated with laser spot size, indicating how grain size affects signal acquisition. Stripping ^{204}Hg from the 204 signal further reduces counts leaving less than 10 and close to 0 in some cases, in addition to those negative values mentioned above. This second method is therefore unreliable based on low counting statistics.

Analysis	Spot size μm	Line length μm	Uncorrected isotope ratios and errors (%)						Common Pb			^{207}Pb corrected ages		^{204}Pb corrected ratios and errors			
			^{207}Pb/ ^{235}U	2σ	^{206}Pb/ ^{238}U	2σ	^{207}Pb/ ^{206}Pb	2σ	^{206}Pb/ ^{204}Pb	^{207}Pb/ ^{204}Pb	f206%	^{206}Pb/ ^{238}U	2σ	^{207}Pb/ ^{235}U	2σ	^{206}Pb/ ^{238}U	2σ
au22a05	30	29	1.1543	3.70	0.0243	3.09	0.3443	2.55	33.8	2.8	56.8	97.3330	26.83	0.1687	3.70	0.0157	3.09
au22a06	25	28	1.1666	7.93	0.0242	6.05	0.3501	6.35	45.9	7.4	57.9	95.8148	28.10	0.3517	7.93	0.0172	6.05
au22a07	25	27	1.0627	6.53	0.0252	5.41	0.3054	5.64	36.3	1.5	49.4	108.7824	24.92	0.0853	6.53	0.0167	5.41
au22a08	30	31	1.0057	3.74	0.0222	4.32	0.3281	4.55	32.6	1.5	53.7	91.8475	23.54	0.0811	3.74	0.0142	4.32
au22a09	15	15	1.746	8.85	0.0308	8.10	0.4116	9.58	10.5	-3.4	69.7	106.5839	44.21	- 0.4616	8.85	0.0111	8.10
au22a10	15	25	1.1694	9.11	0.0242	8.80	0.3507	5.98	-169.0	-69.6	58.0	95.6884	28.37	1.4007	9.11	**0.0272**	**8.80**
au22a11	15	16	2.1796	7.66	0.0378	8.65	0.4186	14.55	14.3	-1.6	71.0	128.5231	59.07	- 0.2250	7.66	0.0164	8.65
au22a12	15	15	1.3897	6.40	0.0258	5.51	0.3913	8.44	19.3	-0.5	65.8	93.5770	34.52	- 0.0413	6.40	0.0131	5.51
au22a13	25	23	1.3841	5.99	0.0269	6.24	0.3737	7.93	23.4	0.4	62.4	101.3504	34.05	0.0347	5.99	0.0150	6.24
au22a14	15	19	1.7399	9.40	0.035	7.69	0.3602	4.97	37.1	4.9	59.9	135.4282	41.52	0.4111	9.40	0.0234	7.69
au22a15	15	17	1.1207	10.56	0.0247	11.96	0.3287	7.30	1145.0	376.0	53.8	102.0208	28.01	1.0621	10.56	0.0243	11.96
au22a16	25	15	1.047	4.14	0.0241	6.48	0.3150	6.72	37.3	2.4	51.2	102.2024	25.06	0.1326	4.14	0.0161	6.48
jn14c05			1.2198	11.49	0.0261	11.32	0.3390	15.86	4.3	-7.5	55.8	105.6286	33.90	- 1.1754	11.49	0.0049	11.32
jn14c06			0.9374	6.04	0.0249	6.09	0.2725	7.76	12.5	-6.8	43.1	114.0752	22.29	- 0.6828	6.04	0.0100	6.09
jn14c07			1.3128	11.05	0.0239	6.39	0.3978	12.69	-244.0	-109.3	67.0	85.4675	34.43	1.4318	11.05	**0.0259**	**6.39**
jn14c08			1.0753	7.50	0.0255	5.78	0.3060	8.75	71.2	13.1	49.5	109.9657	26.11	0.4322	7.50	0.0202	5.78

jn14c09	0.8913	7.99	0.0221	8.13	0.2922	7.76	9.9	-6.9	46.8	97.8134	21.74	-0.6314	7.99	0.0077	8.13
jn14c10	0.9736	6.18	0.0254	7.26	0.2782	11.26	84.3	14.3	44.2	115.1833	24.55	0.4200	6.18	0.0208	7.26
jn14c11	0.8473	6.79	0.0219	8.69	0.2805	8.96	14.1	-6.1	44.6	98.9976	21.09	-0.5109	6.79	0.0095	8.69
jn14c12	0.8473	10.38	0.0213	8.97	0.2878	10.61	60.3	8.1	46.0	95.0498	21.53	0.2825	10.38	0.0163	8.97
jn14c13	0.9408	4.58	0.0214	5.23	0.3182	7.32	6.7	-7.2	51.8	90.2714	22.51	-0.7595	4.58	0.0057	5.23
jn14c14	1.0594	10.12	0.0244	8.15	0.3142	5.93	-197.6	-74.4	51.0	103.6304	25.40	1.4150	10.12	**0.0270**	**8.15**
jn14c15	1.0596	10.12	0.0245	8.15	0.3143	5.93	-197.6	-74.4	51.1	104.0449	25.51	1.4153	10.12	**0.0270**	**8.15**
jn14c16	1.2686	8.96	0.0263	8.23	0.3501	11.95	9.5	-5.4	57.9	104.0844	32.80	-0.6792	8.96	0.0089	8.23

Table D.3: U-Pb data for LA-ICP-MS analysis of perovskites from sample LDD16A_02.

D.4 Discussion of Letlhakane Perovskite Ages

From the age of Orapa and the unpublished, calculated ages of E. Barton, the data from this study which constrain emplacement of the Letlhakane kimberlite between 74.1 ± 7.9 Ma and 101.5 ± 4.0 Ma appear realistic. However, as discussed above these ages are considered unreliable owing to (i) the relatively young age of Letlhakane resulting in low U/Pb abundances, (ii) the problems of constraining the initial common-Pb, and (iii) not fully understanding if data is concordant or discordant. Despite failure in terms of the aims of this study, many interesting and philosophical aspects were brought to light, which are considered below and need to be resolved in order for this, inexpensive, very useful *in situ* method of kimberlite dating to proceed.

Quantifying the initial common-Pb is paramount in calculating real ages from U-Pb analysis of perovskites in kimberlites of similar ages to Letlhakane, of which there are many. To side-step measuring this directly from the perovskite, which is evidently difficult, it can be determined from a co-crystallising phase, or phases which crystallise before and after perovskite stability on the liquidus. Furthermore, measuring common-Pb before and after perovskite crystallisation would establish if it changes, indicating Pb-heterogeneities in the upper mantle. Chapter 8 addressed the crystallisation sequence of the D/K1 kimberlite and demonstrated how perovskite crystallises after titanian-magnesian-aluminous-chromite and co-crystallises with ulvöspinel-magnetite, the peritectic clearly shown in Figure 4.9c. Hypothetically, the measured common-Pb in ulvöspinel-magnetites would match that of the perovskites. In practice this is less tenable because (i) a phase diagram for a kimberlite melt at these pressures and temperatures has not accurately been constrained because we do not know the composition of a primary kimberlite magma, and (ii) at Letlhakane, groundmass ulvöspinel-magnetites are smaller than perovskites, and would therefore require more precise and sensitive common-Pb analysis that LA-ICP-MS. The alternative of measuring common-Pb from phases crystallising before and after perovskite has the same issue of not fully understanding kimberlite phase equilibria, and furthermore many phases have been substantially altered since emplacement, and would therefore produce non-inheritance ages (Cox & Wilton, 2006).

Storey et al. (2006) demonstrated a correlation between signal intensity and deviation of corrected $^{207}Pb/^{206}Pb$ ratios from the ideal, concordant ages. Although this was not observed in Letlhakane perovskites, there was a subtle correlation between laser spot size and corrected $^{207}Pb/^{206}Pb$ ratios implying a link between grain size and reliability of the calculated age, although interestingly this was not observed in the perovskites from Cox & Wilton (2006), however the perovskites used were 0.5 cm, compared with $\leq$50 μm in this study. The effect of parameters including laser spot size, grain size, intensity and predicted age on the reliability of the calculated age must be investigated to develop this technique in the future. It is possible that a quadrapole-based ICP-MS is not sensitive enough for this type of analysis.

An additional point to consider for future U-Pb perovskite dating is to parameterise an external standard, although both Cox & Wilton (2006) and Storey et al. (2006) confidently demonstrate zircon as a veracious candidate, ideally in radiogenic dating a crystallographically-analogous mineral is used to determine U/Pb ratios.

D.5 U-Pb Dating Conclusion

U-Pb dating of a selection of Letlhakane perovskites using the inexpensive *in situ* technique designed by Jeffries et al. (2003) and Storey et al. (2006) produced ages between 74.1 $\pm$ 7.9 Ma and 101.5 $\pm$ 4.0 Ma. However, due to an anomalous initial common-Pb ratio and low counting statistics these ages are considered unreliable. Even so, it is unfortunate the ages do not place emplacement of Letlhakane before or after that of Orapa, which would have been very interesting considering Orapa has a crater whereas Letlhakane does not, even though the two pipes are spatially separated only by 40 km.

Despite the failure of this study in terms of the original goals, important issues have been raised which must be considered to further develop this as a technique. One key issue, relevant to other chapters of this thesis, is the crystallisation path of a kimberlite magma. A fully quantified phase diagram is not yet available,

however we can propose cystallisation sequences based on petrographic relationships and compositional variations, as was done in Chapters 4 and 5, and by Mitchell (1986b).

In situ, accurate dating of perovskites in kimberlite inexpensively and rapidly is important in order to fully understand individual kimberlite bodies and evolving this knowledge towards the development of a more general model for kimberlite emplacement. In particular, the specific variation in pipe ages within the same cluster or province, and how these relate to heterogeneities in mantle xenoliths and diamond proportions, for example. Developing more sensitive analytical procedures will enable accurate dating of individual lithofacies, providing understanding of elapsed time between eruptive phases, enhancing our knowledge of emplacement dynamics in a kimberlite pipe.